Title

Aqueous Degradation of Materials: Studies on Steel Corrosion and Acoustically Stimulated Mineral Dissolution

Author

Dong, Shiqi

Publication Date

2020

Peer reviewed|Thesis/dissertation

UNIVERSITY OF CALIFORNIA

Los Angeles

Aqueous Degradation of Materials:

Studies on Steel Corrosion and Acoustically Stimulated Mineral Dissolution

A dissertation submitted in partial satisfaction of the

requirements for the degree Doctor of Philosophy

in Materials Science and Engineering

By

Shiqi Dong

2020

ABSTRACT OF THE DISSERTATION

Aqueous Degradation of Materials:

Studies on Steel Corrosion and Acoustically Stimulated Mineral Dissolution

By

Shiqi Dong

Doctor of Philosophy in Materials Science and Engineering

University of California, Los Angeles, 2020

Professor Gaurav Sant, Co-Chair

Professor Mathieu Bauchy, Co-Chair

This work probed the two types of solid degradation in aqueous environment: steel corrosion, and acoustically stimulated mineral dissolution.

First, the steel corrosions in gas/oil wells and nuclear power plant environment were studied. The inhibition of corrosion of API-P110 steel by $Ca(NO_3)_2$ was first studied using vertical scanning interferometry (VSI) in halide-enriched solutions. The results indicate that, at low concentrations, $Ca(NO_3)_2$ successfully inhibited steel corrosion in the presence of both $CaCl_2$ and $CaBr_2$. Statistical analysis of surface topography data reveals that such inhibition results from suppression of corrosion at fast corroding pitting sites. Built on the methodology established from above, the effect of grain orientation on the corrosion rates of austenitic AISI 316L stainless steel was studied. The oxidation rates follow a scaling that is given by: {001} < {101} < {111} for grains undergoing both active and transpassive oxidation. The corrosion

tendencies of {001} and {101} grains indicate that the activation energy of dissolution follows a scaling similar to that of the surface energy. However, the high corrosion rates of {111} grains, which featured a surface energy lower than those of the {001} and {101} grains, is attributed to their lower tendency to adsorb passivating species, from solution, that leads to a net reduction in the activation energy of oxidation.

Second, this work further investigated the low-temperature pathway of aqueous activation of minerals and industrial alkaline wastes using acoustic stimulation, as an alternative to calcination process in cement production. It is revealed that the acoustic fields enhance mineral dissolution rates (reactivity) by inducing atomic dislocations and/or atomic-bond rupture. The relative contributions of these mechanisms depend on the mineral's underlying mechanical properties. Based on this new understanding, a unifying model was created that comprehensively describes how cavitation and acoustic stimulation processes affect mineral dissolution rates. On the basis of the mechanisms described above, the effectiveness and efficiency of applying acoustic stimulation in dissolving industrial alkaline wastes were further analyzed. Ultrasonication promoted dissolution of air-cooled blast furnace slag (ACBFS) in a significant and more energy-efficient manner, compared to traditional methods, such as grinding the solute, heating, and/or convectively mixing the solvent. The advantages of acoustic stimulation for dissolution enhancement and for energy savings are also observed for Si release from stainless steel slag (SSS), Class C fly ash, and Class F fly ash. The results demonstrate the wide applicability of acoustic processing, and the outcomes offer new insights into additive-free pathways that enable waste utilization, circularity, and efficient resource extraction from industrial wastes that are produced in abundance globally.

The results yielded from this work provide enhanced understanding of corrosion inhibition and suggest processing pathways for improving the oxidation resistance of steels in different industry scenarios. In addition, the results provide insights of additive-free pathway by using acoustic stimulation to enable fast elemental extraction from mineral species into aqueous solution.

The dissertation of Shiqi Dong is approved.

Dwight Christopher Streit

Jaime Marian

Mathieu Bauchy, Committee Co-Chair

Gaurav Sant, Committee Co-Chair

University of California, Los Angeles

2020

To my family,

for their love, and endless support.

TABLE OF CONTENTS

LIST OF FIGURES

LIST OF TABLES

ACKNOWLEDGEMENT

My Ph.D. study in UCLA would not be accomplished without the support, guidance, companionship, and help from my advisors, family, colleagues and friends. I want to thank all the great people I met in UCLA.

Firstly, I wish to express my sincere gratitude to my advisor Prof. Gaurav N. Sant for offering the opportunity to pursue my Ph.D. degree in such an impactful research group. I would extend my great thanks to both Prof. Gaurav N. Sant and Prof. Mathieu Bauchy, for their mentorship and guidance over the past four years.

Besides, I would also like to thank the rest of my thesis committee, Prof. Dwight C. Streit and Prof. Jaime Marian, for their suggestions and insightful comments to my doctoral research, which led me to think critically and deeply about the research questions.

I appreciate the current and past members in Laboratory for the Chemistry of Construction Materials (LCC) and Physics of AmoRphous and Inorganic Solids Lab (PARIS) for their help in my Ph.D. study. My sincere thanks should first to go Dr. Xin, Chen, Dr. Erika La Plante, Dr. Bu Wang, Dr. Ross A. Arnold, Dr. Longwen Tang, and Dr. Dante Simonetti, for their supervision, help, and guidance in my Ph.D. research. To Sharon, I cherished the time that we supported each other, within and outside of research. To Steven, thank you for making my lab work happier with your optimism and humor.

I would like to extend my appreciation to Prof. Shane White at UCLA and Miss. Xinwen Wang in China for sharing their life philosophy and guided me to the right direction through hard times in my Ph.D. life. I would also like to thank my family for supporting me spiritually throughout my life.

Finally, I would like to acknowledge the journals that made publication of my work possible:

- Chapter 2 is a version of: Dong, S., La Plante, E. C., Chen, X., Torabzadegan, M., Balonis, M., Bauchy, M., and Sant, G. Steel corrosion inhibition by calcium nitrate in halide-enriched completion fluid environments. *npj Materials Degradation* **2018**, 2, 32. DOI: 10.1038/s41529-018-0051-4.
- Chapter 3 is a version of: Dong, S., Chen, X., La Plante, E. C., Gussev, M., Leonard, K., and Sant, G. Elucidating the grain-orientation dependent corrosion rates of austenitic stainless steels. *Materials & Design* **2020**, 191, 108583. DOI: 10.1016/j.matdes.2020.108583.
- Chapter 4 is a version of: Tang. L.*, Dong. S.*, Arnold, R., La Plante, E. C., Vega-Vila, J. C., Prentice, D., Ellison, K., Kumar, A., Neithalath, N., Simonetti, D., Sant, G., and Bauchy, M. Atomic dislocation and bond-breaking govern dissolution enhancement under sonication. Accepted by *ACS Applied Materials & Interfaces*, November 2020. DOI: 10.1021/acsami.0c16424. (*Equal-contribution authors)
- Chapter 5 is a version of: Dong. S., Arnold, R., La Plante, E. C., Bustillos, S., Kumar, A., Simonetti, D., Bauchy, M., and Sant, G. Additive-free dissolution enhancement of industrial alkaline wastes using acoustic stimulation. *In preparation.*

VITA

Education

2014	B.S., Microelectronics
	Fudan University
	Shanghai, China
2020	Ph.D. Candidate, Materials Science and Engineering
	University of California, Los Angeles
	Los Angeles, US

Publications

Dong, S., Chen, X., La Plante, E. C., Gussev, M., Leonard, K., and Sant, G. Elucidating the grain-orientation dependent corrosion rates of austenitic stainless steels. *Materials & Design* **2020**, 191, 108583.

Dong, S., La Plante, E. C., Chen, X., Torabzadegan, M., Balonis, M., Bauchy, M., and Sant, G. Steel corrosion inhibition by calcium nitrate in halide-enriched completion fluid environments. *npj Materials Degradation* **2018**, 2, 32.

Dong. S., Arnold, R., La Plante, E. C., Bustillos, S., Kumar, A., Simonetti, D., Bauchy, M., and Sant, G. Additive-free dissolution enhancement of industrial alkaline wastes using acoustic stimulation. Prepared for submission to *ACS Sustainable Chemistry*, December **2020**).

Tang. L.*, **Dong. S**.*, Arnold, R., La Plante, E. C., Vega-Vila, J. C., Prentice, D., Ellison, K., Kumar, A., Neithalath, N., Simonetti, D., Sant, G., and Bauchy, M. Atomic dislocation and bond-breaking govern dissolution enhancement under sonication. Accepted by *ACS Applied Materials & Interfaces*, November **2020**. (**Equal-contribution authors*)

Dong, S., Liu, Y., Hong, Z., Yao, E., Sun, P., Meng, L., Lin, Y., Huang, J., Li, G., and Yang, Y. Unraveling the High Open Circuit Voltage and High Performance of Integrated Perovskite/Organic Bulk-Heterojunction Solar Cells. *Nano letters* **2017,** 17, 5140-5147.

Liu, H., **Dong, S.**, Tang, L., Krishnan, N. A., Sant, G., and Bauchy, M. Effects of polydispersity and disorder on the mechanical properties of hydrated silicate gels. *Journal of the Mechanics and Physics of Solids* **2019,** 122, 555-565.

Liu, H., **Dong, S.**, Tang, L., Krishnan, N. A., Masoero, E., Sant, G., and Bauchy, M. Long-term creep deformations in colloidal calcium–silicate–hydrate gels by accelerated aging simulations. *Journal of Colloid and Interface Science* **2019**, 542, 339–346.

Zuo, L., **Dong, S.**, De Marco, N., Hsieh, Y.-T., Bae, S.-H., Sun, P., and Yang, Y. Morphology evolution of high efficiency perovskite solar cells via vapor induced intermediate phases. *Journal of the American Chemical Society* **2016**, 138, 15710-15716.

Chen, X., Shah, K., **Dong, S.**, Peterson, L., La Plante, E.C., and Sant, G. Elucidating the Corrosion-Related Degradation Mechanisms of a Ti-6Al-4V Dental Implant. *Dental Materials* **2020**, 36, 431–441.

You, Y., Yang, K., Yuan, S., **Dong, S.**, Zhang, H., Huang, Q., Gillin, W. P., Zhan, Y., and Zheng, L. An Organic Multilevel Non-Volatile Memory Device Based on Multiple Independent Switching Modes. *Organic Electronics* **2014**, 15, 1983–1989.

Yao, E.-P., Yang, Z., Meng, L., Sun, P., **Dong, S.**, Yang, Y. and Yang, Y. High-Brightness Blue and White LEDs Based on Inorganic Perovskite Nanocrystals and Their Composites. *Advanced Materials* **2017**, 29, 1606859.

Zuo, L., Guo, H., deQuilettes, D. W., Jariwala, S., Marco, N. D., **Dong, S.**, DeBlock, R., Ginger, D. S., Dunn, B., Wang, M., and Yang, Y. Polymer-Modified Halide Perovskite Films for Efficient and Stable Planar Heterojunction Solar Cells. *Science Advances* 2017, 3, e1700106.

Zuo, L., Chen, Q., De Marco, N., Hsieh, Y.-T., Chen, H., Sun, P., Chang, S.-Y., Zhao, H., **Dong, S**., and Yang, Y. Tailoring the Interfacial Chemical Interaction for High-Efficiency Perovskite Solar Cells. *Nano Letter* **2017**, 17, 269–275.

Chapter 1. Introduction

1.1 Background and Motivation

This work probed the two types of materials degradation in aqueous environment: steel corrosion, and acoustically stimulated mineral dissolution.

Corrosion is a common chemical attack to metals and alloys by reaction with its environment, which could lead to property degradation of materials and failure of metallic components.[1] Studies of national cost of corrosion revealed that the total estimated direct cost of corrosion in the US was about 3%-4% of the nation's gross domestic product (GDP).[2] For example, in 2002, the US Federal Highway Administration (FHWA) reported that the annual cost of corrosion in the US was US$276 billion, and in 2017 the global cost of corrosion was estimated to be US$2.5 trillion.[2,3] The cost of corrosion in the oil and gas production industries accounted for more than half of cost of all US industries.[4,5] Currently, many components used for oil and gas extraction are made from carbon steel-based alloys.[5] The complex aqueous environment in the well makes the steel susceptible to different types of corrosion including crevice corrosion, pitting corrosion, and stress corrosion cracking (SCC).[6] Stainless steels are widely found in the majority of the components holding radioactive water or gas in the nuclear power plant.[7] Supercritical water reactor (SCWR) is a strongly aggressive oxidizing environment, where the steels of structural materials and fuel elements of reactor are susceptible to general corrosion and stress corrosion cracking.[8] In boiling water reactors (BWR), the coolant water at the core exhibits strong oxidizing properties, which makes the steel susceptible to transpassive corrosion.[9] In both cases, the passive film on stainless steel is broken down, and the steel dissolves progressively.[10]

The rock-forming minerals widely occur in Earth's crust.[11] They are potent sources of alkali, alkaline-earth, and silicon species, the aqueous liberation of which through dissolution enables various applications, such as calcium extraction for CO_2 mineralization and silicon recovery for fertilizer.[12,13] Acoustic stimulation via ultrasonication offers pathways to expedite and control chemical reactions of relevance to element extraction.[14] It is referred to as 'green technology' because the ultrasonic processing mitigate the requirement on energy and chemicals that are harmful to environment.[15] Acoustic perturbation has been shown to yield an significant enhancement in the kinetics of mineral dissolution, which scales with the mineral's hardness and average bond energy, and therefore could offer potential application to aqueous mobilization of mineral and industrial alkaline wastes, as an alternative to calcination process in traditional cement production which features the high energy and carbon footprint.[16]

Surface energy of a solid is the excess free energy compared to the bulk of the material resulted from the broken bonds at the surface.[17] The surface energy is a function of both bond energy of the material and broken bond number at the solid surface.[18] For monophasic polycrystalline solids, e.g., metals and alloys,[19] the variation in energy over the entire solid surface is caused by the randomly oriented grains that are embedded in the solid. Due to the non-uniform surface energy, most solids exhibit chemical heterogeneity, even though the grains have the same chemical composition and crystalline structure.[20] The surface energy influences the kinetics of the interfacial processes such as adsorption, etching, dissolution, and passivation.[21–23] The research described herein was primarily aimed to answer the following two questions:

- What is the effect of grain-specific surface energy on the corrosion rate of stainless steel when the passive film is absent?

- How does the surface energy of minerals control their increases in dissolution rate induced by acoustic stimulation?

In order to drive the answers to these questions, two hypotheses were proposed initially:

- When the passive film is absent, the corrosion of stainless steel becomes more of uniform dissolution. Grains with a higher surface energy are less stable thermodynamically and therefore tend to corrode at a faster rate.
- The collapse of cavitation bubble formed under acoustic stimulation causes atomic bond-breaking of the mineral species. The surface energy can serve as an indicator of the easiness of which bond-breaking occur along the surface of minerals, which lead to processes such as fracture, and thin slice flake-off.

1.2 Steels and Steel Corrosion

1.2.1 Materials selection

Steels are classified by composition and application into four categories: carbon steels, alloy steels, stainless steels, and tool steels.[24] The grades of steels are designated by organizations such as American Society for Testing and Materials (ASTM), American Iron and Steel Institute (AISI), Society of Automotive Engineers (SAE).[25] In this study, the selection of steel materials is based on two specific use cases in industry, i.e., carbon steel (type API 110, Chapter 2) in the petroleum production and stainless steel (type AISI 316, Chapter 3) in the nuclear power plant.[26,27]

1.2.1.1 Carbon steel

Carbon steels, typically with carbon content less than 1.5%, are widely used in various applications, such as industrial pipes, and structural components.[28] In AISI/SAE standards, carbon steels are designated with four-digit number, with the last two digits indicating the approximate middle of the carbon range expressed in hundredth of one percent, and the first two digits indicating a subcategory of carbon steels, such as nonresulfurized high-manganese and free-machining resulfurized.[24] Particularly in oil and gas industry, the steel is graded by American Petroleum Institute (API) standard based on the minimum yield strength. For example, API P110, with minimum yield strength 110 ksi, is a high strength steel grade and can endure high pressure, and thus is used in deep wells.[29] The yield strength of carbon steel typically varies from 300-700 MPa.[30]

1.2.1.2 Stainless steel

Stainless steels contain a minimum of 11% chromium that prevents the iron from corrosion attack by forming a passive protective film.[31] Stainless steel is classified by crystalline structure into: austenitic, ferritic, martensitic, and duplex.[32] Austenitic stainless steels (200 and 300 series) possess a face-centered cubic crystal structure, with a basic composition of 18% chromium and 8% nickel.[33] Addition of elements such as molybdenum, e.g., AISI 316 stainless steel, renders austenitic stainless steel more resistant to pitting corrosion.[34] Ferritic stainless steels possess a body-centered cubic ferrite crystal structure, containing only chromium and little nickel.[35] Martensitic stainless steels possesses a body-centered tetragonal structure.[36] The low chromium and high carbon content renders high strength while low corrosion resistance compared to other stainless steels.[37] Duplex stainless steels possess a mixed structure of ferrite

and austenite, and as a result exhibit the combination properties of the two phases, e.g., the toughness and weldability of austenite and the strength and corrosion resistance of the ferrite.[32]

1.2.2 Steel corrosion

1.2.2.1 Thermodynamic aspects of steel corrosion

Metallic corrosion is an electrochemical process where electrons are released by the metal being oxidized and then consumed by the oxygen or proton being reduced. When expose to an aqueous environment, there is a strong thermodynamic-driving force for steels and most metals to corrode.[38] The Pourbaix Diagrams is a potential-pH diagram and indicates certain regions of potential and pH where the metal undergoes corrosion and other regions of potential an pH where the metal is protected from corrosion.[38] The regions or fields in a Pourbaix diagram between the various lines, i.e., horizontal line (which are for reactions involving only the electrode potential but not the pH), vertical line (which are for reactions involving only the pH but not the electrode potential), and slanted line (which pertain to reactions involving both the electrode potential and the pH), where specific chemical compounds or species are thermodynamically stable.[39] The Pourbaix Diagram for iron suggests that iron can undergo corrosion in acid or neutral solutions in two different oxidation states, i.e., Fe^{2+} or Fe^{3+}.[40] Passivity is provided by oxide films of $Fe^{3}O^{4}$ or $Fe^{2}O^{3}$, and corrosion in alkaline solution occurs at the complex anion $HFeO^{2-}$.[40]

1.2.2.2 Kinetic aspects of steel corrosion

Corrosion rates of metals undergoing uniform corrosion can be determined by various methods, including weight loss method, weight gain method, chemical analysis of solution,

electrical resistance probes, electrochemical techniques.[41–43] Based on the absolute reaction rate theory developed by Glasstone, Laidler, and Eyting,[44] the electrochemical kinetics is described by the Bulter-Volmer equation:[45]

$$j = j_0 \cdot \{\exp\left[\frac{\alpha_a zF}{RT}(E - E_{eq})\right] - \exp\left[-\frac{\alpha_c zF}{RT}(E - E_{eq})\right]\}. \quad (1\text{-}1)$$

Here, j is the electrode current density, j_0 is the exchange current density (i.e., current density at open circuit potential), E is the electrode potential, E_{eq} is the equilibrium potential (i.e., open circuit potential), T is absolute temperature, z is the number of electrons involved in the electrode reaction, F is the Faraday constant, R is the universal gas constant, α_c is the cathodic chare transfer coefficient, α_a is the anodic charge transfer coefficient, and E - E_{eq} is defined as the overpotential. Typically, the charge transfer coefficient follows the relation of α_c = 1- α_a. The Bulter-Volmer equation describes how electrical current through an electrode depends on the voltage difference between the electrode and the bulk electrolyte for a simple, unimolecular redox reaction, considering that both a cathodic and an anodic reaction occur on the same electrode.[46–48] Plots of log j vs. E or vs. (E - E_{eq}) are called *polarization curves*, also called Tafel curves, which are the basic kinetic law for any electrochemical reaction.[38] Determined by the magnitude of the overpotential, there are two limiting cases of the Bulter-Volmer equation. When the overpotential is low (polarization resistance), i.e., when $E \approx E_{eq}$, the Bulter-Volmer equation is simplified to:

$$j = j_0 \frac{zF}{RT}(E - E_{eq}). \quad (1\text{-}2)$$

The Tafel curve is not linear near the open-circuit potential, (i.e., zero overvoltage). This is because the other half-cell reaction is still appreciable and contributes to the total current.[38]

When the overpotential is high, the Bulter-Volmer equation is simplified to the Tafel equation:

$$E - E_{eq} = a_c - b_c log j \text{ for cathodic reaction when } E \ll E_{eq} \quad (1\text{-}3)$$

$$E - E_{eq} = a_a + b_a log j \text{ for anodic reaction when } E \gg E_{eq} \quad (1\text{-}4)$$

where a and b are constants (for a given reaction and temperature) for the Tafel equation.[49]

1.2.2.3 Passivity of steels

As noted by Macdonald, the 'passivity' of metals, where they react with water and/or with oxygen to form stable passive oxide films, is the key to the metals-based civilization, as the metals (such as iron, chromium, and aluminum) are all inherently reactive.[50] The passive film on stainless steel tend to be very thin, i.e., in the range of 10–50 Å.[51,52] The active-passive transition of stainless steel can be identified in the anodic polarization curve, where the current density decreases with the further increase in potential after a critical point, i.e., the Flade potential, indicating the formation of passive film.[38] The structure and chemical composition of the passive oxide film on iron has been described in the well-known *bilayer model*, which states that the passive film on iron consists of an inner layer of Fe_3O_4 adjacent to the metal and an outer layer of γ-Fe_2O_3.[53–55] Modification of this bilayer model that has been proposed states that the outer layer contains hydroxyl groups[56] and is γ-FeOOH,[57,58] or is a mixture of Fe_3O_4, γ-Fe_2O_3, and hydroxide or oxyhydroxide.[59] As for stainless steel, the outer region of the passive film contains oxide of Cr^{3+}, while the inner and outer regions contain both oxides of Cr^{3+} and Ni^{2+}.[60] When the stainless steel contains molybdenum as an alloying element, Mo^{4+} is incorporated into the inner region of the passive layer, whereas Mo^{6+} is incorporated in the outer layer.[61,62] When the aqueous solution contains Cl^-, the chloride ions also participate in the formation of the passive film, both in the hydroxide and oxide layers.[63] Herein, the beneficial effect of Mo in stainless steel, e.g., type AISI 316 stainless steel, is that it forms soluble complex with Cl^- and thereby lowers the amount of Cl^- in the film, making the steel more resistant to pitting.[63] Nevertheless,

studies have suggested that Mo is beneficial to passivity only when Cr is present, as Mo does not help passivity of Fe[64,65] but help with the passivity of Cr and Fe-Cr alloy.[65–67]

1.2.2.4 Types of steel corrosion

Uniform corrosion of steel occurs when the protective oxide layer is absent, e.g., in aggressive environment.[68] In uniform corrosion, the steel attacked evenly over its entire surface. The localized anodes and cathodes still exist but change over time and spread over the metal surface so that the overall effect is that the metal is attacked uniformly.[38]

Crevice corrosion occurs in geometrical clearances, such as between overlapping metal sheets, or under bolt heads, or occurs under deposits, such as corrosion products or dust particles. Within the crevice oxygen is consumed and then depleted rapidly due to either cathodic reaction or passivation, which leads to the formation of a concentration cell.[69] Thus, the metal exposed in the crevice has a more negative (i.e., less positive) potential for oxygen reduction due to the lower concentration of oxygen, which results in the initiation of crevice corrosion.[38] In addition, acidification of the crevice area can take place as a result of anodic reaction and hydrolysis of the metal ions, which in turn enhances the corrosion within a crevice.[70]

Pitting corrosion is one of the most serious and troublesome forms of localized corrosion, where the passive film on the metal surface breaks down locally and the underlying metal is exposed to the corrosive environment.[71] Pitting is a dangerous form of corrosion attack as pits can be the initiation sites for stress-corrosion cracking in the presence of an applied stress.[72] Pitting potential, or breakdown potential, is defined by the American Society for Testing and Materials (ASTM) as the potential beyond which pitting propagates.[73] Once corrosion pits initiate, they usually propagate rapidly, as shown by the sharp rise in current density at electrode

potentials right beyond the pitting potential.[74] Pitting corrosion has been mostly associated with the presence of chloride ions (Cl^-) in the aqueous solution.[75–78] Study has found that the pitting potential decreases as the chloride concentration increases, i.e., more susceptible to pitting attack.[79] Three mechanisms have been proposed to describe the pit initiation process: the *penetration mechanism*, the *film thinning mechanism* and the *film rupture mechanism*.[80–82] In the *penetration mechanism*, aggressive anions are transported through the passive oxide film, possibly through oxygen vacancies as depicted by the point defect model, to the underlying metal surface where they participate in localized dissolution at the metal/oxide interface.[83–85] In the *film thinning mechanism*, the aggressive ions (chloride or others e.g., Br^-, that are larger in size) first adsorb on the oxide surface and then form surface complexes with the oxide film which leads to the local dissolution and thinning of the passive film.[86,87] In the *film rupture mechanism*, chloride ions penetrate the oxide through cracks or defects in the oxide film, and the presence of a high electric field in the oxide can lead to an electromechanical breakdown of the passive film.[88] The propagation of pitting involves the formation of a highly corrosive internal electrolyte, which is acidic (caused by the hydrolysis of accumulated metal cations that cannot diffuse out into the bulk electrolyte due to confined geometric volume) and concentrated in chloride ions and in dissolved cations of the metal or alloy.[89,90]

Transpassive corrosion is closely related to passive film breakdown and localized corrosion phenomena.[91] Transpassive corrosion occurs in the presence of strong oxidants such as chlorine dioxide or hydrogen peroxide, such that the valence state of the chemical species produced in transpassive corrosion is higher than that in the primary passive film formed on the material.[92–94] Transpassive corrosion of stainless steel is known to be due to oxidation of solid Cr(III) oxide in the passive film to soluble Cr (VI), i.e., CrO_4^{2-}, which depletes the protecting

element Cr and leaves the iron exposed to the aggressive anions.[95] Using electrochemical impedance spectroscopy (EIS) method, a generalized model of the transpassivity has been proposed, where the transpassive film is a highly doped n-i-p structure, the injection of negative defects at the transpassive film/solution interface leads to the accumulation of negative surface charge, and the dissolution of Cr as Cr(VI) and Fe as Fe(III) through the transpassive film via parallel reaction paths.[91] In the anodic polarization curve of electrochemical test, the transpassive region lies beyond the passive region, featuring an increase of current density with increasing potential.

Stress-corrosion cracking (SCC) occurs in susceptible alloys by the joint effects of a corrosive environment and sustained tensile stress.[96] In the supercritical water environment of power plant where the operating conditions call for a core coolant temperature up to 620 °C at a pressure of 25 MPa, problems of steel corrosion and stress corrosion cracking are pronounced.[97,98] It has been found that ferritic-martensitic steel generally have the best resistance to stress corrosion cracking but suffer from the worst oxidation, while austenitic stainless steel and Ni-based alloys have better oxidation resistance but are more susceptible to stress corrosion cracking.[98] Particularly, grain boundary engineering, by means of thermomechanical processing, is promising approach to address corrosion and stress corrosion cracking issues as shown to reduce spallation in Alloy 800, an austenitic steel.[98,99]

1.2.3 Steel corrosion inhibition

Theoretically, three corrosion control measures can be derived from the Pourbaix diagram of iron: (1) If the electrode potential is changed in the negative direction to a value below -0.7 V vs. SHE, the iron electrode is forced into a region of immunity; (this process is

called *cathodic protection*) (2) If instead, the electrode potential is changed in the positive direction to values above approximately 0.0 V vs. SHE, the iron electrode is forced into a region of passivity; (this process is called *anodic protection*) (3) The third method of protection is to change the pH of the aqueous solution. If the solution is increased to approximately 8 or higher, the iron electrode will then also reside in a region of passivity.[38]

Practically, metals and steels are usually protected from corrosion with a protective coating at the surface. In terms of metallic coatings, there are two types that are used to protect the underlying metal substrates: sacrificial and noble metal coatings. Sacrificial coatings function by cathodic protection of the substrate, e.g., protect the steel substrate by the sacrificial corrosion of zinc outer layer as zinc has a more negative electrode potential than steel in most corrosive environment.[100] Study has shown that the zinc-aluminum coating provides a longer lasting protection of the underlying steel than the conventional zinc galvanized coatings.[101] The noble metal coating on to top of has been demonstrated by a coating of nickel, which is more corrosion resistant though possessing a more positive potential than steel.[38] In terms of organic coatings, they are formulated by three components: pigment, vehicle or binder, and additives intended to be relatively permanent to serve specific protection of dry film.[102] Pigments provide colorant or other functions. Polymeric binders, e.g., polyaniline, have been widely used in coatings on the surface of materials, especially metals for the protection against corrosion.[103–105] When the polymer binder is in an electronically and ionically insulating form, it acts as a physical barrier to corrosion.[102] When electroactive-conjugated polymer is used in the binder, enhanced corrosion inhibition can be achieved via the formation of a passive layer on the metal as the conjugated polymer coating stores large quantity of charge at the interface.[102] However, the organic coatings are not robust enough is they can be penetrated by water, oxygen and ions (e.g., Cl-) and thus

corrosion may occur beneath the organic coating at the coating/metal interface.[38] Adding corrosion inhibitors (usually in low concentration) into the aggressive solution, on the other hand, is also a commonly used approach to increase the corrosion resistance of metals.[106–108] Generally the corrosion inhibitors fall into two categories: adsorption inhibitors and film-forming inhibitors.[38] Adsorption inhibitors form a chemisorptive bond with the metal surface and impede ongoing electrochemical dissolution reactions.[109] The film-forming inhibitors mitigate corrosion either by promoting the formation of a passive film on the surface (e.g., chromates)[110] or by participating the precipitation reaction that deposits a three-dimensional barrier film on the metal surface (e.g., phosphates).[111]

1.3 Minerals and Mineral Dissolution

1.3.1 Materials selection

1.3.1.1 Minerals

Herein, the term *mineral* refers particularly to rock-forming minerals, which are typically found in Earth's crust.[11] The naturally occurring minerals can be generally divided into silicate minerals and non-silicate minerals based on the composing elements. Silicate minerals makes up to 90% of all minerals in Earth's crust.[112] Silica tetrahedron, the primary building block of silicate minerals, can be arranged and linked together in different ways, forming a series of subgroup of silicate minerals with a variety of Si-O frameworks, such as nesosilicates, sorosilicates, cyclosilicates, inosilicates, phyllosilicates, and tectosilicates.[113] The non-silicate minerals generally include carbonates, oxides, sulfides and sulfates.[112] The carbonate minerals are made up of CO_3^{2-} anion and 2^+ cations, and are found as calcite ($CaCO_3$), magnesite ($MgCO_3$), dolomite ($(Ca,Mg)CO_3$), and siderite ($FeCO_3$).[114] The selection of minerals species in

this work (Chapter 4) is based on the abundancy of minerals in the nature and also covers a wide range of mineral classes and crystal families.

1.3.1.2 Slags and fly ashes

Herein, the term *slag* refers particularly to *ferrous slag*, given that iron and steel makes up more than 90% of the total metal processing industry.[115] In the iron and steel production process, different types of slags can be generated, as shown in Figure 1-1. Blast furnace slag is generated when iron core is melted in a blast furnace.[116] Depending on the rate and method of cooling, there are two major types of blast furnace slag: air-cooled blast furnace slags (ACBFS) formed when the molten iron slag is slowly cooled under atmospheric conditions, and granulated blast furnace slag (GBFS) when the slag is quenched with high-pressure of water.[117] In steel production, steel slag is generated during the conversion of hot metal to crude steel or during the melting of scrap in various kinds of furnaces.[116] Electric arc furnace slag (EAFS) and basic oxygen furnace slag (BOFS) are steel furnace slags produced when iron and/or scrap metals are oxidized either by applying electric current or by adding large amounts of pure oxygen, respectively.[117] In the electric arc furnace, two types of slags can by produced: carbon steel slag (CSS) and stainless steel slag (SSS).[118,119] Ladle slag (LS) is produced by further refining molten steel from electric arc furnace slag or basic oxygen furnace lag slags.[117]

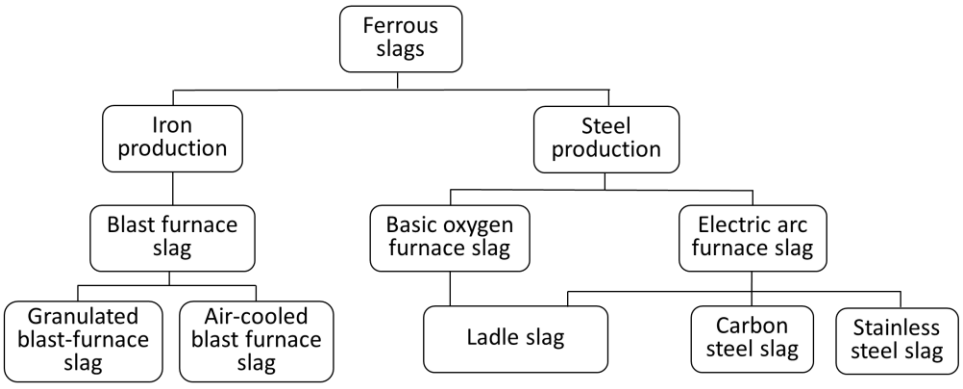

Figure 1-1: Different types of slags obtained in iron and steel production.

Fly ash (FA) is produced in the industrial production of energy which involves combustion of coal.[120] Two major types of fly ashes are classified by the ASTM C618 standards: Class F fly ash possessing pozzolanic properties and Class C fly ash possessing pozzolanic and additional cementitious properties.[121] The two types of fly ash differ in composition, e.g., Class C fly ash contains higher fraction of calcium oxide than Class F fly ash does.[122] Nowadays, fly ash find its application in various fields, such as soil amelioration, construction industry, ceramic industry, environmental protection, zeolite synthesis, and valuable metal recovery.[122–129]

In this study, the selection of slags and fly ashes is based on the abundancy, mineralogy, and chemical composition. For example, air-cooled blast furnace slag makes up over 90% of blast furnace slag due to the simplicity of cooling method. All the slags and fly ashes selected contain mostly oxides of silicon, the element of interest to study in Chapter 5, with variable amount of calcium, aluminum, and magnesium, and iron.[117]

1.3.2 Dissolution of minerals

1.3.2.1 Dissolution rate

The mineral dissolution reaction generally described by Eq. 1-5.

$$A_{\upsilon_A}B_{\upsilon_{B(S)}} \rightarrow \upsilon_A A_{(aq)}^{q_A} + \upsilon_B B_{(aq)}^{q_B} \quad (1\text{-}5)$$

The rate of reaction is expressed in amount of solid solute (in mol) reacted per unit time per unit volume.[130] The dissolution rate is commonly measured by the rate at which the concentration of dissolved species increases over time, or by the rate at which solute surface is recessing or mass is lost into the aqueous phase.[131] Typically, dissolution rates decreases over time due to multiple factors, such as increased reverse reaction with increased products concentration, and the nonstroichiometric dissolution of minerals.[132] For silicate dissolution, the area-normalized release rates of the solute components are found to change over time given by:

$$r = kt^{-0.5} \quad (1\text{-}6)$$

which gives rise to the term characteristic kinetics of *parabolic kinetics*.[133,134] The fast dissolution at the initial stage, e.g., dissolution of fine particles or sites with high surface free energy, is thought to be the cause of the parabolic kinetics of silicate dissolution.[135]

The temperature dependence of dissolution rate is modeled by Arrhenius equation:

$$k = A'\exp\left(-\frac{E_a}{RT}\right) \quad (1\text{-}7)$$

where A' is the pre-exponential factor, E_a is the activation energy, R is the gas constant and T is the temperature in degrees Kelvin.[136] The activation energy is the energy barrier between the reactants and products to overcome to initiate a reaction, and can be calculated from the slope of a plot of *ln k* versus *1/T*.[137]

1.3.2.2 Rate limiting steps of dissolution reaction

The full picture of dissolution reaction may include the following four processes: (1) the hydrated ion diffuses to the solid-liquid interface, (2) the hydrated ion forms a complex with the solute, (3) the surface atom of the solid is detached by desorption, and (4) detached atom (in ion form) diffuses away from the solid-water interface.[138] Dissolution rate of highly soluble and highly insoluble minerals tend to transport-limited and interface-reaction-limited, respectively.[130] The rate limiting step can be roughly indicated by the activation energy of dissolution reaction. For example, rate of dissolution reaction with activation energy as low as 5 kcal/mol is thought to be limited by the diffusion of reactants to the mineral or products away from the mineral.[130] The mass transport control of mineral dissolution can be tested by varying the agitation or flow rate of the reactor.[139] In contrast, rate of dissolution with activation energy as high as 20 kcal/mol is believed to be limited by bond-breaking in the reaction.[130] Both transport and interface limitation of dissolution have been studied for calcite, the most common carbonate mineral, with the dominance of rate-limiting step varying with pH.[140] The following reactions are thought to occur in parallel during calcite dissolution under ambient condition:[140]

$$CaCO_3 + H^+_{(aq)} = Ca^{2+}_{(aq)} + HCO^-_{3(aq)} \quad (1\text{-}8a)$$

$$CaCO_3 + H_2CO_{3(aq)} = Ca^{2+}_{(aq)} + 2HCO^-_{3(aq)} \quad (1\text{-}8b)$$

$$CaCO_3 + H_2O_{(aq)} = Ca^{2+}_{(aq)} + HCO^-_{3(aq)} + OH^-_{(aq)} \quad (1\text{-}8c)$$

Typically, the fastest reaction among all that take place in parallel is the rate controlling reaction, whereas the slowest step between mass transport and interface reaction is the rate-limiting step. For calcite, in the low-pH region, i.e., pH < 3.5, dissolution possesses a low activation energy and the rate is limited by mass transport; when pH is higher than 3.5, the interfacial reaction is

slower than transport and rate is interface-controlled; when above pH 5.5, the effect of precipitation reaction cannot be neglected.[140]

1.3.2.3 Theoretical models describing the variation of dissolution rate

Calcite, as an abundant and widely distributed mineral as well as an important component in the formation of many rocks, has received considerably research focus.[131,140–143] Over the past three-decade years of study, there has been accumulated a large dataset regarding dissolution rate of calcite, where discrepancy in the dissolution rate, particularly at neutral to basic region, has been observed, with variation larger than one order of magnitude.[131]

The dissolution rate of mineral is typically studied under far from equilibrium conditions.[130,144] Therefore, three approaches have been taken to treat the mineral dissolution: (1) treat the crystal dissolution rate as independent of undersaturation, (2) treat system as reaching near-equilibrium condition quickly (assumed by many natural studies), or (3) treat the kinetic rate law as a linear relation between rate and deviation from equilibrium.[145] In the third case, which considered the decreasing undersaturation impact on the temporally evolved dissolution rate, the rate law is given by:

$$Rate = A(1 - e^{\alpha\frac{\Delta G}{RT}}) \quad (1\text{-}9)$$

where A and α are general constants, which could vary with pH, temperature T, or inhibitor molecules. ΔG (<0) is the Gibbs free energy of the dissolution reaction, and R is the gas constant.[146,147] Specifically, the driving force for the reaction, ΔG, is defined as $\Delta G = RTln(\Omega)$, where Ω is the ratio of the reaction activity quotient, Q, and the equilibrium constant, K_{eq}, for the reaction at the specified temperature and pressure.[146] When the undersaturation is low, i.e, close

to equilibrium, etch pits will not open up because nucleation of pits is not energetically favored. Defect sites will not lead to stepwaves forming far from the localized etch pit so that steps only form at edges.[130,145] Therefore, the dissolution rate (e.g., spiral dissolution) is slow. When the undersaturation exceeded some critical value, i.e, $|\Delta G| > |\Delta G_{crit}|$, formation of an etch pit initiates from the hollow core that is opened up either by the zero-dimensional (point) defect or by one-dimensional (line) defect by the strain field of a dislocation in the mineral crystal.[130,148,149] Pits initiated at the point defects become flat-bottomed quickly because the defect is etched away.[130] Particularly at the highest degree of undersaturation, homogeneous nucleation occurs everywhere on the perfect surface.[130] Pits formed at the line defects continue to deepen along the dislocation line and can potentially grow into large pits laterally.[130,150] The Burton Cabrera Frank (BCF) model has been developed to quantify the values of the critical concentration that defines where pitting occurs at defects.[149,151,152] Assuming the pit consists of a cylindrical hole of radius ε and depth a, then the free energy of formation of this small pit is composed of volume, surface and elastic strain energy terms given by:

$$\Delta G_{dislocation} = \frac{\pi\varepsilon^2 aRTln(\frac{[A]}{[A_{eq}]})}{V} + 2\pi\varepsilon a\gamma - \frac{a\tau b^2}{4\pi}\ln(\frac{\varepsilon}{\varepsilon_0}) \quad (1\text{-}10)$$

Here, τ is an energy factor related to the dislocation, b is the Burger's vector describing the dislocation, ε_0 is the dislocation core radius, V is the molar volume, $[A]$ and $[A_{eq}]$ are the aqueous concentration and equilibrium concentration of species A in solution, and γ is the surface energy of the crystal-water interface.[130] The pits under large undersaturation are the source of a train of steps, which move away from the defect into the surface and lead to dissolution stepwaves.[145] The dissolution stepwaves can travel throughout the mineral surface and eventually control the bulk dissolution rate.[145] With the aid of absolute height reference of the dissolving surfaces, it

has been shown that the entire crystal surface is retreating in a global dissolution, i.e., the etch pits are masking the widespread dissolution of the overall surface,[145] and such global retreat has agreed well with the measured bulk dissolution rate or anorthite.[153] Taken all these together, spiral dissolution is not applicable in the high undersaturation region because step retreat occurs from all the sites in parallel.[145]

Generally speaking, steps nucleated at crystal edges, at dislocation etch pits, at impurity etch pits, at point defects, and at perfect surface dominate from low to high undersaturation respectively because the rates of reaction at these sites differs, and the relative number of these sites varies. The nonuniform dissolution rates at different active sites and the variation in the density of the active sites result in the discrepancy of in calcite dissolution rate existing in literature, which is thought to be amplified as the grain dimension, or particle size decreases.[131] Furthermore, a formulation has been developed and validated based on the defect-generation dissolution stepwaves of the variation of dissolution rate with the degree of undersaturation for the case of etch pitting dominated dissolution on smooth calcite crystal terraces.[145] Specifically, the step velocity on an etching pitting site with dislocation center is governed by:

$$v(r) = v_{step}\left[1 - \frac{1-e^{-\frac{\sigma v}{rkT}}e^{\frac{u(r)v}{kT}}}{1-e^{\frac{\Delta G}{kT}}}\right] \quad (1\text{-}11)$$

where $v(r)$ is the modified step velocity with defect and v_{step} is the velocity of a series of straight steps, σ is the surface free energy, v is the molecular volume, *k* is Boltzmann's constant, and $u(r)$ is the strain field of dislocation defects.[145]

1.3.3 Dissolution enhancement induced by acoustic stimulation

The acoustic stimulation of aqueous reaction stems from the cavitation effect. Cavitation can be defined as small gas bubbles being grown, oscillated and collapsed in a fluid while being affected by ultrasound waves.[154] When sound waves propagate in the liquid media, the liquid vibrates at a rate determined by the frequency of oscillating sound waves and exhibits high-pressure (compression) and low-pressure (rarefaction) cycles.[155] During the rarefaction cycle, high-intensity ultrasonic waves create small vacuum bubbles or voids, which normally nucleates from dissolved gas in the liquid.[156] When the bubbles attain a volume at which they can no longer absorb energy, they collapse violently during high-pressure cycle.[155] During the collapse of cavitation bubble, an extreme micro environment is created locally, with high temperature up to 5000 K (i.e., creation of 'hot spots') and pressure up to 1000 atm.[157] The acoustic cavitation may induce physical and chemical effects, typically observed as high heating and cooling rates,[158] luminescence of bubbles,[159–161] high strain rates near the bubble wall,[162] microstreaming of liquid around the bubble,[163] formation of microjet,[164,165] and production of radicals via lysis of solvent molecules.[166,167] Such effects may lead to augmentation of chemical reaction rates, erosion of solid surfaces or pitting, fragmentation of agglomerated powders in solution and particle breakage.[168–172] Acoustic perturbation reduces the activation energy to mineral dissolution, and thus has been demonstrated as an effective approach for isothermal stimulation of mineral dissolution across a range of mineral compositions with widely differing hardness and bond energy.[16]

1.4 Topographical Analysis Using Vertical Scanning Interferometry (VSI)

1.4.1 Basics of vertical scanning interferometry

The vertical scanning interferometry, a combination of white light interferometry and microscope in principle, provides a powerful solution to perform quantitative three-dimensional surface structure analysis.[173]

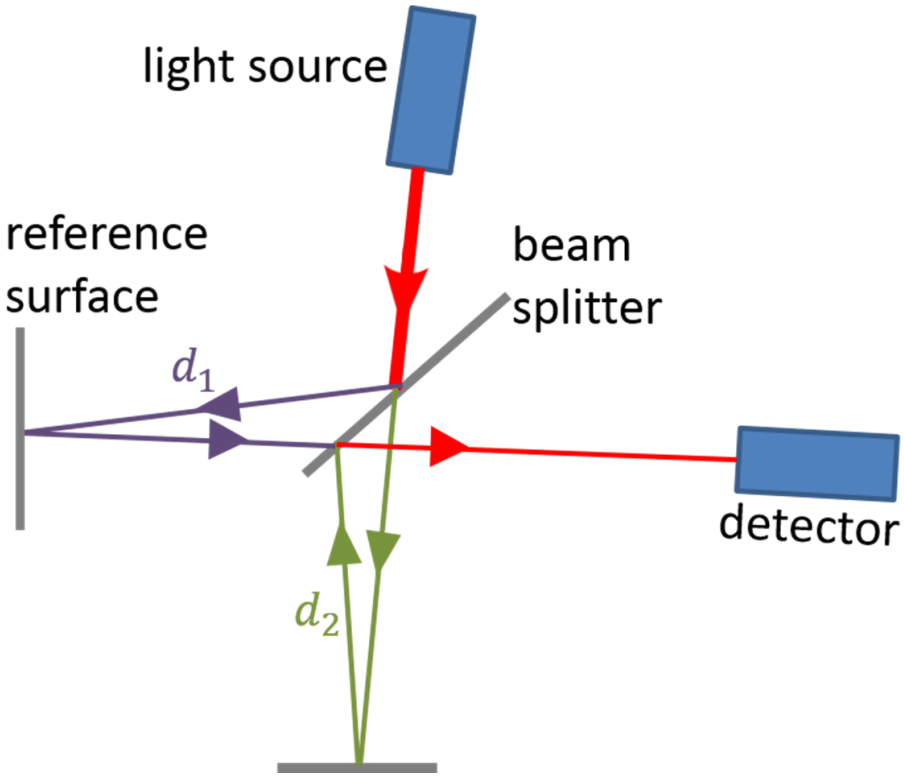

Figure 1-2: The light path through an interferometer. Image adopted from ref.[174,175]

Figure 1-2 shows the light path through a interferometer.[174] A single incoming beam of coherent light is split into two identical beams by a beam splitter (a partially reflecting mirror). Each of these beams travels a different rout, reflected by the reference surface and test surface,

respectively, and combine at the half-silvered mirror to reach the detector. The combination of the two light beams follow the superposition of waves:

$$W_1 + W_2 = I_1 cos(kx - \omega t) + I_2 cos(kx - \omega t + \varphi) \quad (1\text{-}12)$$

where W is wave amplitude, I is peak amplitude, k is wavenumber, ω is angular frequency, t is propagation time and φ is phase difference. Phase difference is given in Eq. (1-13),

$$\varphi = 2\pi \cdot \frac{d_2 - d_1}{\lambda} \quad (1\text{-}13)$$

where d_1 and d_2 are the optical paths of the light beams reflected by the reference surface and test surface, respectively, and λ is the central wavelength of the light beam. The combined light beams may either interfere constructively (strengthening in intensity) if their light waves arrive in phase, or interfere destructively (weakening in intensity) if they arrive out of phase, depending on the exact distances between the three mirrors. In other words, the optical path difference (OPD), given by $d_2 - d_1$ determines whether the detector sees a bright or a dark spot.

The schematic diagram of a typical white light interferometric microscope can be found elsewhere.[176]. The microscope integrated in the VSI system enables the examination of small objects. The objective directs light to test surface and creates interference. A piezoelectric (PZT) motor produces fine linear motion of the objective to realize 'vertical scanning'. Coherence length of light beam, given by Eq. (1-14), is inversely proportional to the bandwidth, or the spread of different frequencies, of the light.[177] White light interferometer is more commonly used than laser interferometer due to the longer coherence length of white light.[176]

$$l_c = \sqrt{\frac{2\ln 2}{\pi}} \frac{\lambda^2}{\Delta\lambda} \quad (1\text{-}14)$$

The interferograms of both laser and white light are shown in Fig. 1-3. The short coherence length of the white light compared to laser light reduces the intensity of the interference rapidly

as the OPD increases from zero. Outside the coherence length the light loses the ability to interfere in an observable way. Thus, the maximum of intensity occurs at the zero OPD point. In laser light interferometer, however, pixels with OPD = $1/4n\lambda$ are of similar intensities and cannot be distinguished. Therefore, white light interferometer is more powerful in resolving a rough surface.[176]

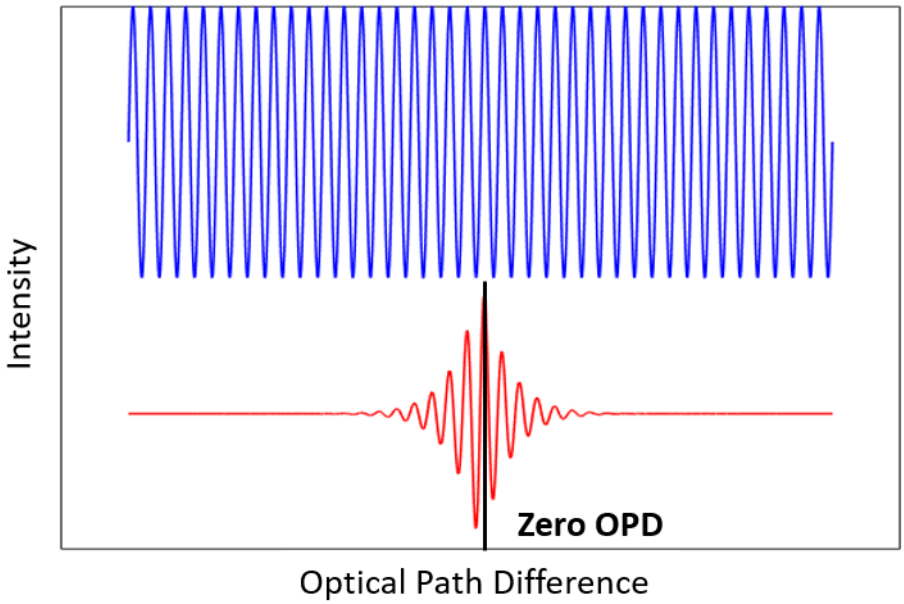

Figure 1-3: Interferogram of laser light (blue) and white light (red).

The topographical mapping of VSI follow the given steps:

1) Scan the objective in the z-axis.
2) Measure the intensity of the fringes over the entire range of the interferogram. Determine the point of zero OPD.
3) Create a relative height map of the entire field of view (FOV) for every pixel.

Principally, the zero OPD points map the surface of the test part.[178] Larger area mapping is enabled by the stage translational motion. The neighboring frames are 'stitched' with certain area overlap (e.g., 20%) to correlate relative height of each frame.[179]

1.4.2 Sample preparation and workflow for topography measurement

The planar samples of steel and minerals are embedded in epoxy to facilitate handling. In order to obtain the absolute height recess in corrosion or dissolution reaction, an unchanged surface, either using an inert material or partially covering the sample surface to preserve an unreacted area, is required to serve as a height reference. Figure 1-4a shows the top view of a steel specimen adjacent to an inert material, polytetrafluoroethylene (PTFE) as the height reference. A kinematic mount was used for positioning and aligning the steel samples on the VSI sample stage over the course of experiment, as shown in Figure 1-4b, so that the same areas on the samples surface and be located and repeatedly imaged over the duration of the test. The typical workflow of topography measurement for determining height change due to corrosion or dissolution is shown in Figure 1-4c. The topography of as-polished samples surface was initially measured to obtain the time-zero surface height. Following immersion test in corrosive solution or solvent, the steel or mineral surface was cleaned and then measured again to obtain absolute height change with the aid of reference (i.e., unchanged) surface.

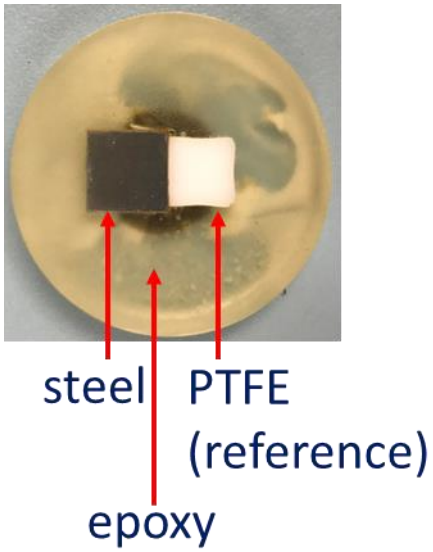

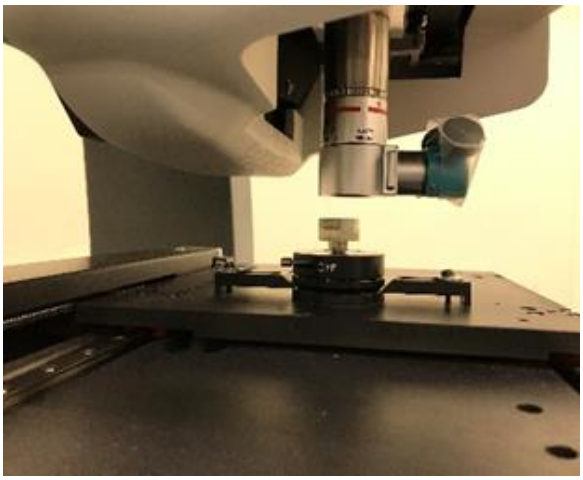

(a) **(b)**

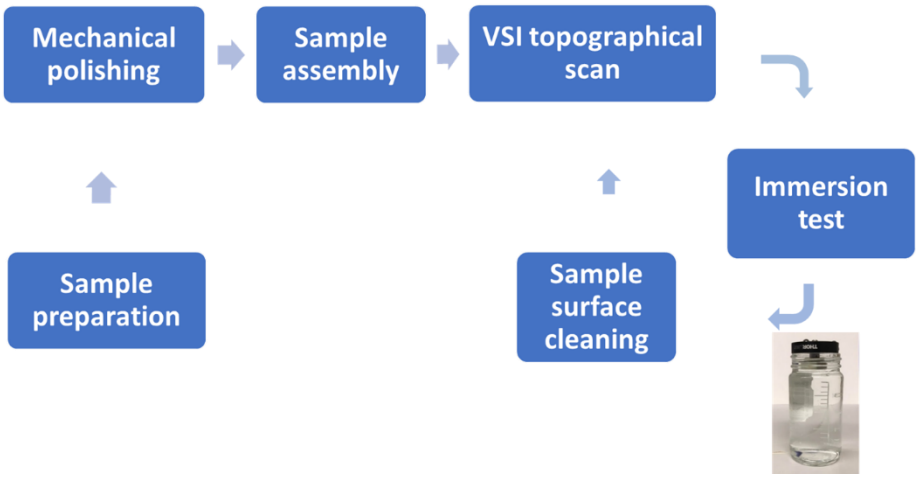

(c)

Figure 1-4: (a) Representative photo of a steel sample embedded in epoxy with the PTFE height reference. (b) Photo of the setup of topography measurement. (c) Workflow of the immersion corrosion test and topography characterization.

1.4.3 Topographical image processing and data analysis

The topography measurement by VSI outputs a 3-channel data detailing the lateral positions (i.e., x,y-coordinates) on the measured surface and vertical height (i.e., z-coordinate), with lateral resolution determined by the objective being used and vertical resolution on the order of 2 nm. For example, the lateral resolution rendered by a 5× and 100× Mirau objective is 0.163 μm and 0.081 μm, respectively. Therefore, the height level of a given area (reacting steel or mineral surface, or the reference surface) can be obtained by spatially averaging over all the pixel points measured within that area. The topographical measurement at each time gives the relative height information among pixel points over the entire surface. The absolute height values represent the vertical positions of objective when focusing at the tested surface and cannot be directly used for height change determination. Alternatively, the absolute height change of the sample surface, Δh, can be quantified by aligning the average reference height levels from consecutive measurements, as shown in the schematic diagram in Figure 1-5.

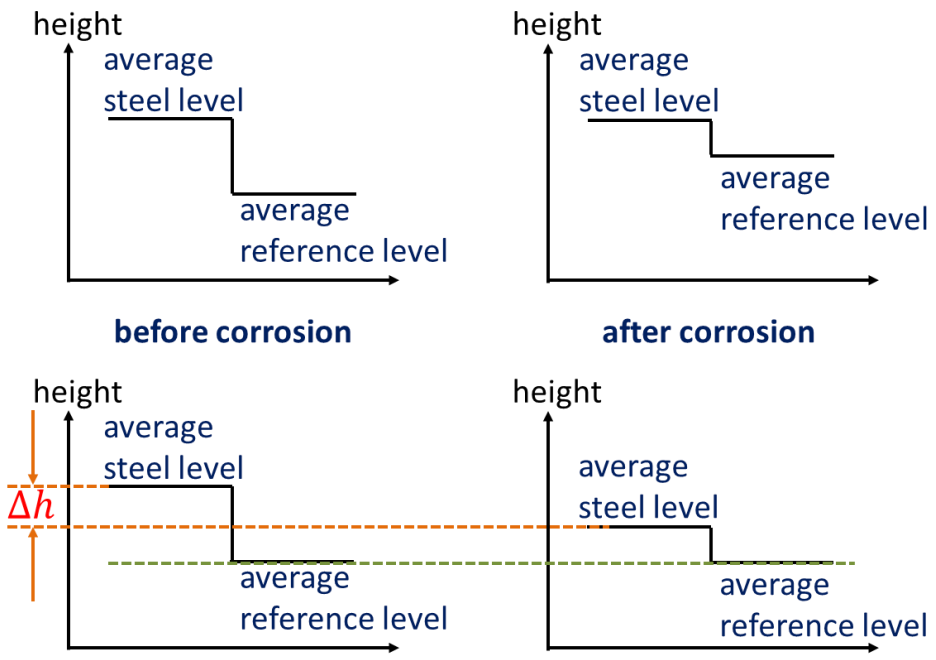

Figure 1- 5: Schematic diagram illustrating the methodology to quantify spatially averaged surface retreat relative to the unchanged reference surface.

1.5 Organization

This document is developed into six chapters.

Chapter one provides a broad overview of the motivation of this work, and gives a general introduction to the important concepts involved in the following chapters, i.e., materials selection for respective study, reaction mechanisms for steel corrosion, mineral dissolution, the acoustic cavitation mechanism which promotes the dissolution reaction in aqueous environment, the working principle of topography measurement and data analysis approach, and lastly the layout and organization of this manuscript.

Chapter two introduced the methodology establishment of drive statistical insights of steel corrosion from topographical analysis, with a case study of the steel corrosion inhibition effect by calcium nitrate ($Ca(NO_3)_2$, CN) in the halide concentrated completion fluid environments. The results indicate that, at low concentrations (≈ 1 mass %), $Ca(NO_3)_2$ successfully inhibited steel corrosion in the presence of both $CaCl_2$ and $CaBr_2$. Statistical analysis of surface topography data reveals that such inhibition results from suppression of corrosion at fast corroding pitting sites. However, at higher concentrations, CN's effectiveness as a corrosion inhibitor is far less substantial.

Chapter three answered the first research question proposed at the beginning of this chapter: What is the effect of grain-specific surface energy on the corrosion rate of stainless steel when the passive film is absent? It also demonstrated how topographical analysis can be coupled and superimposed with the microstructural information to analyze the grain-specific corrosion behavior and the corrosion rate of austenitic stainless steel. The results showed that surface energy control both the dissolution reaction of metals and adsorption of aqueous species forming a barrier layer to corrosion, and resulted in a corrosion rate following the scaling given by: {001} < {101} < {111} for grains undergoing both active and transpassive oxidation.

Chapter four turned to answer the second research question proposed at the beginning of this chapter: How does the surface energy of minerals control their increases in dissolution rate induced by acoustic stimulation? Leveraging both experimental and computational methods, the study revealed a dual mechanism on the enhancement of mineral dissolution by acoustic stimulation. An empirical model was proposed unifying the processes of particulate

fracture and creation of dislocation by sonication, with the probabilities controlled by the surface energy and stacking fault energy, respectively.

Chapter five took a preliminary step in evaluating the acoustic stimulation in application in industrial waste dissolution. The results demonstrate the wide applicability of acoustic processing, and the outcomes offer new insights into the creation of additive-free pathways that enable waste utilization, circularity, and efficient resource extraction from industrial wastes that are produced in abundance globally.

Chapter six summarized work described in this document, revised the initial hypotheses proposed at the beginning of this Chapter to reach the general conclusions, and recommended future work on related topics.

Chapter 2. Steel Corrosion Inhibition by Calcium Nitrate in Halide-enriched Completion Fluid Environments

2.1 Introduction and Background

High-density brines have brines long been used during drilling, completion, and workover operations during oil and gas production.[180] Concentrated aqueous solutions of halide salts of alkali and alkaline earth metals, which provide high fluid density while minimizing cost, are commonly used in these applications.[180] However, such high concentrations of halides, particularly chloride (Cl^-) and bromide (Br^-), are likely to result in significant corrosion of the steel pipe (sheath) that conveys fluid hydrocarbons to the surface.[181–183] Halides induce steel corrosion by a variety of processes including: break down of the air-born oxidation film, accelerating pit formation, and facilitating pit growth.[184–186] Chloride ions are considered to be more aggressive than Br^- due to their higher electron affinity and stronger adsorption on the oxidation film surface.[77]

Inhibitors such as calcium nitrite ($Ca(NO_2)_2$) and calcium nitrate ($Ca(NO_3)_2$) are known to retard the corrosion of reinforcing steel.[187–189] While $Ca(NO_3)_2$ is cheap and abundant, its ability to inhibit corrosion in highly-concentrated halide environments is not known. Nevertheless, it has been suggested that nitrate inhibits corrosion by facilitating the formation of ferric hydroxide ($Fe(OH)_3$) in the anodic corrosion region, decreasing the extent of iron migration as aqueous ferrous/ferric chlorocomplexes, and thereby reducing iron dissolution.[188,190] While corrosion inhibition by $Ca(NO_3)_2$ has been studied using electrochemical methods[191,192] – direct observations of corroding surfaces from the nano- to micron- scales, that can be rationalized against electrochemical studies have remained broadly unavailable.

Vertical scanning interferometry (VSI) can be used to study the kinetics of reactions at solid-liquid interfaces, including mineral dissolution, precipitation and metallic corrosion at unparalleled resolution.[145,173,193] The high lateral and vertical resolution[194] of VSI makes it ideally suited to monitor small changes in the topography of steel surfaces, due to processes such as the dissolution of steel,[195] precipitation of corrosion products[196] and the growth of the passive films[197], from the nano- to micron- scales. This capability offers significant advantages over electrochemical methods which, most often, can only measure bulk behavior.[191,192] Furthermore, the capability to probe spatially localized corrosion over large sample areas (10s of mm^2), presents advantages over scanning probe techniques which are most often restricted to examining small, very localized surface areas.[198,199]

Herein, the retarding effect of $Ca(NO_3)_2$ on the corrosion of American Petroleum Institute (API) P110 steel is examined in the presence of brines composed using calcium chloride ($CaCl_2$) or calcium bromide ($CaBr_2$).[200,201] Vertical scanning interferometry is used to quantitatively and statistically analyze three-dimensional (3-D) surface topographies, and their evolution, in time to reveal the mechanisms by which $Ca(NO_3)_2$ alters and suppresses halide-induced corrosion. The outcomes support the use of $Ca(NO_3)_2$ based brines in completion and workover fluid environments and provide insights into its behavior as a corrosion inhibitor.

2.2 Materials and Methods

2.2.1 Materials: Preparation of steel surfaces and brines

Commercially available API P110 steel (McMahon Steel Supply) with a nominal composition of C (0.25% This study investigated the effectiveness and energy efficiency of Si dissolution enhancement using acoustic stimulation, using air-cooled blast furnace slag

(ACBFS), Ca-poor Class F fly ash (FA), stainless steel slag (SSS) and Ca-rich Class C FA as representative alkaline waste materials in order to probe the under-developed additive-free pathway for Si extraction. The ACBFS and Class F species exhibited parabolic Si dissolution kinetics while dissolutions of SSS and Class C FA approached to saturation rapidly. Based on the case study of the parabolic dissolution of ACBFS, ultrasonication provided the most significant enhancement in the apparent Si release rate, as compared to traditional reaction acceleration approaches, i.e., mechanical grinding, mixing, and heating. Under sonication, the activation energy of dissolution reaction was reduced, lowering the energy barrier for Si-extraction and improving the energy efficiency of ultrasonic processing. The energy savings were primarily due to the shortened reaction time enabled by the higher rate enhancement by ultrasonication. Furthermore, the relative energy savings were correlated with the ratio between the ultrasonic effect and thermal effect, represented by $\Delta Ea/RT$. The kinetic benefit of a reduction in apparent activation energy led to a reduction in energy intensity of the overall dissolution process. The findings in this study demonstrate the potential of ultrasonic processing as an additive-free pathway for utilization of industrial alkaline wastes from both a kinetic (rate enhancing via reduction in activation energy) and practical (overall energy consumption) perspective.), Si (0.36%), Mn (1.24%), P (0.013%), S (0.004%), Cr (0.50%), Al (0.03%) and Fe (97.6%) was used. During its processing, this steel is quenched, giving rise to a microstructure that is characterized as monophasic martensite. The steel was machined into coupons having dimensions of 6 mm × 6 mm × 4 mm (length × width × height) and then embedded in epoxy resin to facilitate handling, while leaving only the top surface of the steel exposed. The steel surface was then polished successively using SiC sandpaper and diamond paste until it featured a surface roughness (S_z) of 1 μm. Thereafter, the sample was ultrasonically rinsed with ethanol and

deionized (DI) water for 3 minutes, and then stored in a desiccator after being dried under an air stream. The epoxy-mounted samples were secured on kinematic mounts (Thorlabs) to maintain imaging positions within ± 3 μm and ± 1 microradians over the course of the experiments.

Brines were prepared by adding ACS reagent grade $CaCl_2$, $CaBr_2$, and $Ca(NO_3)_2$ to deionized (DI) water to produce 10% $CaCl_2$ or 10% $CaBr_2$ solutions that contain 0%, 0.1%, 1%, and 10% $Ca(NO_3)_2$ (mass basis). The measured pH's of these solutions are listed in Table 2-1. These concentrations were chosen to encompass a wide range of $Ca(NO_3)_2$ concentrations to assess the effect(s) of a diversity of dosage levels, and potential changes in inhibition mechanisms and the resulting effects on corrosion evolutions.

Table 2-1. The pH's of the solutions used in the corrosion analysis.

	0% $Ca(NO_3)_2$	0.1% $Ca(NO_3)_2$	1% $Ca(NO_3)_2$	10% $Ca(NO_3)_2$
10% $CaCl_2$	6.09	6.16	6.21	6.25
10% $CaBr_2$	8.91	8.98	8.9	8.87

2.2.2 Methods

2.2.2.1 Surface topography evolutions captured using scanning interferometry

Corrosion behavior under brine immersion was monitored for up to 7 days at 25 ± 0.2 °C in a temperature-controlled environment. The surfaces of the steel samples were exposed to brine volumes on the order of 135 ± 2 mL resulting in a nominal surface-to-volume ratio (s/v, mm-1) of 1/9000. Prior to immersion, approximately half of the sample surface was covered with a peelable silicone mask (Silicone Solutions SS-380) to preserve a portion of the steel surface in a

pristine state, which serves as the reference surface. As a result, absolute height changes can be ascertained by comparing the reference surface with the reacted (i.e., exposed to brine) surface. The effectiveness of this procedure is illustrated in Figure 2-1, which shows VSI images of a steel surface before and following immersion. To assess the chemical stability of the silicone mask, concentrations of dissolved silicon in contact with brine were measured using a Perkin-Elmer Avio 200 inductively coupled plasma optical emission spectrometer (ICP-OES). Measured Si concentrations ranged from 0.13 – 1.14 ppm, with an average value of 0.64 ppm. This level of silicon abundance and negligible changes in the silicon mask's surface topography following immersion indicate that it is inert up on exposure to the brine environment.

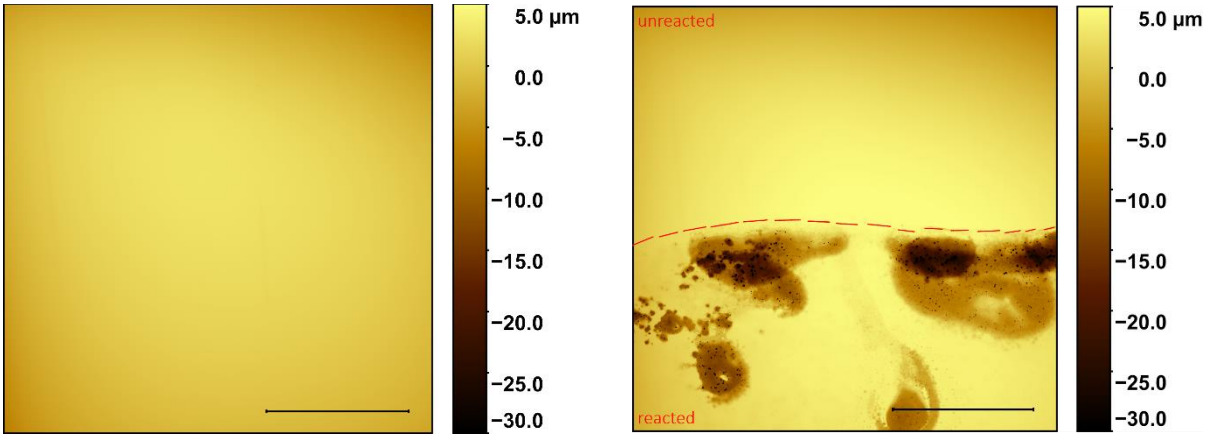

(a) **(b)**

Figure 2-1: Representative VSI topography maps of API P110 steel surface obtained **(a)** as-polished, and **(b)** following immersion in 10 mass % $CaCl_2$ brine for 7 days. The boundary between the unreacted ("masked") surface and reacted surface is labeled by the dashed line. The scale bars represent a length of 2 mm.

The steel's surface topography was monitored following its contact with the brines at time intervals of 0, 1, 3, 5, and 7 days. At each time point (except 0 days), any corrosion products which may have formed on the steel surface were removed following ASTM G1.26 Thereafter, the silicone adhesive was peeled cleanly and the surface topography was examined using vertical scanning interferometry (VSI). The interferometer used, a Zygo NewView 8200 VSI was fitted with a 5× Mirau objective having a numerical aperture of 0.13 and offering a lateral (in the x and y directions) resolution of 1.63 μm. The lateral resolution is determined by both the objective and the spatial sampling of the camera (1024 pixel × 1024 pixel in one field of view (FOV), i.e., 1.67 mm × 1.67 mm). The resolution in the z-direction is estimated to be on the order of ± 2 nm based on analysis of a NIST traceable step-height standard. Imaging of the entire steel surface that encompassed an area on the order of 12-to-15 mm2 was carried out by stitching multiple overlapping sub-images that were acquired sequentially along a grid map. It should be noted that the use of kinematic mounts as described above enabled repeatability in lateral positioning on the order of ± 3 μm which is similar to the resolution of images acquired using this specific (5×) Mirau objective.

2.2.2.2 Analysis of 3D-surface topography data

The three-dimensional (3-D) surface topography images (i.e., height maps) obtained using VSI were processed and analyzed using Matlab® R2017b and rendered using Gwyddion.

Quantification of corrosion rates from average height change: The absolute surface height change at time *t*, Δz_t, was determined from the difference in average heights of the reacted (*s*) and reference (*r*) surfaces, z_t^s and z_t^r, respectively, at time *t*, as compared to that at time 0, as given by:

$$\Delta z_t = (z_t^s - z_t^r) - (z_0^s - z_0^r) \quad (2\text{-}1).$$

Hence, at time $t = 0$, the absolute height change, $\Delta z_0 = 0$, whereas a negative Δz_t would imply a net decrease in surface height at a given pixel location, i.e., loss of metal due to corrosion. Although corrosion is expected to result in the deposition of corrosion products which have a higher molar volume compared to the native alloy, and hence result in a *height increase*, the removal of corrosion products before each imaging sequence eliminates ambiguities in the interpretation of height change – resulting in a height decrease, in time.

Frequency distribution of height change: In addition to surface height changes, the spatial distribution of height change was assessed – pixel by pixel – across a given surface. This offers insights into the frequency distributions of reaction (corrosion) rates. The 3-D images, following alignment in the vertical direction using the known reference surface were each subtracted pixel-by-pixel from that obtained at $t = 0$, to give the *height change map*. The frequency distribution of height changes, normalized to the total number of pixels – which is on the order of 10^7 pixels – is then plotted for each time interval.

2.3 Results and Discussion

2.3.1 Corrosion inhibition by calcium nitrate in the presence of halide-containing brines

Figure 2-2 shows representative height change maps of the steel surfaces following immersion in brines consisting of 10 mass % $CaCl_2$ and 10 mass % $CaBr_2$ solutions for 0, 1, 3, and 7 days. Expectedly, characteristic general corrosion features are observed following exposure to halide brines. This includes processes encompassing the initiation, propagation, and accumulation of corrosion pits. Quantitative evolutions of the average surface height change of API P110 steel over time as a function of $Ca(NO_3)_2$ dosage in the presence of 10% $CaCl_2$ and

10% $CaBr_2$ brines are shown in Figures 2-3(a,b). A linear function fitted to the data set reveals the net reaction rate, i.e., including steel dissolution and corrosion. The uncertainty in rates is estimated to be around 15% based on replicate experiments. The relative corrosion rates in the presence of various dosages of $Ca(NO_3)_2$, RCR_{CN}, were calculated as:

$$RCR_{CN} = \frac{CR_{CN}}{CR_0} \tag{2-2}$$

where CR_{CN} and CR_0 refer to corrosion rates in the presence and absence of $Ca(NO_3)_2$, respectively (see Figures 2-3c,d).

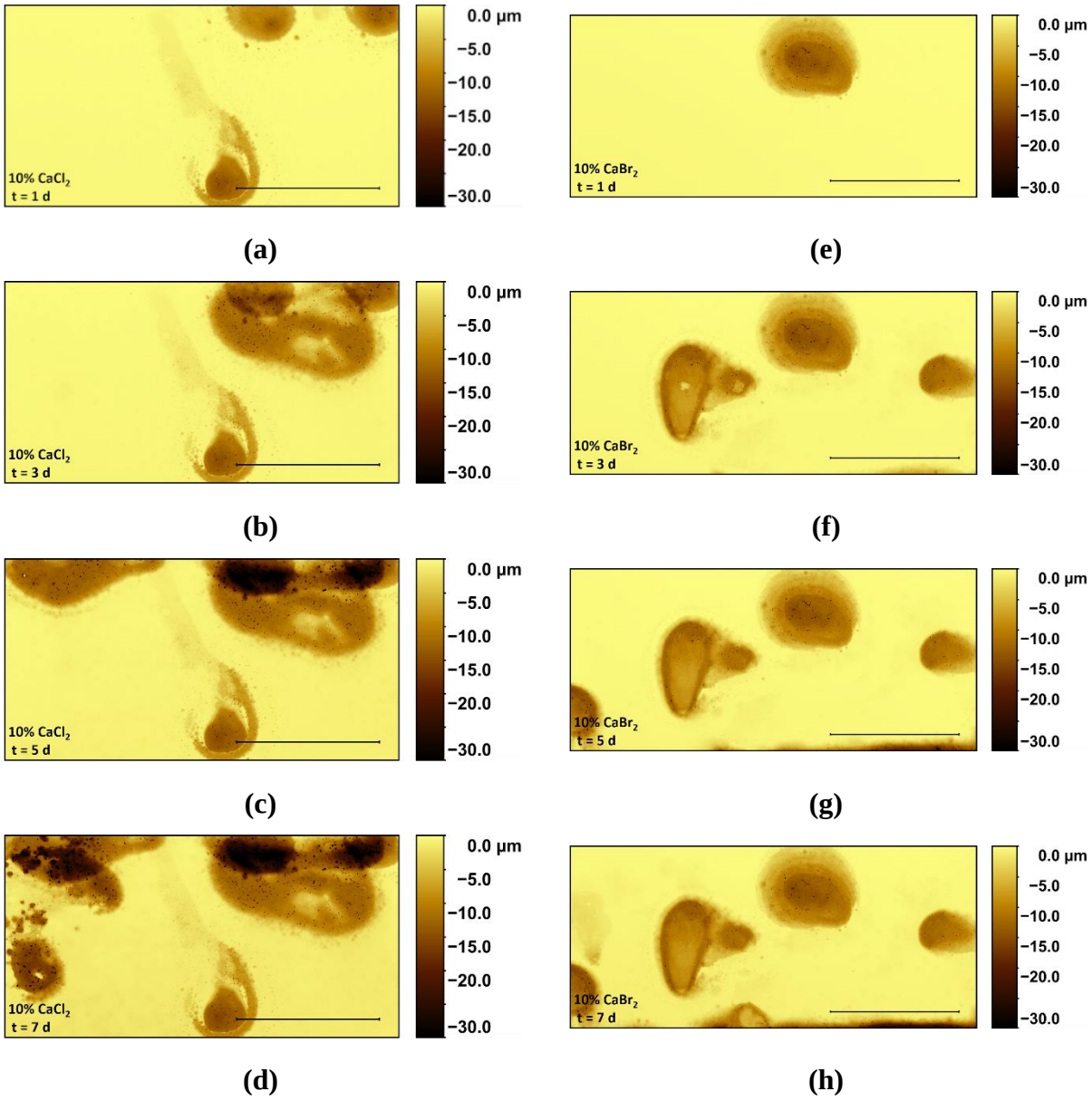

Figure 2-2: Representative height change maps of API P110 steel surfaces obtained using vertical scanning interferometry after immersion in a 10 mass % $CaCl_2$ brine for: **(a)** 1 day, **(b)** 3 days, **(c)** 5 days, and **(d)** 7 days. The height change maps following periods of exposure to a 10 mass % $CaBr_2$ brine are shown in **(e)** to **(h)** for the same reaction times, respectively. The height change is calculated with respect to the initial, pristine (unreacted) steel surface. The scale bars represent a length of 2 mm.

The average height change and corrosion rate data reveals that steel corrosion is enhanced and accelerated in $CaCl_2$ as compared to $CaBr_2$. This is also evident from the VSI images in Figure 2-2, which highlight the smaller dimensions and shallower depths of pits in the latter case. This behavior is expected to be on the account of the somewhat lower pH of the chloride solutions than the bromide solutions (see Table 2-1), and the higher electronic density, and smaller anion size of Cl^- ions as compared to Br^- ions which facilitates their penetration into and subsequent disruption of the air-formed oxide film that is present on steel surfaces.[75,77]

The corrosion rate data also reveal that, in general, lower concentrations of $Ca(NO_3)_2$ are generally more effective at inhibiting corrosion than higher concentrations. Also, at low nitrate concentrations ($\leq$ 1 mass %), the extent of inhibition enhances with increasing $Ca(NO_3)_2$ concentration. Indeed, a minimum in the corrosion rate is observed at a $Ca(NO_3)_2$ concentration of 1 mass % following exposure to both $CaCl_2$ and $CaBr_2$ brines. This result is consistent with previous findings that indicate that lower concentrations of $Ca(NO_3)_2$ are suited for ensuring inhibition.[188] Increasing the dosage of $Ca(NO_3)_2$ to 10 mass % decreased the effectiveness for inhibition in both halide-containing solutions. This observation is further discussed below.

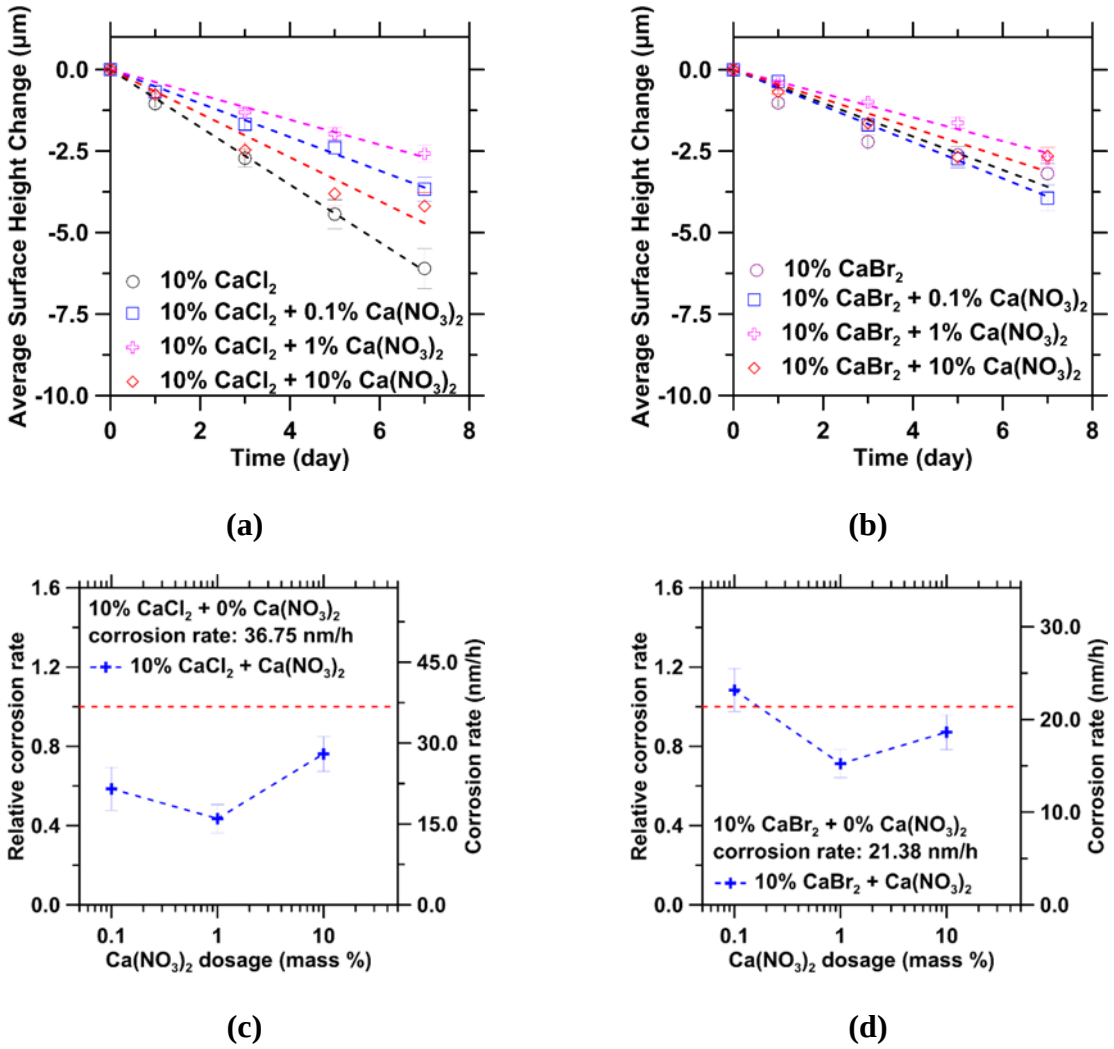

Figure 2-3: The (a-b) average surface height change and (c-d) relative and absolute corrosion rates of API P110 steel surfaces over time in (a, c) 10 mass % $CaCl_2$, and (b, d) 10 mass % $CaBr_2$ brines containing 0, 0.1, 1, and 10 mass % $Ca(NO_3)_2$. The dashed lines in (a, b) indicate the best-fit lines for each data set, whose slope reveals the net corrosion (reaction) rate shown by the secondary y-axis in (c, d). The ratio of corrosion rates in the presence and absence of $Ca(NO_3)_2$, i.e., relative corrosion rates, are also shown in (c, d) on the main y-axis. The dashed lines in (c, d) indicate the corrosion rates and relative corrosion rates when $Ca(NO_3)_2$ is absent. The error bars represent the standard error of the mean.

2.3.2 The mechanism of corrosion inhibition by $Ca(NO_3)_2$ is revealed by statistical analysis of surface height evolutions and microstructural observations

Statistical analysis of corroding surface topographies was carried out for steel samples exposed to $CaCl_2$ brines – both in the absence of and in the presence of $Ca(NO_3)_2$. The representative frequency distributions of surface height change of steel surfaces corresponding to the height change maps in Figures 2-2(a-d) are shown in Figure 2-4(a). The frequency values in the distribution plots are normalized to the total number of pixels – thereby indicative of the percentage of the total surface area that is occupied by a given corrosion feature.

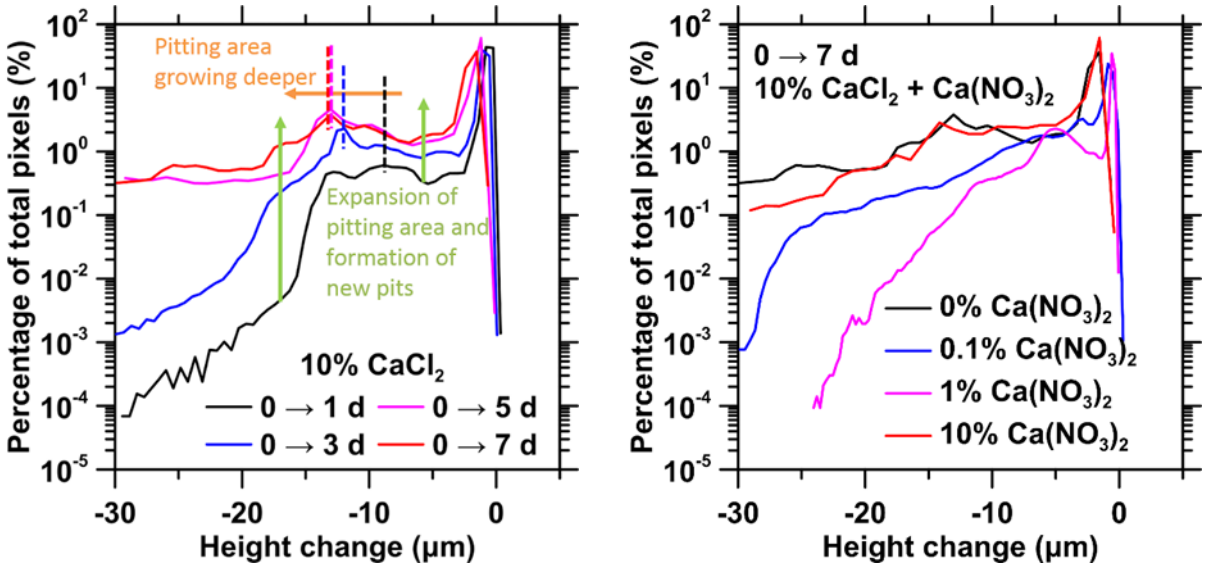

(a) **(b)**

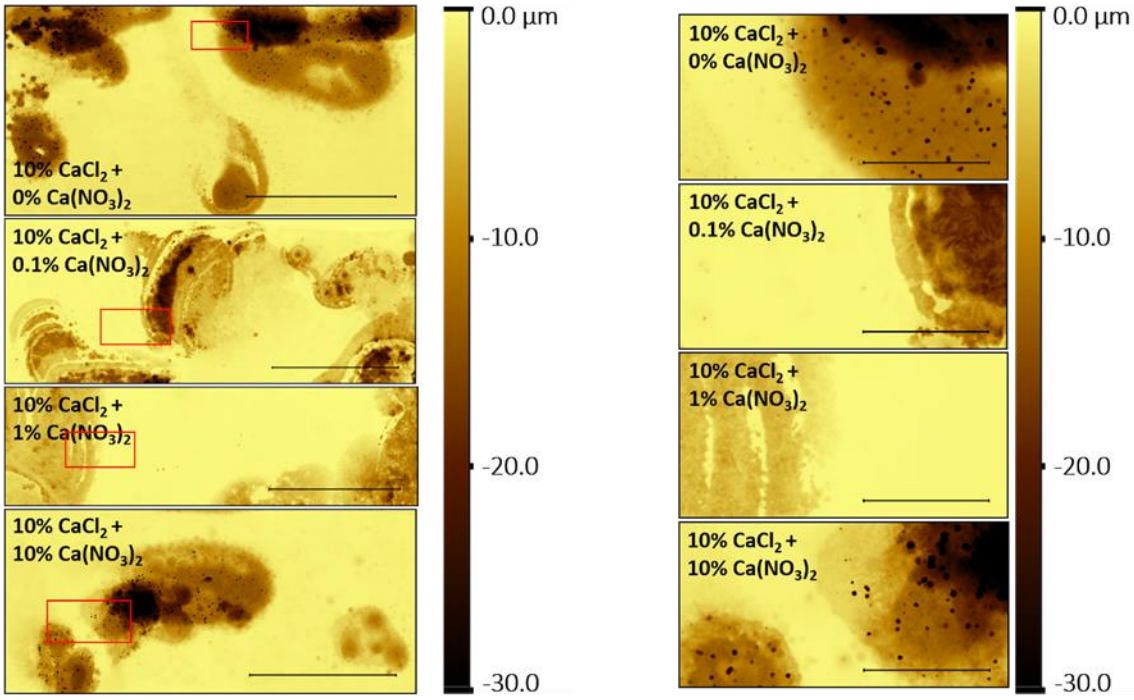

(c) **(d)**

Figure 2-4: The frequency distributions of height change for API P110 steel surfaces following exposure to: (a) 10 mass % CaCl2 brine up to 7 days, and (b) 10 mass % CaCl2 brine containing 0, 0.1, 1, and 10 mass % Ca(NO3)2 for duration of 7 days. The frequency is normalized to the total number of pixels in the image. In (a), the secondary peaks representing pitting are labeled with dashed lines. The horizontal (orange) arrow indicates pit growth in the vertical coordinate and the vertical (green) arrows indicate lateral growth (and coalescence) of existing pits, and the formation of new pitting sites. The corresponding height change maps of (b) are shown in (c). The height change is calculated with respect to the initial, pristine steel surface. Selected areas marked with red box in (c) are shown in more detail in (d). The scale bars represent lengths of (c) 2 mm and (d) 500 µm.

To offer quantitative analysis and the significance of the (height change) frequency distributions, first, the data were fitted using a 2-term Gaussian function of the form:

$$f(x) = a_1 \cdot exp\left(-\left(\frac{x-b_1}{c_1}\right)^2\right) + a_2 \cdot exp\left(-\left(\frac{x-b_2}{c_2}\right)^2\right) \quad (2\text{-}3)$$

where *x*, *a*, *b*, and *c* denote height change, a scaling factor for frequency, mean height change, and the spread in height change, respectively. The subscripts *1* and *2* denote the *main peak* and *secondary peak*, respectively. The fitting exercise revealed *main peaks*, centered at -0.53, -0.88, -1.52, and -1.86 μm for reaction times of 1, 3, 5, and 7 days, respectively. These peak values are smaller than the *average* surface height change, i.e., -1.04, -2.72, -4.44, and -6.10 μm (Figure 2-3a) at the corresponding reaction times. Indeed, the main peaks represent slowly corroding areas (lighter brown shade) shown in Figures 2-2(a-d). The areas identified by the main peak encompass 40-to-60% of all pixels – indicating that a majority of the steel surface is only slightly affected by corrosion. A broader distribution to the left (i.e., more negative values of height change) of the main peak is observed that is labeled by dashed lines in Figure 2-4(a). The *secondary peaks* correspond to height changes in the range of -8 to -20 μm, consistent with localized regions undergoing much higher surface retreat (darker brown in color scale) as compared to the bulk surface seen in Figures 2-2(a-d). As time elapsed, the positions of the secondary peaks shifted by around 5 μm to more negative values as denoted by the horizontal orange arrow, suggesting that localized sites – e.g., pits – serve as fast reaction zones that recess at a rate that is much higher than the bulk alloy surface. In addition, it should be noted that the normalized frequency of pixels increased (as marked by vertical green arrows; see Figure 2-4a) implying that the extent of the surface affected by corrosion increased due to growth and coalescence of existing pitted areas, and the formation of new pits. As such, section loss due to corrosion results from both: (1) general recession of the steel surface to a small extent (by <2 μm

after 7 days), and, (2) fast localized corrosion that manifests by the deepening and lateral growth of pitting sites.

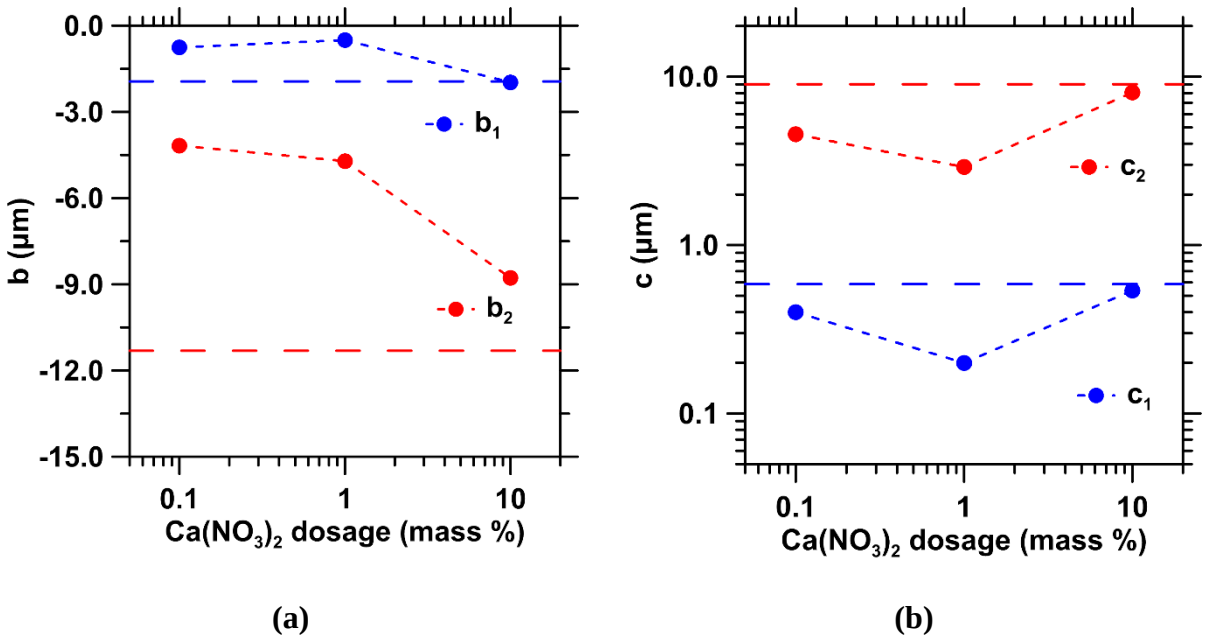

(a) **(b)**

Figure 2-5: A summary of the Gaussian fitting parameters: **(a)** peak positions b_1, b_2, and **(b)** peak widths c_1, c_2 for the frequency distributions of height change for steel surfaces following exposure to 10 mass % $CaCl_2$ brine containing 0, 0.1, 1, and 10 mass % $Ca(NO_3)_2$ for 7 days. The subscripts *1* (blue) and *2* (red) denote the main peak and secondary peak, respectively. The blue and red horizontal dashed lines identify baseline values in $Ca(NO_3)_2$-free systems.

Figures 2-4(b-d) illustrate the effects of $Ca(NO_3)_2$ dosage on corrosion rates for API-P110 steel exposed to 10 mass % $CaCl_2$ brine. Foremost, at low dosages of $Ca(NO_3)_2$ (i.e., 0.1 mass % and 1 mass %), the frequency distribution curves differ from the case with no nitrate in several significant ways. First, both the main and secondary peaks are shifted to less negative

values upon $Ca(NO_3)_2$ additionFi, consistent with the decrease in average height change shown in Figure 2-3(a). Based on analysis of the fitting parameters b_1 and b_2 (see Figure 2-5a) it is suggested that $Ca(NO_3)_2$ reduces corrosion rates by suppressing both general recession (i.e., bulk dissolution) and fast localized corrosion at pitting sites, although the influence on localized corrosion is more pronounced. In addition, peak widths given by the parameters c_1 and c_2 also decreased, as shown in Figure 2-5(b), suggesting a decrease in uniform corrosion with $Ca(NO_3)_2$ dosage. A comparison of the frequency distribution curves in the absence of nitrate and in 1 mass % $Ca(NO_3)_2$, highlights a shift of the secondary peak towards less negative values by around 7 μm, simultaneous with a decrease in the normalized frequency by more than one order of magnitude. Significantly, this indicates that low concentrations of $Ca(NO_3)_2$ inhibit corrosion processes by reducing the rate of vertical and lateral expansion of pits. Notably, further increasing the nitrate ion concentration to 10 mass % resulted in a frequency distribution that closely resembled that of the nitrate-free conditions evidencing that increasing $[NO_3^-]$ beyond an optimal value is detrimental.

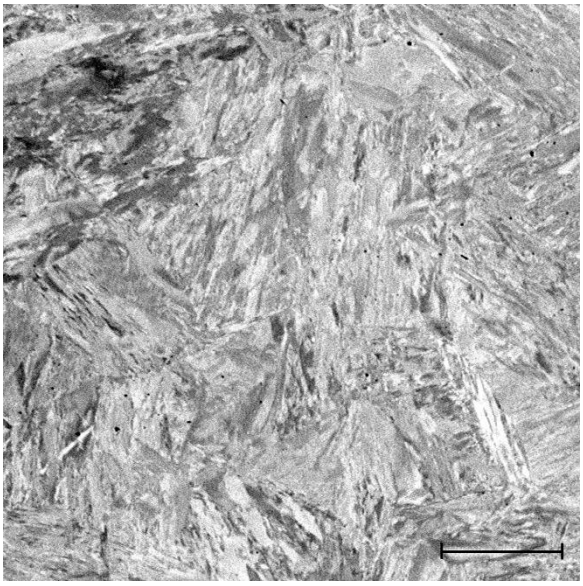

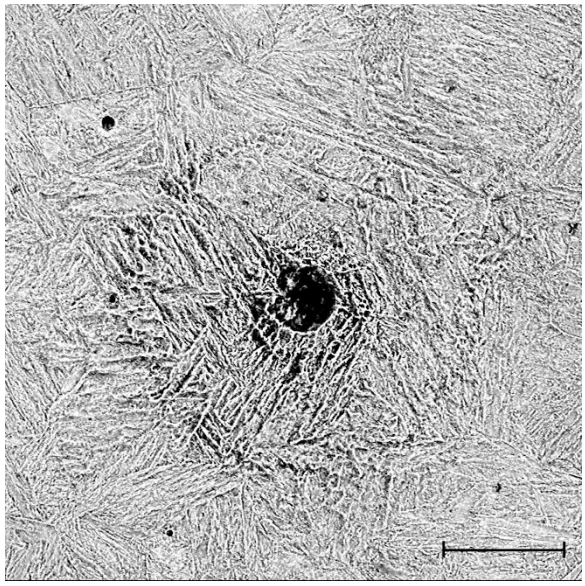

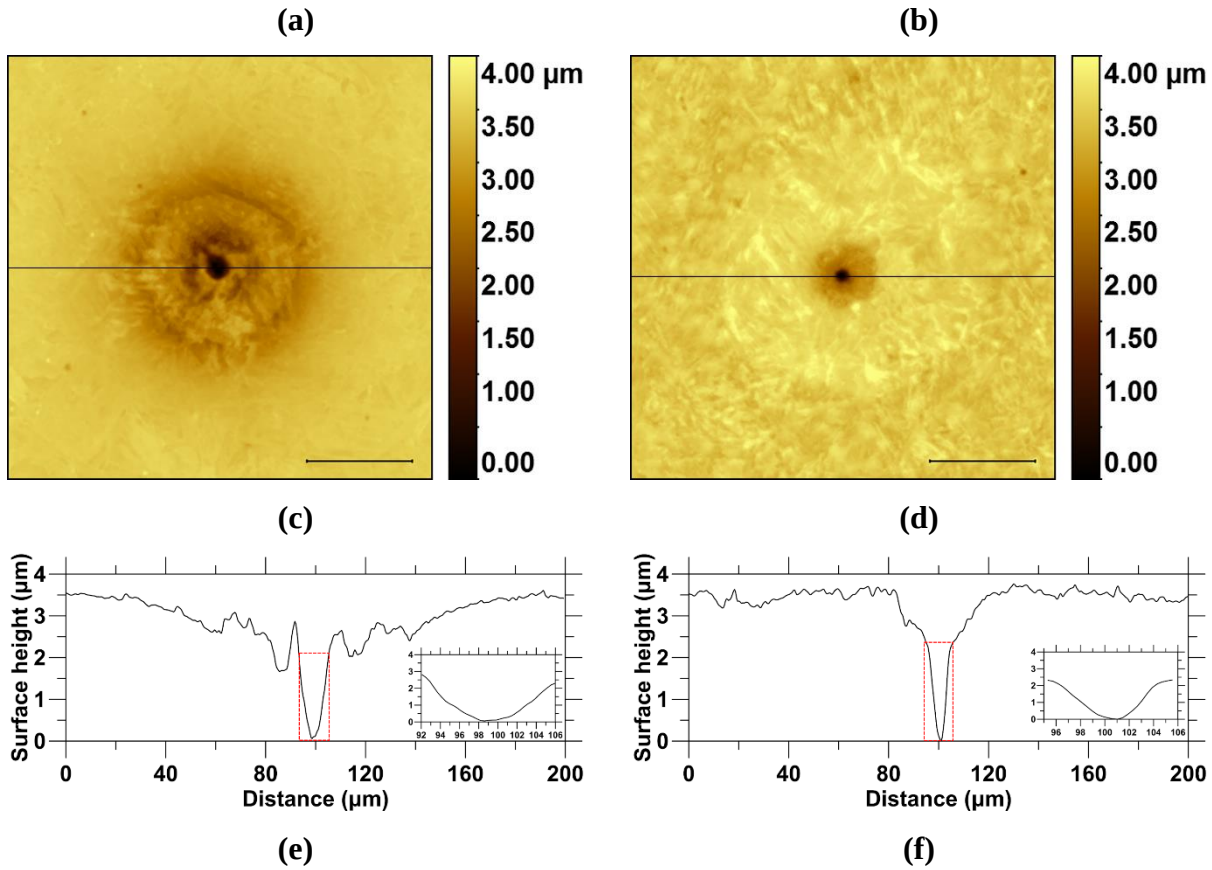

Figure 2-6: SEM micrographs of: **(a)** an as-polished API P110 steel surface, showing its martensitic microstructure, and, **(b)** a representative pit that forms on a steel surface reacted with 10 mass % $CaCl_2$ brine for 20 hours showing a radial depression that forms around a central pitting site. VSI topography images of a representative pit and its vicinity formed following contact with: **(c)** 10 mass % $CaCl_2$ brine, and, **(d)** 10 mass % $CaCl_2$ + 1 mass % $Ca(NO_3)_2$ solution for 20 hours, corresponding line profiles along the central lines are shown in **(e)** and **(f)** with inserted profiles of pit bottoms. The VSI images were acquired using a 20× Mirau objective with a lateral resolution of 0.47 µm. The scale bars represent lengths of **(a)** 10 µm, **(b)** 30 µm, and **(c,d)** 50 µm.

To better elucidate the functions of $Ca(NO_3)_2$ as a corrosion inhibitor, the VSI observations were augmented by SEM visualizations of corroding surfaces. First, as shown in Figure 2-6(a), API-P110 steel presents a single-phase martensitic microstructure with a grain size of around 10 μm. Visualization of corroded microstructures reveals that pits are localized at pre-austenite grain boundaries, e.g., as shown in Figures 2-6(b) and Figure 2-7, consistent with previous observations.[202–205] It is generally thought that in the presence of Cl^- ions, surface defect sites, e.g., grain boundaries, and secondary-phase inclusions are most vulnerable to pitting.[82,203,206] As pitting initiates, the release of iron in the form of Fe^{2+} promotes local acidification within the pit following the reaction: (1) $Fe - 2e^- \rightarrow Fe^{2+}$, (2) $Fe^{2+} + H_2O \rightarrow Fe(OH)^+ + H^+$, and (3) $Fe(OH)^+ + H_2O \rightarrow Fe(OH)_2 + H^+$, resulting in an acidic pH in the bottom of the pit.[207–210] The high local H^+ and Fe^{2+} activities at the bottom of the pit – and the corresponding gradient that develops – results in the transport of anions towards the pitted area. The concentration gradient of ions induces the development of an electrochemical potential difference between the pit bottom and the surface of the steel that can be as high as hundreds of millivolts.[89,211]

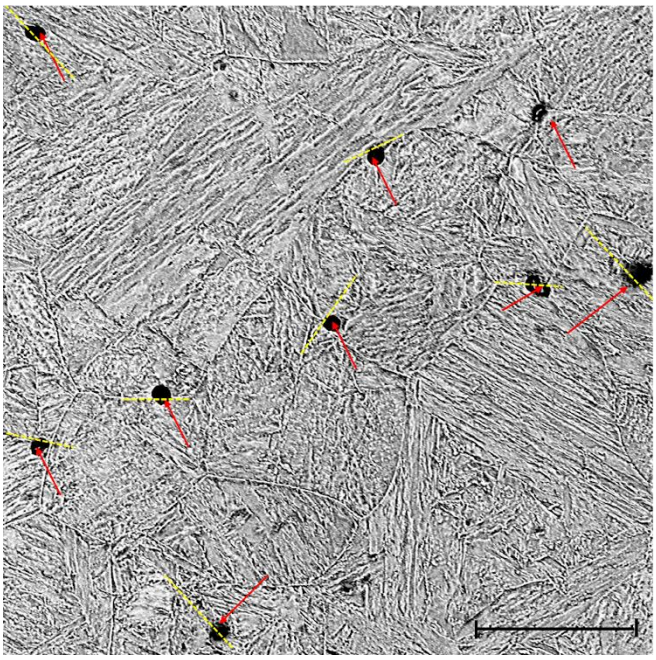

Figure 2-7: A representative SEM micrograph of API P110 steel following reaction with 10 mass % $CaCl_2$ brine for 20 h showing localized corrosion (red arrows) at the pre-austenite grain boundaries (dashed yellow lines). The scale bars represent lengths of 30 μm.

The pit morphologies observed in Figure 5 are significantly smaller than *stable pits* that form on surface of passivated steels.[212] Further, as shown in Figure 2-6(b), herein, a rapidly corroding zone is noted to form around a central pit whose radius is several times larger than that of the pit itself, i.e., in terms of its radial dimension. A line profile (Figure 2-6e) drawn through the center of the pit – using the VSI topography image (Figure 2-6c) – shows that the surrounding radial area ("basin") encompasses a radius of 80 μm whereas the central pit only achieves a maximum radius of 17 μm (and a depth of around 3.5 μm). It is the formation of such radial basins that explains the secondary peaks evident in the frequency distribution curves.

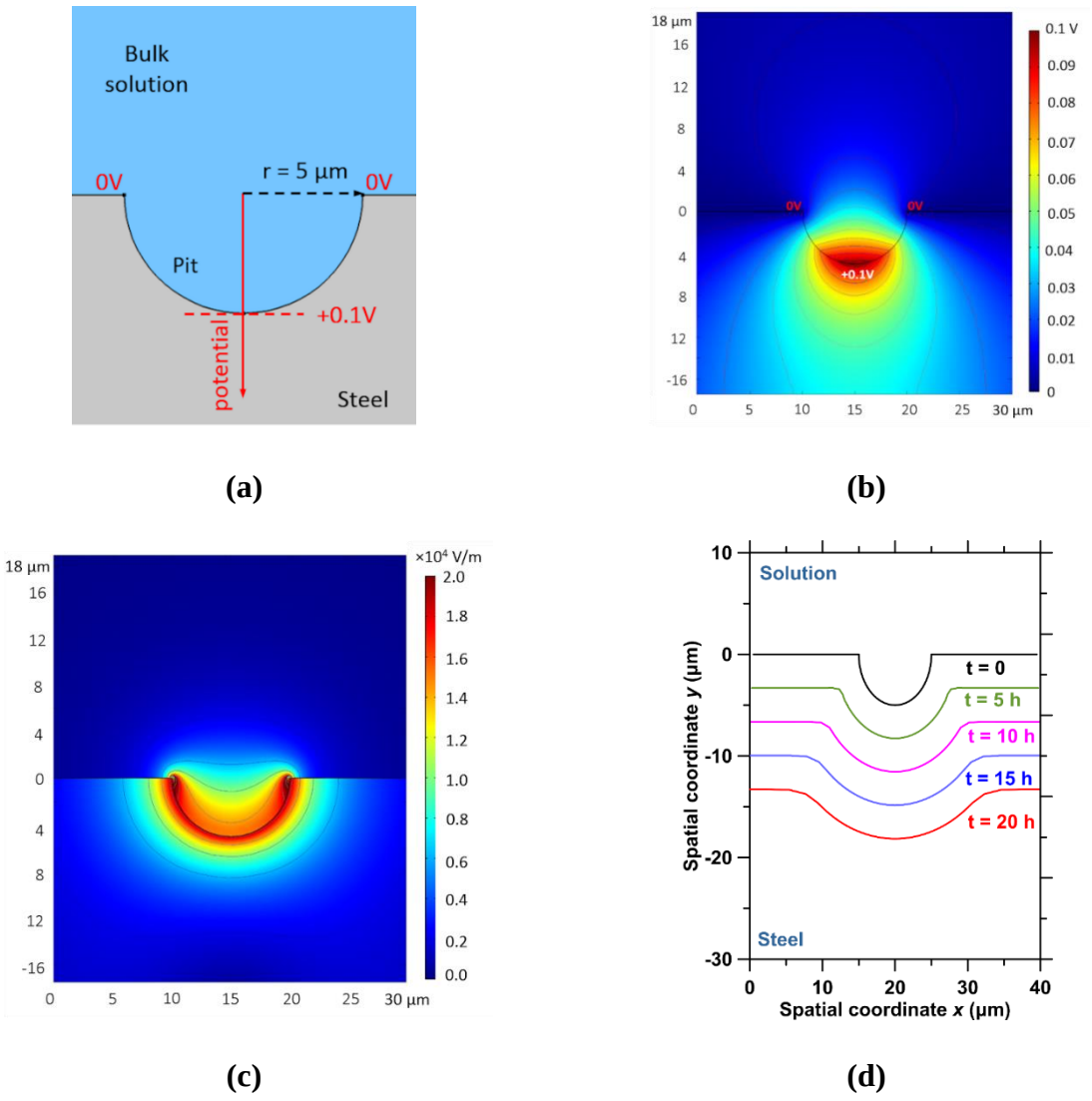

Figure 2-8: **(a)** A schematic showing the pit geometry and the applied potential profile, **(b)** the simulated potential distribution with isopotential contours in the steel and in the vicinity of the pit, **(c)** the simulated electric field strength distribution with isofield contours, the arrows indicate an electric field concentration at the pit mouth due to a convexity, and **(d)** The morphology evolution of an "arrested" pit.

By simulating the effects of anodic corrosion on the evolution of the pit geometry, we attribute the formation of these radial basins as being the result of near-surficial, lateral expansion of the pit mouth (e.g., see Figures 2-6b-f), e.g., as observed in the corrosion of AISI 1045 steel by Guo et al.[213] As such, Figure 6 shows the simulated local potential distribution and resulting electric field strength distribution and the implications on the formation of the radial basin using a finite element approach (COMSOL Multiphysics, ver. 4.4). The simulation considers a hemispherical pit as shown in Figure 2-8(a). This represents a typical morphology for a pit[82] and resembles the central pit shown in Figures 2-6(b,c). Upon the initial formation of the hemispherical pit (e.g., perhaps at a MnS site), fast dissolution results in development of an electrochemical potential difference between the pit bottom and pit mouth. Herein, the pit bottom serves as the anode with an assumed potential that is 100 mV more anodic relative to the pit mouth that serves as a cathode. The potential along the pit wall is assumed following a simple linear distribution written as:

$$\Phi_{wall} = \frac{(\Phi_{bottom} - \Phi_{mouth})}{L} x - \Phi_{mouth} \tag{2-4}$$

where Φ_{wall} is the potential of the pit wall at a depth of x, Φ_{bottom} is 100 mV at the pit bottom where $x = L$, and Φ_{mouth} is referenced as zero. Figures 2-8(b,c) show the simulated spatial distributions of the potential and normalized electric field governed by the harmonic condition: $\nabla^2\Phi = 0$, in both the solution and the adjacent steel surface, respectively. The simulation indicates that the development of an electric field concentration at the pit mouth results from its convexity or curvature, e.g., similar to a stress concentration (see arrows in Figure 2-8c). Significantly, Figure 2-8(c) highlights that the electric field concentration affects both the steel surface at the pit mouth and the solution in the vicinity. In unpassivated alloys, this forebodes the fast expansion of the pit mouth due to an electrostatically induced change in interfacial tension at

the steel-solution interface.[214] At later times, however, such lateral expansion is expected to hinder pit deepening due to attenuation of the local concentration gradients of ions in the pit. This suggests that in simply oxidized, i.e., non-passivated systems, the pit morphology shown in Figure 2-6 is unlikely to sustain a mass-transport limiting current that is required for stable pit growth. Therefore, the potential and concentration gradients will disappear following the discontinuance of the pit growth, and a general corrosion rate can be applied to both the pit wall and the pit mouth. Figure 2-8(d) shows the morphology evolution of an "arrested" pit with the same dissolution rate (5 A/m^2)[78] along the pit wall and the open surface. This indicates that the expansion of the pit mouth is induced as a function of its high surface to volume ratio, i.e., local curvature. This suggests that the corrosion pits that form will eventually transition into "recessed basins" rather than the stable pits that are observed in passivated alloys. [82,212,215]

The radial basins discussed above were also found on steel surfaces reacted with 10 mass % $CaCl_2$ containing 1 mass % $Ca(NO_3)_2$ solution following 20 hours of contact (Figure 2-6d). Although the central pit depths are similar across $Ca(NO_3)_2$-free and $Ca(NO_3)_2$-dosed systems (i.e., 3.5 μm), the central pit features a much smaller opening (8 μm in diameter) when $Ca(NO_3)_2$ is present. Furthermore, unlike the case with no added $Ca(NO_3)_2$ (Figures 2-6c,e), the pits formed in $Ca(NO_3)_2$-dosed environments are less well-developed. For example, first, the region of enhanced corrosion around the central pit is smaller (20 μm vs. 80 μm in radius). Second, the average vertical depression of this area is considerably smaller, i.e. 0.8 μm vs. 1.8 μm. It is interesting to note that a slight increase in height around the pitting area is also apparent, e.g., due to localized formation and attachment of corrosion/oxidation products. This is consistent with the proposed corrosion inhibition mechanism of NO_3^- ions. Specifically, nitrate is thought to consume released Fe^{2+} species by oxidizing it to Fe^{3+}. This results in the precipitation

of solid corrosion products such as Fe-oxides and hydroxides.[188,190] Consequently, the pitting site is isolated by the deposition of such precipitation products and thereby protected from further corrosion by reducing its access to electrolytes in solution. The deposition of corrosion products at the pit mouth is also expected to reduce its convexity, and electrical field concentration at the pit mouth – resulting in the formation of more diffuse, albeit shallower basin depressions as evidenced in Figures 2-6(d,f). Furthermore, the migration and concentration of NO_3^- anions towards the anodically corroding regions is expected to follow the electrical field intensity and compete with the transport of Cl^- to the same sites. These actions alleviate the Cl^- concentration at anodic sites and mitigate Cl^--induced localized corrosion around pitting sites in the presence of $Ca(NO_3)_2$.[216,217] This explains why shallower pits, and smaller basins develop in $Ca(NO_3)_2$ containing systems at moderate dosages. This interpretation is consistent with the trends obtained from the frequency distribution curves above which highlight: (1) a shift in the position of the secondary peak towards less negative values, and (2) a reduction in normalized frequency of pixels associated with secondary peaks. Contrastingly, when the $Ca(NO_3)_2$ concentration is further increased, however, the oxidizing potential of the bulk solution also increases. It is for this reason that high dosages of $Ca(NO_3)_2$ (10 mass %) enhance the oxidative dissolution of iron and compromise the corrosion inhibition effect that is offered by $Ca(NO_3)_2$ additions at lower concentrations.[218]

2.4 Summary and Conclusions

This paper has comprehensively examined the corrosion of API P110 steel in concentrated halide environments in the presence of $Ca(NO_3)_2$ as a corrosion inhibitor. Special focus is placed on examining the evolution of corroding topographies – at unparalleled resolution

– across large fields of view using vertical scanning interferometry (VSI) for samples reacted in a controlled environment under isothermal conditions. Careful analysis of surface topographies, pixel-by-pixel, indicates that while moderate concentrations of $Ca(NO_3)_2$ can effectively inhibit corrosion in the presence of Cl^- and Br^-, such inhibition is compromised at higher dosages which induce a significant oxidizing potential of the bulk solution. By statistical analysis of surface height data ("frequency distributions"), it is highlighted that $Ca(NO_3)_2$ suppresses localized corrosion primarily, although a measurable effect on general corrosion was also observed. Localized corrosion is manifested by a fast dissolution zone (i.e., basin) which forms in the vicinity of central pitting sites. Simulations of the electrochemical evolutions within a pit suggest that these features arise from the fast expansion of the pit mouth whose local curvature results in the concentration of an electric field distribution. The mechanism of NO_3^- inhibition is consistent with this model such in the presence of nitrate the oxidation of Fe^{2+} to Fe^{3+} leads to the precipitation and deposition of Fe oxides and hydroxides, hindering further pit expansion. To the best of our knowledge, this is the first time that the inhibition effect of $Ca(NO_3)_2$ has been evidenced from quantitative and statistical analysis of corroding surfaces. These findings provide new insights regarding the role of the water chemistry and inhibitor dosage to suppress steel corrosion evolutions in aggressive halide-rich environments.

Chapter 3. Elucidating the Grain-orientation Dependent Corrosion Rates of Austenitic Stainless Steels

3.1 Introduction and Background

Austenitic alloys such as 304L and 316L stainless steels, and nickel-based alloys are often used in core-reactor internal components in nuclear power plants.[219] These alloys, as a rule, exhibit a face-centered-cubic (FCC) lattice structure and feature excellent high-temperature oxidation resistance.[220] However, the degradation of these alloys, e.g., due to mechanisms such as stress corrosion cracking (SCC) renders these components susceptible to hyperbolic failure, and to violate the "leak-before-break" criterion.[221] So far, considerable efforts have been made to uncover the effects of grain boundary structures on SCC susceptibility.[8,222–224] However, less is known about how crystallographic orientations may influence electrochemical (i.e., oxidation) degradation of such alloys.

Crystallographic orientation is well-known to affect surface reactions including: dissolution, adsorption, oxidation, and pitting that are of relevance to both single-crystal, and polycrystalline metals and ceramics.[16,225–228] In each of these cases, the anisotropy of atomic arrangements on the surface results in spatially and temporally non-uniform reaction kinetics – even for chemically equivalent reactions – amongst grains with different orientations. For example, for austenitic alloys oxidized in simulated reactor environments, the morphology and thickness of the oxide layers formed show a strong dependence on the orientation of the underlying grains.[229] Furthermore, in the case of 316L stainless steel, the substantial difference in oxidation rates between diversely oriented grains results in the formation of a "step structure" at grain boundaries that could lead to crack initiation and a reduction in service-life.[230]

Many studies have attributed the dependence of corrosion rates on grain orientation to differences in the surface energy. The prevailing theory depicts the corrosion rates following the surface energy scaling, i.e., the higher the surface energy the greater the corrosion susceptibility.[227,231,232] However, in the majority of studies, grain-specific corrosion behavior is examined only for a few grains which feature a limited diversity of (families of) crystallographic planes.[233–235] Furthermore, corrosion susceptibility is often ranked through the analysis of line profiles which show a height difference across adjacent grains,[236,237] i.e., instead of presenting a spatially averaged corrosion rate that applies to the entire exposed surface of a grain. Therefore, this study undertakes analyses of a large number of grains (>100 unique grains) to reveal statistically relevant insights into how grain orientation affects oxidation rates.

The equilibrium potential of reactor components, which is influenced by the radiation fluence and water chemistry, can vary from -0.9 to 0.2 $V_{Ag/AgCl}$.[238] Across such wide potential range, both active and transpassive corrosion may occur; the former takes place at lower potentials and results in oxidation products having lower valence (e.g., Fe^{2+}, Cr^{3+}, etc.), whereas the latter is driven by strong oxidants (e.g., radiolytic radicals [239]) and produces metal species with higher valence (e.g., Fe^{3+} and $HCrO_4^-$).[38,240] Therefore, the effects of crystallographic orientation on both active (i.e., potential-free) and transpassive (i.e., potential-promoted) oxidation of AISI 316L stainless steel were systematically examined by coupling topographical measurements using vertical scanning interferometry (VSI) with microstructural analyses using electron backscatter diffraction (EBSD). The VSI analysis allows access to representative scanning areas (0.5 mm × 0.5 mm) at lateral and height resolutions of ±80 nm and ±2 nm, respectively,[241] allowing superposition of orientation-specific oxidation rates onto an EBSD-

derived grain orientation map. The outcomes unambiguously reveal the effects of grain orientation on corrosion sensitivity and its mechanistic origins.

3.2 Materials and Methods

3.2.1 Sample preparation

A commercially available 316L stainless steel (McMaster-Carr) was used. The elemental composition of the steel used as given by the manufacturer is noted in Table 3-1. Herein, the steel sections were solution-annealed using a vacuum tube furnace at 1000 °C for 1 h and then furnace-cooled to room temperature. Annealing produced a monophasic austenitic microstructure with easily distinguishable grains. The annealed steel was then sectioned in to smaller coupons of 6 mm in diameter and 6 mm in height. Thereafter, the coupons were embedded in epoxy, and then wet-polished using SiC abrasives and diamond paste, and finally polished using a 50 nm colloidal silica suspension.

Table 3-1. The chemical composition of the 316L stainless steel used (mass %).

Fe	Cr	Ni	Mo	Mn	N	C	Si	Cu
bal.	16.630	10.070	2.080	1.530	0.054	0.025	0.550	0.490

3.2.2 Crystallographic analysis

The crystallographic orientations of the grains were determined using a Scanning Electron Microscopy (SEM: TESCAN MIRA3) equipped with an EBSD detector (Oxford ULTIM MAX). The acceleration voltage and step size used were 20 kV and 0.5 μm, respectively. The EBSD data were analyzed using OIM Analysis® and the MTEX toolbox in

MATLAB® R2017b.[242,243] The averaged Euler angles over all pixels within individual grains provided by the EBSD analyses were used to represent the rotations for each grain. The Miller indices, *h, k, l* of each individual grain were computed using:

$$h = n \cdot sin\varphi_2 \cdot sin\Phi \tag{3-1}$$

$$k = n \cdot cos\varphi_2 \cdot sin\Phi \tag{3-2}$$

$$l = n \cdot cos\Phi \tag{3-3}$$

where φ_2 and Φ are the Bunge's notation of Euler angles ($\varphi_1, \Phi, \varphi_2$) and *n* is a scaling factor to attain integer indices.[244]

3.2.3 Oxidation (corrosion) rate analysis

Active corrosion was Induced by immersing the steel coupon's surface in a 0.5 M H_2SO_4 + 0.1 M LiCl solution for up to 80 h in a temperature-controlled chamber (45 ± 0.2 °C). Transpassive corrosion was induced by immersing the surface of the steel coupon in a 10 mass % oxalic acid ($H_2C_2O_4$, Fisher Scientific) solution for 45 s while imposing a constant current density of 1 A/cm^2. The surface topographies of corroding sections were examined using a Zygo NewView 8200 vertical scanning interferometry (VSI). A 20× Mirau (numerical aperture, NA = 0.4) and a 100× (NA = 0.85) interferometric objective were used. The former, and latter objectives provide spatial resolutions (i.e., single pixel size in *x* and *y* directions) of 410 nm and 80 nm, respectively. The vertical (height) resolution of both objectives is equivalent and on the order of 2 nm. The surface topographies were analyzed using Gwyddion, v2.54.[245] A surface area (500 μm × 500 μm) of the as-polished steel coupon was analyzed using EBSD and VSI, and then partially covered by a peelable room-temperature vulcanizing (RTV) silicone mask (Silicone Solutions SS-380). The mask was removed after each corrosion test to expose the unreacted

surface, which reveals the zero surface height ("pristine") position. The topography of the same area was then measured, and the corrosion-induced height change, i.e., surface retreat, was determined by comparing the corroded surface with the preserved surface that remained unchanged beneath the masked region.[246] The corrosion rate (R_c, nm/s) is simply represented, as a spatial average of all the pixels that constitute a single grain as: $\Delta h/\Delta t$, where, Δh is the average surface retreat and t is time period over which oxidation occurred.

3.2.4 Data analysis workflow

The workflow of data analysis used in this work is summarized in Figure 3-1. The entire exercise was performed in two steps. First, overlap EBSD measurement with VSI measurement to obtain the average height change of individual grain on the scanned region. Second, compute the surface energy pre-factor using the surface indices provided by EBSD analysis and construct the dependence of corrosion kinetics on surface energy pre-factor. All data processing and computing were performed in Matlab® R2017b.

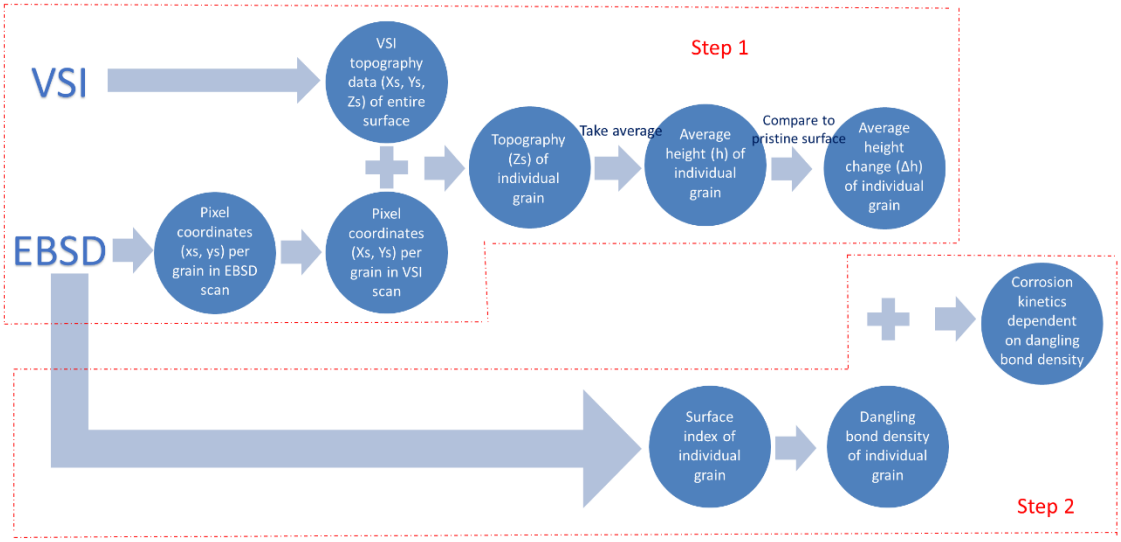

Figure 3-1: Workflow of data analysis employed in this chapter.

3.3 Results and Discussion

3.3.1 Grain orientation impacts on the potential-free active corrosion of 316L

The microstructure of an as-polished 316L stainless steel was examined using EBSD and is shown in Figure 3-2. The solution-annealed sample only consists of austenite grains and is free from deformation-induced features. Over 100 grains were identified within the selected area, with their orientations mapped by EBSD as shown in Figure 3-2a. The orientations of these grains are plotted in the inverse pole figure (IPF) triangle of Figure 3-2b, which shows grains having diverse orientations within the examined area.

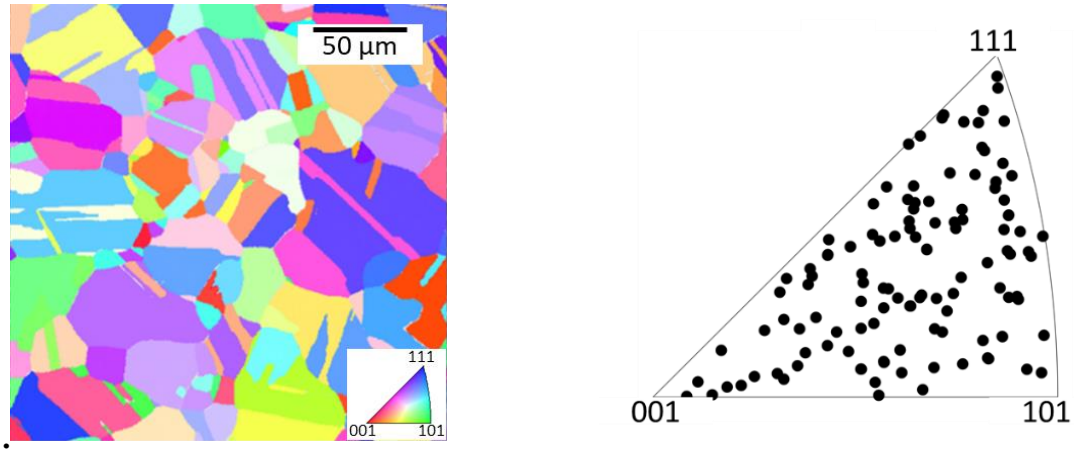

(a) **(b)**

Figure 3-2: EBSD analysis showing the microstructure of the solution-annealed 316L stainless steel surface: **(a)** The grain orientation map of the analyzed surface, with the color code shown in the inverse pole figure (IPF) as the inset, and **(b)** The distribution of grain orientations over the examined surface area. The grain orientations are given with respect to the surface normal direction.

First, unstimulated (*potential-free*) corrosion studies were carried out by immersing the 316L steel in a 0.5 M H_2SO_4 + 0.1 M LiCl solution at 45 °C for up to 80 hours. The equilibrium potential of 316L in the solution is around -400 $mV_{Ag/AgCl}$,[247] i.e., equivalent to about -150 mV_{SHE} which is within the range of stainless steels in reactor environments.[238] Moreover, the immersion solution resembles the solution present in crevices (or cracks) in reactor environments wherein high concentrations of chlorine (Cl^-) and protons (H^+) are attained.[248] In this environment, 316L is expected to undergo active corrosion and be oxidized to lower valence oxidation products (e.g., Fe^{2+}, Cr^{3+}, etc.).[38,240] Subsequently, the actively corroded surface was characterized and its (dissolution-precipitation) corrosion rates were determined using VSI (see

Figure 3-3). The topography map (see Figure 3-3a) of the same area as mapped by EBSD shows that the uncorroded polished surface has an overall height variance of around ±80 nm.

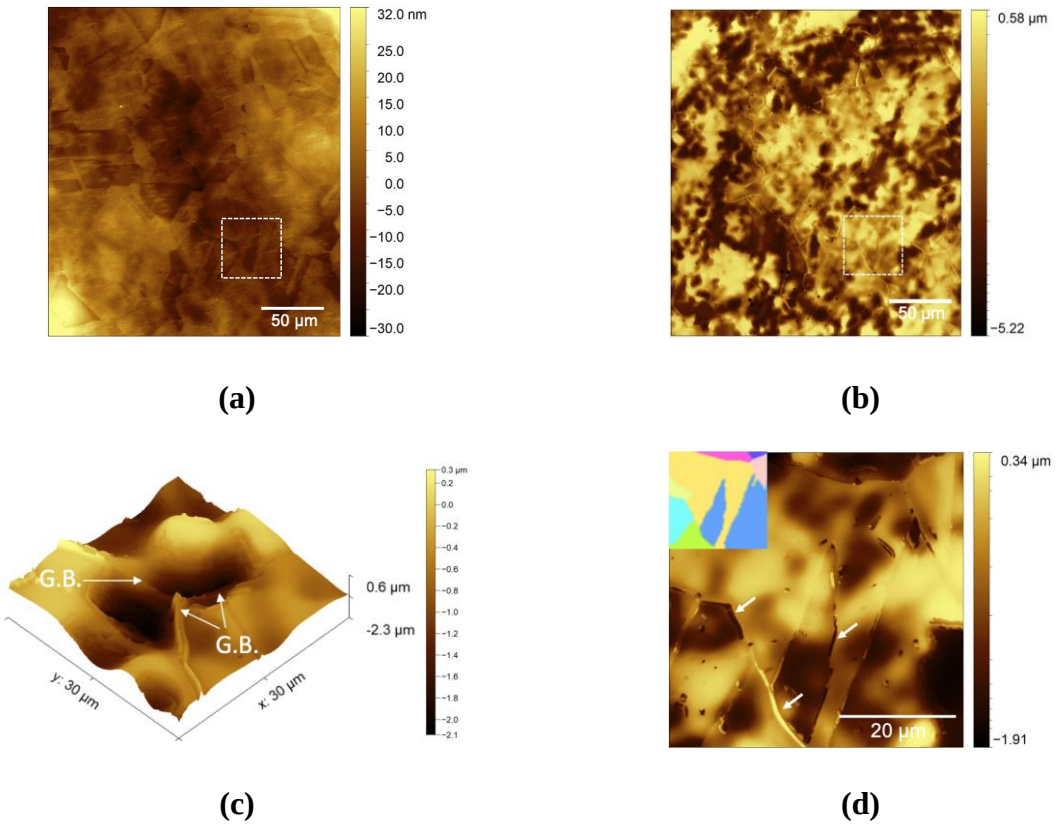

Figure 3-3: Representative VSI topography images of **(a)** an as-polished 316L stainless steel and **(b)** a corroded steel surface following corrosion reaction for 20 h. **(c)** A shallow pit, i.e., basin formed at the junction of three grain boundaries (G.B.) **(d)** The "step structure" (marked by the arrows) formed between adjacent grains resulting from the difference in crystallographic orientation. An EBSD map of the same area is shown in the inset figure.

On the other hand, the height difference between adjacent grains is on the order of a few nanometers. Following immersion/corrosion in a 0.5 M H_2SO_4 + 0.1 M LiCl solution at 45 °C for 20 hours the surface recessed by up to 2.0 µm (Figure 3-3b), suggesting the onset of active corrosion. The morphology of the corroded surface indicates that active corrosion occurred in two forms: localized corrosion and general surface retreat. Localized corrosion sites resemble

saucer-shipped shallow pits (i.e., the basins) and are represented by dark brown regions in the topography map (see Figure 3-3c). Pitting corrosion took place following the local breakdown of an air-formed passive film, and the formed semi-spherical pits evolve into basins during the transition from pitting to general corrosion.[213,246] The rest of the steel surface experienced general corrosion. Surface recession rates in the areas undergoing general corrosion are lower, but are more evidently dependent on grain orientation. For example, the "step" structure resulting from distinct corrosion rates of differently oriented grains is seen in Figure 3-3d. The height difference between the adjacent grains which is on the order of ±5 nm prior to solution exposure increased to around 1.0 μm after 20 h of active corrosion in the immersion solution.

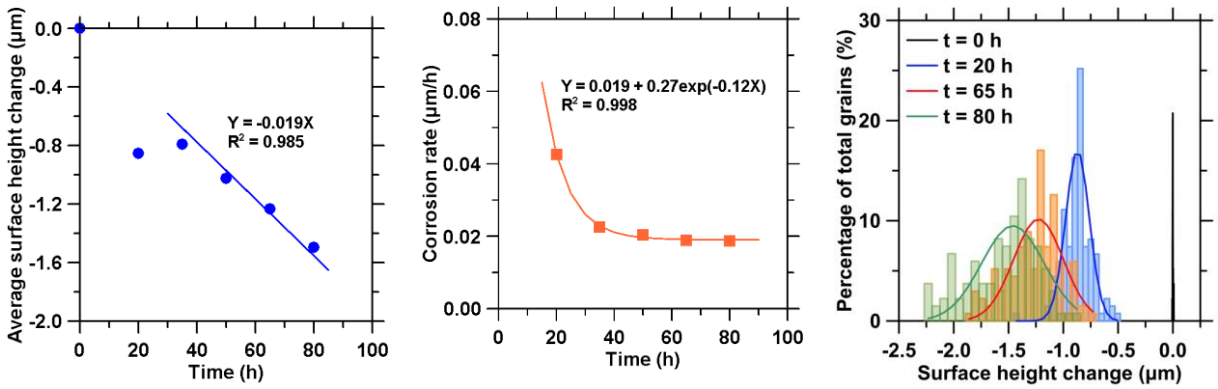

(a) **(b)** **(c)**

Figure 3-4: (a) The average surface height change, and **(b)** the corrosion rate of the actively corroding 316L surface over time. **(c)** The grain-averaged surface height change frequency distributions of surfaces corroded for 20 h, 65 h, and 80 h. The black curve represents the frequency distribution of the as-polished steel surface that is centered at 0.0 μm (mean), and spread over a range of 20 nm (standard deviation). The sample was corroded in a 0.5 M H_2SO_4 + 0.1 M LiCl solution at 45 °C.

The average height of the steel surface progressively decreased with prolonged immersion as shown in Figure 3-4a. Note that the active corrosion rate followed an exponential decay and attenuated to an asymptotic ("steady-state") rate (see Figure 3-4b). Faster corrosion at the initial stage can be explained by the steel dissolution under large undersaturation accompanied by localized corrosion (e.g., pitting).[249] The long term surface recession, i.e., at t > 20 h reveals the steady-state active corrosion rate of 0.019 μm/h or 170 μm/year (see the fittings in Figure 3-4a and 3-4b), suggesting a completely depassivated surface, i.e., no intermediate or metastable passive films were formed.[93] The average heights of individual grains were obtained by overlapping the VSI topographies and EBSD microstructure maps. The frequency

distributions of the grain-averaged surface height (Figure 3-4c) were fitted using a Gaussian function written as:

$$f_{(x)} = a \cdot \exp\left[-\left(\frac{x-b}{c}\right)^2\right] \quad (3\text{-}4)$$

where x is the height change, a, b, and c are fitting parameters denoting the scaling factor for frequency, mean height change, and the spread in height change, respectively. Up to 20 hours of corrosion, the average surface retreat (i.e., as averaged over the exposed surface area of the grain) is around 0.82 μm (Figure 3-4c) and the variance in height of most grains is ±0.35 μm. With increasing reaction time, the dissolution/corrosion rates of the differently oriented grains diverge. The broadening of the distribution profiles over time implies that the numerous grains, which feature a variety of surface orientations, corroded at different rates.

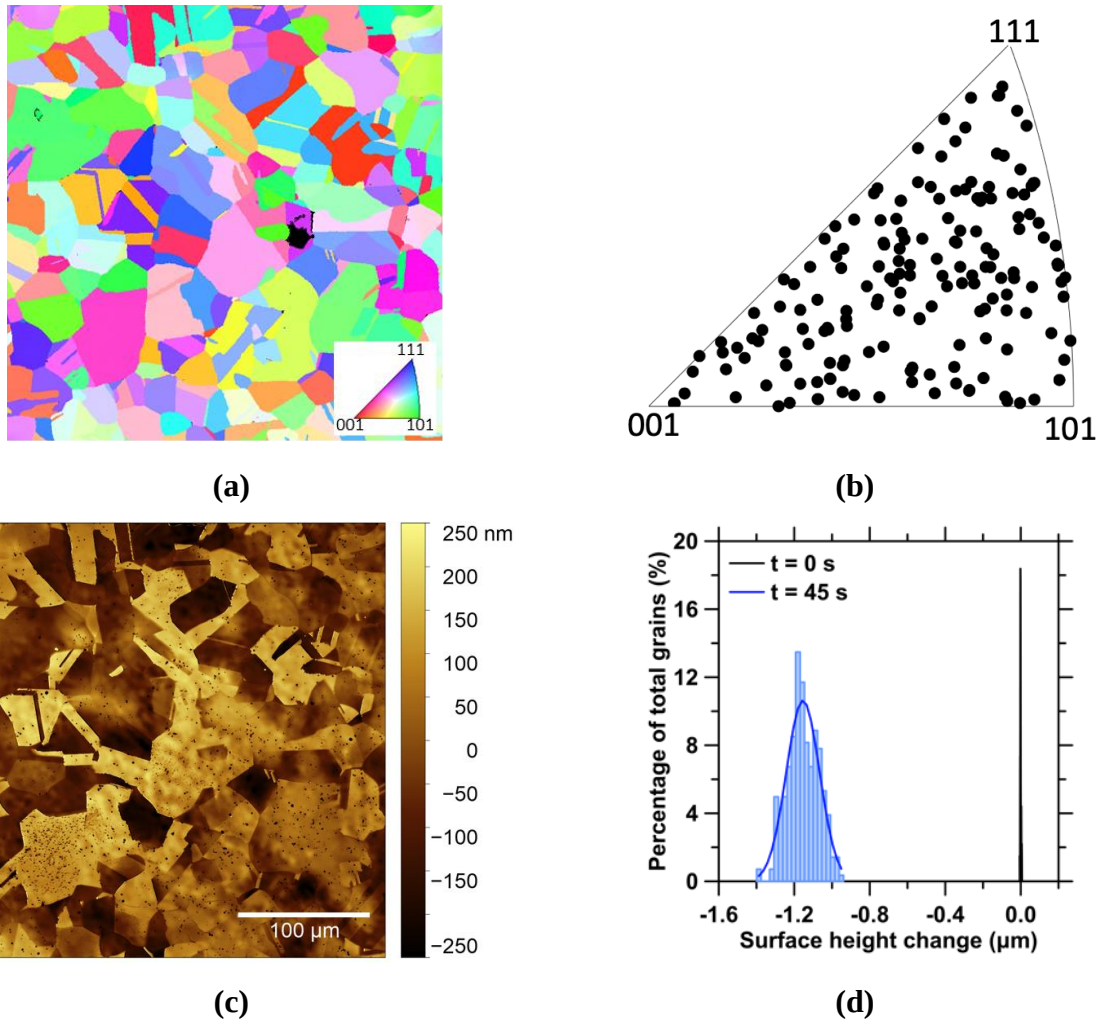

Figure 3-5: EBSD analysis of the microstructure of the solution-annealed 316L stainless steel surface showing: **(a)** grain orientation map with the color code shown in the inverse pole figure (IPF) as inset, and **(b)** collective orientation distribution of around 200 grains investigated herein. The grain orientations are given with respect to the surface normal direction. **(c)** The same area after transpassive corrosion in oxalic acid, and **(d) t**he grain-averaged surface height change frequency distributions of the corroded surface. The black curve in **(d)** represents the surface height change frequency distribution of the as-polished steel surface, which is centered at 0.0 µm (mean), and spread over a range of 20 nm (standard deviation). The sample was corroded in a 10 mass % oxalic acid solution at 20 °C for 45 s while imposing to a constant current density of 1 A/cm^2.

3.3.2 Grain orientation impacts on the potential-induced transpassive corrosion of 316L

The "potential-free" corrosion of 316L steel once again indicates that its corrosion rates are dependent on crystallographic orientation with respect to the surface normal direction. But herein, the "step-structure" is less pronounced due to the formation of recessed basins. To better understand 316L corrosion under conditions of electrochemical stimulation, a potential was applied to the steel surface to induce transpassive corrosion. When a high anodic potential is applied, the surface-proximate passivation layer breaks down instantly, and steel dissolves transpassively to form high valence species including Fe^{3+} and $HCrO_4^-$.[38] Although these oxidation products differ from those produced during the initial oxidation of stainless steel in reactor environments, such products do form, in time in reactor environments, due to interactions with oxidants that represent radiolytic products (e.g., hydroxyl radical and H_2O_2).[250] Therefore, anisotropic corrosion of about 200 randomly oriented grains (Figure 3-5a,b) as promoted by an applied potential was analyzed. Following transpassive corrosion in oxalic acid, the surface topography showed prominent grain contours (Figure 3-5c) arising from the formation of steps at grain boundaries with the average surface height having recessed by about 1.1 μm in just 45 seconds. Since the height variations within individual grains are much smaller compared to the actively corroded surface, the variance of ±0.25 μm as shown in Figure 3-5d dominantly resulted from differences in corrosion rates among grains which feature diverse orientations.

3.3.3 Correlating corrosion rates with grain orientations

By combining EBSD and VSI analyses, the corrosion rates of individual grains were extracted and then correlated with their respective orientations. Both the active and transpassive corrosion rates of grains are presented in inverse pole figure (IPF) plots. The scatter in the active

corrosion rates (see Figure 3-6a) is unexpectedly, substantial. Since remnant corrosion products were not observed on the corroded surface, this scatter is attributed to the formation of orientation-independent basins on the corroding surface [246,251], which affect an individual grain's average corrosion rate. Nevertheless, orientation dependence is evident in the dashed circles which show grains that are slightly oriented to the basis directions (i.e., <001>, <101>, and <111>). Indeed, the corrosion rates of these grains scaled as: {001} < {101} < {111}. In addition, because the {111} grains corrode the fastest, the orientation-specific corrosion rate was examined as a function of the angle (θ) between the surface normal and the <111> basis direction, as shown in Figures 3-6b that was computed as follows:

$$\theta_{(111)} = cos^{-1}\left(\frac{h+k+l}{\sqrt{3}\cdot\sqrt{h^2+k^2+l^2}}\right) \quad (3\text{-}5)$$

where h, k, l are the Miller indices of the surface normal. Interestingly, despite the large scatter, the corrosion rates show a decreasing trend as $\theta_{(111)}$ increases.

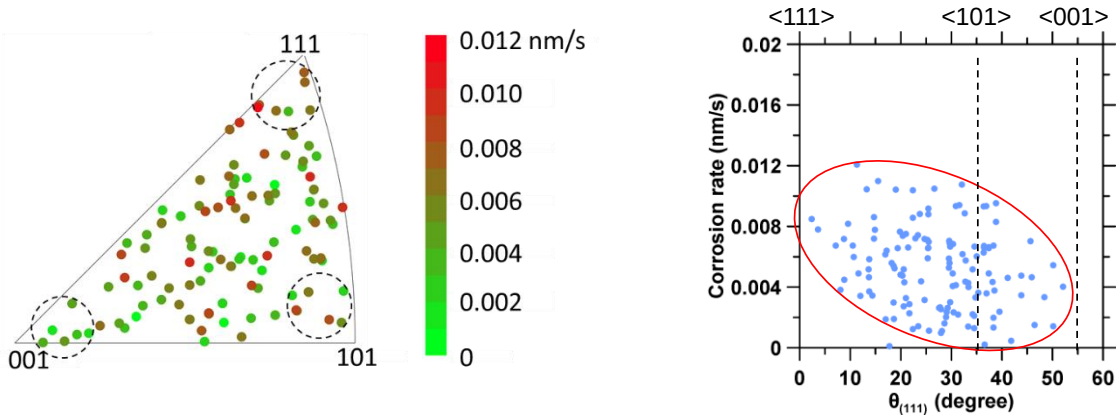

(a) **(b)**

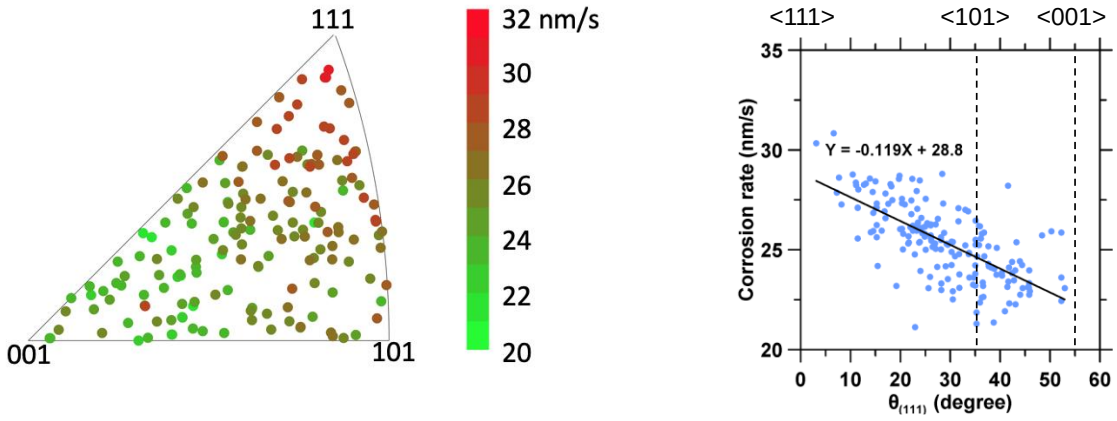

(c) **(d)**

Figure 3-6: (a) Active and **(c)** transpassive corrosion rates plotted in inverse pole figures showing grain orientation dependence. **(b)** Active and **(d)** transpassive corrosion rates as a function of $\theta_{(111)}$. Note that all data and results are presented with respect to the surface normal direction.

Far more convincingly than the active corrosion rate map, the transpassive corrosion rate map (see Figure 3-6c) shows that the grains strongly associated with the {111} planes rapidly dissolve, whereas the grains oriented close to the {001} planes show the highest resistance to corrosion. The scatter in the grain-averaged corrosion rates is significantly reduced, so that a more pronounced linear trend in corrosion rates is seen in grains with orientations intermediate between {111} and {001} (see Figure 3-6d). In general, the transpassive corrosion rates confirm that the general corrosion susceptibility ranks from {001} grains having the lowest to {111} grains having the highest susceptibility. Taken together, these findings indicate that crystallographic control of corrosion rates is, in fact, independent of the applied potential and the nature of solubilized species that may be mobilized due to alloy dissolution; i.e., the pathway by

which corrosion may be stimulated – so long as no transport (mass transfer) limitations are present.

3.3.4 Effects of surface and activation energies on corrosion rates

The initial step in corrosion is expected to require alloy dissolution. Therefore, simply speaking, in analogy to the traditional dissolution of other solutes, corrosion is expected to initiate by the provision of the energy that is needed to overcome the energy barrier between the reactants and products, i.e., the activation energy (ΔG^a) in Arrhenius-type kinetics.[252,253] This requires that the steel surface oxidizes to form aqueous ions; which involves the removal of surface atoms, in turn exposing the underlying planes. Thus, some of the energy cost for corrosion is associated with overcoming the interatomic forces between the surface atoms and their nearest neighbors. Such energy demands are inversely proportional to the surface energy (SE), which reflects the excess free energy resulting from dangling bonds [17] and that has been previously estimated as follows [236,254–256]:

$$SE = 2\frac{2|h|+|k|}{\sqrt{h^2+k^2+l^2}} \cdot \frac{E_b}{{d_0}^2} \quad (3\text{-}6)$$

where *h,k,l* are the Miller indices of a given grain that are arranged as $h \geq k \geq l$, E_b is the bond energy for a representative atomic bond and d_0 is the bond length. The absense of nearest neighbors of the surface atoms resulted in dangling bonds.[257] The dangling bond density is given as the number of dangling bonds ($2|h| + |k|$) per unit surface area ($\frac{1}{2}{d_0}^2\sqrt{h^2+k^2+l^2}$).[254–256] In Equation 3-6, E_b and d_0 are constants for a given material and independent of grain orientation assuming that the alloying elements randomly occupy lattice sites on the grain surfaces and in the bulk alloy. Therefore, for the same material, the surface energy is solely

determined by the pre-factor (unitless): $\frac{2|h|+|k|}{\sqrt{h^2+k^2+l^2}}$, which is proportional to both the dangling bond density and the surface energy. Figures 3-7a and 3-7b show the distribution of the pre-factor for grains featuring diverse orientations for grains which were exposed to both active and transpassive corrosion processes. The surface energy scales as: {101} > {001} > {111}. In general, the corrosion rates of {001} and {101} grains follow intuitively from their surface energy scaling, whereas the {111} grains exhibited the fastest corrosion rates although they feature the lowest surface energy.

These observations imply that surface energy is not the sole factor influencing the activation energy, and rates of alloy corrosion. Typically, a solute in contact with a solvent that contains, e.g., solvated ions tends to minimize its surface energy via adsorption of species on its surface. In turn, higher rates and extents of adsorption are usually attained on surfaces having high surface energies.[258,259] The adsorption of reactive site-blocking species (e.g., anions, oxygen, and other surfactants), from solution, impedes surface-solution interactions, and can enhance the activation energy of dissolution/corrosion, as previously observed for nickel or steel in contact with corrosion inhibitors.[260,261] Thus, the high corrosion rate of {111} grains despite their low surface energy can be explained by the lack of blocking layers containing adsorbed ionic species.[258,259] Evidence for such behavior is shown by the {111} surfaces of FCC-gold and FCC-cobalt which have been shown to have a lower affinity to many adsorbates because of their compact atomic arrangement and low dangling bond density.[262,263]

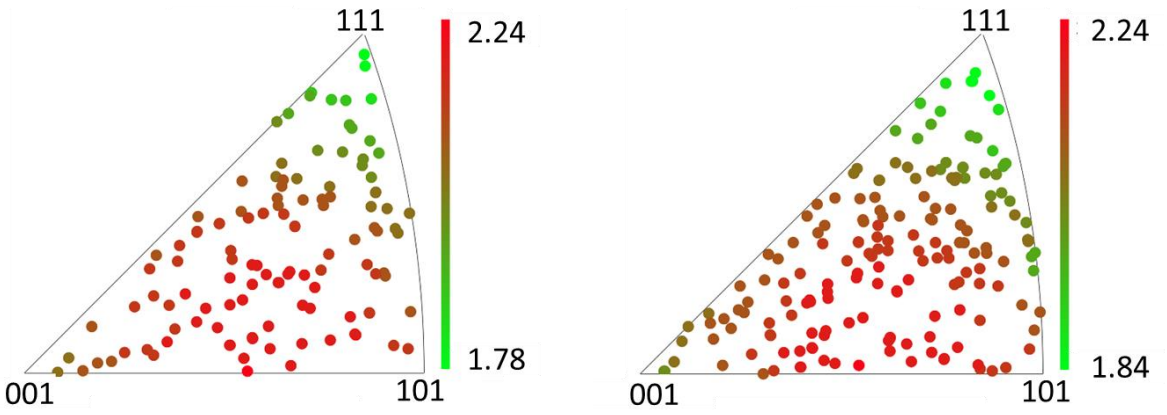

(a) **(b)**

Figure 3-7: The calculated surface energy pre-factor (unitless), $\frac{2|h|+|k|}{\sqrt{h^2+k^2+l^2}}$, for grains having different orientations correlated with their: **(a)** active and **(b)** transpassive corrosion rates. The grain orientations are given with respect to the surface normal direction.

Consistent with our observations of 316L surfaces undergoing active corrosion (Figure 3-6a), the adsorption of chlorine ions (Cl^-) on the {001} surfaces of FCC-platinum has been shown to strongly inhibit surface reactivities whereas Cl^- adsorption was barely observed on the {111} surfaces, which possesses high surface reactivity.[264] Other work has shown that adsorbed oxygen on the {001} surfaces of FCC-nickel prevented its oxidation, while {111} surfaces, which were characterized by low extents of oxygen adsorption, underwent the fastest oxidation.[260,265] In fact, nickel is an important constituent of 316L stainless steel that stabilizes the FCC-Fe phase at room temperature.[266] Moreover, the anisotropic oxidation rates of Ni-based alloys follow the same scaling as compared to the corrosion rates observed in this work,[236,260,265,267] suggesting the corrosion of 316L is kinetically analogous to the Ni oxidation process. Under conditions similar to the transpassive corrosion of 316L in oxalic acid (see Figure 3-6b), the anodic adsorption of

corrosion-inhibiting [268,269] oxalate ($C_2O_4^{2-}$) and bioxalate ($HC_2O_4^-$) anions, has been shown to be weaker on {111} than on the {001} and {101} surfaces of FCC-gold single crystals.[270] Therefore, the apparent activation energy of oxidation, which reflects both the direct (solute dictated) and indirect (solution imposed) influences of surface energy, produces an energetic scaling that follows as: $\Delta G^a_{\{001\}} > \Delta G^a_{\{101\}} > \Delta G^a_{\{111\}}$, consistent with the observed corrosion rates. This in turn explains why the lower energy {111} surface corrodes somewhat faster than the higher energy {001} and {101} surfaces which, intuitively, i.e., on account of their more unstable nature might be expected to show faster dissolution (corrosion) kinetics.

3.4 Summary and Conclusions

This work has examined the corrosion rates of 316L stainless steel by examining hundreds of grains which feature diverse crystallographic orientations. A 316L stainless steel was corroded under active and tranpassive conditions, which respectively represent reactor steel corrosion in crevices and as promoted by radiolytic products that serve as oxidants. The absolute active and transpassive corrosion rates were quantified by measuring the surface height retreat in conditions wherein the formation of overlying corrosion products was restricted. The grain-specific corrosion rates decrease as the surface plane progressively deviated from the {111} direction (i.e., with respect to the surface normal). Particularly, the corrosion rates follow the scaling {001} < {101} < {111}, whereas surface energy, which is expected to negatively correlate with the activation energy of corrosion and thus its rate, increased according to {111} < {001} < {101}. The rapid oxidation of {111} planes, despite their lowest surface energy, is postulated to be on account of minimal ion adsorption and reactive-site barrier formation on these planes. As a result, the activation energy of corrosion of the {111} planes is lower than that

of the {001} and {101} grains. The approach presented herein is significant in that it establishes the mechanisms by which grain orientation affects the rate of general corrosion; on account of effects that are imposed not simply by the solute (alloy), but also its interaction with its surrounding solvent, and ions contained therein. Our findings highlight a microstructural linkage to corrosion sensitivity and suggest that metallurgical processing that produces surface textures that promote exposure of {001} planes may yield improve oxidation resistance. Moreover, the findings indicate that the orientation dependence (mismatch) of corrosion rates of adjacent grains indeed causes the formation of "step structures" (see Figure 3-3d), which could result in stress concentration and localization in components subjected to mechanical loading. Not only could the presence of step structures result in the formation of localized weak planes, but it may also amplify local reaction rates (i.e., due to the effects of applied stress on enhancing reaction rates,[271–273] and the tendency for stress-corrosion cracking (SCC) in such regions.

Chapter 4. Atomic Dislocations and Bond-rupture Govern Dissolution Enhancement under Acoustic Stimulation

4.1 Introduction and Background

When high-intensity (i.e., energy per unit volume) ultrasound is transmitted through a liquid, microscale bubbles form, grow, and collapse.[274,275] The collapse of microscale bubbles causes the formation of shock waves or high velocity microjets, which can locally induce high pressures (up to several GPa)[276] and impart mechanical energy (up to dozens of mJ per bubble)[277] onto adjoining surfaces and interfaces. This can damage the surfaces of immersed solids,[278,279] e.g., ship propellers and hydraulic turbines.[280] On the other hand, such energetic perturbations offer a cost-efficient, reagent-free route to promote mineral dissolution, radical formation while mitigating energy consumption and toxic reagent requirement.[15,281–283] Therefore, sonication promotes "green chemistry" approaches for control and affectation of chemical reactions. The enhanced dissolution of inorganic minerals and solids is of interest for numerous applications, e.g., to enhance the beneficial utilization of industrial by-products (e.g., slags and fly ash) and rocks, to promote CO_2 mineralization, for rare-earth element extraction used as precursors for zeolite synthesis, etc.[284,285] Each of these approaches is foundational to achieve waste utilization, CO_2 mitigation (and utilization), and to broadly promote the principles and mandate of circular economy.

In spite of the many benefits and associated anecdotal observations, our understanding of the mechanisms of action—i.e., by which acoustic stimulation promotes mineral dissolution—has remained uncertain.[286,287] For example, the increase in reactivity upon sonication has often been attributed to a "temperature effect," which arises from the high temperature achieved within

cavitation bubbles.[157] However, recent results have suggested that, even under isothermal (i.e., macroscopically thermostatic) conditions, the effects of sonication are substantive.[16] On the other hand, sonication has been thought to impose a "pressure effect," wherein the pressure resulting from the shock waves deforms or fractures solid surfaces.[288] Finally, the increase in dissolution kinetics upon sonication has been postulated to be on account of improved mass transfer in solution, especially at solid–liquid interfaces due to mixing.[289] However, for equivalent conditions of convection (i.e., at constant Reynolds number: Re), the dissolution enhancement produced by convection alone is substantively inferior to that resulting from sonication.[16,290] For these reasons, it is necessary to mechanistically unravel how the chemical composition, structure and properties of the mineral solute, and the imposed attributes of the acoustic field affect the enhancement in dissolution rate that results upon sonication.[16] Towards this end, and building on the work of Wei *et al.*,[16] we offer a new theoretical framework to describe the effects of bubble cavitation on interfacial dissolution processes. As a complement to experiments, molecular dynamics simulations (MD) can provide a direct access to the effect of sonication on materials at the atomic scale and over a typical timescale of a few nanoseconds—which is largely invisible to experiments. The formation of dislocations in crystals subjected to a shock impact can be directly observed using non-equilibrium MD simulations.[279,291,292] In addition, the dynamics of the collapse of nanobubbles formed upon sonication can also be described by MD simulations.[293,294]

In this study, we seek to investigate the nature of the underlying mechanism(s) that controls the enhancement in dissolution kinetics featured by minerals upon sonication and, based on this knowledge, to establish a predictive model describing the effect of sonication on dissolution kinetics. To this end, we identify the key material properties that govern the potential for sonication to accelerate dissolution. Specifically, we show that the acoustic stimulation

affects minerals' reactivity through the breaking of interatomic bonds and the formation of atomic dislocations. Based on these results, we introduce a new framework to describe the effects of sonication on minerals' dissolution. This model rationalizes and explains the effects of acoustic stimulation on mineral reactivity as a combinatorial effect associated with atomic dislocations and bond breaking, and offers a unique framework to describe the effects of bubble cavitation on interfacial dissolution processes.

4.2 Materials and Methods

4.2.1 Materials

We considered a selection of naturally occurring minerals sourced from Ward's Science (see Table 4-1). To prepare the particulate samples, all the minerals were ground using a ball mill, and then sieved to isolate particles that have a size in the range of 300-to-600 μm. To prepare planar solute surfaces, the minerals were sectioned (i.e., with dimension smaller than 2 cm) and then embedded in epoxy resin to facilitate handling. The exposed mineral surfaces were polished successively using SiC abrasives and diamond paste and, finally polished using a 50 nm colloidal silica suspension. The surface topography maps of as-polished calcite and quartz surfaces used in the dissolution analyses are shown in Figure 4-1 and Figure 4-2, respectively. The calcite and quartz surfaces feature an initial root mean square (RMS) roughness (S_a) of around 5 and 10 nm, respectively.

Table 4-1. List of the minerals considered in the study, together with their chemical composition, mineral family, crystal system, and tracing element used for dissolution tests.

Minerals	**Chemical formula**	**Mineral family**	**Crystal system**	**Measured element**
Albite	$NaAlSi_3O_8$	Tectosilicate	Triclinic	Si
Anorthite	$CaAl_2Si_2O_8$	Tectosilicate	Triclinic	Si
Antigorite	$Mg_3(Si_2O_5)(OH)_4$	Phyllosilicate	Monoclinic	Si
Calcite	$CaCO_3$	Carbonate mineral	Trigonal	Ca
Dolomite	$CaMg(CO_3)_2$	Carbonate mineral	Trigonal	Ca
Fluorite	CaF_2	Halide mineral	Isometric	Ca
Orthoclase	$KAlSi_3O_8$	Tectosilicate	Monoclinic	Si
α-Quartz	SiO_2	Quartz	Trigonal	Si

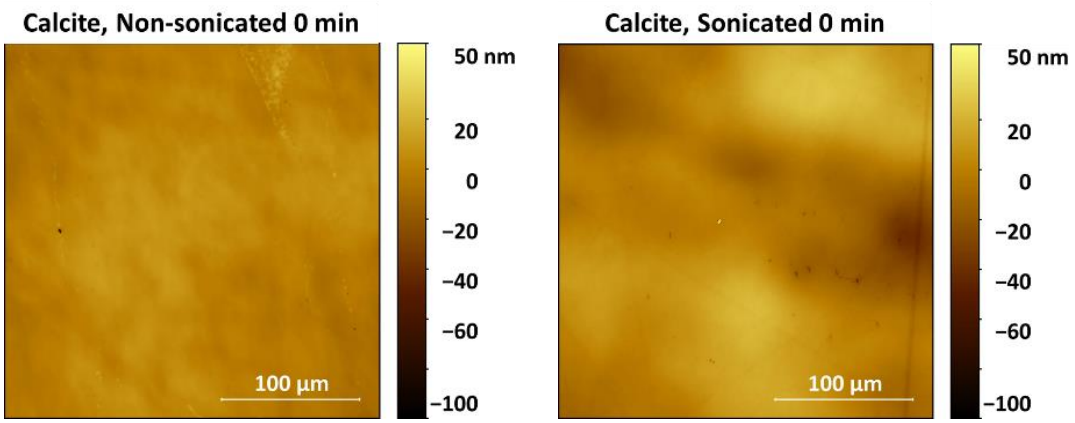

(a) **(b)**

Figure 4-1: Topography maps of as-polished calcite surfaces before dissolution reactions under (a) non-sonicated and (b) sonicated conditions. The surfaces feature a surface roughness on the order of 5 nm.

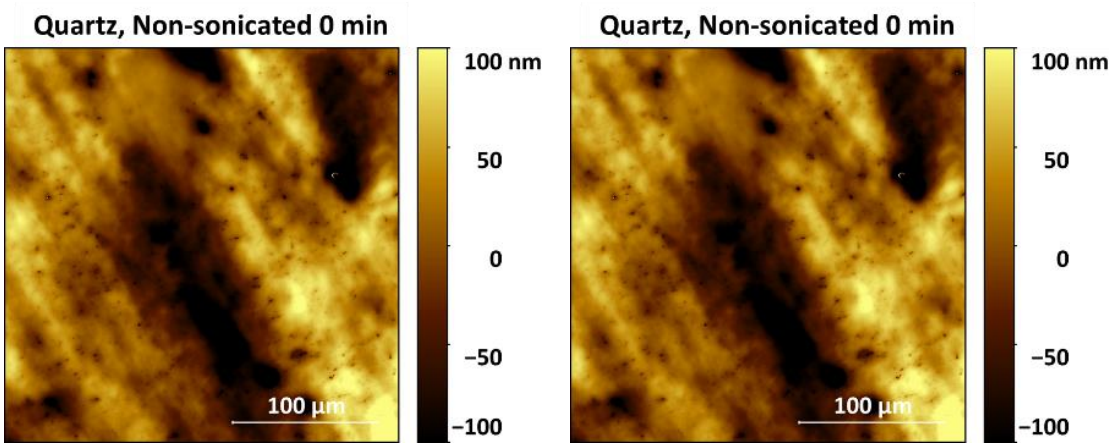

(a) **(b)**

Figure 4-2: Topography maps of as-polished quartz surfaces before dissolution reactions under (a) non-sonicated and (b) sonicated conditions. The surfaces feature a surface roughness on the order of 10 nm.

4.2.2 Experimental methods

4.2.2.1 Batch dissolution

Batch dissolution experiments were conducted in a manner similar to Wei *et al.*[16] by adding 0.1-0.5 g ground mineral samples into 100 mL of 18 MΩ·cm deionized (DI) water, thereby resulting in solid-to-liquid ratios (s/l) in the range of 1:200-to-1:1000. The solids were reacted with water under isothermal conditions (25 ± 0.5 °C) for up to 2 h to maintain dissolution in the far-from-equilibrium region, i.e., wherein amount of solute dissolved yields a linear expression as a function of time. Non-sonicated dissolution analyses were conducted in environmental chambers. Dissolution under conditions of sonication were carried out by circulating cooling water in a water-jacketed batch reactor.[16] In the case of non-sonicated dissolution, the solution was stirred using a magnetic stirrer at 350 rpm. Sonication was applied using a horn type ultrasonic system (Fisher Scientific 505 Sonic Dismembrator; 500 W; 1/2-inch tip diameter) operating at a constant ultrasonic power of 30 W.

Over the course of dissolution, the solutions were sampled at different time intervals and diluted in 5% HNO_3 (v/v) for elemental analysis following filtration through a 0.2 μm filter. The elemental analysis was carried out using a Perkin Elmer Avio 200 inductively coupled plasma-optical emission spectrometer (ICP-OES), with calibration standards prepared from concentrated (1000 ppm) standards (Inorganic Ventures). Dissolution rates are calculated based on a linear fitting of the concentration-time profiles. The uncertainty in the dissolution rates is determined based on two replicated experiments (which has been found to be large enough for monophasic minerals[16]), which, on average, yields an uncertainty of 15% and 10% for non-sonicated and sonicated conditions, respectively.

4.2.2.2 Particulate analysis

The particle size distributions (PSDs) of the particulate samples were measured using a LS13-320 Beckman Counter static light scattering analyzer based on three replicate experiments. One gram of ground and sieved particulates for each mineral species were analyzed prior to dissolution to obtain their particle size. The median diameter, d_{50}, the dispersion range, and the specific surface area (SSA) of the samples, estimated based on the assumption of spherical particulates are presented in Table 4-2. It is noted that antigorite forms sheet-like grains upon grinding (see Figure 4-5), so that, for this mineral, the spherical assumption may lead to inaccurate median diameter and SSA values. However, this assumption should not impact the measured relative dissolution enhancement data (Eq. 4-1). Following a desired period of dissolution, the particulates were retrieved from the reaction solution using a sieve with a 10 μm opening and subsequently examined using: a) light microscopy (Leica DM750P), and b) light scattering to assess changes in the particle size and/or surface morphology following dissolution under non-sonicated or sonicated conditions. For augmented morphology analysis, the dried particulates were dipped and attached to adhesive carbon tape and characterized using scanning electron microscope (SEM), model Phenom G-2.

Table 4-2. Median diameter, d_{50}, dispersion range and specific surface area (SSA) of the particulate-based mineral samples used in dissolution batch experiment.

Minerals	**d_{50} (μm)**	**Dispersion range (μm)**	**SSA (cm^2/g)**
Albite	541.9	309.6 – 1255	76.3
Anorthite	583.4	309.6 – 1143	59.5
Antigorite	310.5	6.2 – 1143	652.0
Calcite	493.6	234.0 – 1255	74.6
Dolomite	560.1	282.1 – 1041	78.8
Fluorite	555.7	282.1 – 1041	49.4
Orthoclase	493.6	282.1 – 1041	80.2
α-Quartz	373.1	234.0 – 653	59.2

4.2.2.3 Surface topography characterization

The topographies of dissolving surfaces were examined using a Zygo NewView 8200 vertical scanning interferometry (VSI). A 50× Mirau objective (numerical aperture, NA = 0.55) was used that yields a lateral resolution of 0.16 μm and a vertical resolution on the order of 2 nm. The three-dimensional (3D) topography data was analyzed using Gwyddion (v2.54) and MATLAB® R2017b.[246,295]

4.2.3 Molecular dynamics simulations

4.2.3.1 Force field

We carried out a series of molecular dynamics (MD) simulation to compute select mechanical properties of the minerals considered herein. In general, the accuracy of MD simulations largely depends on that of the interatomic forcefield. Although using a universal interatomic potential for all the minerals would be desirable, such a forcefield is not presently available for the wide variety of the minerals selected herein (i.e., silicates, carbonates, etc.). Rather, here, we selected two types of interatomic potentials based on their ability to offer a realistic prediction of the structure and properties of the minerals. On the one hand, we selected a Buckingham-based potential for α-quartz,[296] fluorite,[297] calcite,[298] and dolomite[298]—wherein the forcefield parameters can be found each relevant reference. On the other hand, we adopted the ClayFF classical forcefield[299] for the other minerals. In both cases, Coulombic interactions are resolved by using the particle-particle particle-mesh (PPPM) method.[300] Each system comprises about 2,000-to-9,000 atoms (depending on the size of the unit cell), which is found to be large enough to avoid any spurious finite size effect (see Figure 4-3 for more detail). Periodic boundary conditions are employed along all directions, except for the calculation of stacking fault energy (see below). All of the simulations are performed with the open source molecular dynamics code LAMMPS.[301]

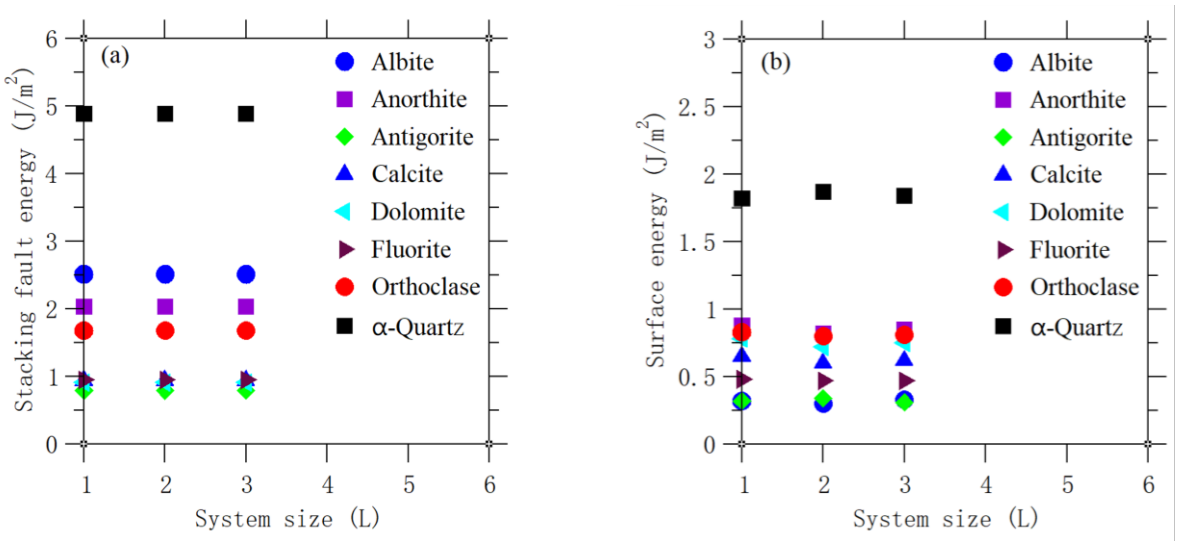

(a) **(b)**

Figure 4-3: Simulated (a) stacking fault energy and (b) surface energy as the function of system size. The length L refers to the initial dimensions of the simulated box.

To validate our MD results, we first ensured that the crystalline structure at 300 K of the minerals considered herein is well described (i.e., vis-à-vis experimental observations) by the selected forcefields. Towards this end, starting from initial crystal structures sourced from experiments (see Table 4-3), each crystal was equilibrated at 1 K and zero pressure for 1 ns. Then, the equilibrated structures were further relaxed at 300 K and zero pressure for an additional 1 ns. All simulations were conducted in the isothermal-isobaric (*NPT*) ensemble, wherein both the box length and tilt angles were free to change to ensure a zero stress in all directions. The Nosé–Hoover thermostat[302,303] was used for temperature control. For all simulations, the timestep was fixed as 1 fs. To filter out the effect of thermal fluctuations, all of the computed properties were averaged over 100 ps of statistical averaging after full equilibration. As shown in Figure 4-4, the mineral densities calculated from the MD simulations

agree well with experimental data. Moreover, the relative errors of the predicted lattice constants are well below 3.5% (see Table 4-3). These results indicate that our MD simulations are able to offer a realistic prediction of the structures of all the minerals considered herein.

It should be noted that forcefields are typically parameterized based on equilibrium bulk properties and do not always perform well when used to predict more complex properties (e.g., surface energy or stacking fault energy). Here, to assess the level of accuracy of the forcefields in predicting such properties, we compared the simulated surface energy obtained for quartz with available experimental results. Available experimental data suggests that the surface energy data of quartz range from 1.8 to 2.4 J/m2 depending on the surface orientation,[304] while our simulation data range from 1.82 to 2.93 J/m2. The surface energy along the [001] cleavage plane was found to be 2.23 J/m2 based on ab initio simulations,[305] which is fairly close to the value obtained herein (i.e., 1.82 J/m2). This suggests that the forcefield selected herein offers reasonable predictions of the surface energy of quartz. We also compared the simulated surface energy obtained for fluorite along its cleavage plane (i.e., [111] plane) with available results from ab initio simulations.[306] We find that the surface energy predicted by the present forcefield (i.e., 0.48 J/m2) indeed exhibits a close match with the ab initio data (i.e., 0.47 J/m2).

4.2.3.2 Calculation of surface energy

To calculate the surface energy, the equilibrated crystals were first cut along a given plane into two parts by switching off the interactions between atoms across the plane. Then, the cut system was further relaxed at zero pressure for equilibration. The surface energy γ_surf associated with this plane was calculated as $\Delta U/\Delta A$, where ΔU is the variation in the potential energy of equilibrated structures before and after cleaving, while ΔA is the surface area created

by the cleavage. To identify the cleavage plane, we first selected a series of tentative plane orientations (all the plane orientations considered herein are listed in Table 4-4). Then, we systematically attempted to cut the system into two parts along varying plane locations. Since cracks preferentially initiate and propagate along the weakest plane, we then identified the cleavage plane as the one featuring the lowest surface energy (i.e., which characterizes the plane that exhibits the lowest/weakest cohesion within the mineral). For statistical purposes, the surface energy is obtained by averaging the results from three independent simulations

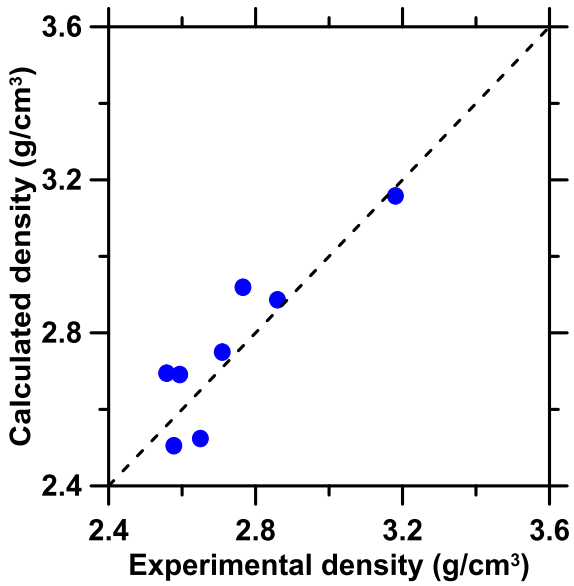

Figure 4-4: Comparison between the mineral densities computed from molecular dynamics simulation and experimental values.

Table 4-3. Lattice parameters of the minerals considered herein computed by molecular dynamics (MD) simulations. These values are compared with reference experimental data.

Minerals		***a* (Å)**	***b* (Å)**	***c* (Å)**	***α* (°)**	***β* (°)**	***γ* (°)**	**Forcefield**	**Ref.**
	Exp.	8.2	12.9	7.1	93.5	116.5	90.3		
Albite	MD	8.1	12.6	7.1	95.2	117.2	90.1	ClayFF	[307]
	Error (%)	0.7	1.7	0.3	1.7	0.7	0.2		
	Exp.	8.2	12.9	14.2	93.1	115.9	91.3		
Anorthite	MD	8.1	12.6	14.0	93.4	6.6	90.4	ClayFF	[308]
	Error (%)	1.4	2.0	1.4	0.3	0.6	1.0		
	Exp.	43.5	9.3	7.3	90.0	91.3	90.0		
Antigorite	MD	44.3	9.3	7.3	90.0	91.3	90.0	ClayFF	[309]
	Error (%)	1.9	1.0	0.1	0.0	0.0	0.0		
	Exp.	5.0	5.0	17.1	90.0	90.0	120.0		
Calcite	MD	4.9	4.0	17.1	90.0	90.1	120.0	Buckingham	[310]
	Error (%)	0.9	0.9	0.4	0.0	0.1	0.0		
	Exp.	4.8	4.8	16.0	90.0	90.0	120.0		
Dolomite	MD	4.8	4.8	16.2	93.1	88.3	121.4	Buckingham	[311]
	Error (%)	0.5	1.2	1.3	3.4	1.9	1.1		
	Exp.	5.5	5.5	5.5	90.0	90.0	90.0		
Fluorite	MD	5.5	5.5	5.5	90.0	90.0	90.0	Buckingham	[312]
	Error (%)	0.2	0.2	0.2	0.0	0.0	0.0		
	Exp.	8.6	13.0	7.2	90.0	116.1	90.0		
Orthoclase	MD	8.5	12.8	7.2	90.0	116.2	90.0	ClayFF	[313]
	Error (%)	1.4	1.8	1.8	0.0	0.1	0.0		
α-Quartz	Exp.	4.9	4.9	5.4	90.0	90.0	120.0	ClayFF	[314]

Table 4-4. Orientations of the cleavage planes considered for each mineral and associated surface energy values (γ_{surf}).

Minerals	Surface 1		Surface 2		Surface 3		Surface 4	
	Plane	γ_{surf}	Plane	γ_{surf}	Plane	γ_{surf}	Plane	γ_{surf}
Albite	[001]	0.48 ± 0.01	[010]	0.33 ± 0.01	[100]	0.71 ± 0.01		
Anorthite	[001]	0.93 ± 0.02	[010]	0.88 ± 0.03	[100]	1.14 ± 0.02		
Antigorite	[001]	0.32 ± 0.01	[010]	0.76 ± 0.01				
Calcite	[001]	1.47 ± 0.04	[104]	0.65 ± 0.03				
Dolomite	[001]	1.18 ± 0.02	[104]	0.78 ± 0.03				
Fluorite	[100]	2.65 ± 0.04	[010]	2.72 ± 0.04	[001]	2.11 ± 0.04	[111]	0.48 ± 0.01
Orthoclase	[001]	1.21 ± 0.03	[010]	0.83 ± 0.02	[100]	0.85 ± 0.02		
α-Quartz	[100]	2.96 ± 0.04	[010]	2.93 ± 0.03	[001]	1.82 ± 0.02		

4.2.3.3 Calculation of stacking fault energy

The stacking fault energy characterizes the energy barrier that needs to be overcome to activate a stacking fault defect, which plays an important role in dislocation formation of minerals.[315] The computation of the stacking fault energy was performed as follows. Starting from the equilibrated crystal structure, the structure is relaxed toward its inherent configuration (i.e., the local minimum position in the energy landscape) by using the conjugate gradient algorithm. The boundary conditions were set as a free boundary along the direction that is perpendicular to the selected slip plane and periodic along the other two directions (with fixed length). During the stacking fault calculation, the two halves of the crystal are rigidly laterally displaced with respect to each other along the slip plane. In detail, the upper part of the system is gradually displaced

along the slip line with an increment of 0.1 Å while the lower part was kept fixed. After each displacement increment, the crystal is allowed to relax in the direction that is orthogonal to the slip plane using the conjugate gradient algorithm (while the atomic coordinates remain frozen along the two other directions). We then tracked the evolution of the energy of the system as a function of the slip plane displacement. The stacking fault energy γ_{stack} of the selected slip plane was calculated from the difference between the maximum potential energy achieved during the deformation and that of the equilibrium configuration (i.e., before any deformation). Similar to the surface energy, we calculated the stacking fault energy along a large number of slip planes (see Table 4-5 for more details) and identified the slip plane as the one featuring the lowest stacking fault energy (i.e., along which dislocation formation is energetically preferred). For statistical purposes, the stacking fault energy is also obtained by averaging the results obtained from three independent simulations.

Table 4-5. Orientations of the slip planes considered for each mineral and associated stacking fault energy values (γ_{stack}).

Minerals	Slip plane 1		Slip plane 2		Slip plane 3		Slip plane 4	
	Plane	γ_{stack}	Plane	γ_{stack}	Plane	γ_{stack}	Plane	γ_{stack}
Albite	[001]	2.51 ± 0.00	[010]	10.48 ± 0.00				
Anorthite	[001]	2.03 ± 0.00	[010]	5.03 ± 0.00				
Antigorite	[001]	0.79 ± 0.00	[010]	1.58 ± 0.00				
Calcite	[001]	0.94 ± 0.00	[104]	1.47 ± 0.00				
Dolomite	[001]	0.91 ± 0.00	[104]	1.73 ± 0.00				
Fluorite	[001]	1.55 ± 0.00	[010]	1.73 ± 0.00	[001]	0.95 ± 0.00	[111]	1.03 ± 0.00
Orthoclase	[001]	1.68 ± 0.00	[010]	4.58 ± 0.00				
α-Quartz	[001]	7.04 ± 0.00	[010]	7.59 ± 0.00	[001]	4.89 ± 0.00		

The orientations of cleavage and slip planes that are identified herein for each mineral are listed in Table 4-6, and the calculated surface energy and stacking fault energy of minerals considered herein are listed in Table 4-7.

Table 4-6. Orientations of the cleavage and slip planes that are identified herein for each mineral. The list of the interatomic bonds crossing the planes is provided. Results are compared to previous experimental observations whenever available.

Minerals	Cleavage plane			Slip plane		
	This study	Crossing bond	Previous results	This study	Crossing bond	Previous results
Albite	[010]	Al–O	[010][316]	[001]	Al–O, Na-O	[001][317]
Anorthite	[010]	Si–O, Al–O	[010][153]	[001]	Si–O, Al–O, Ca–O	
Antigorite	[001]	Mg–OH	[001][318]	[010]	Mg–OH	
Calcite	[104]	Ca–O	[104][319]	[001]	Ca–O	
Dolomite	[104]	Ca–O, Mg–O	[104][320]	[001]	Mg–O	[001][321]
Fluorite	[111]	Ca–F	[111][322]	[001]	Ca–F	[001][306]
Orthoclase	[010]	Al–O	[001] or[010][323]	[001]	Si–O, Al–O, K–O	
α-Quartz	[001]	Si–O	[001][324]	[001]	Si–O	

4.2.3.4 Calculation of the average bond energy

The average bond energy, S_{bond}, is calculated based on the dissociation enthalpy D° of each bond crossing the cleavage plane as: $S_{\text{bond}} = \sum_{i=1}^{N} x_i D^{\circ}$, where *N* is the total number of chemical bond types on the cleavage plane, i represents the type of chemical bond, and x_i are the fractions of each type of bond. The dissociation enthalpy D° values are obtained from Ref.[325]

4.2.3.5 Calculation of the average degree of covalency

The average degree of covalency f_{cov} of the bonds crossing the slip plane of each mineral is calculated as: $f_{\text{cov}} = \sum_{i=1}^{N} x_i \exp(-0.25\Delta E_i^2)$, where *N* is the total number of chemical bond types on the slip plane, *i* represents the type of chemical bond, x_i are fractions of each type of bond, and ΔE_i *i*s the associated difference in the electronegativity of the pair of elements forming the bond.

Table 4-7. Surface energy and stacking fault energy computed from molecular dynamics simulations.

Minerals	Surface energy (J/m^2)	Stacking fault energy (J/m^2)
Albite	0.33	2.51
Anorthite	0.88	2.03
Antigorite	0.32	0.79
Calcite	0.65	0.94
Dolomite	0.78	0.91
Fluorite	0.48	0.95
Orthoclase	0.83	1.68
α-Quartz	1.82	4.89

4.3 Results and Discussion

4.3.1 Effect of sonication on dissolution kinetics

We focused on 8 archetypical minerals (see Table 4-8)—chosen based on their abundance in Earth's crust[326] and so as to cover a wide range of mineral families and crystal classes (see Table 4-1). We measured their far-from-equilibrium dissolution rates both under sonicated (acoustically stimulated) and non-stimulated conditions (see Methods section). To

quantify the effects of acoustic stimulation on reactivity, we ascertained the relative increase in dissolution rate under stimulation as:

$$D_{\mathrm{r}}(\%) = \frac{k_s - k_0}{k_0} \times 100\% \quad (4\text{-}1)$$

where k_s and k_0 are the dissolution rates measured under stimulated and stimulation-free conditions, respectively. As observed previously, we find that acoustic stimulation systematically enhances dissolution rates (see Table 4-8). However, we observe that the effect of stimulation on dissolution significantly depends on the mineral. For instance, the relative increase in dissolution rate ranges from 6.5% for quartz (i.e., wherein the effect of sonication is negligible) to 1300% for antigorite (i.e., a notable 14× increase). In line with previous observations,[16] this demonstrates that the magnitude of stimulation-induced dissolution acceleration is strongly solute-dependent. Note that, to enable meaningful comparisons: (i) for the dissolution analyses, all analyses are uniformly conducted under isothermal conditions (25 ± 0.5°C) and (ii) the stimulation-free analyses are carried out under *matched conditions* of convective mixing (of equivalent Reynolds number).[16] When considered within this context, the data in Table 4-8 highlights that the dissolution amplifications produced by acoustic stimulation are not on account of bulk heating and/or convection, as previously suggested.[327,328]

Table 4-8. Minerals studied herein along with their dissolution rates under non-sonicated and sonicated conditions, and their relative increases in dissolution rate upon sonication. Dissolution rates are averaged over two independent measurements.

Minerals (25°C, 1 bar)	**Non-sonicated dissolution rate ($\times 10^{-9}$ mol/m^2/s)**	**Sonicated dissolution rate ($\times 10^{-9}$ mol/m^2/s)**	**Relative increase in dissolution**
Albite ($NaAlSi_3O_8$)	3.80 ± 0.42	18.9 ± 2.0	400% ± 86%
Anorthite ($CaAl_2Si_2O_8$)	9.10 ± 0.67	22.4 ± 1.5	150% ± 22%
Antigorite ($Mg_3(Si_2O_5)(OH)_4$)	4.50 ± 0.52	60.9 ± 5.8	1300% ± 270%
Calcite ($CaCO_3$)	1950 ± 190	9400 ± 680	380% ± 65%
Dolomite ($Ca,Mg(CO_3)_2$)	256 ± 49	1590 ± 190	520% ± 160%
Fluorite (CaF_2)	491 ± 28	1960 ± 210	300% ± 50%
Orthoclase ($KAlSi_3O_8$)	4.51 ± 0.52	19.7 ± 1.3	340% ± 62%
α-Quartz (SiO_2)	27.0 ± 1.7	28.8 ± 1.0	6.50% ± 0.63%

4.3.2 Role of surface area increase caused by particulate fracture

We now seek to assess whether the stimulated dissolution acceleration arises from an increase in the exposed surface area of dissolving solids (e.g., due to fracture or deformation). Indeed, the collapse of cavitation bubbles can generate surface stresses on solid surfaces, which may, for instance, result in surface damage and fracture.[329] Therefore, we first examined, superficially, the shape, size and morphology of solid particulates (i.e., around 4-6 particulates of antigorite, calcite, and quartz, shown in Figure 4-5) prior to and following 30 min of dissolution under conditions of acoustic stimulation; for solids which show high-, intermediate-, and low-

sensitivity to acoustic stimulation, respectively (see Table 4-8). We observed that antigorite and calcite particulates have small "chips" broken off, and that the edges and corners of the antigorite and calcite particulates tended to become smoother following stimulation due to interactions with high-velocity microjets.[330] In contrast, the quartz particles appear virtually unaffected by sonication (see Figure 4-5). While qualitative, these observations—although coarse—are consistent with the fact that the dissolution kinetics of quartz are broadly unaffected by acoustic stimulation.

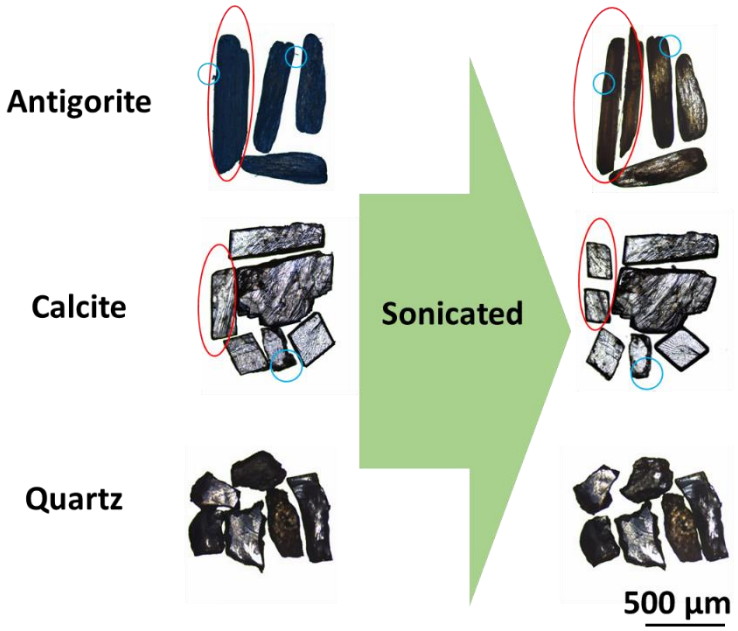

Figure 4-5: Evidence of fracture under sonication. Polarized light microscope images of solute particulates for antigorite, calcite, and quartz, both before and after 30 min of dissolution under sonicated conditions. The red circles highlight that the particulates have small "chips" broken off, and the blue circles highlight that the edges and corners of the particulates tended to become smoother.

The morphology changes of calcite particulate following dissolution are augmented by scanning electron microscope (SEM). Following non-sonicated dissolution, calcite particulates exhibit well-defined cleavage edges and planes, which are formed during sample preparation, i.e., mechanical grinding (see Figure 4-6a). However, these edges and corners become smoothened after dissolution under sonication (see Figure 4-6b). One the one hand, the implosion of cavitation bubbles tends to break the calcite particulates into smaller pieces. For example, in Figure 4-6b, the dimension of the majority of the particulates becomes lower than 300 μm, wherein many particulates have a size below 50 μm. The smaller sized pieces are likely to be flaked off from the corner and/or edges of the original particulates—as shown in Figure 4-6c, which highlights a newly-formed sharp concave corner (red circle) of a particulate present in Figure 4-6b (labeled with red square). On the other hand, the high-frequency interparticle collisions driven by ultrasound tend to accelerate the rounding of the newly-formed cleavage edges and planes and, therefore, facilitate the smoothening of the edges and corners[331]. These observations suggest that sonication-induced fracture—and resulting changes in the surface of the particles—might impact their dissolution kinetics.

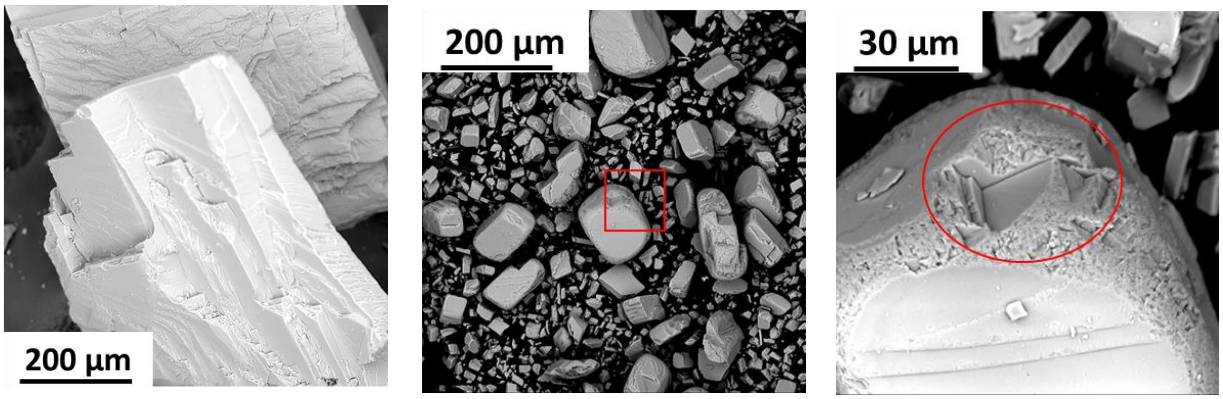

(a) **(b)** **(c)**

Figure 4-6: Morphology images of calcite particulates following 30 min of dissolution under (**a**) non-sonicated and (**b,c**) sonicated conditions, as observed by scanning electron microscope (SEM). The corner of one particulate labeled with a red square in (**b**), is enlarged and shown in (**c**) and exhibits smoothened edges and newly-formed sharp concave corner (red circle).

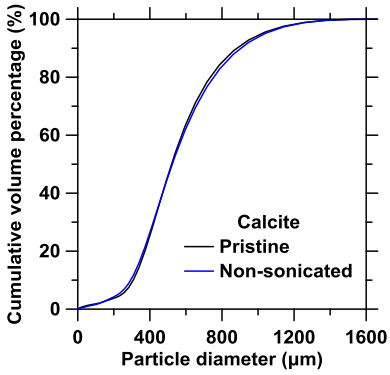

Figure 4-7: Cumulative volume distribution of calcite particulates before and after 30 min of dissolution under non-sonicated condition. The overlap of the two curves indicates neglectable changes in particulate size due to dissolution reaction.

To more quantitatively validate our visual observations, we measured the particle size distribution (PSD) of stimulated, and non-stimulated dissolving particulates (see **Methods**). First, we note that the PSD of the solute remains effectively unchanged over the time period of non-sonicated dissolution (see Figure 4-7). For example, even for calcite (i.e., the mineral that exhibits the fastest dissolution kinetics among the solutes considered herein, see Table 4-8), 30 min of non-sonicated dissolution reduces the size of a median particle ($d_{50} \approx 493.6$ μm) by at most 0.13 μm, which is negligible as compared to its pristine dimension. In contrast, as shown in Figure 4-8a, the PSD features a considerable leftward shift upon sonication, which is indicative of particle size reduction. For example, for calcite we note a reduction in particle diameters of nearly 100 μm (see Figure 4-8a). Based on the dissolution rate measured under sonicated conditions (9.40×10^{-6} mol/m^2/s) and the short reaction time of 30 min, this decrease in particle size cannot be explained solely by amplified dissolution. Rather, sonication appears to induce significant fracture and comminution—wherein calcite particulates break into smaller pieces. Such fracture results in a 20% increase in specific surface area (SSA) of calcite (see Figure 4-8a; as measured using light scattering data and assuming spherical particles), which, in turn, is expected to result in a proportionate increase in its dissolution rate–although not to the extent shown in Table 4-8 (see below). For reference, herein (20 kHz ultrasound), the collapsing cavitation bubbles are estimated to have an average diameter of ~150 μm,[331] as labelled with a black vertical dashed line in Figure 4-8a. We find that the shift in PSD resulting from sonication is notably more pronounced for the particulates exhibiting a diameter that is larger than the average bubble size. This suggests that the fracture of the particulates upon sonication is primarily on account of asymmetric bubble collapse and microjet formation.[16,331,332] It is noted that the shift in the PSD curve in the small particle diameter region might be underestimated, as

the small flakes (see Figure 4-6b) cannot be completely retrieved from solution. Nevertheless, in contrast with calcite, the PSD of quartz shows a surface area increase of only around 1% (see Figure 4-8b), which could also be due to variations within samples. This begins to explain, at least in part, the differing effects of acoustic stimulation on the dissolution behavior of calcite and quartz. More broadly, these results suggest that sonication-induced fracture is at least partially at the origin of the dissolution rate amplification observed herein.

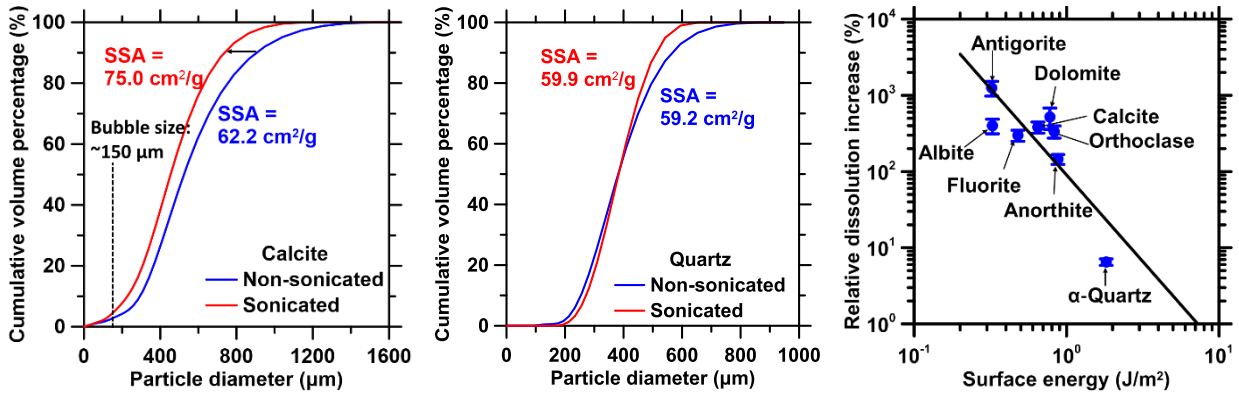

(a) **(b)** **(c)**

Figure 4-8: Effect of particulate fracture on dissolution enhancement. Cumulative volume distribution of solute particulates following 30 min of dissolution under non-sonicated and sonicated conditions for **(a)** calcite and **(b)** quartz. The vertical dashed line in **(a)** indicates the estimated average size of collapsing bubbles.[331] **(c)** Measured relative increase in dissolution rate (D_r) as a function of the surface energy computed by molecular dynamics simulations for all the minerals considered herein. In **(c)**, the data is fitted by an equation of the form: $\log(D_r) = -2.27\log(\gamma_{surf}) + 4.50$, where γ_{surf} (J/m^2) is the surface energy of the solute. The error bars represent the standard deviation.

To better understand the linkages between sonication-induced dissolution acceleration and solute fracture, for the range of solutes considered herein, molecular dynamics (MD) simulations were used to compute their surface energy in vacuum (see Methods) along the cleavage surface of the minerals—i.e., the weakest surface along which cracks are expected to propagate. Indeed, following linear elastic fracture mechanics (i.e., assuming brittle fracture), the fracture energy required to propagate a preexisting surface flaw is approximately equal to the energy needed to create new surfaces (i.e., 2 times the surface energy; γ_{surf}).[333] For a fixed energy provided via cavitation (i.e., since for monochromated ultrasound, the mechanical energy arising from cavitation at a given temperature is fixed at constant sonication power), the surface energy captures the relative propensity for minerals to crack/fracture under sonication. As shown in Figure 4-8c, we observe a strong, although inverse correlation (solid black line) between the extent of dissolution acceleration as a function of the mineral's surface energy. This observation implicates the role of fracture in the dissolution stimulation, wherein minerals associated with lower surface energy tend to break more easily, hence revealing additional surface area and, as a result, are more affected by sonication. Nevertheless, the increase in exposed surface area upon sonication remains disproportionately inferior (around 20%) to the observed increase in dissolution rate (about 300% for calcite); in agreement with the conclusions of Wei *et al.*.[204] This indicates that, besides fracture, additional acoustic stimulation-activated mechanisms are operative.

4.3.3 Role of localized expedited dissolution kinetics

To further probe how sonication affects the solute's surface, we used vertical scanning interferometry (VSI) to examine the evolution of the surface topography of calcite and quartz

under sonicated and non-sonicated conditions (see Methods). We first focus on calcite. As shown in Figure 4-1, pristine calcite surfaces (i.e., before dissolution) are rather smooth—with a root mean square (RMS) roughness that is on the order of 5 nm. After 30 min of non-sonicated dissolution, we find that the surface roughness increases up to 10 nm. As shown in Figure 4-9a, we observe the formation of a few deep etch pits (i.e., local regions deeper than 200 nm) on the dissolving surface. We then calculate the distribution of the pixel-wise heights of the surface, both before and after dissolution (see Figure 4-9e, blue bar plot). We observe that these distributions are largely symmetric. Importantly, we note that non-sonicated dissolution does not notably affect the width of the surface height distribution at the nanometer level. This suggests that, within the exposure time period (30 min) under non-sonicated dissolution, the dissolving surface exhibits a fairly homogeneous form of "layer-by-layer" retreat, i.e., each point of the surface dissolves at similar rates and only a few etch pits are formed[142]—as labeled with red circles in Figure 4-9a.

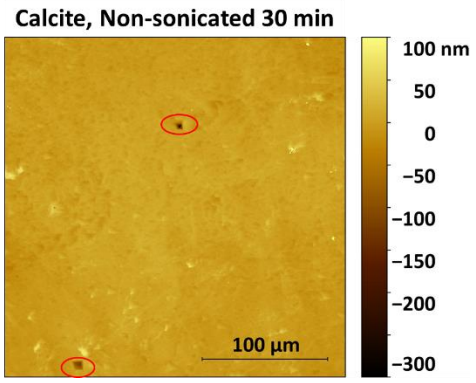
Calcite, Non-sonicated 30 min
100 nm
50
0
−50
−100
−150
−200
−300
100 µm

(a)

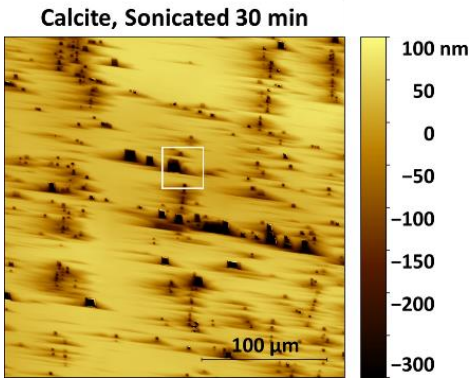
Calcite, Sonicated 30 min
100 nm
50
0
−50
−100
−150
−200
−300
100 µm

(b)

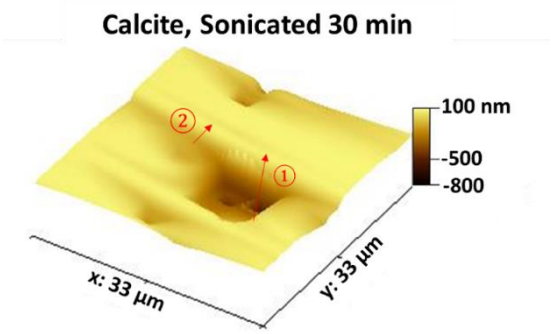
Calcite, Sonicated 30 min
100 nm
-500
-800
x: 33 µm
y: 33 µm

(c)

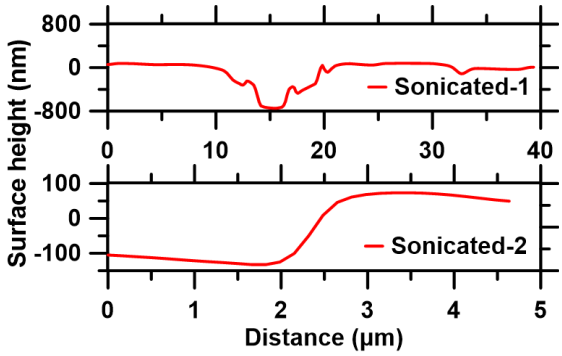
Surface height (nm)
800
0
-800
Sonicated-1
0
10
20
30
40
100
0
-100
Sonicated-2
0
1
2
3
4
5
Distance (µm)

(d)

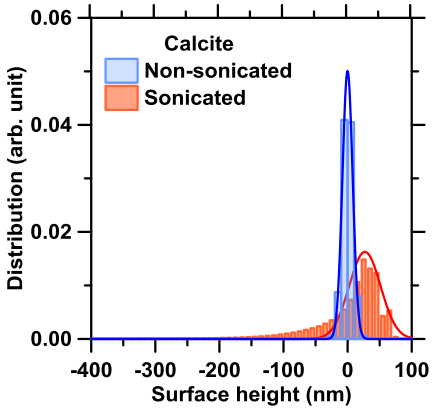
Calcite
Non-sonicated
Sonicated
Distribution (arb. unit)
0.06
0.04
0.02
0.00
-400
-300
-200
-100
0
100
Surface height (nm)

(e)

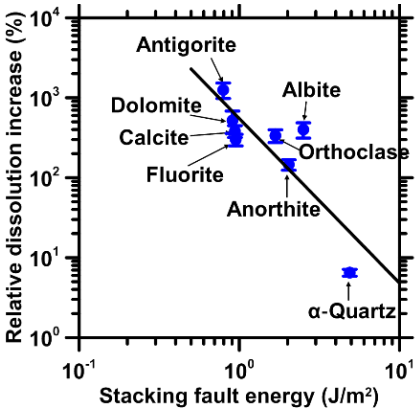
Relative dissolution increase (%)
Antigorite
Albite
Dolomite
Calcite
Orthoclase
Fluorite
Anorthite
α-Quartz
Stacking fault energy (J/m²)

(f)

Figure 4-9: Effect of sonication on the topography of dissolving calcite surfaces. (a,b) Representative topography images of calcite surfaces following 30 min of dissolution under **(a)** non-sonicated and **(b)** sonicated conditions. Etch pits developed under non-sonicated dissolution are marked with red circles in panel **(a)**. **(c)** Associated surface height frequency distributions, wherein the solid lines show Gaussian fits. **(d)** 3D topography map and **(e)** surface height line profiles of representative pits that are marked with white boxes in panel **(b)**. The mean height in each topography profile is normalized to be 0 nm. **(f)** The measured relative increase in dissolution rate (D_r) as a function of the stacking fault energy computed by molecular dynamics simulations for all the minerals considered herein. In **(f)**, the data is fitted by an equation of the form: $\log(D_r) = -2.06\log(\gamma_{fault}) + 6.30$, where γ_{fault} is the stacking fault energy (J/m^2) for a given solute. The error bars represent the standard deviation.

In contrast, sonicated dissolution results in the formation of a significantly higher number of characteristic rhombohedral etch pits (see Figure 4-9b). For example, Figure 4-8c illustrates the local topography of a typical etch pit that shows a depth of about 800 nm and a lateral (equi-axed) width of around 5 μm (see Figure 4-9d), Line 1). In addition, we observe the systematic existence of a fast-dissolving region surrounding each pit (see the directional dark brown areas in Figure 4-9b). In line with the stepwave model, these areas are formed by dissolution waves emanating from an etch pit.[145] An example of this behavior is illustrated in Figure 4-9d (Line 2), which shows a fast-dissolving area up to 200 nm deep that is around 10× deeper than the local height variance on the calcite surface following non-sonicated dissolution. The pits (and associated fast-dissolving areas surrounding each pit) forming under sonication result in a large degree of spatial heterogeneity in the local dissolution rate over the calcite surface. This is

apparent from the distribution of the pixel-wise surface height (Figure 4-9e, orange bar plot), which exhibits a wide, non-symmetric shape, with a long-tail toward negative height indicating fast dissolving regions. The formation of deep etch pits is also observed for fluorite, which, like calcite, exhibits a notable increase in dissolution kinetics upon sonication (see **Figure 4-10** for more details). Overall, the notable difference in the topographies of the calcite and fluorite surfaces—in the presence and absence of acoustic stimulation—suggests that the enhanced propensity for pit formation largely explains the sonication-induced dissolution acceleration. This is further confirmed by the fact that quartz does not exhibit any notable signature of pit formation under sonication (see Figure 4-2 and Figure 4-11), which echoes that the dissolution kinetics of quartz are very weakly affected by sonication (Table 4-8).

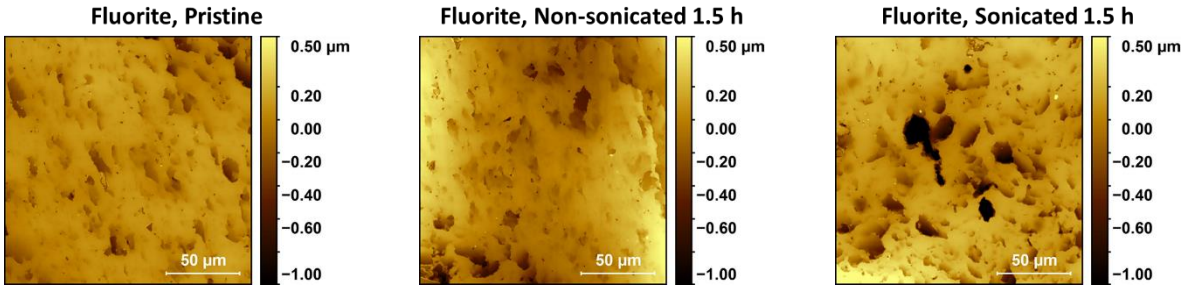

(a) **(b)** **(c)**

Figure 4-10: Representative topography images of fluorite surfaces **(a)** before dissolution and following 1.5 h dissolution under **(b)** non-sonicated and **(c)** sonicated conditions.

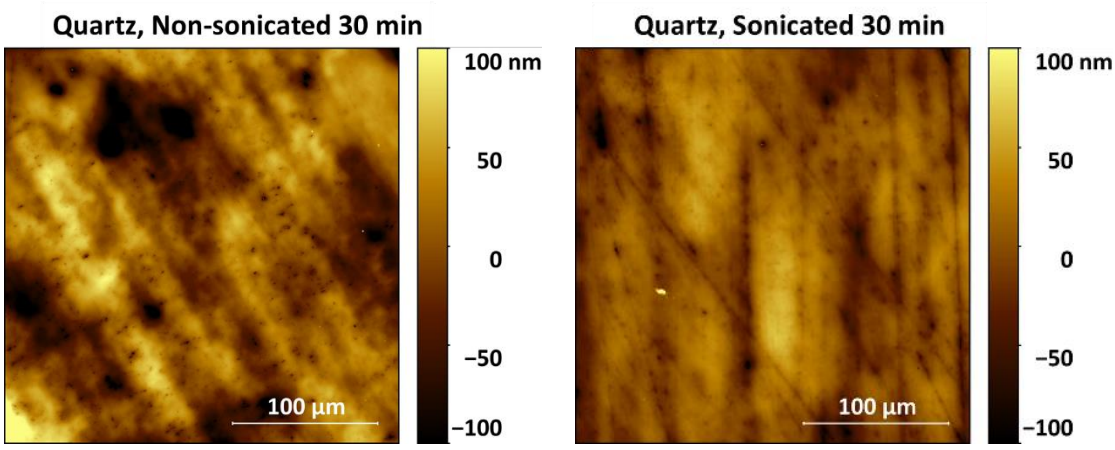

(a) **(b)**

Figure 4-11: Topography maps of quartz surfaces following 30 min dissolution reactions under **(a)** non-sonicated and **(b)** sonicated conditions. The changes in topography compared to the as-polished surfaces are negligible.

The effect of sonication on pit formation can be understood as follows. Under sonication, shock waves or micro-jets induced by the collapse of cavitation bubbles cause severe local plastic deformations. It should be noted that such plastic deformations differ from the fracture effects illustrated in Figure 4-5, since they consist of spatially-distributed atomic dislocations rather than crack propagation. These spatially-distributed dislocations serve as initiation sites for dislocation etching and, eventually, etch pit formation and growth.[130,334] The strain energy resulting from such irreversible deformations results in a Gibbs free energy penalty, which, in turn, promotes local dissolution.[145,271,335] In contrast to the formation of vacancy islands (i.e., pits forming on an atomically smooth surface),[334] dislocation etch pits are more likely to develop alongside preexisting defects and result in the formation of deeper (than typical) pits; for

instance, see the comparison of the calcite dissolving surfaces in Figure 4-9a,b.[150] Based on this mechanism, we propose that sonication-induced atomic dislocations (and the associated plastic deformations) are key to understanding how sonication accelerates dissolution.

To further demonstrate the role of atomic dislocations on sonication-induced dissolution acceleration, we compute using MD simulations the stacking fault energy of the minerals considered herein (see Methods). The stacking fault energy quantitatively captures the propensity for a mineral to form dislocations under an applied surface stress,[315] wherein lower stacking fault energies indicate that the formation of atomic dislocations is facilitated (i.e., due to a low energy cost). As shown in Figure 4-9f, we observe a strong negative correlation (black solid line) between the extent of dissolution acceleration upon sonication and the stacking fault energy. This confirms that low stacking fault energy (and, hence, the facilitation of atomic dislocations) tends to promote sonication-induced dissolution acceleration. In that regard, it is notable that albite acts as an outlier in Figure 4-9f—since it exhibits a fairly large increase in dissolution kinetics upon sonication despite showing a large stacking fault energy. In fact, albite's large stacking fault energy is consistent with the fact that, like in the case of quartz, sonication does not notably affect the surface topography of this mineral (see Figure 4-12 for more details). Rather, the large dissolution enhancement exhibited by albite is on account of its low surface energy (see Figure 4-8c). This illustrates the importance of simultaneously considering the surface and stacking fault energy to understand the effect of sonication on minerals' reactivity.

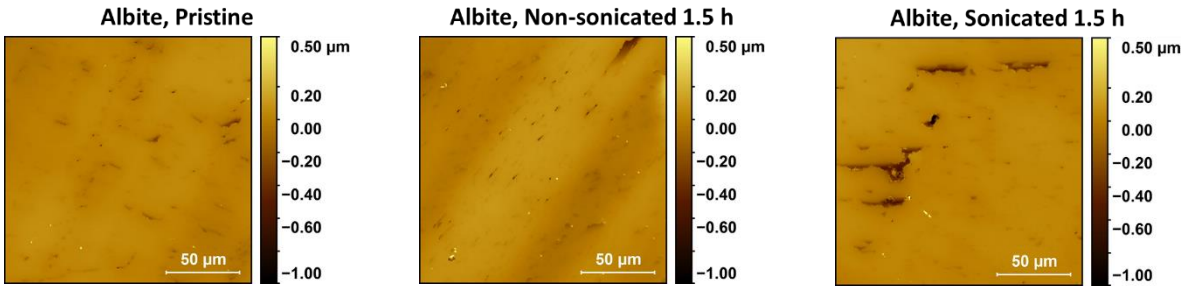

(a) **(b)** **(c)**

Figure 4-12: Representative topography images of albite surfaces (a) before dissolution and following 1.5 h dissolution under (b) non-sonicated and (c) sonicated conditions.

Overall, these results indicate that atomic dislocations and fracture (bond rupture) are the two primary mechanisms by which sonication increases dissolution kinetics. This indicates that the effect of sonication on the dissolution rate of a given mineral is governed by (i) its surface energy (i.e., which controls its propensity to break) and (ii) its stacking fault energy (i.e., which controls its propensity to produce and tolerate plastic dislocations). It should be noted that surface energy and stacking fault energy are largely independent of each other (see Figure 4-13); therefore, these properties capture two distinct contributions of the sonication-induced enhancement in the dissolution kinetics.

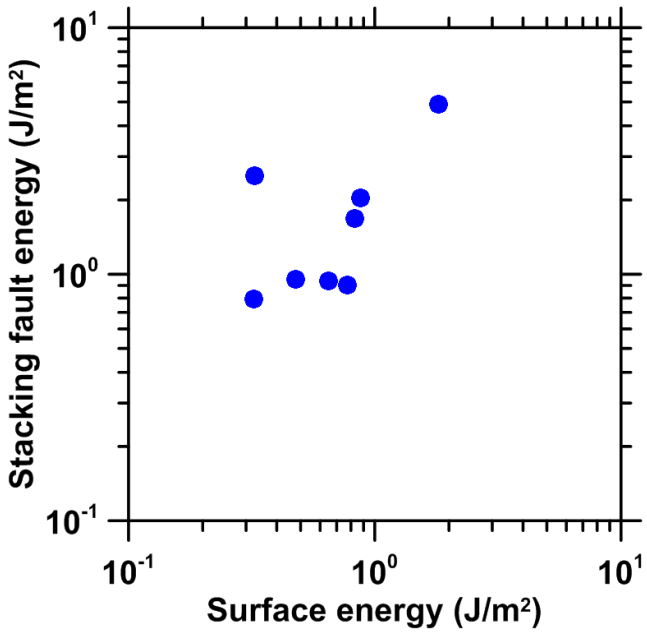

Figure 4-13: Surface energy vs. stacking fault energy values computed by molecular dynamics. The absence of correlation between these quantities (at the exception of quartz, which simultaneously exhibits high surface and stacking fault energy) confirms that both of these properties capture two distinct, independent contributions to sonication-induced dissolution enhancement.

4.3.4 Theoretical framework

Our experimental data and simulations suggest that both bond breaking and dislocations synergistically contribute to the increase in dissolution rates that is observed under acoustic stimulation. Based on these observations, we propose a new theoretical framework that accounts for this dual mechanism (see Figure 4-14). First, the collapse of cavitation bubbles in proximity to mineral surfaces results in shock waves or micro-jets, which locally generate high stresses on mineral surfaces; i.e., due to the "water hammer" effect.[336] Due to the stochastic nature of the

size, internal pressure, anisotropy, and collapse time of the cavitation bubbles, the resulting shock energy that is imposed on the mineral surface exhibits some variability.[337,338] Here, for simplicity, we assume for the frequency and power of acoustic stimulated applied herein (20 kHz, 30W) that the shock energy follows a Gaussian distribution (see Figure 4-15a). Since the sonication frequency and power are fixed, the average value μ and standard deviation σ of the shock energy distribution are invariant and do not depend on the solute. Note that the parameters μ and σ are not easily assessed *a priori* and, herein, are determined *a posteriori* by fitting the experimental data of sonication-induced dissolution enhancement (see below).

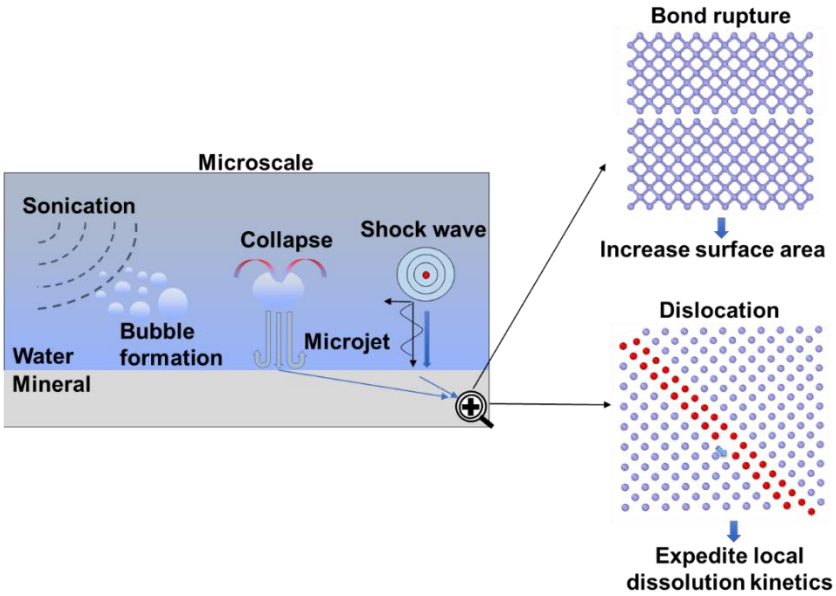

Figure 4-14: An illustration of the atomistic mechanism of dissolution amplification under acoustic stimulation.

Based on the shock energy distribution, a given fraction of the cavitation bubbles will successfully activate fracture or dislocation effects (i.e., if the shock energy is large enough). The probabilities for such activation is determined by comparing the shock energy distribution to the threshold energies that are needed to activate fracture and dislocation, namely, the surface energy γ_{surf} and stacking fault energy γ_{stack}, respectively (see Figure 4-15a). The probability to trigger fracture (p_{frac}) and dislocation (p_{dis}) effects are then obtained by analytically integrating the Gaussian distribution starting from the threshold energy, i.e., the minimum energy that is needed to activate fracture or dislocations:

$$p_{\text{frac}} = \left(\frac{1}{2} - \frac{1}{2}\text{erf}\left(\frac{\gamma_{\text{surf}} - \mu}{\sigma\sqrt{2}}\right)\right) \tag{4-2a}$$

$$p_{\text{dis}} = \left(\frac{1}{2} - \frac{1}{2}\text{erf}\left(\frac{\gamma_{\text{stack}} - \mu}{\sigma\sqrt{2}}\right)\right) \tag{4-2b}$$

where erf() is the error function.

We first focus on fracture. To the first order, the increase in the dissolution kinetics arising from fracture is simply related to the associated increase in exposed surface area. Assuming that the resulting fracture pattern (i.e., that results when the cavitation energy exceeds the surface energy of a given solute) does not depend on the considered solute, the relative increase in the dissolution rate ($D_{\text{r}}^{\text{frac}}$) resulting from the increase in surface area due to fracture is given by:

$$D_{\text{r}}^{\text{frac}} = D_1\left(\frac{1}{2} - \frac{1}{2}\text{erf}\left(\frac{\gamma_{\text{surf}} - \mu}{\sigma\sqrt{2}}\right)\right) \tag{4-3}$$

where D_1 is a non-dimensional constant that captures the increase in exposed surface area resulting from a single fracture event.

We then focus on dislocation events. Previous studies have noted that increasing dislocation density tend to increase minerals' dissolution kinetics by affecting their Gibbs free

energy.[339–341] However, at this time, we note that no direct, quantitative relationship exists between dislocation density and associated dissolution enhancement. For simplicity, we assume that the dissolution enhancement ($D_{\mathrm{r}}^{\mathrm{dis}}$) resulting from dislocation events is proportional to the surface density of dislocations as follows:

$$D_{\mathrm{r}}^{\mathrm{dis}} = D_2 \left(\frac{1}{2} - \frac{1}{2} \mathrm{erf} \left(\frac{\gamma_{\mathrm{stack}} - \mu}{\sigma \sqrt{2}} \right) \right) \tag{4-4}$$

where D_2 is a non-dimensional constant that captures how much a single dislocation feature increases the dissolution rate (i.e., which is assumed to be similar for all minerals; a conservative assumption). Thus, taken together, the total dissolution enhancement resulting for these two mechanisms can be expressed as:

$$D_{\mathrm{r}} = D_{\mathrm{r}}^{\mathrm{frac}} + D_{\mathrm{r}}^{\mathrm{dis}} \tag{4-5}$$

This analytical basis yields four currently unknown parameters (i.e., D_1, D_2, μ, and σ), wherein the parameters μ and σ are the average and standard deviation of the shock energy distribution. The energy of shock waves emitted by a single collapsing bubble is reported to be up to tens of mJ and is dependent on the anisotropy parameter, i.e., the dimensionless equivalent of the Kelvin impulse.[277,342,343] However, experimentally measured distributions of shock energies, e.g., as shown in Figure 4-1a, strongly depend on the system and process parameters.[344] Therefore, we ascertain these four parameters (D_1, D_2, μ, and σ) by fitting Eq. (4-5) to our experimental dissolution enhancement data (D_r) across all minerals considered using a least squares method–i.e., by solving 8 equations, with 4 unknowns that are the same across all minerals: D_1 (3.4, unitless), D_2 (9.9, unitless), μ (0.86 J/m^2), and σ (0.063 J/m^2). Note that, due to the nonlinear nature of the error function, this fitting is carried out using the trust-region-reflective and Monte Carlo algorithms[345,346] to ensure that the optimization is not trapped in a local minimum. Figure 4-15a shows the distribution of the microjet energy *a posteriori* inferred

from this fitting. To assess the accuracy of this model, Figure 4-15b shows the comparison between the sonication-induced increase in dissolution rates estimated by Eq. (4-5) and the experimental values presented in Table 4-8. In general, we observe excellent agreement between predicted and experimental values—with a coefficient of determination R^2 of 0.993. This supports the ability of our model to offer a realistic description of sonication-induced dissolution enhancement.

Also shown, in Figure 4-15c, is the combined influence of surface energy and stacking fault energy on the relative increase in dissolution kinetics, which properly explains, for the first time, our collective of experimental observations. For instance, the difference in surface energy explains why albite is more affected by sonication than anorthite (despite their fairly similar stacking fault energy), while the difference in stacking fault energy explains why antigorite is more affected than albite (despite their fairly similar surface energy). Overall, as shown in Figure 4-15c, diverse minerals can be classified into four categories based on the dominant underlying mechanism. First, albite exhibits a combination of high stacking fault energy and moderate surface energy—as compared to the average shock energy (μ) for the nature of acoustic stimulation applied herein (dotted line)—so that the sonication-induced dissolution enhancement observed for this mineral is primarily governed by fracture ("fracture-controlled" region in Figure 4-15c). In contrast, minerals exhibiting a combination of high surface energy and moderate stacking fault energy would be primarily governed by dislocation events ("dislocation-controlled" region in Figure 4-15c). No example of such mineral is found herein. In between these extreme cases, antigorite simultaneously shows moderate values of surface energy and stacking fault energy. As such, for antigorite, sonication-induced dissolution enhancement is simultaneously governed by fracture and dislocation events ("mixed region" in Figure 4-15c).

Finally, in contrast, quartz exhibits a combination of high surface energy and stacking fault energy and, hence, is only very weakly affected by sonication ("no sonication effect" in Figure 4-15c). This classification is less clear in the case of anorthite and orthoclase, which present a surface energy that is close to the average shock energy. Similarly, calcite, dolomite, and fluorite exhibit a stacking fault energy that is close the average shock energy and, hence, are located at the boundary between the "fracture-controlled" and "mixed" regions. Overall, the "acoustic stimulation map" presented in Figure 4-15c) offers a convenient representation to quickly estimate whether the dissolution kinetics of a given mineral is likely to be affected by sonication and, if so, which mechanism is expected to be predominant. Expectedly, however, this analytical framework does not yet account for 2nd-order features of minerals that may affect their dissolution rates, e.g., point defects, chemical impurities, porosity, etc.

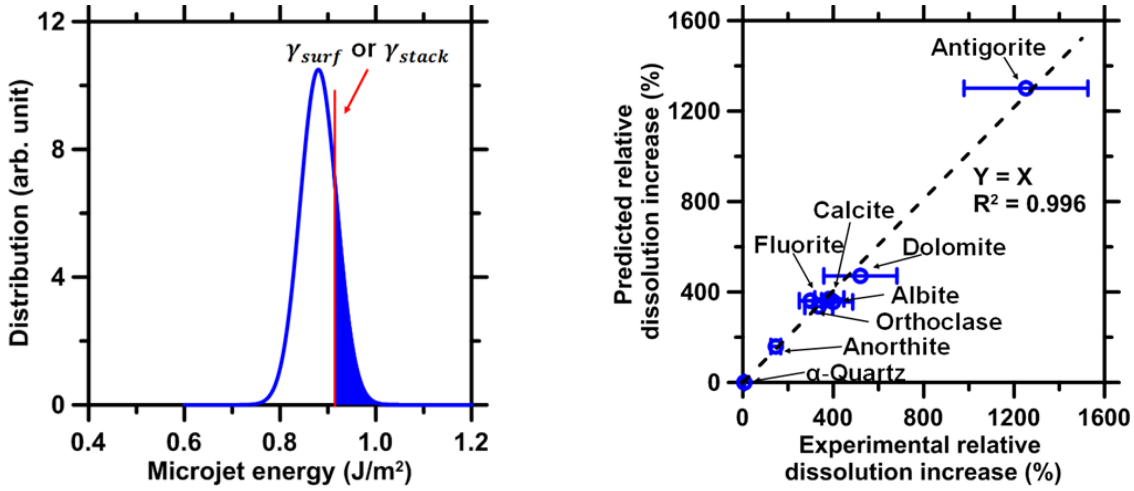

(a) **(b)**

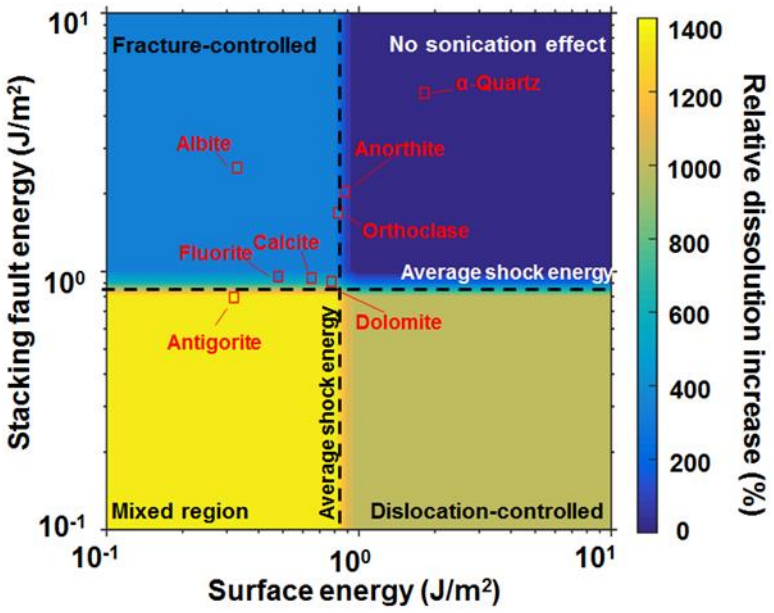

(c)

Figure 4-15: Combined effects of bond breaking and dislocation on dissolution enhancement. **(a)** The probability distribution of the microjet energy resulting from the collapse of cavitation bubbles, as inferred from Eq. (4-5). The red vertical line indicates the surface or stacking fault energy for a given solute, which is a used as a threshold to calculate the probability for a cavitation bubble to activate a fracture or dislocation event (represented by the blue region). **(b)** Comparison between the sonication-induced increase in dissolution rate predicted by our model and experimental data. The $y = x$ dashed line indicates a perfect agreement. The error bars represent the standard deviation. **(c)** Relative increase in dissolution rate (color scale) as a function of both surface and stacking fault energy. The positions on this map of all the minerals considered herein are indicated by square symbols, with their experimentally measured relative dissolution increase indicated using the color scale.

Finally, we explore whether the effect of sonication on reactivity could in some ways be directly encoded in the nature of the interatomic bonds the minerals are made of. As shown in Figure 4-16a, we observe the existence of a strong (inverse) correlation between the average bond energy (calculated over the cleavage plane of each mineral) and dissolution enhancement. This is not surprising since the average bond energy is reflected in the surface energy of the minerals. However, we do not observe any obvious correlation between the average degree of covalency of the bonds (calculated over the slip plane of each mineral) and dissolution enhancement (see Figure 4-16b). This suggests that the ionic vs. covalent nature of the interatomic bonds (and their degree of directionality) in minerals does not have a first-order effect on their sensitivity to sonication. Overall, the fact that dissolution enhancement exhibits a stronger correlation with surface and stacking fault energy (as compared to bond energy and degree of covalency) suggests that, besides the nature of the interatomic bonds in minerals, the atomic structure itself also plays an important role in governing dissolution enhancement upon sonication. In that regard, as macroscopic materials' properties, the surface and stacking fault energy (which are used as inputs for the present model) simultaneously capture the effects of interatomic bonds and crystalline structure.

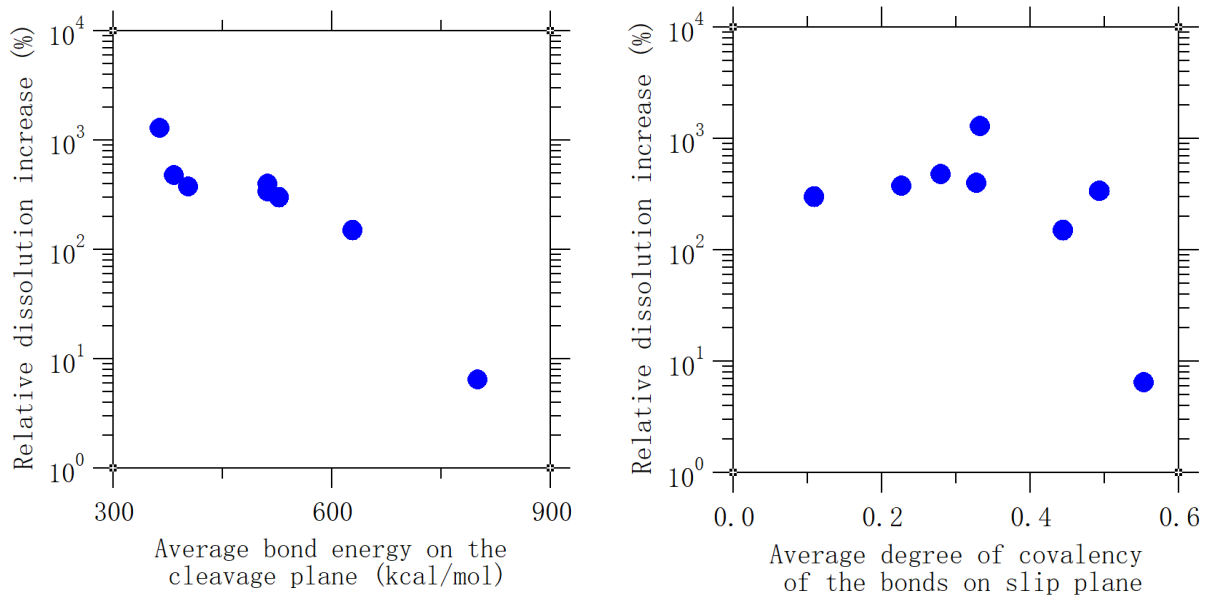

(a) **(b)**

Figure 4-16: Relative dissolution increase upon sonication as a function of **(a)** the average bond energy over the cleavage surface and **(b)** the average degree of covalency of the bonds over the slip plane of each mineral.

4.4 Summary and Conclusions

By combining dissolution rate observations and MD simulations, this study reveals two underlying atomic mechanisms that control the increase in dissolution kinetics that are produced across a wide range of minerals following acoustic stimulation. Importantly, we find that dissolution enhancement arises both from fracture and dislocation events. This dual mechanism helps explains previously contrasting conclusions—i.e., since the dominant mechanism depends on the mechanical attributes of the solute considered (i.e., fracture energy vs. stacking fault energy). Simultaneously considering both of these mechanisms allows rationalization of available experimental data and introduces a unifying model that explains the roles and extents of these two

phenomena during sonication-induced dissolution enhancement. Furthermore, it would be of great value to explicitly simulate by non-equilibrium molecular dynamics simulations the effect of sonication on minerals—which would offer a direct access to the dynamics of bond breaking and dislocation upon shock wave propagation. Such simulations would also enable a direct estimation of the energy that is released from cavitation or nanobubble collapse. In that regard, the availability of a universal reactive forcefield that could model all the minerals considered herein (and their interaction with the solution) while relying on a consistent parameterization would be key.

The ability to enhance the dissolution kinetics of minerals using electrically driven acoustic fields (e.g., that are powered by renewable energy) would be of great value in numerous applications wherein mineral (solute) reactivity is a bottleneck. However, its cost and energy efficiency must be compared with alternative approaches (e.g., accelerating dissolution by increasing temperature, or the use of reagents) to ensure practical feasibility. The outcomes of this study offer original insights to assess for which minerals sonication may be most effective. For instance, minerals characterized with high surface energy and stacking fault energy are only very weakly affected by sonication—which limits the use of this approach for such minerals. However, for other minerals, sonication results in notable enhancements in dissolution kinetics without the need to externally increase the reaction temperature (although, this may indeed accompany sonication for non-thermostated systems). As such, sonication offers a promising route to stimulate reactivity in a cost- and energy-efficient manner.[347] It should be noted that this study focuses on room-temperature dissolution (i.e., 300 K). However, temperature could offer an additional degree of freedom to tune the efficiency of sonication for a given material. For instance, many phases exhibit a decrease in their stacking fault energy with even small increases

in temperature,[348,349] which, in turn, would increase the efficiency of sonication (i.e., even for minerals that are largely insensitive to sonication at room temperature). In addition, understanding the underlying features that affect rate-enhancement (or not) would be foundational to unlock green chemistry approaches for several applications. For example, enhancing the dissolution rate of minerals is of critical importance to increase the efficiency of CO_2 mineralization applications. Accelerating the dissolution of minerals could also be key to bypass the need for high-temperature clinkering during the manufacturing of cementing agents—which is the main contribution to concrete's embodied CO_2.[350] Finally, sonication offers a promising pathway to accelerate the dissolution of industrial waste by-products (e.g., fly ash or slag), which could facilitate their recycling and beneficial use—which is key to create a meaningful circular economy for industrial waste.

Chapter 5. Additive-free dissolution enhancement of industrial alkaline wastes using acoustic stimulation

5.1 Introduction and Background

Industrial wastes, such as slags and fly ash (FA), are potent sources of oxides of silicon (Si) and light metals, such as sodium, potassium, calcium, magnesium, and aluminum. These wastes are produced in large volumes annually, estimated at 130 Mt of slag[351] and 750 Mt of FA,[352] globally. If they could be readily solubilized ("dissolved") at sub-boiling temperatures and ambient pressures into aqueous solution, they could serve as feedstocks for applications including Ca-extraction for CO_2 mineralization, Si-recovery for fertilizer production, etc.[12,13] Most studies thus far, however, have typically sought to improve elemental extraction from such wastes using additives such as acetic acid (CH_3COOH), ammonium acetate (CH_3COONH_4), and ammonium chloride (NH_4Cl).[353,354] Because these additives are produced in substantially inferior quantities as compared to the volume of waste produced, as well as their high costs (e.g., $1,000 per ton for CH_3COONH_4 and $8,000 per ton for NH_4Cl),[355,356] and the substantial carbon intensity associated with their production, it has remained infeasible, practically, to beneficially utilize or otherwise valorize these wastes as raw materials in the production of other materials even wherein the additive could be fractionally recovered and reused in elemental extractions.[9] An additional challenge associated with industrial wastes is their highly heterogeneous manner of dissolution. In other words, since their dissolution is typically incongruent; some elements are liberated in larger quantities, while others are released in much more modest quantities (e.g., Ca is often released much more abundantly than Si or Al[357,358]). For this reason, while Ca-extraction

is often a topic of interest, fewer works have examined the extractions of species such as Si or Al.

Beyond additive-based methods (e.g., using mineral acids, or lixiviants),[359–363] the reactivity (i.e., aqueous dissolution rate) of a solute can be increased by: (a) *stirring* (i.e., convective mixing) which enhances ion transport (e.g., away from the dissolving surface, into bulk solution) in solution, (b) *grinding* the solute into increasingly finer particles to increase the interfacial surface area (i.e., at the solute-solvent interface) available for dissolution, and (c) *heating* the solute-solvent system given the strong dependence of chemical reaction rates on the temperature. While indeed capable of affecting dissolution rates, these interventions imply significant (unsustainable) energy expenditure that makes them unviable in practical industrial applications. Recently, acoustic stimulation has been shown to be effective at greatly enhancing the dissolution rates of inorganic minerals (e.g. calcite dissolution rate was enhanced 11×)[16] and glasses[16,364,365] (e.g., obsidian's dissolution rate was enhanced 2.7×).[16] This has been attributed to the ability of acoustic energy to: 1) induce solute fracture, 2) activate dislocations on the solute's surface, and 3) reduce the activation energy of the dissolution reaction. While the mechanisms of dissolution enhancement by sonication have been clarified, the energy intensity of acoustic stimulation – as an approach for enhancing dissolution and elemental extractions – has not been ascertained.

Herein, we examine the potential for dissolution activation of four industrial wastes: air-cooled blast furnace slag (ACBFS), stainless steel slag (SSS), a Ca-poor Class F fly ash, and a Ca-rich Class C fly ash in deionized (DI) water. We examine the effectiveness of different methods, e.g., grinding of the particulates, convective mixing of the solution, heating of the solute-solvent system and acoustic stimulation, to enhance dissolution kinetics. Special focus is

paid to elaborate the pathway by which dissolution is enhanced (e.g., increase of surface area in the case of grinding) and to quantify the amount of energy that is expended to obtain target Si concentrations via different dissolution activations. The outcomes of this work have implications on identifying optimal process pathways to enable waste utilization, as feedstocks, in practical industrial operations.

5.2 Materials and Methods

5.2.1 Materials and sample preparation

The slags and fly ashes were sourced from TMS International, and Boral Resources, respectively. The chemical composition of the alkaline solids (represented as simple oxides) is given in Table 5-1.

Table 5-1. The chemical composition (in mass %) of the air-cooled blast furnace slag (ACBFS), Class F fly ash (FA), stainless steel slag (SSS) and Class C fly ash (FA) tested in this study, with undetected components (i.e., <0.1 mass %) indicated by '-'.

	ACBFS	Class F FA	SSS	Class C FA
SiO_2	32.7	50.7	26.3	39.5
CaO	36.8	2.2	48.7	18.1
Al_2O_3	8.8	23.4	1.5	17.4
Fe_2O_3	4.9	16.7	5.9	6.8
MgO	9.2	1.0	7.3	9.1
Na_2O	-	1.5	-	2.0
K_2O	-	2.6	-	0.5
Cr_2O_3	2.0	-	4.0	-
MnO	0.5	-	1.2	-
TiO_2	-	1.2	-	1.7
SrO	-	0.1	-	0.6
BaO	-	-	-	0.9
P_2O_5	-	0.1	-	1.0
SO_3	2.7	0.5	0.3	2.5
Others	*2.4*	*0.0*	*4.8*	*0.0*

The mineralogy of the waste species was determined by X-ray diffraction (XRD). The crystalline ACBFS was composed of melilite ($(Ca,Na)_2(Al,Mg,Fe^{2+})[(Al,Si)SiO_7]$, sorosilicate) in the forms of akermanite ($Ca_2Mg[Si_2O_7]$) and gehlenite ($Ca_2Al[AlSiO_7]$). The stainless steel slag primarily contained calcium carbonate and calcium silicates including larnite (Ca_2SiO_4) and cuspidine ($Ca_4F_2SiO_7$), The fly ashes, following a pre-wash (explained below), were comprised primarily of amorphous aluminosilicates (for Class F FA) and calcium aluminosilicate (for Class C FA) glasses. Furthermore, crystalline quartz (SiO_2), mullite ($3[Al_2O_3]2[SiO_2]$, $2[Al_2O_3][SiO_2]$), and magnetite (Fe_3O_4) were observed in the XRD patterns of both FAs.

The slag samples were dried in an oven at 45 °C for 72 h and then ground in a ball mill (at 4000 rpm) for 20-60 min. The ACBFS particulates were then sieved in series into four particle size fractions: (1) 300-600 μm, (2) 180-300 μm, (3) 53-180 μm, and (4) <53 μm. The cumulative particle distributions for the slag samples, prepared in this manner, and measured using a LS13-320 Beckman Coulter static light scattering analyzer, are shown in Figure 5-1. The median diameter, d_{50}, the 80th-percentile particle diameter, d_{80}, and BET surface area of the slag particles for each particle size fraction measured using nitrogen (N_2) adsorption (Micrometrics ASAP 2020 Plus I system) are summarized in Table 5-2. Initially, the FAs were washed (in deionized water, at a solid-to-liquid (s/l) ratio of 1:1000 [mass basis], while being shaken at 200 rpm, 50 °C, 50 min) prior to the dissolution experiments to remove readily-soluble components (e.g., CaO: free lime). Both washed FAs exhibited small native particle sizes (<20 μm) and thus were examined as received.

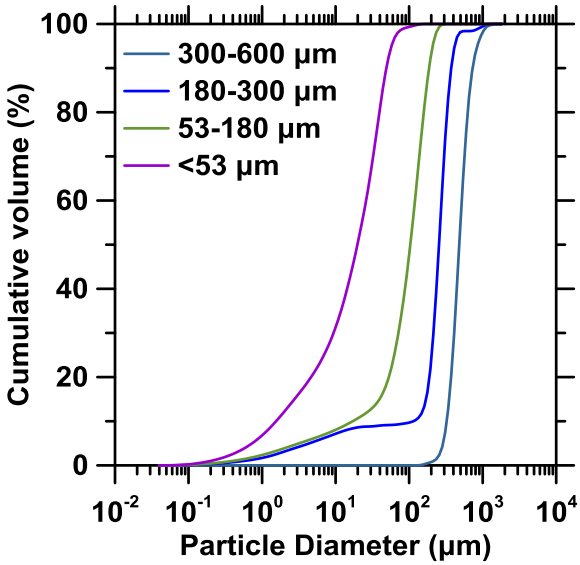

Figure 5-1: Cumulative particle size distribution of the air-cooled blast furnace slag (ACBFS) samples with four size fractions.

Table 5-2. d_{50}, d_{80} of the slag fractions estimated from the particle size distributions and BET surface area measured by nitrogen (N_2) adsorption

Particle size fraction (µm)	***d*$_{50}$ (µm)**	***d*$_{80}$ (µm)**	**BET Surface area (m^2/g)**
<53	18.9	36.3	7.5
53-180	101.1	146.8	6.8
180-300	241.6	309.6	6.7
300-600	449.7	594.8	4.3

5.2.2 Batch dissolution experiments

Batch dissolution experiments involved reacting 0.1 g, 0.2 g, 1.0 g, 2.0 g, or 10.0 g of the particulate solids with 100 mL of 18 MΩ·cm deionized water in a 250 mL beaker; yielding solid-to-liquid ratios (s/l; mass basis) of 1:1000, 1:500, 1:100, 1:50 and 1:10. The (acoustic) stimulation-free dissolution experiments were carried out in a jacketed beaker using water as the thermal fluid to maintain isothermal conditions at 25 ± 0.2 °C, 35 ± 0.5°C, 50 ± 0.5°C, or 60 ± 1.0 °C, in a static or stirred (1.0 inch magnetic stir bar, 350 rpm) environment. Under acoustically stimulated conditions, a horn type ultrasonic system (Fisher Scientific 505 Sonic Dismembrator; 500 W; 1/2-inch tip diameter) was immersed into the DI water within the jacketed beaker to induce dissolution enhancement. The stimulated reaction temperature was maintained at the same isothermal conditions as in the stirred experiments (25 ± 0.5 °C, 35 ± 0.5°C, 50 ± 1.0°C, or 60 ± 1.0 °C) by circulating cooling water through the jacket. In general, dissolution was monitored for no more than 3 h. Aliquots were taken from the solution (1.0 mL) at designated time intervals and then filtered through 0.2 μm filters for analysis of total dissolved Si concentrations. Si was used to assess dissolution as it forms the dominant network-forming species in these solutes (i.e., the presence of Si in solution indicates solutal-network rupture). Elemental analysis was carried out using a Perkin Elmer Avio 200 inductively coupled plasma optical emission spectrometer (ICP-OES), with calibration standards prepared from more concentrated (1000 ppm) standards (Inorganic Ventures).

5.3 Energy intensity

The energy analysis for each dissolution activation method considers the net quantity of energy delivered into the system, i.e., solute and water. In other words, we do not consider the inefficiency that is associated with a specific method (e.g., the combustion of fuel to generate heat and/or electricity). For consistency, we apply this energy analysis to a liquid-reaction volume of 100 mL (i.e., representing the size of the dissolution reactor), although the findings may be scaled to larger reactor sizes and reaction volumes.

5.3.1 Grinding (surface area enhancement)

The energy needed for mechanical grinding of mineral particulates can be generally described using the Bond Work Index:

$$W = W_i \cdot \left(\frac{\sqrt{100}}{\sqrt{P80}} - \frac{\sqrt{100}}{\sqrt{F80}}\right) \quad (5\text{-}1)$$

where, W_i is the work index, and *F80* and *P80* are the 80% passing sizes of the feed and product particles.[366] The work index for slag is estimated as 15 kWh/t.[367] Here, *F80* is taken as 1.0 cm, i.e., the estimated size of slag particles as received. We do not consider any grinding energy for the fly ash particulates since, as received, they present a median diameter, $d_{50} \approx 2.50$ for the Class F fly ash. While Eq. 5-1 is not truly applicable for particle sizes smaller than 100 μm,[368,369] we make no attempt to offer a correction since grinding, generally, is not as effective at enhancing dissolution as the other methods as is elaborated below and grinding energy is around 3 orders of magnitudes lower than energy intensities of heating and sonication.

5.3.2 Convective mixing

The energy input for mechanical stirring of a solution (i.e., a solute-solvent mixture) can be estimated using a Reynolds number, *Re*, induced by a given impeller as:

$$Re = NL^2\rho/\mu \tag{5-2}$$

where, *N* is the number of rotations per second, *L* is the impeller length (m), and ρ and μ are the density (kg/m^3) and dynamic viscosity of the solution (taken as water, given the low s/l[370]) (Pa·s).[371] The viscosity is temperature-dependent whereas *N* was fixed at 350 rpm and *L* was fixed at 2.54 cm. The calculated Reynolds number indicates that flow was near-turbulent (*Re* = 4000) or fully turbulent (up to *Re* = 10^6) across all temperatures.[371,372] Thus, the power (P_{mixing}) was calculated from the turbulent mixing power equation:

$$P_{mixing} = N_P\rho N^3 L^5 \tag{5-3}$$

where, N_P is the power number which has a value of 2.0 in the turbulent region for paddle-type stirrers.[371] At a stirring speed of 350 rpm and a temperature of 25 °C, the power required to mix 100 mL of water is 2.14×10^{-3} W. The density of water varies ~1% across the temperature range studied, and thus the mixing power was considered to be independent of temperature.

5.3.3 Heating

The energy required to heat a solute-solvent mixture, E_h, encompasses: (a) the heat required to raise the temperature of the reactants (water and slag) to the desired temperature, Q_T, and (b) the energy required to maintain isothermal conditions (estimated from the heat loss to the surroundings from the reactor surface) during the reaction, $\dot{Q}_C$. The first component was not considered, as this value was unchanged whether or not acoustic stimulation was applied, and

thus cancels out during energy comparison (see Figure 5-9). The second contribution in the unstimulated case can be determined using Eq. 5-4:

$$\dot{Q_C} = h \cdot A \cdot (T_{air} - T) \tag{5-4}$$

where $\dot{Q_C}$ is the heat loss per unit time, h is the convective heat transfer coefficient, taken as 20 W/(m^2·K),[373,374] A is the surface area of the system that is open to the atmosphere (taken as 132.7 cm^2, the area of the top opening of the jacketed beaker, assuming no heat losses through the thermal fluid over the course of reaction), and T_{air} is estimated as 25 °C. As $\dot{Q}_C$ is a rate, its cumulative value depends on the reaction time.

5.3.4 Acoustic stimulation

Acoustic energy was transmitted into the aqueous solution through the high-frequency vibrations transmitted into the solution by the ultrasonic horn tip.[375] The ultrasonic power, P_u, and its accumulated energy over time were output by the signal generator. As energy was constantly withdrawn from the reactor – to maintain macroscopically isothermal conditions – by the cooling water the net consumed power was calculated by Eq. 5-5:

$$P = P_u - P_c \tag{5-5}$$

where, P_c is the rate at which heat is transferred into the cooling water to maintain isothermal conditions, and thus it is equivalent to the rate at which the aqueous solution is heated by acoustic energy at a given temperature, i.e., the calorimetric power,[376,377] as given by:

$$P_c = (\frac{dT}{dt}) \cdot \ c_{water} \cdot m_{water} \tag{5-6}$$

In Eq. 5-6, dT is the increase in temperature over an infinitesimally small time period dt by sonication without isothermal control, and c_{water} (4.18 J/g.K) and m_{water} (100 g) are the heat capacity and mass of water, respectively. The contribution of the solute to P_c was neglected

because the solute represented at most 9 mass % of the system, and the heat capacities of the solutes were less than one-fifth that of water.[378,379] The slope, *dT/dt*, at each temperature was determined from the slope of a temperature vs. time curve during the sonication of DI water in the same reactor without temperature regulation. The calorimetric power reflects the combined effects of sonication and convective heat loss. At low solid-to-liquid ratios as for the systems studied herein, the majority of calorimetric power was consumed to maintain isothermal conditions rather than to induce dissolution activation.

5.4 Results and Discussion

5.4.1 Si dissolution kinetics of air-cooled blast furnace slag

Batch-scale dissolution of all four alkaline wastes deviated from linear kinetics (i.e., far-from-equilibrium dissolution with a first order rate expression) within 10 min of reaction, and showed a temporal-decrease in the rate of Si release into solution (e.g., see representative curves shown in Figure 5-2). For longer term dissolution experiments, i.e. up to 3 h, of the crystalline ACBFS and Class F FA, the concentration of dissolved Si (*C*) from ACBFS and Class F FA was found to increase linearly with the square root of time, sometimes referred to as *parabolic kinetics* for silicate dissolution.[380] Thus, the apparent Si dissolution kinetics were modeled by Eq. 5-7:

$$C = a \cdot \sqrt{t} \tag{5-7}$$

where, *a* is the apparent rate constant of Si release into the aqueous solution.

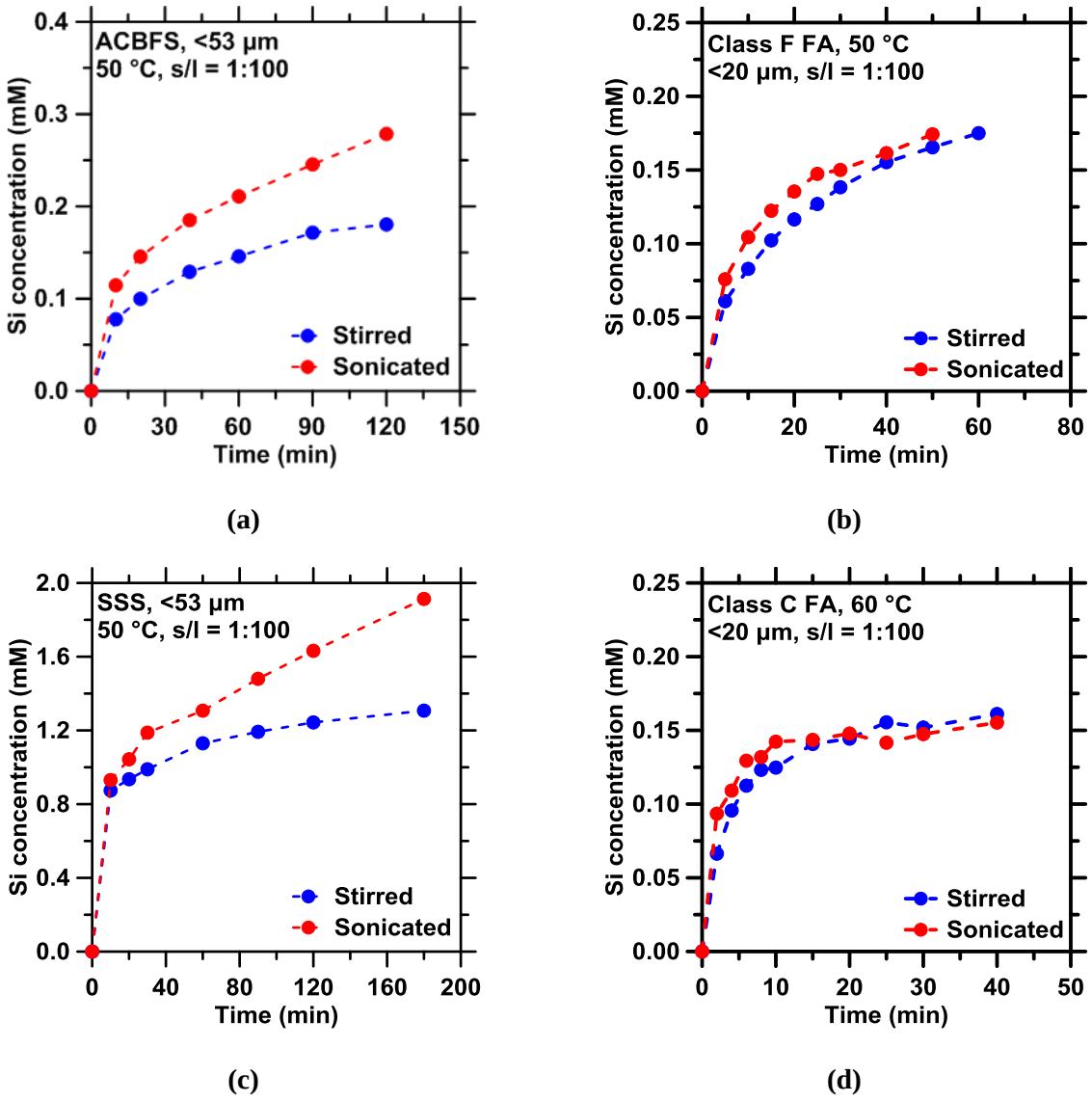

Figure 5-2: Representative silicon release over time from **(a)** air-cooled blast furnace slag (ACBFS), and **(b)** Class F fly ash (FA), **(c)** stainless steel slag (SSS), and **(d)** Class C fly ash (FA) under stirred and sonicated conditions. The curves show that Si release rate decreases over time, exhibiting non-linear dissolution kinetics.

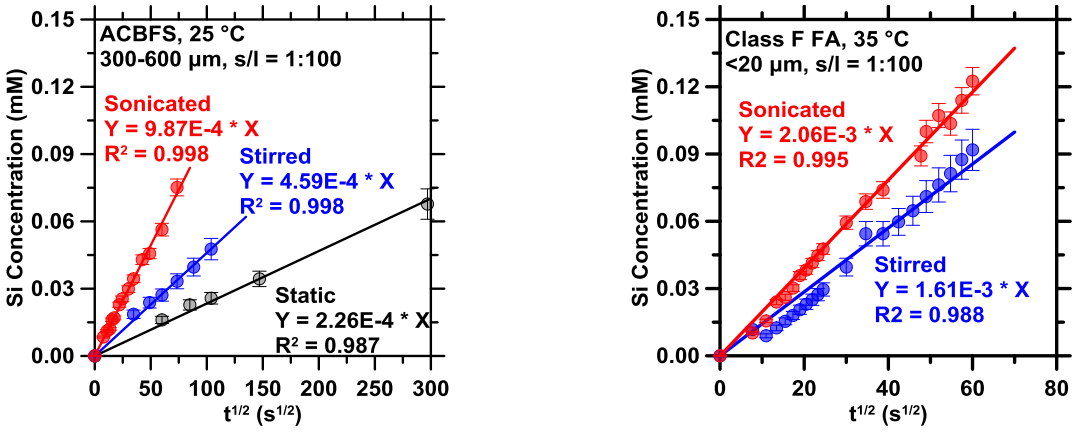

(a) **(b)**

Figure 5-3: Representative parabolic plots of dissolved silicon concentration from **(a)** air-cooled blast furnace slag (ACBFS) at 25 °C with 300-600 µm slag particle fraction at solid-to-liquid ratio of 1:100 under static, stirred and sonicated conditions, and **(b)** Class F fly ash (FA) at 35 °C at solid-to-liquid ratio of 1:100 under stirred and sonicated conditions. The solid lines represent the best linear fittings of the parabolic plots.

Figure 5-3 shows representative parabolic plots for the evolution of silicon concentration in solution over time for dissolving ACBFS and Class F FA particles under static, stirred, and sonicated conditions. The linear fitting to the parabolic plots reveals the parabolic rate, in $mM/s^{1/2}$. It is noted that parabolic kinetics held for the long-term dissolution of ACBFS at 25 °C under static conditions for up to 7 days (see Figure 5-4). The apparent rate constants, *a*, for Si release from ACBFS at all tested conditions are listed in Table 5-3. Parabolic dissolution behavior has been extensively reported for silicates such as feldspar, serpentine, and olivine.[133,380–384] It is generally claimed that ion diffusion within the minerals leads to the parabolic behavior for cation extraction.[133,383] Holdren *et al*. (1982) further demonstrated that the apparent parabolic release of silicon could result from the precipitation reactions occurring

concurrently with the dissolution reaction.[380] It is, therefore, noted that the parabolic coefficient in Eq. 5-7, *a*, obtained herein refers to the *apparent release rate* of Si into the solution.

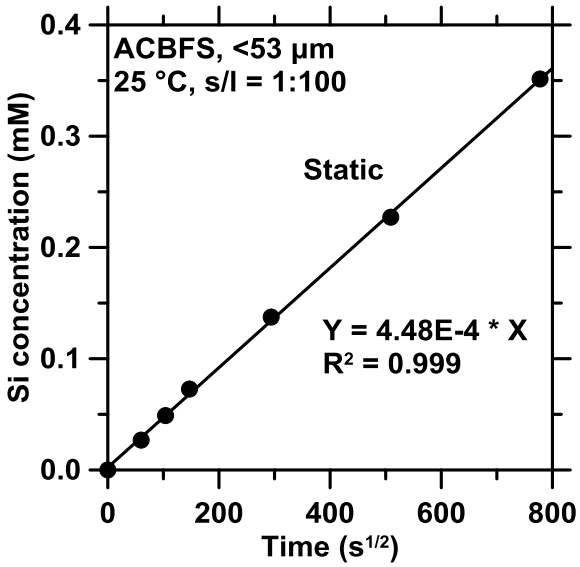

Figure 5-4: Representative parabolic plot of dissolved silicon concentration from ACFBS at 25 °C with <53 μm slag particle fraction at solid-to-liquid ratio of 1:100 under static condition for up to 7 days. The solid line indicates best linear fittings of the parabolic plot.

Table 5-3: The apparent rate constant, a ($mM/s^{1/2}$), of Si dissolution from air-cooled blast furnace slag (ACBFS) at all tested conditions.

Table 5-3a. The apparent rate constant, *a* ($mM/s^{1/2}$), of Si dissolution from the 300-600 µm particles of ACBFS with varied solid-to-liquid ratios (s/l) at 25 °C under static and stirred conditions.

s/l	1:500	1:100	1:50	1:10
Static	1.19E-04	2.26E-04	2.32E-04	2.37E-04
Stirred	2.95E-04	4.59E-04	7.98E-04	9.54E-04

Table 5-3b. The apparent rate constant, *a* ($mM/s^{1/2}$), of Si dissolution from ACBFS of varied median particle diameters, d_{50}, with a solid-to-liquid ratio (s/l) of 1:100 at 25 °C under static and stirred conditions.

d_{50} (µm)	449.7	241.6	101.1	18.9
Static	2.26E-04	2.33E-04	2.97E-04	4.49E-04
Stirred	4.59E-04	6.56E-04	6.99E-04	8.61E-04

Table 5-3c. The apparent rate constant, *a* ($mM/s^{1/2}$), of Si dissolution from the 300-600 µm particle fraction of ACBFS with a solid-to-liquid ratio (s/l) of 1:100 at varied temperatures under static, stirred and sonicated conditions.

Temperature (°C)	25.0	35.0	50.0	60.0
Static	2.26E-04	3.06E-04	7.77E-04	1.34E-03
Stirred	4.59E-04	7.45E-04	1.57E-03	2.20E-03
Sonicated	9.87E-04	1.44E-03	2.07E-03	2.69E-03

5.4.2 Rate enhancement by mixing, grinding, heating and ultrasonication

Mechanical mixing, grinding the solute into finer particle sizes, and heating the reactants are common methods to expedite the accumulation of dissolved species in solution. These methods function by: facilitating mass transport, increasing the contact area between solute and solvent, and promoting surface reactions, respectively.[137,385,386] ACBFS was the sole solute considered in this context as its particle size can be altered and a rate constant easily modeled using parabolic kinetics. The parabolic kinetics equation (Eq.5- 7) was found to apply to the evolution of silicon from ACBFS at all tested conditions. Therefore, the effectiveness of the four dissolution accelerating methods was evaluated using a so-called rate enhancement factor (f_e), which is calculated as:

$$f_e = \frac{a}{a_0} \tag{5-8}$$

where, a and a_0 are the *apparent rates* (i.e., slopes of concentration versus square root of time curves) at a given condition and at the baseline condition (i.e, static, 25 °C, s/l = 1:100, for 300-600 µm particles), respectively. The rate enhancement factors of Si release from ACBFS slag upon varying the solid-to-liquid ratio (s/l), mechanical mixing, grinding, heating, and acoustic activation are shown in Figure 5-5.

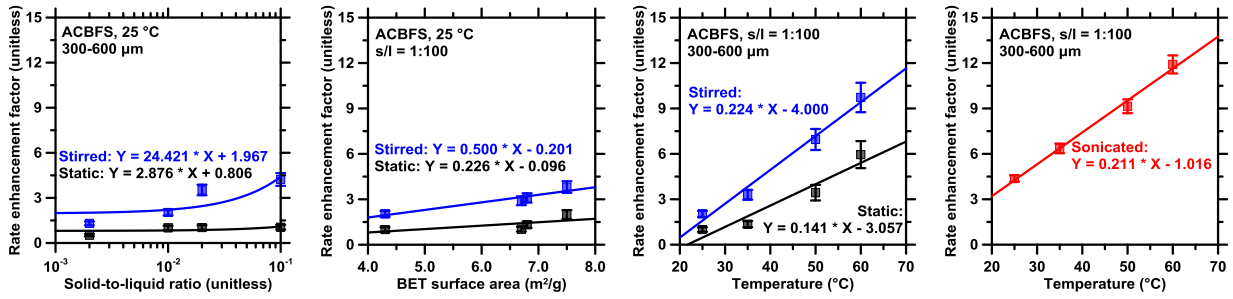

(a) **(b)** **(c)** **(d)**

Figure 5-5: Rate enhancement factors for air-cooled blast furnace slag (ACBFS) dissolution by **(a)** varying solid-to-liquid ratio (s/l), **(b)** grinding the slag into smaller particles (i.e. increasing BET surface area), **(c)** heating the reactants, and **(d)** sonicating the solution. The solid lines represent the best fittings of the data using a linear equation of $Y = a *X + b$.

Under static conditions, the rate of dissolution was effectively insensitive to the effects of grinding and changing the solid-to-liquid ratio (Figure 5-5a,b, black curves). Specifically, in Figure 5-5a, no dissolution enhancement was observed as the solid-to-liquid ratio decreased from 1:100 to 1:50 and 1:10. Unsurprisingly, solutal saturation occurred rapidly near the particle surface in unstirred systems, as a result of which increasing the s/l was only marginally effective in increasing the dissolution rate; a common-issue for surface-limited dissolution. For example, the apparent rate enhancement was only around 1.31 and 1.42 when the median particle size decreased from 449.7 to 101.1 and 18.9 µm, i.e., BET surface area increased from 4.3 to 6.8 and 7.5 m^2/g as shown in Figure 5-5b. Two concurrent processes were suggested to produce the small enhancement under static conditions: slag agglomeration and precipitation of reaction products.[380,387] First, agglomeration – which increased with decreasing particle size – significantly reduced the effective surface area as the solute particles clumped together.

Expectedly, the agglomeration effect was found to be less notable at lower solute particle populations, at lower solid-to-liquid ratio (s/l = 0.002) or with larger particle size (>300 μm). Second, compromised mass transport in solution due to lack of agitation resulted in the accumulation of dissolved ions near particle surfaces, which favored the formation of secondary precipitates.[380,388] Such precipitation that is evidenced by the decrease of aluminum concentration after 20 min of reaction (representative curve in Figure 5-6), withdraws dissolved silicon (along with other solubilized cations) from aqueous solution so that the accumulated Si in solution does not rise as expected when increasing the solid-to-liquid ratio or dissolving slag with finer grains. The precipitates in the vicinity of dissolving particles, form upon and mask reacting surfaces, which decelerates the further release of Si into solution. However, agitation of the water-slag mixture drastically reduced agglomeration and surface coverage, precipitation, and resulted in a dissolution enhancement of 4.2 times for s/l of 1:10 (Figure 5-5a, blue curve) and of 3.8 with particle size <53 μm (Figure 5-5b, blue curve). Expectedly, and given the activation energy of slag dissolution, Figure 5-5c shows that substantially greater rate enhancements were achieved at elevated temperatures, e.g., 6.0 times and 9.7 times at 60 °C under static and stirred conditions, respectively. This is because heating leads to expedited Si dissolution by increasing the surface reaction rate and by raising the solubility of SiO_2,[389] and thus the undersaturation that can be sustained prior to the onset of precipitation. As such, while both agitation and grinding can accelerate the release of Si from slag (i.e., as compared to static/unstirred cases) by reducing mass transport limitations and by exposing reactive surfaces, respectively, heating provides the greatest extent of rate enhancement because of the exponential dependence of reaction rates on temperature.

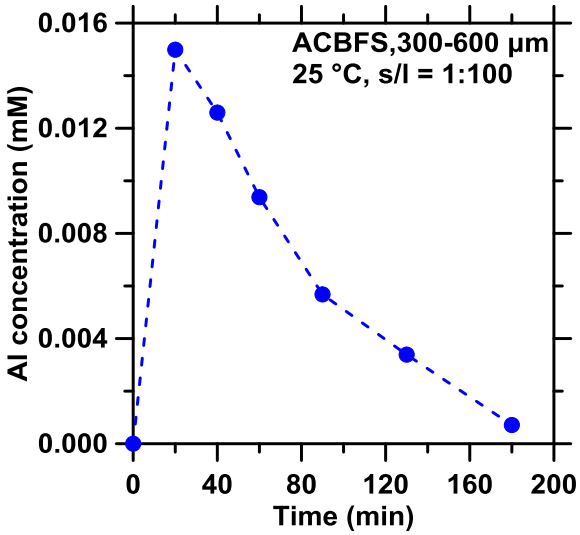

Figure 5-6: Representative aluminum release over time from air-cooled blast furnace slag (ACBFS) at 25 °C with 300-600 µm slag particle fraction at solid-to-liquid ratio of 1:100 under stirred condition for up to 2h.

Acoustic stimulation produces chemical and physical effects through cavitation and can greatly expedite dissolution processes[390] by reducing activation barriers associated with reactions.[16] In the case of slag dissolution, the bubble cavitation is thought to dislodge the porous silica layer which forms on the solute surface, and thus enhances elemental extraction from slag.[391] Herein, isothermal slag dissolution was carried out at temperatures from 25 to 60 °C (i.e., to match Figure 5-5c) for a fixed vibration amplitude, i.e., 60 µm, of the horn tip. The rate enhancement of Si-dissolution by sonication as a function of temperature was shown in Figure 5-5d. At room temperature, the rate enhancement induced by acoustic stimulation was prominent compared to stirring, i.e., 4.4 times vs. 2.0 times, respectively. As the temperature increased, the rate enhancement by sonication also increased, owing to the (additional) effect of thermal activation, but with a slope slightly inferior to that of heating under stirred conditions (Figure 5-

5c, blue curve). This suggests a reduction in cavitation effects with increasing temperature. At the highest temperature tested in this study, i.e., 60 °C, the rate enhancement of ACBFS dissolution by ultrasonication, 11.9 times, was however substantively higher than that of heating and stirring, 9.7 times, demonstrating the advantage of acoustic stimulation across all conditions considered. It should be noted that the reduction in cavitation effect with temperature, as observed elsewhere,[392–394] is thought to be caused by the increased vapor pressure (i.e. higher vapor pressure within cavitation bubbles, leading to lower energy release upon bubble collapse) and the reduction in the amount of dissolved air (in water).[392,395] Taken together, these effects lead to reduction of the cavitation energy, and the number of cavitation events per unit volume, as a result of which the ultrasonication power, P_u (Eq. 5-5), decreased from 40.7 W to 34.0 W when temperature increased from 25 °C to 60 °C (see Figure 5-7a).[377,392,396]

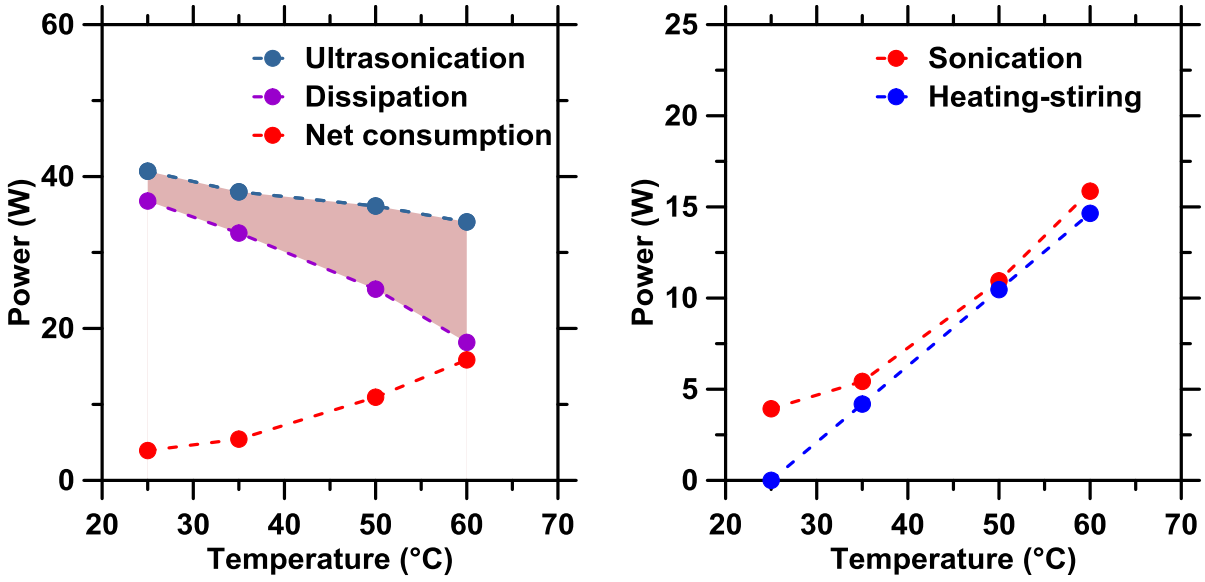

(a) **(b)**

Figure 5-7: (a) Breakdown of power consumption as a function of operation temperature for ultrasonication, as given by Eq. 5-5 and Eq. 5-6. **(b)** Comparison of power consumption as a function of operation for sonicated and stirred dissolution, as given by Eq.5-4 and Eq.5-5. The operation power is equivalent to process 100 mL of solution. In **(a)**, the ultrasonication power is the total amount transmitted into the liquid from the ultrasonic probe; and the dissipation power is the heat withdrawn by the cooling agent to maintain the isothermal reaction. The net consumption power is the difference between the ultrasonication power and the dissipation.

To understand the kinetic origin of rate enhancement by acoustic stimulation, the activation energy, E_a, was quantified (see Figures 5-8) using the apparent parabolic rates, a (Eq. 5-7), for Si release under static, stirred and sonicated conditions. Without sonication, the E_a of ACBFS dissolution under static and stirred conditions, respectively, were similar: 41.5 ± 0.51 and 37.6 ± 0.16 kJ/mol (see Figures 5-8a). Thus, and expectedly, mechanical agitation did not change the kinetic mechanism of Si release from ACBFS, or fly ash (not shown). Upon

sonication, the apparent activation energy of Si release decreased to 23.1 kJ/mol for ACBFS (ΔE_a = -14.5 kJ/mol). For Class F fly ash, a similar, albeit smaller, decrease in the apparent activation energy was observed between stirred and sonicated dissolution, from 47.4 kJ/mol to 39.9 kJ/mol (ΔE_a = -7.5 kJ/mol). The decrease in the activation energy indicates a lower-energy-barrier pathway for Si release when exposed to acoustic stimulation.[16] In a previous study of the acoustically-accelerated Grignard reaction, the reduction of the apparent activation energy was attributed to mechanical activation, i.e., creation of activated dislocations, by the action of the liquid microjets.[397] Such effects, i.e., fracture and dislocation generation, have been systematically investigated recently.[398]

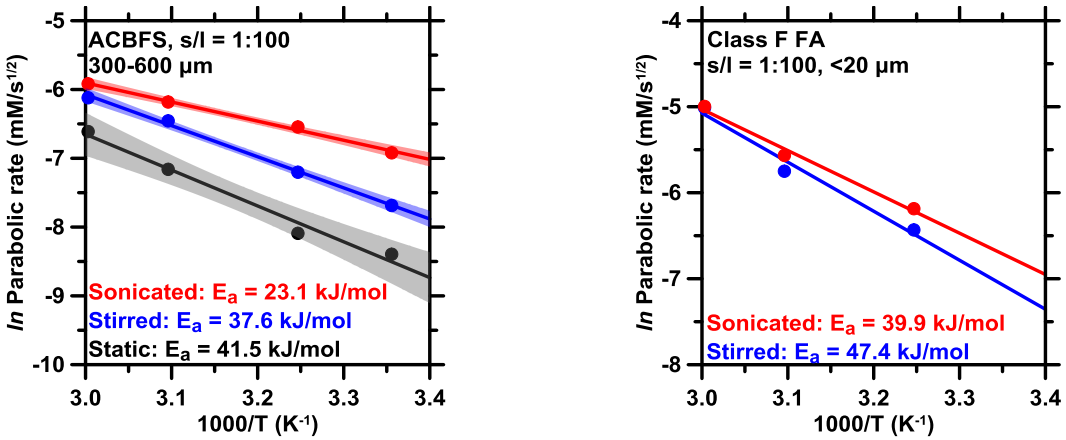

Figure 5-8: Representative Arrhenius plots of parabolic rate vs. inverse temperature to determine the activation energy of static, stirred, and sonicated dissolution for: **(a)** air-cooled blast furnace slag (ACBFS) and **(b)** Class F fly ash (FA). The solid lines represent the best-fit to the data and the shadowed regions in **(a)** indicate the 95% confidence interval.

5.4.3 Energy intensity reductions

The reduction in the energy barrier for Si-release upon sonication leads to higher rate enhancements as compared to other methods of dissolution activation (see Figure 5-5). This suggests, perhaps, the most efficient energy usage per unit of dissolution enhancement. Thus, the rate enhancement of Si release was compared against the power requirements for a single s/l, across a range of isothermal temperatures, as shown in Figure 5-9a. At temperatures higher than 25 °C, stirring requires energy additions to compensate for heat loss, given by Eq. 5-4, while the mixing power is around 3 orders of magnitude smaller. At 35, 50 and 60 °C, the power requirements for sonicated dissolution (given by Eq. 5-5) are similar to those for stirred dissolution (Figure 5-9a and Figure 5-7b), which suggests that a majority of the ultrasonic power input compensates for convective heat losses. In spite of this, sonication was able to produce higher apparent rate enhancement values for Si-release compared to stirring for the same power input in temperature range of 25 to 60 °C.

Figures 5-9b,c show the processing energy as a function of the amount of dissolved Si into water for the ACBFS and Class F FA, respectively, for both stirred and sonicated dissolution at 35, 50 and 60 °C. The processing energy was found to increase with the target Si concentration while decrease with the reaction temperature. This is because the kinetics of Si dissolution at higher temperatures was rapid enough to offset the increase in the power requirement with the reaction (Eq. 5-4, Figure 5-9a), leading to an overall energy reduction. Increasing temperature more substantively reduced the processing energy demand in the case of stirred dissolution than sonicated dissolution, as seen by the separation in the blue and red curves in Figure 5-9b. This is in agreement with the results in Figure 5-5c,d in which the relative

enhancement of sonication as compared to stirring decreased with increasing temperature. Nevertheless, the processing energy for sonicated dissolution was *lower than* and *no higher than* stirred dissolution within the tested temperature range (see shadowed regions, Figure 5-9b,c). This energy saving stems from the higher rate enhancement rendered by sonication, i.e., shortened reaction time, which is consistent with the observations in Figure 5-9a. The relative energy saving for ultrasonic processing was calculated as:

$$Relative\ energy\ saving\ (\%) = \frac{E_{Stirred} - E_{Sonicated}}{E_{Stirred}} \times 100\% \quad (5\text{-}9)$$

where $E_{Stirred}$ and $E_{Sonicated}$ are the processing energies required to dissolve a given amount of Si under stirred and sonicated conditions, respectively. For parabolic kinetics, the relative energy saving at a given temperature for a solute is given by:

$$Relative\ energy\ saving\ (\%) = (1 - \frac{P_{Sonicated}}{P_{Stirred}} \cdot (\frac{a_{Stirred}}{a_{Sonicated}})^2) \times 100\% \quad (5\text{-}10)$$

where $P_{Stirred}$ and $P_{Sonicated}$ are the net consumed power by stirred and sonicated dissolutions and $a_{Stirred}$ and $a_{Sonicated}$ parabolic rate constants (Eq. 7) of sonicated and stirred dissolution at a given temperature. The relative energy savings of ultrasonic processing for ACBFS and Class F dissolution across temperatures are summarized in Table 5-4. The relative energy saving for ACBFS dissolution spanned from 65% to 28% as the temperature increased from 35 to 60 °C (Figure 5-9d), and are substantially lower for the Ca-poor Class F FA, varying from 28.5% at 35 °C to ~0% at 60 °C (Figure 5-9d). The rate of Si release from Ca-poor FA was an order of magnitude greater than for ACBFS (Figure 5-9b,c), suggesting that sonication showed a greater energy savings for a solute with a lower unstimulated dissolution rate; i.e., which has a lower intrinsic reactivity.

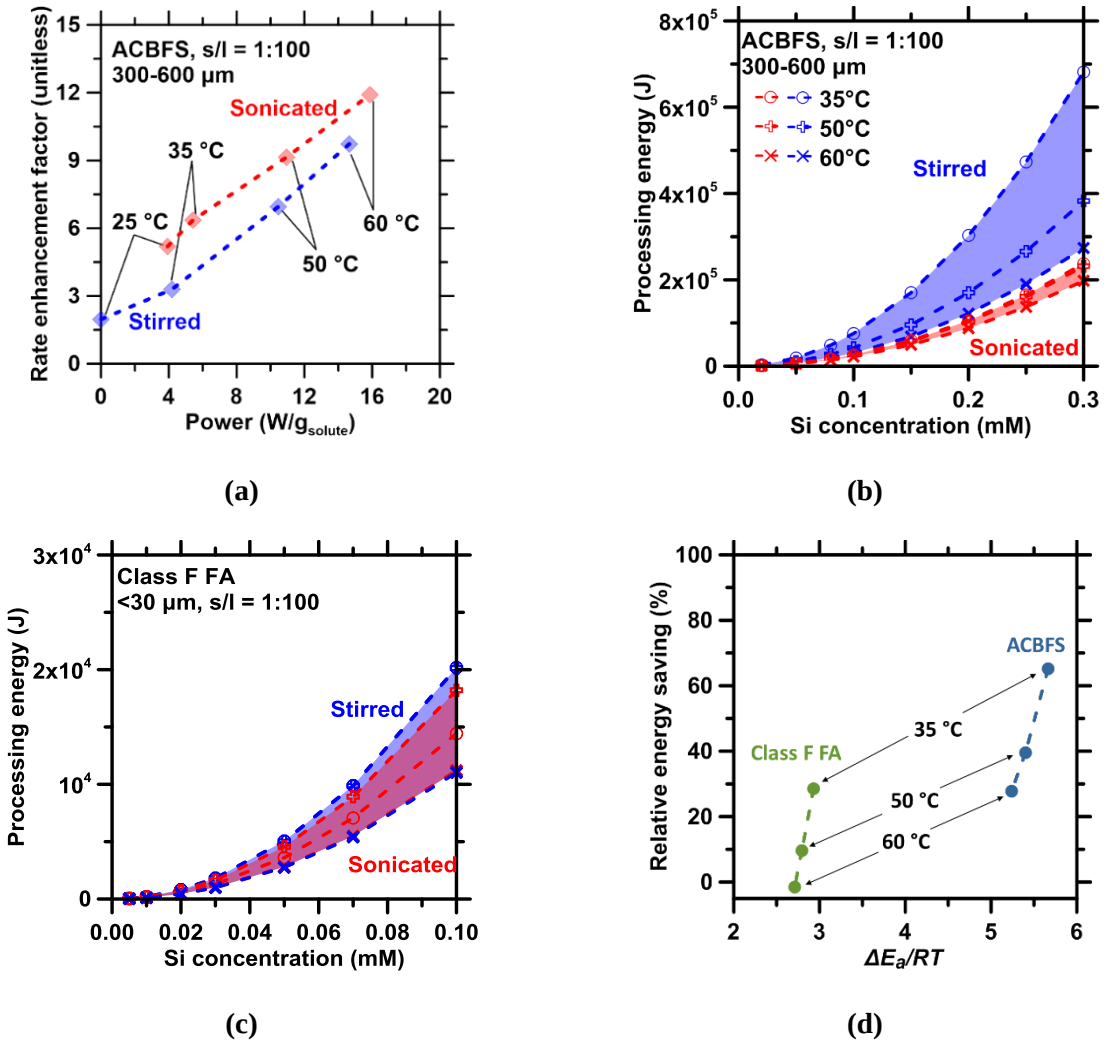

Figure 5-9: (a) The power supplied during reaction as a function of temperature for stirred and sonicated conditions as given by Eq. 5-4 and Eq. 5-5, respectively. Processing energy as a function of the concentration of dissolved Si in solution for both sonicated dissolution and stirred dissolution at 35, 50 and 60°C for **(b)** air-cooled blast furnace slag (ACBFS) and **(c)** Class F fly ash (FA). **(d)** The relative energy saving as a function of the ratio of the thermodynamic burden $\Delta E_a/RT$. The values of ΔE_a in **(d)** were obtained from **Figure 5-8**.

Table 5-4. The relative energy saving of ultrasonic processing for dissolving Si from air-cooled blast furnace slag (ACBFS) and Class F fly ash (FA) across different isothermal temperatures.

	35 °C	50 °C	60 °C
ACBFS	65.2%	39.5%	27.8%
Class F FA	28.5%	9.6	0%

The relative energy saving values were found to strongly correlate with the reduction in activation energy. For example, $\Delta E_a/RT$ was plotted against the relative energy saving in Figure 5-9d, where ΔE_a is the activation energy reduction, i.e., 14.5 kJ/mol for ACBFS and 7.5 kJ/mol for Class F FA (see Figure 5-8a,b). The reduction in the activation energy of Si release was solely induced by acoustic stimulation, and RT was indicative of the thermal effect on the rate enhancement. The positive trends in Figure 5-9d, for each solute, suggest that the relative significance of the two effects governs the energy saving. The energy required for the surface dissolution reaction, i.e., heat of reaction, was several orders of magnitude lower than the energy provided to the system, and thus the energy saving in this system was not directly caused by the lower activation energy. In determining the activation energy from isothermal reaction data, the (logarithm of) reaction time may be used as a proxy for reaction rate.[399] As such, a reduction in activation energy corresponds to a proportional reduction in reaction time, which corresponds to reduction in energy delivered to the system. Nevertheless, in comparing ACBFS and Class F FA dissolution, the variation in the $\Delta E_a/RT$ value is due to the difference in activation energy reduction, as the thermal contribution of T is the same between the solutes (shown by arrows in Figure 5-9d). Therefore, the higher energy saving for ACBFS as compared to Class F FA (Table 5-4), is a result of the more significant reduction in energy barrier induced by sonication for the

dissolution reaction, which is in turn due to the mineralogical differences between the two species.

5.3.4 Towards the application of acoustic stimulation in industrial waste dissolution

This study has demonstrated the ability of acoustic stimulation to enhance Si (and other element) dissolution from alkaline wastes. However, further questions remain:

(1) Process conditions – The influence of reaction temperature on processing energy is shown in Figure 5-9b,c. By coupling slag grinding (three orders of magnitude lower energy contribution than sonication) or increased s/l with stirring and sonication, the processing energies for sonicated dissolution and stirred dissolution are both further reduced (see Figure 5-10). The resultant relative energy saving for ultrasonic processing was increased to 80.5% (Figure 5-11a) for the smallest particle size (<53 μm) and the highest s/l (1:10) studied. The grinding energy (67.6 J for s/l=100, 100 ml water) is three orders of magnitude lower than the energy required to heat or sonicate a system (e.g., 3.0×10^5 J for sonicating 100 mL solution at 50 °C for 30 min), while increasing the s/l requires no energetic input. Thus, these low-energy sample preparation techniques, while leading to minimal rate enhancement in isolation (Figure 5-5a,b), have a significant impact on the energy savings obtained when coupled with acoustic stimulation. Thus, further work is needed to optimize the combinatorial method to maximize the dissolution rate, and to minimize the energy input.

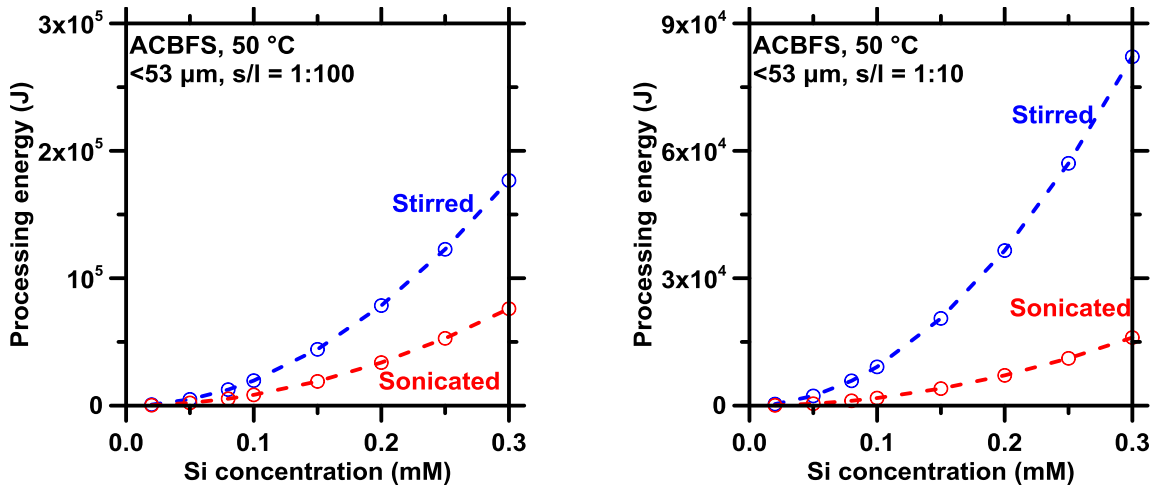

Figure 5-10: The effect of (a) particle size and (b) solid-to-liquid ratio on processing energy as a function of amount of dissolved Si into solution for both stirred dissolution and sonicated dissolution at 50 °C. All energy analyses are based on 100 ml of solvent.

(2) Material selection – The rate enhancement and energy analyses were performed for a crystalline ACBFS and amorphous Class F FAs. Other types and compositions of slags and fly ashes can be generated in iron and steel production and coal combustion, respectively.[117,400] Herein, the energy saving of ultrasonic processing for dissolution of SSS and Class C FA (see Figure 5-2c,d dissolution curves) were also investigated and are shown in Figure 5-11b. As the Si release from these two species does not follow linear or parabolic kinetics in the testing timeframe, the relative energy saving of ultrasonic processing from SSS and Class C FA was not constant with varied Si concentration (i.e. Eq. 5-9 does not apply). For SSS a higher energy saving was achieved at higher Si concentrations as the decrease in dissolution rate occurred less rapidly under sonicated conditions than under stirred conditions (see Figure 5-2c). This suggests that for SSS, sonication was able to increase the solubility of Si in solution, while stirred

dissolution showed a sharp decrease in dissolution rate consistent with approaching the solubility limit of Si. Contrarily, the decrease in energy saving for Class C FA, following an initial ramp up with Si concentration, was due to arrival at the saturation level for both sonicated and stirred dissolution (see Figure 5-2d). Taken together with the energy reduction for ACBFS and Class F FA (see Table 5-4 and Figure 5-9), energy saving provided by ultrasonic perturbation depends strongly on the solute, which is consistent with the solute-specific enhancement as observed in literature.[16] Nevertheless, this universal relative energy saving demonstrates that sonication can serve as a viable method for reducing the energetic costs of dissolution for a suitable feed solid.

(3) Si Extractability – The maximum Si fractional release value at 50 °C in this study was 3% (s/l = 1:100) after 3.0 h of dissolution as observed for stainless steel slag. For comparison, the highest Si extraction from serpentine was 17% (s/l = 1:20) after 1.5 h of dissolution at 100 °C using NH_4SO_4 as an additive.[401] Therefore, future studies in the area of ultrasonic enhancement of Si dissolution should improve the fractional extraction of Si while avoiding (or minimizing) the usage of additives, e.g., by recycling the solute to reduce the (approach to) saturation-induced reaction rate suppression.

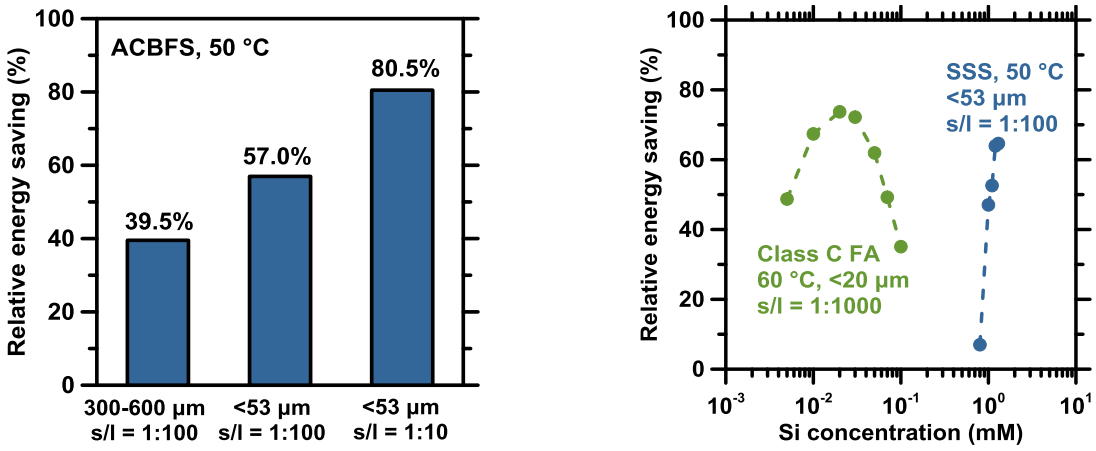

(a) **(b)**

Figure 5-11: (a) The effect of particle size and solid-to-liquid ratio (s/l) on the relative energy saving of acoustic processing for air-cooled blast furnace slag (ACBFS)s dissolution at 50 °C. (b) Relative energy saving of acoustic processing for stainless steel slag (SSS) and Class C fly ash (FA) dissolution at 50 and 60 °C, respectively, which exhibits dependence on the dissolved Si concentration.

5.5 Summary and Conclusions

This study investigated the effectiveness and energy efficiency of Si dissolution enhancement using acoustic stimulation, using air-cooled blast furnace slag (ACBFS), Ca-poor Class F fly ash (FA), stainless steel slag (SSS) and Ca-rich Class C FA as representative alkaline waste materials in order to probe the under-developed additive-free pathway for Si extraction. The ACBFS and Class F species exhibited parabolic Si dissolution kinetics while dissolutions of SSS and Class C FA approached to saturation rapidly. Based on the case study of the parabolic dissolution of ACBFS, ultrasonication provided the most significant enhancement in the apparent Si release rate, as compared to traditional reaction acceleration approaches, i.e., mechanical

grinding, mixing, and heating. Under sonication, the activation energy of dissolution reaction was reduced, lowering the energy barrier for Si-extraction and improving the energy efficiency of ultrasonic processing. The energy savings were primarily due to the shortened reaction time enabled by the higher rate enhancement by ultrasonication. Furthermore, the relative energy savings were correlated with the ratio between the ultrasonic effect and thermal effect, represented by $\Delta E_a/RT$. The kinetic benefit of a reduction in apparent activation energy led to a reduction in energy intensity of the overall dissolution process. The findings in this study demonstrate the potential of ultrasonic processing as an additive-free pathway for utilization of industrial alkaline wastes from both a kinetic (rate enhancing via reduction in activation energy) and practical (overall energy consumption) perspective.

Chapter 6. Summary and Future Work

6.1 Summary and Conclusion

This dissertation studied the corrosion behavior and inhibition in gas wells and nuclear power plant environments. It also investigated the additive-free pathway of dissolving minerals and industrial alkaline wastes using acoustic stimulation to obtain precursor solutions for cement production, to mitigate the energy and emission problem in the traditional processes.

As research questions, the primary objective of this dissertation is to study the effect of surface energy (i.e., the extra energy due to the broken bonds at the solute surface compared to the bulk material) on the corrosion of steels and dissolution enhancement of minerals by ultrasound. The two hypotheses that are initially proposed in Chapter 1 have been tested as detailed in Chapter 2 to 5 and are further revised based on the results of the studies to formulate the general conclusions herein.

Firstly, the rates of active corrosion and transpassive corrosion of stainless steel can be controlled by grain-specific surface energy, which stems from the diverse crystallographic orientation of grain surfaces. The surface energy controls the surface recession rate of stainless steel in the corrosive environment via two competing mechanisms. On the one hand, corrosion progresses more rapidly on the grain surfaces having higher surface energy which gives rise to a smaller activation energy for corrosion reaction to occur. On the other hand, higher surface energy of grain surface leads to the formation of a denser barrier layer by the adsorption of aqueous ions, which hinders the corrosion reaction between the aqueous solution and the underlying steel. The two concurrent effects result in the corrosion rate of grain surfaces with the lowest Miller Indices following the scaling of $\{001\} < \{101\} < \{111\}$, while their surface energy increases according to $\{111\} < \{001\} < \{101\}$.

Furthermore, the rate increases of mineral dissolution by acoustic stimulation, i.e, ultrasonication, is partially controlled by surface energy of the mineral species. The surface energy governs the probability at which the solute particulates can be fractured by the violent attack resulted from the collapse of the cavitation bubble. Fracture of solute particulate exposes new surfaces which promotes the dissolution reaction. However, the creation of dislocation upon the collapse of cavitation bubbles, the probability of which was found to decrease with the stacking fault energy of the mineral solid, contributed more significantly to the overall rate increase. Dislocation induces local kinetic enhancement of dissolution reaction and lead to rapid formation of etch pits on the dissolving surface. An empirical model unifying the two mechanisms was proposed, which matches well with experimental results, to predict the dissolution increase of mineral dissolution by acoustic stimulation.

6.2 Future Work

6.2.1 Effect of grain-specific surface energy on steel corrosion

Firstly, Chapter 2 discussed the corrosion inhibiting effect and mechanism by calcium nitrate for carbon steel, from a macroscopic perspective, i.e., averaged over the entire steel surface without discriminating among grains. Therefore, one of the research questions of interest will be: what is the impact of grain orientation on the corrosion inhibiting effectiveness of nitrate? When nitrate ion is present in the aqueous solution, it may participate in the ion adsorption to form the barrier layer, the process of which is found to controlled by grain surface energy. Therefore, grain surface with lower surface energy may have a lower tendency to adsorb the nitrate ion and consequently a less pronounced corrosion inhibition effect. Such process may be collectively influenced by the water chemistry of the aqueous environment, the gained

knowledge will provide guidance in corrosion protection to the ‘week sites’ that are more susceptible to corrosion attack.

From a different point of view, Chapter 3 studied the effect of surface energy, which arises from the crystallographic orientation, on two types corrosions, i.e., active corrosion and transpassive corrosion, of stainless steel, which are typically found in the scenarios of crevice and presence of radiolytic radicals. In both cases which feature strongly oxidative and corrosive environment, the air-born oxide film is broken down and absent on the steel surface. However, the passive film is critical to corrosion resistance of austenitic stainless steel. One of the research questions of interest will be: what is the effect of grain orientation on the formation of passive film? A further step may be undertaken to address the question related with susceptibility of differently oriented grain to corrosion due to breakdown of the passive film, e.g., pitting corrosion, which is one of the most dangerous type of corrosion due to difficulty to detect.[402] Answers to these questions will enable early detection and inform better prevention of pitting corrosion.

From another perspective, the motivation of the present study originates from the problem that the ‘step’ structure formed due to different recession rate between adjacent grains may initiate crack formation and lead to structural failure under stress. The present work focuses on the spatially averaged corrosion rate within each grain, while the corrosion behavior at the grain boundary is not probed. As the boundary region between the adjacent grains that are corroding at different rates is where crack is more likely to occur,[222,403] one research question of interest will be: what is the effect of grain orientation (or relation of orientations between adjacent grains) on the corrosion at the grain boundary? Such knowledge will provide insights to

understand stress corrosion cracking (SCC) and intergranular corrosion (a typical problem for sensitized steels),[404] and will inform better prevention of structural failure.

6.2.2 Effect of mineral-specific surface energy on the dissolution enhancement by acoustic stimulation

Firstly, Chapter 4 unravels the dual mechanisms in which the dissolution increase of minerals by ultrasonication is simultaneously controlled by mineral surface energy and stacking fault energy. The study focuses the dissolution reaction in the far-from-saturation region, where the dissolution rate is not affected by the degree of undersaturation, so that the proposed model describes the acoustic effect on the kinetics of pure dissolution reaction. Eq. 1-9 suggests that as undersaturation decreases the driving force for dissolution reaction becomes smaller so that dissolution gradually slows down. From this standing point, one research question of interest will be: how do the surface energy controlled particulate fracture and stacking fault energy governed creation of dislocation impact the attenuated driving force at low undersaturation, i.e., close to equilibrium? This problem is preliminarily probed in Chapter 5, which revealed a reduction in activation energy of crystalline slag dissolution by ultrasonication at the parabolic kinetics region, the transition from a linear dissolution rate to a zero rate upon reaching dynamic equilibrium. Further studies are required to correlate the physical effects with the kinetic origin, which will enable a comprehensive understanding of acoustic stimulation in mineral dissolution processes.

From the application point of view, Chapter 5 took the initial step to evaluate the feasibility of the additive-free pathway of enhancing dissolution of industrial waste materials using acoustic stimulation. With an ultimate goal to achieve production scale application, a series

of more problems need to be addressed first on the laboratory batch scale as also mapped out in that chapter, including process optimization which is able to achieve the highest yield while requiring the lowest energy input, material selection with combined considerations of material abundancy and elemental content and reactivity, and improved extractability.

Bibliography

(1) Fu, C.; Zheng, J.; Zhao, J.; Xu, W. Application of Grey Relational Analysis for Corrosion Failure of Oil Tubes. *Corros. Sci.* **2001**, *43* (5), 881–889. https://doi.org/10.1016/S0010-938X(00)00089-5.

(2) Koch, G. 1 - Cost of Corrosion. In *Trends in Oil and Gas Corrosion Research and Technologies*; El-Sherik, A. M., Ed.; Woodhead Publishing Series in Energy; Woodhead Publishing: Boston, 2017; pp 3–30. https://doi.org/10.1016/B978-0-08-101105-8.00001-2.

(3) Koch, G. H.; Brongers, M. P. H.; Thompson, N. G.; Virmani, Y. P.; Payer, J. H. Corrosion Cost and Preventive Strategies in the United States [Final Report]. **2002**, No. FHWA-RD-01-156, R315-01.

(4) Tuttle, R. N. Corrosion in Oil and Gas Production. *J. Pet. Technol.* **1987**, *39* (07), 756–762. https://doi.org/10.2118/17004-PA.

(5) Popoola, L. T.; Grema, A. S.; Latinwo, G. K.; Gutti, B.; Balogun, A. S. Corrosion Problems during Oil and Gas Production and Its Mitigation. *Int. J. Ind. Chem.* **2013**, *4* (1), 35. https://doi.org/10.1186/2228-5547-4-35.

(6) Brondel, D.; Edwards, R.; Hayman, A.; Hill, D.; Mehta, S.; Semerad, T. Corrosion in the Oil Industry. *Oilfield Rev.* **1994**, *6* (2), 4–18.

(7) Cattant, F.; Crusset, D.; Féron, D. Corrosion Issues in Nuclear Industry Today. *Mater. Today* **2008**, *11* (10), 32–37. https://doi.org/10.1016/S1369-7021(08)70205-0.

(8) Was, G. S.; Ampornrat, P.; Gupta, G.; Teysseyre, S.; West, E. A.; Allen, T. R.; Sridharan, K.; Tan, L.; Chen, Y.; Ren, X.; Pister, C. Corrosion and Stress Corrosion Cracking in Supercritical Water. *J. Nucl. Mater.* **2007**, *371* (1), 176–201. https://doi.org/10.1016/j.jnucmat.2007.05.017.

(9) Hayashi, M.; Kiuchi, K.; Hayakawa, H.; Kikuchi, M. Trans-Passive Corrosion Mechanism of Austenitic Stainless Steels in Boiling Nitric Acid Solution. *Proc. Int. Symp. Mater. Chem. Nucl. Environ.* **1992**.

(10) Moayed, M. H.; Golestanipour, M. An Investigation on the Effect of Bleaching Environment on Pitting Corrosion and Transpassive Dissolution of 316 Stainless Steel. *Mater. Corros.* **2005**, *56* (1), 39–43. https://doi.org/10.1002/maco.200403809.

(11) Condie, K. C. Origin and Early Development of the Earth's Crust. *Precambrian Res.* **1980**, *11* (3), 183–197. https://doi.org/10.1016/0301-9268(80)90064-9.

(12) Huijgen, W. J. J.; Comans, R. N. J. Mineral CO2 Sequestration by Steel Slag Carbonation. *Environ. Sci. Technol.* **2005**, *39* (24), 9676–9682. https://doi.org/10.1021/es050795f.

(13) Kato, N.; Owa, N. Evaluation of Si Availability in Slag Fertilizers by an Extraction Method Using a Cation Exchange Resin. *Soil Sci. Plant Nutr.* **1997**, *43* (2), 351–359. https://doi.org/10.1080/00380768.1997.10414759.

(14) He, H.; Cao, J.; Duan, N. Synergistic Effect between Ultrasound and Fierce Mechanical Activation towards Mineral Extraction: A Case Study of ZnO Ore. *Ultrason. Sonochem.* **2018**, *48*, 163–170. https://doi.org/10.1016/j.ultsonch.2018.05.025.

(15) Sillanpää, M.; Pham, T.-D.; Shrestha, R. A. Ultrasound Technology in Green Chemistry. In *Ultrasound Technology in Green Chemistry*; Sillanpää, M., Ed.; SpringerBriefs in Molecular Science; Springer Netherlands: Dordrecht, 2011; pp 1–21. https://doi.org/10.1007/978-94-007-2409-9_1.

(16) Wei, Z.; Hsiao, Y.-H.; Chen, X.; La Plante, E. C.; Mehdipour, I.; Simonetti, D.; Neithalath, N.; Pilon, L.; Bauchy, M.; Israelachvili, J.; Sant, G. Isothermal Stimulation of Mineral Dissolution Processes by Acoustic Perturbation. *J. Phys. Chem. C* **2018**, *122* (50), 28665–28673. https://doi.org/10.1021/acs.jpcc.8b08343.

(17) Vitos, L.; Ruban, A. V.; Skriver, H. L.; Kollár, J. The Surface Energy of Metals. *Surf. Sci.* **1998**, *411* (1), 186–202. https://doi.org/10.1016/S0039-6028(98)00363-X.

(18) Eberhart, J. G.; Horner, S. Bond-Energy and Surface-Energy Calculations in Metals. *J. Chem. Educ.* **2010**, *87* (6), 608–612. https://doi.org/10.1021/ed100189v.

(19) Schwarz, R. B.; Johnson, W. L. Formation of an Amorphous Alloy by Solid-State Reaction of the Pure Polycrystalline Metals. *Phys. Rev. Lett.* **1983**, *51* (5), 415–418. https://doi.org/10.1103/PhysRevLett.51.415.

(20) Takabatake, Y.; Kitagawa, Y.; Nakanishi, T.; Hasegawa, Y.; Fushimi, K. Heterogeneity of a Thermal Oxide Film Formed on Polycrystalline Iron Observed by Two-Dimensional Ellipsometry. *J. Electrochem. Soc.* **2016**, *163* (14), C815. https://doi.org/10.1149/2.0211614jes.

(21) Grabke, H. J.; Petersen, E. M.; Srinivasan, S. R. Influence of Adsorbed Sulfur on Surface Reaction Kinetics and Surface Self-Diffusion on Iron. *Surf. Sci.* **1977**, *67* (2), 501–516. https://doi.org/10.1016/0039-6028(77)90011-5.

(22) Gray, J. J.; El Dasher, B. S.; Orme, C. A. Competitive Effects of Metal Dissolution and Passivation Modulated by Surface Structure: An AFM and EBSD Study of the Corrosion of Alloy 22. *Surf. Sci.* **2006**, *600* (12), 2488–2494. https://doi.org/10.1016/j.susc.2006.04.002.

(23) Thompson, C. V.; Smith, H. I. Surface-energy-driven Secondary Grain Growth in Ultrathin (<100 Nm) Films of Silicon. *Appl. Phys. Lett.* **1984**, *44* (6), 603–605. https://doi.org/10.1063/1.94842.

(24) Isakov, E. *Cutting Data for Turning of Steel*; Industrial Press Inc., 2009.

(25) Bringas, J. E. *Handbook of Comparative World Steel Standards*; ASTM data series; ASTM International, 2004.

(26) Nascimento, R. C.; Furtado, L. B.; Guimarães, M. J. O. C.; Seidl, P. R.; Rocha, J. C.; Ponciano, J. A. C.; Cruz, M. T. M. Synergistic Effect of Propargyl Alcohol, Octadecylamine, and 1,3-Dibutyl Thiourea for API P110 Alloys in Acetic and Formic Acidic Solutions Used in Oil Well Acidizing. *J. Mol. Liq.* **2018**, *256*, 548–557. https://doi.org/10.1016/j.molliq.2018.02.082.

(27) Hinojos, A.; Mireles, J.; Reichardt, A.; Frigola, P.; Hosemann, P.; Murr, L. E.; Wicker, R. B. Joining of Inconel 718 and 316 Stainless Steel Using Electron Beam Melting Additive Manufacturing Technology. *Mater. Des.* **2016**, *94*, 17–27. https://doi.org/10.1016/j.matdes.2016.01.041.

(28) Dwivedi, D.; Lepková, K.; Becker, T. Carbon Steel Corrosion: A Review of Key Surface Properties and Characterization Methods. *RSC Adv.* **2017**, *7* (8), 4580–4610. https://doi.org/10.1039/C6RA25094G.

(29) API steel grades for tubing and casing http://www.oiltubulars.com/What-is-News/api-steel-grades-for-tubing-and-casing.html (accessed Jul 15, 2020).

(30) Yield Strength of Steel https://amesweb.info/Materials/Yield-Strength-of-Steel.aspx.

(31) Davis, J. R. *Stainless Steel, ASM Speciality Handbook*; ASM International, 1994.

(32) Davison, R. M.; Laurin, T. R.; Redmond, J. D.; Watanabe, H.; Semchyshen, M. A Review of Worldwide Developments in Stainless Steels. *Mater. Des.* **1986**, *7* (3), 111–119. https://doi.org/10.1016/0261-3069(86)90001-4.

(33) Igata, N.; Chen, H. B.; Miyahara, K. Internal Friction Peaks of Cold Worked and/or Hydrogen Charged 18-8 Austenitic Stainless Steel. *Scr. Metall.* **1982**, *16* (2), 169–172. https://doi.org/10.1016/0036-9748(82)90379-9.

(34) Ilevbare, G. O.; Burstein, G. T. The Role of Alloyed Molybdenum in the Inhibition of Pitting Corrosion in Stainless Steels. *Corros. Sci.* **2001**, *43* (3), 485–513. https://doi.org/10.1016/S0010-938X(00)00086-X.

(35) Malitckii, E.; Remes, H.; Lehto, P.; Yagodzinskyy, Y.; Bossuyt, S.; Hänninen, H. Strain Accumulation during Microstructurally Small Fatigue Crack Propagation in Bcc Fe-Cr Ferritic Stainless Steel. *Acta Mater.* **2018**, *144*, 51–59. https://doi.org/10.1016/j.actamat.2017.10.038.

(36) Henriksson, K. O. E.; Björkas, C.; Nordlund, K. Atomistic Simulations of Stainless Steels: A Many-Body Potential for the Fe–Cr–C System. *J. Phys. Condens. Matter* **2013**, *25* (44), 445401. https://doi.org/10.1088/0953-8984/25/44/445401.

(37) Garrison, W. M.; Amuda, M. O. H. Stainless Steels: Martensitic. In *Reference Module in Materials Science and Materials Engineering*; Elsevier, 2017. https://doi.org/10.1016/B978-0-12-803581-8.02527-3.

(38) McCafferty, E. *Introduction to Corrosion Science*; Springer Science & Business Media, 2010.

(39) González, J. A.; Feliú, S.; Rodríguez, P.; Ramírez, E.; Alonso, C.; Andrade, C. Some Questions on the Corrosion of Steel in Concrete—Part I: When, How and How Much Steel Corrodes. *Mater. Struct.* **1996**, *29* (1), 40. https://doi.org/10.1007/BF02486005.

(40) Beverskog, B.; Puigdomenech, I. Revised Pourbaix Diagrams for Iron at 25–300 °C. *Corros. Sci.* **1996**, *38* (12), 2121–2135. https://doi.org/10.1016/S0010-938X(96)00067-4.

(41) Zou, Y.; Wang, J.; Zheng, Y. Y. Electrochemical Techniques for Determining Corrosion Rate of Rusted Steel in Seawater. *Corros. Sci.* **2011**, *53* (1), 208–216. https://doi.org/10.1016/j.corsci.2010.09.011.

(42) Hao, L.; Zhang, S.; Dong, J.; Ke, W. Evolution of Corrosion of MnCuP Weathering Steel Submitted to Wet/Dry Cyclic Tests in a Simulated Coastal Atmosphere. *Corros. Sci.* **2012**, *58*, 175–180. https://doi.org/10.1016/j.corsci.2012.01.017.

(43) Amin, M. A.; Ibrahim, M. M. Corrosion and Corrosion Control of Mild Steel in Concentrated H2SO4 Solutions by a Newly Synthesized Glycine Derivative. *Corros. Sci.* **2011**, *53* (3), 873–885. https://doi.org/10.1016/j.corsci.2010.10.022.

(44) Kincaid, J. F.; Eyring, Henry.; Stearn, A. E. The Theory of Absolute Reaction Rates and Its Application to Viscosity and Diffusion in the Liquid State. *Chem. Rev.* **1941**, *28* (2), 301–365. https://doi.org/10.1021/cr60090a005.

(45) Kulikovsky, A. A. Chapter 1 - Fuel Cell Basics. In *Analytical Modeling of Fuel Cells (Second Edition)*; Kulikovsky, A. A., Ed.; Elsevier, 2019; pp 1–33. https://doi.org/10.1016/B978-0-44-464222-6.00008-3.

(46) Dreyer, W.; Guhlke, C.; Müller, R. A New Perspective on the Electron Transfer: Recovering the Butler–Volmer Equation in Non-Equilibrium Thermodynamics. *Phys. Chem. Chem. Phys.* **2016**, *18* (36), 24966–24983. https://doi.org/10.1039/C6CP04142F.

(47) Fletcher, S.; Stephen Varley, T. Beyond the Butler–Volmer Equation. Curved Tafel Slopes from Steady-State Current–Voltage Curves. *Phys. Chem. Chem. Phys.* **2011**, *13* (12), 5359–5364. https://doi.org/10.1039/C0CP02471F.

(48) Adler, S. B. Chapter 11 - Sources of Cell and Electrode Polarisation Losses in SOFCs. In *High-Temperature Solid Oxide Fuel Cells for the 21st Century (Second Edition)*; Kendall, K., Kendall, M., Eds.; Academic Press: Boston, 2016; pp 357–381. https://doi.org/10.1016/B978-0-12-410453-2.00011-7.

(49) de Rooij, D. M. R. Electrochemical Methods: Fundamentals and Applications. *Anti-Corros. Methods Mater.* **2003**, *50* (5). https://doi.org/10.1108/acmm.2003.12850eae.001.

(50) Macdonald, D. D. PassivityÐthe Key to Our Metals-Based Civilization. *Pure Appl Chem* **1999**, 28.

(51) Bulman, G. M.; Tseung, A. C. C. An Ellipsometric Study of Passive Film Growth on Stainless Steel. *Corros. Sci.* **1973**, *13* (7), 531–544. https://doi.org/10.1016/S0010-938X(73)80003-4.

(52) Mohammadi, F.; Nickchi, T.; Attar, M. M.; Alfantazi, A. EIS Study of Potentiostatically Formed Passive Film on 304 Stainless Steel. *Electrochimica Acta* **2011**, *56* (24), 8727–8733. https://doi.org/10.1016/j.electacta.2011.07.072.

(53) Stockbridge, C. D.; Sewell, P. B.; Cohen, M. Cathodic Behavior of Iron Single Crystals and the Oxides Fe3 O 4, Gamma - Fe2 O 3, and Alpha - Fe2 O 3. *J. Electrochem. Soc.* **1961**, *108* (10), 928. https://doi.org/10.1149/1.2427923.

(54) Sewell, P. B.; Stockbridge, C. D.; Cohen, M. An Electrometric and Electron Diffraction Study of Air-Formed Oxide Films on Iron. *J. Electrochem. Soc.* **1961**, *108* (10), 933. https://doi.org/10.1149/1.2427924.

(55) Nagayama, M.; Cohen, M. The Anodic Oxidation of Iron in a Neutral Solution: I . The Nature and Composition of the Passive Film. *J. Electrochem. Soc.* **1962**, *109* (9), 781. https://doi.org/10.1149/1.2425555.

(56) McCafferty, E.; C. Zettlemoyer, A. Adsorption of Water Vapour on α -Fe 2 O 3. *Discuss. Faraday Soc.* **1971**, *52* (0), 239–254. https://doi.org/10.1039/DF9715200239.

(57) Kruger, J. Passivity of Metals – a Materials Science Perspective. *Int. Mater. Rev.* **1988**, *33* (1), 113–130. https://doi.org/10.1179/imr.1988.33.1.113.

(58) Tjong, S. C.; Yeager, E. ESCA and SIMS Studies of the Passive Film on Iron. *J. Electrochem. Soc.* **1981**, *128* (10), 2251. https://doi.org/10.1149/1.2127229.

(59) Schroeder, V.; Devine, T. M. Surface Enhanced Raman Spectroscopy Study of the Galvanostatic Reduction of the Passive Film on Iron. *J. Electrochem. Soc.* **1999**, *146* (11), 4061. https://doi.org/10.1149/1.1392592.

(60) Castle, J. E.; Clayton, C. R. The Use of in the X-Ray Photo-Electron Spectroscopy Analyses of Passive Layers on Stainless Steel. *Corros. Sci.* **1977**, *17* (1), 7–26. https://doi.org/10.1016/0010-938X(77)90036-1.

(61) Clayton, C. R.; Lu, Y. C. A Bipolar Model of the Passivity of Stainless Steel: The Role of Mo Addition. *J. Electrochem. Soc.* **1986**, *133* (12), 2465. https://doi.org/10.1149/1.2108451.

(62) Marcus, P. *Corrosion Mechanisms in Theory and Practice, Third Edition*; CRC Press, 2011.

(63) Wegrelius, L.; Falkenberg, F.; Olefjord, I. Passivation of Stainless Steels in Hydrochloric Acid. *J. Electrochem. Soc.* **1999**, *146* (4), 1397. https://doi.org/10.1149/1.1391777.

(64) Stout, D. A.; Lumsden, J. B.; Staehle, R. W. An Investigation of Pitting Behavior of Iron-Molybdenum Binary Alloys. *CORROSION* **1979**, *35* (4), 141–147. https://doi.org/10.5006/0010-9312-35.4.141.

(65) Sugimoto, K.; Sawada, Y. The Role of Molybdenum Additions to Austenitic Stainless Steels in the Inhibition of Pitting in Acid Chloride Solutions. *Corros. Sci.* **1977**, *17* (5), 425–445. https://doi.org/10.1016/0010-938X(77)90032-4.

(66) Klimmeck, M. A Study of the Kinetics of Passive Layer Formation on Cr-Mo Alloys. *Electrochimica Acta* **1980**, *25* (11), 1375–1381. https://doi.org/10.1016/0013-4686(80)87152-0.

(67) B.rockel, M. The Effect of Molybdenum on the Corrosion Behavior of Iron-Chromium Alloys. *CORROSION* **1973**, *29* (10), 393–396. https://doi.org/10.5006/0010-9312-29.10.393.

(68) Nesic, S.; Postlethwaite, J.; Olsen, S. An Electrochemical Model for Prediction of Corrosion of Mild Steel in Aqueous Carbon Dioxide Solutions. *CORROSION* **1996**, *52* (4), 280–294. https://doi.org/10.5006/1.3293640.

(69) Latha, G.; Rajeswari, S. Versatility of Superaustenitic Stainless Steels in Marine Applications. *J. Mater. Eng. Perform.* **1996**, *5* (5), 577–582. https://doi.org/10.1007/BF02646084.

(70) Isaacs, H. S.; Huang, S.-M.; Jovancicevic, V. Location of Corrosion on Iron and Carbon Steel Surfaces with Crevices. *J. Electrochem. Soc.* **1996**, *143* (8), L178. https://doi.org/10.1149/1.1837022.

(71) M. Jayalakshmi; V. S. Muralidharan. EMPIRICAL AND DETERMINISTIC MODELS OF PITTING CORROSION - AN OVERVIEW. *Corros. Rev.* **1996**, *14* (3–4), 375–402. https://doi.org/10.1515/CORRREV.1996.14.3-4.375.

(72) Rios, E. R. de los; Wu, X. D.; Miller, K. J. A Micro-Mechanics Model of Corrosion-Fatigue Crack Growth in Steels. *Fatigue Fract. Eng. Mater. Struct.* **1996**, *19* (11), 1383–1400. https://doi.org/10.1111/j.1460-2695.1996.tb00174.x.

(73) G01 Committee. *G48 - 11(2015) Standard Test Methods for Pitting and Crevice Corrosion Resistance of Stainless Steels and Related Alloys by Use of Ferric Chloride Solution*; ASTM International. https://doi.org/10.1520/G0048-11R15.

(74) Popov, B. N. Chapter 7 - Pitting and Crevice Corrosion. In *Corrosion Engineering*; Popov, B. N., Ed.; Elsevier: Amsterdam, 2015; pp 289–325. https://doi.org/10.1016/B978-0-444-62722-3.00007-0.

(75) Hoar, T. P.; Jacob, W. R. Breakdown of Passivity of Stainless Steel by Halide Ions. *Nature* **1967**, *216* (5122), 1299–1301. https://doi.org/10.1038/2161299a0.

(76) Dayal, R. K.; Parvathavarthini, N.; Gnanamoorthy, J. B. A Study of Various Critical Pitting Potentials for Type 316 Stainless Steel in Sulfuric Acid Containing Chloride Ions. *CORROSION* **1980**, *36* (8), 433–436. https://doi.org/10.5006/0010-9312-36.8.433.

(77) Lee, S. U.; Ahn, J. C.; Kim, D. H.; Hong, S. C.; Lee, K. S. Influence of Chloride and Bromide Anions on Localized Corrosion of 15%Cr Ferritic Stainless Steel. *Mater. Sci. Eng. A* **2006**, *434* (1), 155–159. https://doi.org/10.1016/j.msea.2006.06.132.

(78) Cáceres, L.; Vargas, T.; Herrera, L. Influence of Pitting and Iron Oxide Formation during Corrosion of Carbon Steel in Unbuffered NaCl Solutions. *Corros. Sci.* **2009**, *51* (5), 971–978. https://doi.org/10.1016/j.corsci.2009.02.021.

(79) Leckie, H. P.; Uhlig, H. H. Environmental Factors Affecting the Critical Potential for Pitting in 18–8 Stainless Steel. *J. Electrochem. Soc.* **1966**, *113* (12), 1262. https://doi.org/10.1149/1.2423801.

(80) Loto, R. T. Pitting Corrosion Evaluation of Austenitic Stainless Steel Type 304 in Acid Chloride Media. *J Mater Env. Sci* **2013**, *4* (4), 448.

(81) McCafferty, E. Sequence of Steps in the Pitting of Aluminum by Chloride Ions. *Corros. Sci.* **2003**, *45* (7), 1421–1438. https://doi.org/10.1016/S0010-938X(02)00231-7.

(82) Frankel, G. S. Pitting Corrosion of Metals: A Review of the Critical Factors. *J. Electrochem. Soc.* **1998**, *145* (6), 2186–2198. https://doi.org/10.1149/1.1838615.

(83) Natishan, P. M.; O'Grady, W. E.; McCafferty, E.; Ramaker, D. E.; Pandya, K.; Russell, A. Chloride Uptake by Oxide Covered Aluminum as Determined by X-Ray Photoelectron and X-Ray Absorption Spectroscopy. *J. Electrochem. Soc.* **1999**, *146* (5), 1737. https://doi.org/10.1149/1.1391835.

(84) Froment, M. *Passivity of Metals and Semiconductors: Proceedings of the Fifth International Symposium on Passivity, Bombannes, France, May 30-June 3, 1983, Organized by the Société de Chimie Physique*; Elsevier, 2013.

(85) Macdonald, D. D. The Point Defect Model for the Passive State. *J. Electrochem. Soc.* **1992**, *139* (12), 3434–3449. https://doi.org/10.1149/1.2069096.

(86) Yu, S. Y.; O'Grady, W. E.; Ramaker, D. E.; Natishan, P. M. Chloride Ingress into Aluminum Prior to Pitting Corrosion An Investigation by XANES and XPS. *J. Electrochem. Soc.* **2000**, *147* (8), 2952. https://doi.org/10.1149/1.1393630.

(87) Khalil, W.; Haupt, S.; Strehblow, H.-H. The Thinning of the Passive Layer of Iron by Halides. *Mater. Corros.* **1985**, *36* (1), 16–21. https://doi.org/10.1002/maco.19850360104.

(88) Sato, N. A Theory for Breakdown of Anodic Oxide Films on Metals. *Electrochimica Acta* **1971**, *16* (10), 1683–1692. https://doi.org/10.1016/0013-4686(71)85079-X.

(89) Butler, G.; Stretton, P.; Beynon, J. G. Initiation and Growth of Pits on High-Purity Iron and Its Alloys with Chromium and Copper in Neutral Chloride Solutions. *Br. Corros. J.* **1972**, *7* (4), 168–173. https://doi.org/10.1179/000705972798322991.

(90) *Proceedings of the Fifth International Congress on Metallic Corrosion, Tokyo, Japan, May, 1972*; National Association of Corrosion Engineers, 1974.

(91) Fattah-alhosseini, A.; Saatchi, A.; Golozar, M. A.; Raeissi, K. The Transpassive Dissolution Mechanism of 316L Stainless Steel. *Electrochimica Acta* **2009**, *54* (13), 3645–3650. https://doi.org/10.1016/j.electacta.2009.01.040.

(92) Macdonald, D. D. On the Tenuous Nature of Passivity and Its Role in the Isolation of HLNW. *J. Nucl. Mater.* **2008**, *379* (1–3), 24–32. https://doi.org/10.1016/j.jnucmat.2008.06.004.

(93) Macdonald, D. D. On the Existence of Our Metals-Based Civilization I. Phase-Space Analysis. *J. Electrochem. Soc.* **2006**, *153* (7), B213–B224. https://doi.org/10.1149/1.2195877.

(94) Zhang, L.; Macdonald, D. D. On the Transport of Point Defects in Passive ®lms. 13.

(95) Laycock, N. J.; Newman, R. C.; Stewart, J. The Transpassive Corrosion of Stainless Steel in Stabilized Alkaline Peroxide Solution. *Corros. Sci.* **1995**, *37* (10), 1637–1642. https://doi.org/10.1016/0010-938X(95)00113-X.

(96) Sankaran, K. K.; Mishra, R. S. Chapter 4 - Aluminum Alloys. In *Metallurgy and Design of Alloys with Hierarchical Microstructures*; Sankaran, K. K., Mishra, R. S., Eds.; Elsevier, 2017; pp 57–176. https://doi.org/10.1016/B978-0-12-812068-2.00004-7.

(97) Novotny, R.; Hähner, P.; Siegl, J.; Haušild, P.; Ripplinger, S.; Penttilä, S.; Toivonen, A. Stress Corrosion Cracking Susceptibility of Austenitic Stainless Steels in Supercritical Water Conditions. *J. Nucl. Mater.* **2011**, *409* (2), 117–123. https://doi.org/10.1016/j.jnucmat.2010.09.018.

(98) Teysseyre, S.; Was, G. S. Stress Corrosion Cracking of Austenitic Alloys in Supercritical Water. *CORROSION* **2006**, *62* (12), 1100–1116. https://doi.org/10.5006/1.3278244.

(99) Tan, L.; Sridharan, K.; Allen, T. R.; Nanstad, R. K.; McClintock, D. A. Microstructure Tailoring for Property Improvements by Grain Boundary Engineering. *J. Nucl. Mater.* **2008**, *374* (1), 270–280. https://doi.org/10.1016/j.jnucmat.2007.08.015.

(100) Edavan, R. P.; Kopinski, R. Corrosion Resistance of Painted Zinc Alloy Coated Steels. *Corros. Sci.* **2009**, *51* (10), 2429–2442. https://doi.org/10.1016/j.corsci.2009.06.028.

(101) Townsend, H. E.; Borzillo, A. R. Thirty Year Atmospheric Corrosion Performance of 55% Aluminum-Zinc Alloy-Coated Sheet Steel. *Mater. Perform.* **1996**, *35* (4).

(102) Kar, P. Chapter 8 - Anticorrosion and Antiwear. In *Nanomaterials-Based Coatings*; Nguyen Tri, P., Rtimi, S., Ouellet Plamondon, C. M., Eds.; Micro and Nano Technologies; Elsevier, 2019; pp 195–236. https://doi.org/10.1016/B978-0-12-815884-5.00008-9.

(103) Lacroix, J.-C.; Camalet, J.-L.; Aeiyach, S.; Chane-Ching, K. I.; Petitjean, J.; Chauveau, E.; Lacaze, P.-C. Aniline Electropolymerization on Mild Steel and Zinc in a Two-Step Process. *J. Electroanal. Chem.* **2000**, *481* (1), 76–81. https://doi.org/10.1016/S0022-0728(99)00490-8.

(104) Kinlen, P. J.; Menon, V.; Ding, Y. A Mechanistic Investigation of Polyaniline Corrosion Protection Using the Scanning Reference Electrode Technique. *J. Electrochem. Soc.* **1999**, *146* (10), 3690. https://doi.org/10.1149/1.1392535.

(105) Kinlen, P. J.; Ding, Y.; Silverman, D. C. Corrosion Protection of Mild Steel Using Sulfonic and Phosphonic Acid-Doped Polyanilines. *CORROSION* **2002**, *58* (6), 490–497. https://doi.org/10.5006/1.3277639.

(106) de Souza, F. S.; Spinelli, A. Caffeic Acid as a Green Corrosion Inhibitor for Mild Steel. *Corros. Sci.* **2009**, *51* (3), 642–649. https://doi.org/10.1016/j.corsci.2008.12.013.

(107) Elayyachy, M.; El Idrissi, A.; Hammouti, B. New Thio-Compounds as Corrosion Inhibitor for Steel in 1M HCl. *Corros. Sci.* **2006**, *48* (9), 2470–2479. https://doi.org/10.1016/j.corsci.2005.09.016.

(108) Obot, I. B.; Obi-Egbedi, N. O.; Umoren, S. A. Antifungal Drugs as Corrosion Inhibitors for Aluminium in 0.1M HCl. *Corros. Sci.* **2009**, *51* (8), 1868–1875. https://doi.org/10.1016/j.corsci.2009.05.017.

(109) Cao, C. N.; Zhou, S. Q. Adsorption of Aliphatic Amines on Iron Surface Form Acidic Solutions. *Key Eng. Mater.* **1991**, *20–28*, 2777–2785. https://doi.org/10.4028/www.scientific.net/KEM.20-28.2777.

(110) McCafferty, E.; Bernett, M. K.; Murday, J. S. An XPS Study of Passive Film Formation on Iron in Chromate Solutions. *Corros. Sci.* **1988**, *28* (6), 559–576. https://doi.org/10.1016/0010-938X(88)90024-8.

(111) Bastidas, D. M.; Criado, M.; La Iglesia, V. M.; Fajardo, S.; La Iglesia, A.; Bastidas, J. M. Comparative Study of Three Sodium Phosphates as Corrosion Inhibitors for Steel Reinforcements. *Cem. Concr. Compos.* **2013**, *43*, 31–38. https://doi.org/10.1016/j.cemconcomp.2013.06.005.

(112) Rafferty, J. P. *Minerals (Geology: Landforms, Minerals, and Rocks)*; Britannica Educational Publishing, 2011.

(113) Earle, S. Chapter 2.4 - Silicate Minerals. In *Physical Geology*; BCcampus, 2015.

(114) Earle, S. Chapter 2.3 - Mineral Groups. In *Physical Geology*; BCcampus, 2015.

(115) Iron and Steel Statistics and Information https://www.usgs.gov/centers/nmic/iron-and-steel-statistics-and-information?qt-science_support_page_related_con=0#qt-science_support_page_related_con (accessed Jul 16, 2020).

(116) Netinger Grubeša, I.; Barišić, I.; Fucic, A.; Bansode, S. S. 2 - Ferrous Slag: Characteristics and Properties. In *Characteristics and Uses of Steel Slag in Building Construction*; Netinger Grubeša, I., Barišić, I., Fucic, A., Bansode, S. S., Eds.; Woodhead Publishing, 2016; pp 15–30. https://doi.org/10.1016/B978-0-08-100368-8.00002-6.

(117) Piatak, N. M.; Parsons, M. B.; Seal, R. R. Characteristics and Environmental Aspects of Slag: A Review. *Appl. Geochem.* **2015**, *57*, 236–266. https://doi.org/10.1016/j.apgeochem.2014.04.009.

(118) Mombelli, D.; Mapelli, C.; Barella, S.; Di Cecca, C.; Le Saout, G.; Garcia-Diaz, E. The Effect of Microstructure on the Leaching Behaviour of Electric Arc Furnace (EAF) Carbon Steel Slag. *Process Saf. Environ. Prot.* **2016**, *102*, 810–821. https://doi.org/10.1016/j.psep.2016.05.027.

(119) Rosales, J.; Agrela, F.; Entrenas, J. A.; Cabrera, M. Potential of Stainless Steel Slag Waste in Manufacturing Self-Compacting Concrete. *Materials* **2020**, *13* (9). https://doi.org/10.3390/ma13092049.

(120) Kumar, S. S.; Kumar, A.; Singh, S.; Malyan, S. K.; Baram, S.; Sharma, J.; Singh, R.; Pugazhendhi, A. Industrial Wastes: Fly Ash, Steel Slag and Phosphogypsum- Potential Candidates to Mitigate Greenhouse Gas Emissions from Paddy Fields. *Chemosphere* **2020**, *241*, 124824. https://doi.org/10.1016/j.chemosphere.2019.124824.

(121) C09 Committee. *Specification for Coal Fly Ash and Raw or Calcined Natural Pozzolan for Use in Concrete*; ASTM International. https://doi.org/10.1520/C0618-19.

(122) Yao, Z. T.; Ji, X. S.; Sarker, P. K.; Tang, J. H.; Ge, L. Q.; Xia, M. S.; Xi, Y. Q. A Comprehensive Review on the Applications of Coal Fly Ash. *Earth-Sci. Rev.* **2015**, *141*, 105–121. https://doi.org/10.1016/j.earscirev.2014.11.016.

(123) Ram, L. C.; Srivastava, N. K.; Tripathi, R. C.; Jha, S. K.; Sinha, A. K.; Singh, G.; Manoharan, V. Management of Mine Spoil for Crop Productivity with Lignite Fly Ash and Biological Amendments. *J. Environ. Manage.* **2006**, *79* (2), 173–187. https://doi.org/10.1016/j.jenvman.2005.06.008.

(124) Nath, P.; Sarker, P. Effect of Fly Ash on the Durability Properties of High Strength Concrete. *Procedia Eng.* **2011**, *14*, 1149–1156. https://doi.org/10.1016/j.proeng.2011.07.144.

(125) Erol, M.; Küçükbayrak, S.; Ersoy-Meriçboyu, A. Characterization of Sintered Coal Fly Ashes. *Fuel* **2008**, *87* (7), 1334–1340. https://doi.org/10.1016/j.fuel.2007.07.002.

(126) Jain, D.; Khatri, C.; Rani, A. Fly Ash Supported Calcium Oxide as Recyclable Solid Base Catalyst for Knoevenagel Condensation Reaction. *Fuel Process. Technol.* **2010**, *91* (9), 1015–1021. https://doi.org/10.1016/j.fuproc.2010.02.021.

(127) Panday, K. K.; Prasad, G.; Singh, V. N. Copper(II) Removal from Aqueous Solutions by Fly Ash. *Water Res.* **1985**, *19* (7), 869–873. https://doi.org/10.1016/0043-1354(85)90145-9.

(128) Murayama, N.; Yamamoto, H.; Shibata, J. Mechanism of Zeolite Synthesis from Coal Fly Ash by Alkali Hydrothermal Reaction. *Int. J. Miner. Process.* **2002**, *64* (1), 1–17. https://doi.org/10.1016/S0301-7516(01)00046-1.

(129) Font, O.; Querol, X.; López-Soler, A.; Chimenos, J. M.; Fernández, A. I.; Burgos, S.; García Peña, F. Ge Extraction from Gasification Fly Ash. *Fuel* **2005**, *84* (11), 1384–1392. https://doi.org/10.1016/j.fuel.2004.06.041.

(130) Brantley, S. L. Kinetics of Mineral Dissolution. In *Kinetics of Water-Rock Interaction*; Springer, New York, NY, 2008; pp 151–210. https://doi.org/10.1007/978-0-387-73563-4_5.

(131) Arvidson, R. S.; Ertan, I. E.; Amonette, J. E.; Luttge, A. Variation in Calcite Dissolution Rates:: A Fundamental Problem? *Geochim. Cosmochim. Acta* **2003**, *67* (9), 1623–1634. https://doi.org/10.1016/S0016-7037(02)01177-8.

(132) Hamilton, J. P.; Brantley, S. L.; Pantano, C. G.; Criscenti, L. J.; Kubicki, J. D. Dissolution of Nepheline, Jadeite and Albite Glasses: Toward Better Models for Aluminosilicate Dissolution. *Geochim. Cosmochim. Acta* **2001**, *65* (21), 3683–3702. https://doi.org/10.1016/S0016-7037(01)00724-4.

(133) Luce, R. W.; Bartlett, R. W.; Parks, G. A. Dissolution Kinetics of Magnesium Silicates. *Geochim. Cosmochim. Acta* **1972**, *36* (1), 35–50. https://doi.org/10.1016/0016-7037(72)90119-6.

(134) Paces, T. Steady-State Kinetics and Equilibrium between Ground Water and Granitic Rock. *Geochim. Cosmochim. Acta* **1973**, *37* (12), 2641–2663. https://doi.org/10.1016/0016-7037(73)90270-6.

(135) Holdren, G. R.; Berner, R. A. Mechanism of Feldspar Weathering—I. Experimental Studies. *Geochim. Cosmochim. Acta* **1979**, *43* (8), 1161–1171. https://doi.org/10.1016/0016-7037(79)90109-1.

(136) Brantley, S. L.; Conrad, C. F. Analysis of Rates of Geochemical Reactions. In *Kinetics of Water-Rock Interaction*; Brantley, S. L., Kubicki, J. D., White, A. F., Eds.; Springer: New York, NY, 2008; pp 1–37. https://doi.org/10.1007/978-0-387-73563-4_1.

(137) Chen, Y.; Brantley, S. L. Temperature- and PH-Dependence of Albite Dissolution Rate at Acid PH. *Chem. Geol.* **1997**, *135* (3), 275–290. https://doi.org/10.1016/S0009-2541(96)00126-X.

(138) Hsiao, Y.-H. Studies on Irradiation and Electric Potential Effects toward Mineral Atomic Structure and Chemical Reactivity, UCLA, 2019.

(139) Rosso, J. J.; Rimstidt, J. D. A High Resolution Study of Forsterite Dissolution Rates. *Geochim. Cosmochim. Acta* **2000**, *64* (5), 797–811. https://doi.org/10.1016/S0016-7037(99)00354-3.

(140) Plummer, L. N.; Wigley, T. M. L.; Parkhurst, D. L. The Kinetics of Calcite Dissolution in CO2 -Water Systems at 5 Degrees to 60 Degrees C and 0.0 to 1.0 Atm CO 2. *Am. J. Sci.* **1978**, *278* (2), 179–216. https://doi.org/10.2475/ajs.278.2.179.

(141) Alkattan, M.; Oelkers, E. H.; Dandurand, J.-L.; Schott, J. An Experimental Study of Calcite and Limestone Dissolution Rates as a Function of PH from Y1 to 3 and Temperature from 25 to 808C. **1998**, 16.

(142) Bibi, I.; Arvidson, R. S.; Fischer, C.; Lüttge, A. Temporal Evolution of Calcite Surface Dissolution Kinetics. *Minerals* **2018**, *8* (6), 256. https://doi.org/10.3390/min8060256.

(143) Busenberg, E. *A Comparative Study of the Dissolution and Crystal Growth Kinetics of Calcite and Aragonite*; U.S. Department of the Interior, Geological Survey; Washington, D.C., 1949.

(144) Zhang, S.; Yang, L.; DePaolo, D. J.; Steefel, C. I. Chemical Affinity and PH Effects on Chlorite Dissolution Kinetics under Geological CO2 Sequestration Related Conditions. *Chem. Geol.* **2015**, *396*, 208–217. https://doi.org/10.1016/j.chemgeo.2015.01.001.

(145) Lasaga, A. C.; Luttge, A. Variation of Crystal Dissolution Rate Based on a Dissolution Stepwave Model. *Science* **2001**, *291* (5512), 2400–2404. https://doi.org/10.1126/science.1058173.

(146) Ganguly, J. Lasaga, A. C. 1998. Kinetic Theory in the Earth Sciences. Princeton Series in Geochemistry.X+811 Pp. Princeton, Chichester: Princeton University Press. Price £65.00 (Hard Covers). ISBN 0 691 03748 5. *Geol. Mag.* **2000**, *137* (5), 594–595.

(147) Helgeson, H. C.; Murphy, W. M.; Aagaard, P. Thermodynamic and Kinetic Constraints on Reaction Rates among Minerals and Aqueous Solutions. II. Rate Constants, Effective Surface Area, and the Hydrolysis of Feldspar. *Geochim. Cosmochim. Acta* **1984**, *48* (12), 2405–2432. https://doi.org/10.1016/0016-7037(84)90294-1.

(148) Frank, F. C. Capillary Equilibria of Dislocated Crystals. *Acta Crystallogr.* **1951**, *4* (6), 497–501. https://doi.org/10.1107/S0365110X51001690.

(149) Cabrera, N.; Levine, M. M.; Plaskett, J. S. Hollow Dislocations and Etch Pits. *Phys. Rev.* **1954**, *96* (4), 1153–1153. https://doi.org/10.1103/PhysRev.96.1153.

(150) Maclnnis, lan N.; Brantley, S. L. The Role of Dislocations and Surface Morphology in Calcite Dissolution. *Geochim. Cosmochim. Acta* **1992**, *56* (3), 1113–1126. https://doi.org/10.1016/0016-7037(92)90049-O.

(151) Burton, W. K.; Cabrera, N.; Frank, F. C.; Mott, N. F. The Growth of Crystals and the Equilibrium Structure of Their Surfaces. *Philos. Trans. R. Soc. Lond. Ser. Math. Phys. Sci.* **1951**, *243* (866), 299–358. https://doi.org/10.1098/rsta.1951.0006.

(152) Cabrera, N.; Levine, M. M. On the Dislocation Theory of Evaporation of Crystals. *Philos. Mag.* **1956**, *1*, 450–458. https://doi.org/10.1080/14786435608238124.

(153) Luettge, A. An Interferometric Study of the Dissolution Kinetics of Anorthite; the Role of Reactive Surface Area. *Am. J. Sci.* **1999**, *299* (7–9), 652–678. https://doi.org/10.2475/ajs.299.7-9.652.

(154) Shahidian, A.; Afshar, H.; Habibi, M. R.; Ghassemi, M. Chapter 1 - Therapeutic Nanostructures: Application of Mechanical Engineering in Drug Delivery. In *Nanoarchitectonics for Smart Delivery and Drug Targeting*; Holban, A. M., Grumezescu, A. M., Eds.; William Andrew Publishing, 2016; pp 3–34. https://doi.org/10.1016/B978-0-323-47347-7.00001-X.

(155) Bargoshadi, J. A.; Najafiaghdam, E. Ultrasonic Dispersion System Design and Optimization Using Multiple Transducers. In *2009 Symposium on Piezoelectricity, Acoustic Waves, and Device Applications (SPAWDA 2009)*; 2009; pp 96–96. https://doi.org/10.1109/SPAWDA.2009.5428876.

(156) Belova, V.; Krasowska, M.; Wang, D.; Ralston, J.; G. Shchukin, D.; Möhwald, H. Influence of Adsorbed Gas at Liquid/Solid Interfaces on Heterogeneous Cavitation. *Chem. Sci.* **2013**, *4* (1), 248–256. https://doi.org/10.1039/C2SC21321D.

(157) Suslick, K. S.; McNamara, W. B.; Didenko, Y. Hot Spot Conditions during Multi-Bubble Cavitation. In *Sonochemistry and Sonoluminescence*; Crum, L. A., Mason, T. J., Reisse, J. L., Suslick, K. S., Eds.; NATO ASI Series; Springer Netherlands: Dordrecht, 1999; pp 191–204. https://doi.org/10.1007/978-94-015-9215-4_16.

(158) Suslick, K. S.; Price, G. J. Applications of Ultrasound to Materials Chemistry. *Annu. Rev. Mater. Sci.* **1999**, *29* (1), 295–326. https://doi.org/10.1146/annurev.matsci.29.1.295.

(159) Suslick, K. S.; Flannigan, D. J. Inside a Collapsing Bubble: Sonoluminescence and the Conditions During Cavitation. *Annu. Rev. Phys. Chem.* **2008**, *59* (1), 659–683. https://doi.org/10.1146/annurev.physchem.59.032607.093739.

(160) Brenner, M. P.; Hilgenfeldt, S.; Lohse, D. Single-Bubble Sonoluminescence. *Rev. Mod. Phys.* **2002**, *74* (2), 425–484. https://doi.org/10.1103/RevModPhys.74.425.

(161) Putterman, S. J.; Weninger, K. R. Sonoluminescence: How Bubbles Turn Sound into Light. *Annu. Rev. Fluid Mech.* **2000**, *32* (1), 445–476. https://doi.org/10.1146/annurev.fluid.32.1.445.

(162) Basedow, A. M.; Ebert, K. H. Ultrasonic Degradation of Polymers in Solution. In *Physical Chemistry*; Advances in Polymer Science; Springer: Berlin, Heidelberg, 1977; pp 83–148. https://doi.org/10.1007/3-540-07942-4_6.

(163) Marmottant, P.; Versluis, M.; de Jong, N.; Hilgenfeldt, S.; Lohse, D. High-Speed Imaging of an Ultrasound-Driven Bubble in Contact with a Wall: "Narcissus" Effect and Resolved Acoustic Streaming. *Exp. Fluids* **2006**, *41* (2), 147–153. https://doi.org/10.1007/s00348-005-0080-y.

(164) Blake, J. R.; Ohl, C.; Kurz, T.; Geisler, R.; Lindau, O.; Lauterborn, W. Bubble Dynamics, Shock Waves and Sonoluminescence. *Philos. Trans. R. Soc. Lond. Ser. Math. Phys. Eng. Sci.* **1999**, *357* (1751), 269–294. https://doi.org/10.1098/rsta.1999.0327.

(165) Ohl, C.-D.; Arora, M.; Ikink, R.; de Jong, N.; Versluis, M.; Delius, M.; Lohse, D. Sonoporation from Jetting Cavitation Bubbles. *Biophys. J.* **2006**, *91* (11), 4285–4295. https://doi.org/10.1529/biophysj.105.075366.

(166) González-García, J.; Sáez, V.; Tudela, I.; Díez-Garcia, M. I.; Deseada Esclapez, M.; Louisnard, O. Sonochemical Treatment of Water Polluted by Chlorinated Organocompounds. A Review. *Water* **2010**, *2* (1), 28–74. https://doi.org/10.3390/w2010028.

(167) Lifka, J.; Ondruschka, B.; Hofmann, J. The Use of Ultrasound for the Degradation of Pollutants in Water: Aquasonolysis – A Review. *Eng. Life Sci.* **2003**, *3* (6), 253–262. https://doi.org/10.1002/elsc.200390040.

(168) Li, H.; Li, S.; Peng, J.; Srinivasakannan, C.; Zhang, L.; Yin, S. Ultrasound Augmented Leaching of Nickel Sulfate in Sulfuric Acid and Hydrogen Peroxide Media. *Ultrason. Sonochem.* **2018**, *40*, 1021–1030. https://doi.org/10.1016/j.ultsonch.2017.08.031.

(169) Wang, R. Influence of Ultrasound on Pitting Corrosion and Crevice Corrosion of SUS304 Stainless Steel in Chloride Sodium Aqueous Solution. *Corros. Sci.* **2008**, *50* (2), 325–328. https://doi.org/10.1016/j.corsci.2007.11.001.

(170) Suslick, K. S.; Casadonte, D. J.; Green, M. L. H.; Thompson, M. E. Effects of High Intensity Ultrasound on Inorganic Solids. *Ultrasonics* **1987**, *25* (1), 56–59. https://doi.org/10.1016/0041-624X(87)90013-8.

(171) Raman, V.; Abbas, A. Experimental Investigations on Ultrasound Mediated Particle Breakage. *Ultrason. Sonochem.* **2008**, *15* (1), 55–64. https://doi.org/10.1016/j.ultsonch.2006.11.009.

(172) Kusters, K. A.; Pratsinis, S. E.; Thoma, S. G.; Smith, D. M. Ultrasonic Fragmentation of Agglomerate Powders. *Chem. Eng. Sci.* **1993**, *48* (24), 4119–4127. https://doi.org/10.1016/0009-2509(93)80258-R.

(173) Kumar, A.; Reed, J.; Sant, G. Vertical Scanning Interferometry: A New Method to Measure the Dissolution Dynamics of Cementitious Minerals. *J. Am. Ceram. Soc.* **2013**, *96* (9), 2766–2778. https://doi.org/10.1111/jace.12482.

(174) Hariharan, P.; Hariharan, P. Chapter 3 - Two-Beam Interferometers. In *Basics of Interferometry (Second Edition)*; Hariharan, P., Hariharan, P., Eds.; Academic Press: Burlington, 2007; pp 13–22. https://doi.org/10.1016/B978-012373589-8/50005-5.

(175) Interferometry. *Wikipedia*; 2020.

(176) Wyant, J. C. White Light Interferometry. In *Holography: A Tribute to Yuri Denisyuk and Emmett Leith*; International Society for Optics and Photonics, 2002; Vol. 4737, pp 98–107. https://doi.org/10.1117/12.474947.

(177) Akcay, C.; Parrein, P.; Rolland, J. P. Estimation of Longitudinal Resolution in Optical Coherence Imaging. *Appl. Opt.* **2002**, *41* (25), 5256. https://doi.org/10.1364/AO.41.005256.

(178) Dandridge, A. Zero Path-Length Difference in Fiber-Optic Interferometers. *J. Light. Technol.* **1983**, *1* (3), 514–516. https://doi.org/10.1109/JLT.1983.1072134.

(179) Petzing, J.; Coupland, J.; Leach, R. K. The measurement of rough surface topography using coherence scanning interferometry. http://eprintspublications.npl.co.uk/4833/ (accessed Jun 22, 2020).

(180) Downs, J. Formate Brines: Novel Drilling and Completion Fluids for Demanding Environments. *SPE Repr. Ser.* **1993**. https://doi.org/10.2118/25177-MS.

(181) Kadhim, F. S. *Investigation of Carbon Steel Corrosion in Water Base Drilling Mud*.

(182) Liu, Y.; Xu, L.; Lu, M.; Meng, Y.; Zhu, J.; Zhang, L. Corrosion Mechanism of 13Cr Stainless Steel in Completion Fluid of High Temperature and High Concentration Bromine Salt. *Appl. Surf. Sci.* **2014**, *314*, 768–776. https://doi.org/10.1016/j.apsusc.2014.07.067.

(183) Liu, Y.; Xu, L. N.; Zhu, J. Y.; Meng, Y. Pitting Corrosion of 13Cr Steel in Aerated Brine Completion Fluids. *Mater. Corros.* **2014**, *65* (11), 1096–1102. https://doi.org/10.1002/maco.201307489.

(184) Kaneko, M.; Isaacs, H. S. Pitting of Stainless Steel in Bromide, Chloride and Bromide/Chloride Solutions. *Corros. Sci.* **2000**, *42* (1), 67–78. https://doi.org/10.1016/S0010-938X(99)00056-6.

(185) Pinkus, P.; Eliezer, D.; Itzhak, D. The Influence of Alkali-Halide Additions on the Stress Corrosion Cracking of an Austenitic Stainless Steel in MgCl2 Solution. *Corros. Sci.* **1981**, *21* (6), 417–423. https://doi.org/10.1016/0010-938X(81)90040-8.

(186) Tanno, K.; Itoh, M.; Takahashi, T.; Yashiro, H.; Kumagai, N. The Corrosion of Carbon Steel in Lithium Bromide Solution at Moderate Temperatures. *Corros. Sci.* **1993**, *34* (9), 1441–1451. https://doi.org/10.1016/0010-938X(93)90239-D.

(187) Królikowski, A.; Kuziak, J. Impedance Study on Calcium Nitrite as a Penetrating Corrosion Inhibitor for Steel in Concrete. *Electrochimica Acta* **2011**, *56* (23), 7845–7853. https://doi.org/10.1016/j.electacta.2011.01.069.

(188) Justnes, H. Calcium Nitrate as Corrosion Inhibitor for Reinforced Concrete. *Innov. Dev. Concr. Mater. Constr. Thomas Telford Publ.* **2002**, 391–401.

(189) Ngala, V. T.; Page, C. L.; Page, M. M. Corrosion Inhibitor Systems for Remedial Treatment of Reinforced Concrete. Part 1: Calcium Nitrite. *Corros. Sci.* **2002**, *44* (9), 2073–2087. https://doi.org/10.1016/S0010-938X(02)00012-4.

(190) Gaidis, J. M. Chemistry of Corrosion Inhibitors. *Cem. Concr. Compos.* **2004**, *26* (3), 181–189. https://doi.org/10.1016/S0958-9465(03)00037-4.

(191) Dhouibi, L.; Triki, E.; Raharinaivo, A. The Application of Electrochemical Impedance Spectroscopy to Determine the Long-Term Effectiveness of Corrosion Inhibitors for Steel in Concrete. *Cem. Concr. Compos.* **2002**, *24* (1), 35–43. https://doi.org/10.1016/S0958-9465(01)00062-2.

(192) Al-Amoudi, O. S. B.; Maslehuddin, M.; Lashari, A. N.; Almusallam, A. A. Effectiveness of Corrosion Inhibitors in Contaminated Concrete. *Cem. Concr. Compos.* **2003**, *25* (4), 439–449. https://doi.org/10.1016/S0958-9465(02)00084-7.

(193) Davis, K. J.; Lüttge, A. Quantifying the Relationship between Microbial Attachment and Mineral Surface Dynamics Using Vertical Scanning Interferometry (VSI). *Am. J. Sci.* **2005**, *305* (6–8), 727–751. https://doi.org/10.2475/ajs.305.6-8.727.

(194) Waters, M. S.; El-Naggar, M. Y.; Hsu, L.; Sturm, C. A.; Luttge, A.; Udwadia, F. E.; Cvitkovitch, D. G.; Goodman, S. D.; Nealson, K. H. Simultaneous Interferometric Measurement of Corrosive or Demineralizing Bacteria and Their Mineral Interfaces. *Appl. Environ. Microbiol.* **2009**, *75* (5), 1445–1449. https://doi.org/10.1128/AEM.02039-08.

(195) Rigg, T.; Rahaman, M. S. Dissolution of Ferritic Stainless Steel Scrap in Hydrochloric Acid. *Can. J. Chem. Eng.* **1971**, *49* (4), 550–551. https://doi.org/10.1002/cjce.5450490422.

(196) Lister, D. H.; Davidson, R. D.; McAlpine, E. The Mechanism and Kinetics of Corrosion Product Release from Stainless Steel in Lithiated High Temperature Water. *Corros. Sci.* **1987**, *27* (2), 113–140. https://doi.org/10.1016/0010-938X(87)90068-0.

(197) Chao, C. Y.; Lin, L. F.; Macdonald, D. D. A Point Defect Model for Anodic Passive Films I . Film Growth Kinetics. *J. Electrochem. Soc.* **1981**, *128* (6), 1187–1194. https://doi.org/10.1149/1.2127591.

(198) Sánchez, J.; Fullea, J.; Andrade, C.; Gaitero, J. J.; Porro, A. AFM Study of the Early Corrosion of a High Strength Steel in a Diluted Sodium Chloride Solution. *Corros. Sci.* **2008**, *50* (7), 1820–1824. https://doi.org/10.1016/j.corsci.2008.03.013.

(199) Sekine, I.; Hayakawa, T.; Negishi, T.; Yuasa, M. Analysis for Corrosion Behavior of Mild Steels in Various Hydroxy Acid Solutions by New Methods of Surface Analyses and Electrochemical Measurements. *J. Electrochem. Soc.* **1990**, *137* (10), 3029–3033. https://doi.org/10.1149/1.2086153.

(200) Li, J. L.; Ma, H. X.; Zhu, S. D.; Qu, C. T.; Yin, Z. F. Erosion Resistance of CO2 Corrosion Scales Formed on API P110 Carbon Steel. *Corros. Sci.* **2014**, *86*, 101–107. https://doi.org/10.1016/j.corsci.2014.04.051.

(201) Zhu, S. D.; Wei, J. F.; Bai, Z. Q.; Zhou, G. S.; Miao, J.; Cai, R. Failure Analysis of P110 Tubing String in the Ultra-Deep Oil Well. *Eng. Fail. Anal.* **2011**, *18* (3), 950–962. https://doi.org/10.1016/j.engfailanal.2010.11.013.

(202) Streicher, M. A. Pitting Corrosion of 18Cr-8Ni Stainless Steel. *J. Electrochem. Soc.* **1956**, *103* (7), 375–390. https://doi.org/10.1149/1.2430359.

(203) Marcus, P.; Maurice, V.; Strehblow, H.-H. Localized Corrosion (Pitting): A Model of Passivity Breakdown Including the Role of the Oxide Layer Nanostructure. *Corros. Sci.* **2008**, *50* (9), 2698–2704. https://doi.org/10.1016/j.corsci.2008.06.047.

(204) Nilsson, J. O.; Wilson, A. Influence of Isothermal Phase Transformations on Toughness and Pitting Corrosion of Super Duplex Stainless Steel SAF 2507. *Mater. Sci. Technol.* **1993**, *9* (7), 545–554. https://doi.org/10.1179/mst.1993.9.7.545.

(205) Szklarska-Smialowska, Z.; Janik-Czachor, M. Pitting Corrosion of 13Cr-Fe Alloy in Na2SO4 Solutions Containing Chloride Ions. *Corros. Sci.* **1967**, *7* (2), 65–72. https://doi.org/10.1016/S0010-938X(67)80103-3.

(206) Tsutsumi, Y.; Nishikata, A.; Tsuru, T. Pitting Corrosion Mechanism of Type 304 Stainless Steel under a Droplet of Chloride Solutions. *Corros. Sci.* **2007**, *49* (3), 1394–1407. https://doi.org/10.1016/j.corsci.2006.08.016.

(207) Park, J. O.; Böhni, H. Local PH Measurements during Pitting Corrosion at MnS Inclusions on Stainless Steel. *Electrochem. Solid-State Lett.* **2000**, *3* (9), 416–417. https://doi.org/10.1149/1.1391164.

(208) Fregonese, M.; Idrissi, H.; Mazille, H.; Renaud, L.; Cetre, Y. Initiation and Propagation Steps in Pitting Corrosion of Austenitic Stainless Steels: Monitoring by Acoustic Emission. *Corros. Sci.* **2001**, *43* (4), 627–641. https://doi.org/10.1016/S0010-938X(00)00099-8.

(209) Williams, D. E.; Newman, R. C.; Song, Q.; Kelly, R. G. Passivity Breakdown and Pitting Corrosion of Binary Alloys. *Nature* **1991**, *350* (6315), 216–219. https://doi.org/10.1038/350216a0.

(210) Mankowski, J.; Szklarska-Smialowska, Z. Studies on Accumulation of Chloride Ions in Pits Growing during Anodic Polarization. *Corros. Sci.* **1975**, *15* (6), 493–501. https://doi.org/10.1016/0010-938X(75)90015-3.

(211) Walton, J. C. Mathematical Modeling of Mass Transport and Chemical Reaction in Crevice and Pitting Corrosion. *Corros. Sci.* **1990**, *30* (8), 915–928. https://doi.org/10.1016/0010-938X(90)90013-U.

(212) Ernst, P.; Newman, R. C. Pit Growth Studies in Stainless Steel Foils. I. Introduction and Pit Growth Kinetics. *Corros. Sci.* **2002**, *44* (5), 927–941. https://doi.org/10.1016/S0010-938X(01)00133-0.

(213) Guo, P.; La Plante, E. C.; Wang, B.; Chen, X.; Balonis, M.; Bauchy, M.; Sant, G. Direct Observation of Pitting Corrosion Evolutions on Carbon Steel Surfaces at the Nano-to-Micro- Scales. *Sci. Rep.* **2018**, *8* (1), 7990. https://doi.org/10.1038/s41598-018-26340-5.

(214) Merola, C.; Cheng, H.-W.; Schwenzfeier, K.; Kristiansen, K.; Chen, Y.-J.; Dobbs, H. A.; Israelachvili, J. N.; Valtiner, M. In Situ Nano- to Microscopic Imaging and Growth Mechanism of Electrochemical Dissolution (e.g., Corrosion) of a Confined Metal Surface. *Proc. Natl. Acad. Sci.* **2017**, *114* (36), 9541–9546. https://doi.org/10.1073/pnas.1708205114.

(215) Chen, X.; Ebert, W. L.; Indacochea, J. E. Electrochemical Corrosion of a Noble Metal-Bearing Alloy-Oxide Composite. *Corros. Sci.* **2017**, *124*, 10–24. https://doi.org/10.1016/j.corsci.2017.04.010.

(216) Hill, D. Diffusion Coefficients of Nitrate, Chloride, Sulphate and Water in Cracked and Uncracked Chalk. *J. Soil Sci.* **1984**, *35* (1), 27–33. https://doi.org/10.1111/j.1365-2389.1984.tb00256.x.

(217) Hilca, B. R.; Triyono. The Effect of Inhibitor Sodium Nitrate on Pitting Corrosion of Dissimilar Material Weldment Joint of Stainless Steel AISI 304 and Mild Steel SS 400. *AIP Conf. Proc.* **2016**, *1717* (1), 040009. https://doi.org/10.1063/1.4943452.

(218) Kalkar, C. D.; Doshi, S. V. Effect of Nitrate Ions on the Oxidation of Iodide Ions during the Dissolution of γ-Irradiated NaCl in Aqueous Binary Mixture of Iodide and Nitrate. *J. Radioanal. Nucl. Chem.* **1988**, *127* (3), 161–167. https://doi.org/10.1007/BF02164861.

(219) Giron, R. G. P.; Chen, X.; La Plante, E. C.; Gussev, M. N.; Leonard, K. J.; Sant, G. Revealing How Alkali Cations Affect the Surface Reactivity of Stainless Steel in Alkaline Aqueous Environments. *ACS Omega* **2018**, *3* (11), 14680–14688. https://doi.org/10.1021/acsomega.8b02227.

(220) Shen, Z.; Du, D.; Zhang, L.; Lozano-Perez, S. An Insight into PWR Primary Water SCC Mechanisms by Comparing Surface and Crack Oxidation. *Corros. Sci.* **2019**, *148*, 213–227. https://doi.org/10.1016/j.corsci.2018.12.020.

(221) Deformation and Fracture Mechanics of Engineering Materials, 5th Edition | Wiley https://www.wiley.com/en-us/Deformation+and+Fracture+Mechanics+of+Engineering+Materials%2C+5th+Edition-p-9780470527801 (accessed May 28, 2020).

(222) King, A.; Johnson, G.; Engelberg, D.; Ludwig, W.; Marrow, J. Observations of Intergranular Stress Corrosion Cracking in a Grain-Mapped Polycrystal. *Science* **2008**, *321* (5887), 382–385. https://doi.org/10.1126/science.1156211.

(223) Shimada, M.; Kokawa, H.; Wang, Z. J.; Sato, Y. S.; Karibe, I. Optimization of Grain Boundary Character Distribution for Intergranular Corrosion Resistant 304 Stainless Steel by Twin-Induced Grain Boundary Engineering. *Acta Mater.* **2002**, *50* (9), 2331–2341. https://doi.org/10.1016/S1359-6454(02)00064-2.

(224) Kuang, W.; Was, G. S. The Effect of Grain Boundary Structure on the Intergranular Degradation Behavior of Solution Annealed Alloy 690 in High Temperature, Hydrogenated Water. *Acta Mater.* **2020**, *182*, 120–130. https://doi.org/10.1016/j.actamat.2019.10.041.

(225) Saldi, G. D.; Voltolini, M.; Knauss, K. G. Effects of Surface Orientation, Fluid Chemistry and Mechanical Polishing on the Variability of Dolomite Dissolution Rates. *Geochim. Cosmochim. Acta* **2017**, *206*, 94–111. https://doi.org/10.1016/j.gca.2017.02.007.

(226) Yang, C.; Yu, X.; Heißler, S.; Weidler, P. G.; Nefedov, A.; Wang, Y.; Wöll, C.; Kropp, T.; Paier, J.; Sauer, J. O2 Activation on Ceria Catalysts—The Importance of Substrate Crystallographic Orientation. *Angew. Chem. Int. Ed.* **2017**, *56* (51), 16399–16404. https://doi.org/10.1002/anie.201709199.

(227) Bland, L. G.; Gusieva, K.; Scully, J. R. Effect of Crystallographic Orientation on the Corrosion of Magnesium: Comparison of Film Forming and Bare Crystal Facets Using Electrochemical Impedance and Raman Spectroscopy. *Electrochimica Acta* **2017**, *227*, 136–151. https://doi.org/10.1016/j.electacta.2016.12.107.

(228) Ma, A.; Zhang, L.; Engelberg, D.; Hu, Q.; Guan, S.; Zheng, Y. Understanding Crystallographic Orientation Dependent Dissolution Rates of 90Cu-10Ni Alloy: New Insights Based on AFM/SKPFM Measurements and Coordination Number/Electronic Structure Calculations. *Corros. Sci.* **2020**, *164*, 108320. https://doi.org/10.1016/j.corsci.2019.108320.

(229) Was, G. S.; Teysseyre, S.; Jiao, Z. Corrosion of Austenitic Alloys in Supercritical Water. *CORROSION* **2006**, *62* (11), 989–1005. https://doi.org/10.5006/1.3278237.

(230) Jiao, Z.; Was, G. Oxidation of a Proton-Irradiated 316 Stainless Steel in Simulated BWR NWC Environment. In *Proceedings of the 15th International Conference on Environmental Degradation of Materials in Nuclear Power Systems — Water Reactors*; Busby, J. T., Ilevbare, G., Andresen, P. L., Eds.; Springer International Publishing: Cham, 2016; pp 1329–1338. https://doi.org/10.1007/978-3-319-48760-1_81.

(231) Godinho, J. R. A.; Piazolo, S.; Evins, L. Z. Effect of Surface Orientation on Dissolution Rates and Topography of CaF2. *Geochim. Cosmochim. Acta* **2012**, *86*, 392–403. https://doi.org/10.1016/j.gca.2012.02.032.

(232) Verchère, L.; Aubert, I.; Devos, O. Influence of the Crystallographic Orientation on the Electrochemical Reactivity Measured by Scanning Electrochemical Microscopy on Nickel-Based Alloy 600. *Electrochimica Acta* **2019**, *313*, 292–302. https://doi.org/10.1016/j.electacta.2019.05.026.

(233) Fushimi, K.; Miyamoto, K.; Konno, H. Anisotropic Corrosion of Iron in PH 1 Sulphuric Acid. *Electrochimica Acta* **2010**, *55* (24), 7322–7327. https://doi.org/10.1016/j.electacta.2010.07.044.

(234) Miao, Y.; Mo, K.; Yao, T.; Lian, J.; Fortner, J.; Jamison, L.; Xu, R.; Yacout, A. M. Correlation between Crystallographic Orientation and Surface Faceting in UO2. *J. Nucl. Mater.* **2016**, *478*, 176–184. https://doi.org/10.1016/j.jnucmat.2016.05.044.

(235) Brito, P.; Schuller, É.; Silva, J.; Campos, T. R.; Araújo, C. R. de; Carneiro, J. R. Electrochemical Corrosion Behaviour of (100), (110) and (111) Fe3Al Single Crystals in Sulphuric Acid. *Corros. Sci.* **2017**, *126*, 366–373. https://doi.org/10.1016/j.corsci.2017.05.029.

(236) Wang, S.; Wang, J. Effect of Grain Orientation on the Corrosion Behavior of Polycrystalline Alloy 690. *Corros. Sci.* **2014**, *85*, 183–192. https://doi.org/10.1016/j.corsci.2014.04.014.

(237) Wang, W.; Alfantazi, A. Correlation between Grain Orientation and Surface Dissolution of Niobium. *Appl. Surf. Sci.* **2015**, *335*, 223–226. https://doi.org/10.1016/j.apsusc.2015.01.208.

(238) Was, G. S.; Andresen, P. L. Irradiation-Assisted Stress-Corrosion Cracking in Austenitic Alloys. *JOM* **1992**, *44* (4), 8–13. https://doi.org/10.1007/BF03222812.

(239) Raiman, S. S.; Bartels, D. M.; Was, G. S. Radiolysis Driven Changes to Oxide Stability during Irradiation-Corrosion of 316L Stainless Steel in High Temperature Water. *J. Nucl. Mater.* **2017**, *493*, 40–52. https://doi.org/10.1016/j.jnucmat.2017.05.042.

(240) Santamaria, M.; Di Franco, F.; Di Quarto, F.; Pisarek, M.; Zanna, S.; Marcus, P. Photoelectrochemical and XPS Characterisation of Oxide Layers on 316L Stainless Steel Grown in High-Temperature Water. *J. Solid State Electrochem.* **2015**, *19* (12), 3511–3519.

(241) Chen, X.; Shah, K.; Dong, S.; Peterson, L.; Callagon La Plante, E.; Sant, G. Elucidating the Corrosion-Related Degradation Mechanisms of a Ti-6Al-4V Dental Implant. *Dent. Mater.* **2020**, *36* (3), 431–441. https://doi.org/10.1016/j.dental.2020.01.008.

(242) Bachmann, F.; Hielscher, R.; Schaeben, H. Texture Analysis with MTEX – Free and Open Source Software Toolbox https://www.scientific.net/SSP.160.63 (accessed Aug 31, 2019). https://doi.org/10.4028/www.scientific.net/SSP.160.63.

(243) Bachmann, F.; Hielscher, R.; Schaeben, H. Grain Detection from 2d and 3d EBSD Data—Specification of the MTEX Algorithm. *Ultramicroscopy* **2011**, *111* (12), 1720–1733. https://doi.org/10.1016/j.ultramic.2011.08.002.

(244) Bunge, H.-J. *Texture Analysis in Materials Science: Mathematical Methods*; Elsevier, 2013.

(245) Nečas, D.; Klapetek, P. Gwyddion: An Open-Source Software for SPM Data Analysis. *Cent. Eur. J. Phys.* **2012**, *10* (1), 181–188. https://doi.org/10.2478/s11534-011-0096-2.

(246) Dong, S.; La Plante, E. C.; Chen, X.; Torabzadegan, M.; Balonis, M.; Bauchy, M.; Sant, G. Steel Corrosion Inhibition by Calcium Nitrate in Halide-Enriched Completion Fluid Environments. *Npj Mater. Degrad.* **2018**, *2* (1), 32.

(247) Aydoğdu, G. H.; Aydinol, M. K. Determination of Susceptibility to Intergranular Corrosion and Electrochemical Reactivation Behaviour of AISI 316L Type Stainless Steel. *Corros. Sci.* **2006**, *48* (11), 3565–3583. https://doi.org/10.1016/j.corsci.2006.01.003.

(248) MacDonald, D. D.; Urquidi-MacDonald, M. A Coupled Environment Model for Stress Corrosion Cracking in Sensitized Type 304 Stainless Steel in LWR Environments. *Corros. Sci.* **1991**, *32* (1), 51–81.

(249) Frankel, G. S.; Vienna, J. D.; Lian, J.; Scully, J. R.; Gin, S.; Ryan, J. V.; Wang, J.; Kim, S. H.; Windl, W.; Du, J. A Comparative Review of the Aqueous Corrosion of Glasses, Crystalline Ceramics, and Metals. *Npj Mater. Degrad.* **2018**, *2* (1), 1–17. https://doi.org/10.1038/s41529-018-0037-2.

(250) Lin, C. C. A Review of Corrosion Product Transport and Radiation Field Buildup in Boiling Water Reactors. *Prog. Nucl. Energy* **2009**, *51* (2), 207–224. https://doi.org/10.1016/j.pnucene.2008.05.005.

(251) Ansari, T. Q.; Luo, J.-L.; Shi, S.-Q. Modeling the Effect of Insoluble Corrosion Products on Pitting Corrosion Kinetics of Metals. *Npj Mater. Degrad.* **2019**, *3* (1), 1–12. https://doi.org/10.1038/s41529-019-0090-5.

(252) He, A.; Xie, G.; Zhang, H.; Wang, X. A Comparative Study on Johnson–Cook, Modified Johnson–Cook and Arrhenius-Type Constitutive Models to Predict the High Temperature Flow Stress in 20CrMo Alloy Steel. *Mater. Des. 1980-2015* **2013**, *52*, 677–685. https://doi.org/10.1016/j.matdes.2013.06.010.

(253) Peng, W.; Zeng, W.; Wang, Q.; Yu, H. Comparative Study on Constitutive Relationship of As-Cast Ti60 Titanium Alloy during Hot Deformation Based on Arrhenius-Type and Artificial Neural Network Models. *Mater. Des.* **2013**, *51*, 95–104. https://doi.org/10.1016/j.matdes.2013.04.009.

(254) Mackenzie, J. K.; Moore, A. J. W.; Nicholas, J. F. Bonds Broken at Atomically Flat Crystal Surfaces—I: Face-Centred and Body-Centred Cubic Crystals. *J. Phys. Chem. Solids* **1962**, *23* (3), 185–196. https://doi.org/10.1016/0022-3697(62)90001-X.

(255) Galanakis, I.; Papanikolaou, N.; Dederichs, P. H. Applicability of the Broken-Bond Rule to the Surface Energy of the Fcc Metals. *Surf. Sci.* **2002**, *511* (1–3), 1–12.

(256) Wang, S. G.; Tian, E. K.; Lung, C. W. Surface Energy of Arbitrary Crystal Plane of Bcc and Fcc Metals. *J. Phys. Chem. Solids* **2000**, *61* (8), 1295–1300.

(257) Tran, R.; Xu, Z.; Radhakrishnan, B.; Winston, D.; Sun, W.; Persson, K. A.; Ong, S. P. Surface Energies of Elemental Crystals. *Sci. Data* **2016**, *3*, 160080. https://doi.org/10.1038/sdata.2016.80.

(258) Zhou, Z.-Y.; Tian, N.; Li, J.-T.; Broadwell, I.; Sun, S.-G. Nanomaterials of High Surface Energy with Exceptional Properties in Catalysis and Energy Storage. *Chem. Soc. Rev.* **2011**, *40* (7), 4167–4185. https://doi.org/10.1039/C0CS00176G.

(259) Xu, L.; Liang, H.-W.; Yang, Y.; Yu, S.-H. Stability and Reactivity: Positive and Negative Aspects for Nanoparticle Processing. *Chem. Rev.* **2018**, *118* (7), 3209–3250. https://doi.org/10.1021/acs.chemrev.7b00208.

(260) Liu, H.-T.; Armitage, A. F.; Woodruff, D. P. Anisotropy of Initial Oxidation Kinetics of Nickel Single Crystal Surfaces. *Surf. Sci.* **1982**, *114* (2–3), 431–444.

(261) Free, M. L. Understanding the Effect of Surfactant Aggregation on Corrosion Inhibition of Mild Steel in Acidic Medium. *Corros. Sci.* **2002**, *44* (12), 2865–2870. https://doi.org/10.1016/S0010-938X(02)00080-X.

(262) Pessoa, A. M.; Fajín, J. L. C.; Gomes, J. R. B.; Cordeiro, M. N. D. S. Ionic and Radical Adsorption on the Au(Hkl) Surfaces: A DFT Study. *Surf. Sci.* **2012**, *606* (1), 69–77. https://doi.org/10.1016/j.susc.2011.08.023.

(263) Nakhaei Pour, A.; Keyvanloo, Z.; Izadyar, M.; Modaresi, S. M. Dissociative Hydrogen Adsorption on the Cubic Cobalt Surfaces: A DFT Study. *Int. J. Hydrog. Energy* **2015**, *40* (22), 7064–7071. https://doi.org/10.1016/j.ijhydene.2015.04.028.

(264) Stamenkovic, V.; M. Markovic, N.; Ross, P. N. Structure-Relationships in Electrocatalysis: Oxygen Reduction and Hydrogen Oxidation Reactions on Pt(111) and Pt(100) in Solutions Containing Chloride Ions. *J. Electroanal. Chem.* **2001**, *500* (1), 44–51. https://doi.org/10.1016/S0022-0728(00)00352-1.

(265) Stuckless, J. T.; Wartnaby, C. E.; Al-Sarraf, N.; Dixon-Warren, S. J.; Kovar, M.; King, D. A. Oxygen Chemisorption and Oxide Film Growth on Ni {100},{110}, and {111}: Sticking Probabilities and Microcalorimetric Adsorption Heats. *J. Chem. Phys.* **1997**, *106* (5), 2012–2030.

(266) Schaeffler, A. L. Constitution Diagram for Stainless Steel Weld Metal. *Met. Prog.* **1949**, *56* (11), 680.

(267) Muñoz-Márquez, M. A.; Tanner, R. E.; Woodruff, D. P. Surface and Subsurface Oxide Formation on Ni(100) and Ni(111). *Surf. Sci.* **2004**, *565* (1), 1–13. https://doi.org/10.1016/j.susc.2004.06.204.

(268) Lyberatos, G.; Kobotiatis, L. Inhibition of Aluminum 7075 Alloy Corrosion by the Concerted Action of Nitrate and Oxalate Salts. *CORROSION* **1991**, *47* (11), 820–824. https://doi.org/10.5006/1.3585856.

(269) Pastore, T.; Cabrini, M.; Coppola, L.; Lorenzi, S.; Marcassoli, P.; Buoso, A. Evaluation of the Corrosion Inhibition of Salts of Organic Acids in Alkaline Solutions and Chloride Contaminated Concrete. *Mater. Corros.* **2011**, *62* (2), 187–195. https://doi.org/10.1002/maco.201005789.

(270) Berná, A.; Delgado, J. M.; Orts, J. M.; Rodes, A.; Feliu, J. M. In-Situ Infrared Study of the Adsorption and Oxidation of Oxalic Acid at Single-Crystal and Thin-Film Gold Electrodes: A Combined External Reflection Infrared and ATR−SEIRAS Approach. *Langmuir* **2006**, *22* (17), 7192–7202. https://doi.org/10.1021/la060400l.

(271) Tromans, D.; Meech, J. A. Enhanced Dissolution of Minerals: Stored Energy, Amorphism and Mechanical Activation. *Miner. Eng.* **2001**, *14* (11), 1359–1377. https://doi.org/10.1016/S0892-6875(01)00151-0.

(272) Zhou, X.; Luo, C.; Ma, Y.; Hashimoto, T.; Thompson, G. E.; Hughes, A. E.; Skeldon, P. Grain-Stored Energy and the Propagation of Intergranular Corrosion in AA2xxx Aluminium Alloys. *Surf. Interface Anal.* **2013**, *45* (10), 1543–1547. https://doi.org/10.1002/sia.5218.

(273) Sidane, D.; Devos, O.; Puiggali, M.; Touzet, M.; Tribollet, B.; Vivier, V. Electrochemical Characterization of a Mechanically Stressed Passive Layer. *Electrochem. Commun.* **2011**, *13* (12), 1361–1364. https://doi.org/10.1016/j.elecom.2011.08.010.

(274) Wei, Z.; Villamena, F. A.; Weavers, L. K. Kinetics and Mechanism of Ultrasonic Activation of Persulfate: An in Situ EPR Spin Trapping Study. *Environ. Sci. Technol.* **2017**, *51* (6), 3410–3417. https://doi.org/10.1021/acs.est.6b05392.

(275) Suslick, K. S. Sonochemistry. *Science* **1990**, *247* (4949), 1439–1445. https://doi.org/10.1126/science.247.4949.1439.

(276) Pecha, R.; Gompf, B. Microimplosions: Cavitation Collapse and Shock Wave Emission on a Nanosecond Time Scale. *Phys. Rev. Lett.* **2000**, *84* (6), 1328–1330. https://doi.org/10.1103/PhysRevLett.84.1328.

(277) Supponen, O.; Obreschkow, D.; Kobel, P.; Tinguely, M.; Dorsaz, N.; Farhat, M. Shock Waves from Nonspherical Cavitation Bubbles. *Phys. Rev. Fluids* **2017**, *2* (9), 093601. https://doi.org/10.1103/PhysRevFluids.2.093601.

(278) Chen, Y. L.; Israelachvili, J. New Mechanism of Cavitation Damage. *Science* **1991**, *252* (5009), 1157–1160. https://doi.org/10.1126/science.252.5009.1157.

(279) Holian, B. L.; Lomdahl, P. S. Plasticity Induced by Shock Waves in Nonequilibrium Molecular-Dynamics Simulations. *Science* **1998**, *280* (5372), 2085–2088. https://doi.org/10.1126/science.280.5372.2085.

(280) Escaler, X.; Egusquiza, E.; Farhat, M.; Avellan, F.; Coussirat, M. Detection of Cavitation in Hydraulic Turbines. *Mech. Syst. Signal Process.* **2006**, *20* (4), 983–1007. https://doi.org/10.1016/j.ymssp.2004.08.006.

(281) Sancheti, S. V.; Gogate, P. R. A Review of Engineering Aspects of Intensification of Chemical Synthesis Using Ultrasound. *Ultrason. Sonochem.* **2017**, *36*, 527–543. https://doi.org/10.1016/j.ultsonch.2016.08.009.

(282) Pawar, S. V.; Rathod, V. K. Ultrasound Assisted Process Intensification of Uricase and Alkaline Protease Enzyme Co-Production in Bacillus Licheniformis. *Ultrason. Sonochem.* **2018**, *45*, 173–179. https://doi.org/10.1016/j.ultsonch.2018.03.004.

(283) Shirsath, S. R.; Sonawane, S. H.; Gogate, P. R. Intensification of Extraction of Natural Products Using Ultrasonic Irradiations—A Review of Current Status. *Chem. Eng. Process. Process Intensif.* **2012**, *53*, 10–23. https://doi.org/10.1016/j.cep.2012.01.003.

(284) Krevor, S. C. M.; Lackner, K. S. Enhancing Serpentine Dissolution Kinetics for Mineral Carbon Dioxide Sequestration. *Int. J. Greenh. Gas Control* **2011**, *5* (4), 1073–1080. https://doi.org/10.1016/j.ijggc.2011.01.006.

(285) Ragipani, R.; Bhattacharya, S.; Suresh, A. K. Towards Efficient Calcium Extraction from Steel Slag and Carbon Dioxide Utilisation via Pressure-Swing Mineral Carbonation. *React. Chem. Eng.* **2018**, *4* (1), 52–66. https://doi.org/10.1039/C8RE00167G.

(286) Shchukin, D. G.; Skorb, E.; Belova, V.; Möhwald, H. Ultrasonic Cavitation at Solid Surfaces. *Adv. Mater.* **2011**, *23* (17), 1922–1934. https://doi.org/10.1002/adma.201004494.

(287) Gogate, P. R. Cavitational Reactors for Process Intensification of Chemical Processing Applications: A Critical Review. *Chem. Eng. Process. Process Intensif.* **2008**, *47* (4), 515–527. https://doi.org/10.1016/j.cep.2007.09.014.

(288) Pérez-Maqueda, L. A.; Franco, F.; Avilés, M. A.; Poyato, J.; Pérez-Rodríguez, J. L. Effect of Sonication on Particle-Size Distribution in Natural Muscovite and Biotite. *Clays Clay Miner.* **2003**, *51* (6), 701–708. https://doi.org/10.1346/CCMN.2003.0510613.

(289) Birkin, P. R.; Silva-Martinez, S. A Study of the Effect of Ultrasound on Mass Transport to a Microelectrode. *J. Electroanal. Chem.* **1996**, *416* (1), 127–138. https://doi.org/10.1016/S0022-0728(96)04742-0.

(290) Kannan, A.; Pathan, S. K. Enhancement of Solid Dissolution Process. *Chem. Eng. J.* **2004**, *102* (1), 45–49. https://doi.org/10.1016/j.cej.2004.01.022.

(291) Tanguy, D.; Mareschal, M.; Lomdahl, P. S.; Germann, T. C.; Holian, B. L.; Ravelo, R. Dislocation Nucleation Induced by a Shock Wave in a Perfect Crystal: Molecular Dynamics Simulations and Elastic Calculations. *Phys. Rev. B* **2003**, *68* (14), 144111. https://doi.org/10.1103/PhysRevB.68.144111.

(292) Germann, T. C.; Holian, B. L.; Lomdahl, P. S.; Ravelo, R. Orientation Dependence in Molecular Dynamics Simulations of Shocked Single Crystals. *Phys. Rev. Lett.* **2000**, *84* (23), 5351–5354. https://doi.org/10.1103/PhysRevLett.84.5351.

(293) Adhikari, U.; Goliaei, A.; Berkowitz, M. L. Mechanism of Membrane Poration by Shock Wave Induced Nanobubble Collapse: A Molecular Dynamics Study. *J. Phys. Chem. B* **2015**, *119* (20), 6225–6234. https://doi.org/10.1021/acs.jpcb.5b02218.

(294) Vedadi, M.; Choubey, A.; Nomura, K.; Kalia, R. K.; Nakano, A.; Vashishta, P.; van Duin, A. C. T. Structure and Dynamics of Shock-Induced Nanobubble Collapse in Water. *Phys. Rev. Lett.* **2010**, *105* (1), 014503. https://doi.org/10.1103/PhysRevLett.105.014503.

(295) Dong, S.; Chen, X.; La Plante, E. C.; Gussev, M.; Leonard, K.; Sant, G. Elucidating the Grain-Orientation Dependent Corrosion Rates of Austenitic Stainless Steels. *Mater. Des.* **2020**, *191*, 108583. https://doi.org/10.1016/j.matdes.2020.108583.

(296) van Beest, B. W. H.; Kramer, G. J.; van Santen, R. A. Force Fields for Silicas and Aluminophosphates Based on Ab Initio Calculations. *Phys. Rev. Lett.* **1990**, *64* (16), 1955–1958. https://doi.org/10.1103/PhysRevLett.64.1955.

(297) Leeuw, N. H. de; G. Cooper, T. A Computational Study of the Surface Structure and Reactivity of Calcium Fluoride. *J. Mater. Chem.* **2003**, *13* (1), 93–101. https://doi.org/10.1039/B208004D.

(298) Raiteri, P.; Demichelis, R.; Gale, J. D. Thermodynamically Consistent Force Field for Molecular Dynamics Simulations of Alkaline-Earth Carbonates and Their Aqueous

Speciation. *J. Phys. Chem. C* **2015**, *119* (43), 24447–24458. https://doi.org/10.1021/acs.jpcc.5b07532.

(299) Cygan, R. T.; Liang, J.-J.; Kalinichev, A. G. Molecular Models of Hydroxide, Oxyhydroxide, and Clay Phases and the Development of a General Force Field. *J. Phys. Chem. B* **2004**, *108* (4), 1255–1266. https://doi.org/10.1021/jp0363287.

(300) Hockney, R. W. *Computer Simulation Using Particles*; CRC Press, 1988. https://doi.org/10.1201/9780367806934.

(301) Plimpton, S. Fast Parallel Algorithms for Short-Range Molecular Dynamics. *J. Comput. Phys.* **1995**, *117* (1), 1–19. https://doi.org/10.1006/jcph.1995.1039.

(302) Hoover, W. G. Canonical Dynamics: Equilibrium Phase-Space Distributions. *Phys. Rev. A* **1985**, *31* (3), 1695–1697. https://doi.org/10.1103/PhysRevA.31.1695.

(303) Nosé, S. A Unified Formulation of the Constant Temperature Molecular Dynamics Methods. *J. Chem. Phys.* **1984**, *81* (1), 511–519. https://doi.org/10.1063/1.447334.

(304) Ball, A.; Payne, B. W. The Tensile Fracture of Quartz Crystals. *J. Mater. Sci.* **1976**, *11* (4), 731–740. https://doi.org/10.1007/BF01209461.

(305) I. Malyi, O.; V. Kulish, V.; Persson, C. In Search of New Reconstructions of (001) α-Quartz Surface: A First Principles Study. *RSC Adv.* **2014**, *4* (98), 55599–55603. https://doi.org/10.1039/C4RA10726H.

(306) Puchin, V. E.; Puchina, A. V.; Huisinga, M.; Reichling, M. Theoretical Modelling of Steps on the CaF2(111) Surface. *J. Phys. Condens. Matter* **2001**, *13* (10), 2081–2094. https://doi.org/10.1088/0953-8984/13/10/304.

(307) Prewitt, C. T.; Sueno, S.; Papike, J. J. The Crystal Structures of High Albite and Monalbite at High Temperatures. *Am. Mineral.* **1976**, *61*, 1213–1225.

(308) Wainwright, J. E.; Starkey, J. A Refinement of the Structure of Anorthite. *Z. Für Krist. - Cryst. Mater.* **1971**, *133* (1–6), 75–84. https://doi.org/10.1524/zkri.1971.133.16.75.

(309) Capitani, G.; Mellini, M. The Modulated Crystal Structure of Antigorite: The m = 17 Polysome. *Am. Mineral.* **2004**, *89* (1), 147–158. https://doi.org/10.2138/am-2004-0117.

(310) Beran, A.; Zemann, J. Refinement and Comparison of the Crystal Structures of a Dolomite and of an Fe-Rich Ankerite. *Tschermaks Mineral. Petrogr. Mitteilungen* **1977**, *24* (4), 279–286. https://doi.org/10.1007/BF01081130.

(311) Maslen, E. N.; Streltsov, V. A.; Streltsova, N. R. X-Ray Study of the Electron Density in Calcite, CaCo3. *Acta Crystallogr. Sect. B* **1993**, *49* (4), 636–641. https://doi.org/10.1107/S0108768193002575.

(312) Speziale, S.; Duffy, T. S. Single-Crystal Elastic Constants of Fluorite (CaF2) to 9.3 GPa. *Phys. Chem. Miner.* **2002**, *29* (7), 465–472. https://doi.org/10.1007/s00269-002-0250-x.

(313) Chao, S. H.; Hargreaves, A.; Taylor, W. H. The Structure of Orthoclase. *Mineral. Mag. J. Mineral. Soc.* **1940**, *25* (168), 498–512. https://doi.org/10.1180/minmag.1940.025.168.05.

(314) Will, G.; Bellotto, M.; Parrish, W.; Hart, M. Crystal Structures of Quartz and Magnesium Germanate by Profile Analysis of Synchrotron-Radiation High-Resolution Powder Data. *J. Appl. Crystallogr.* **1988**, *21* (2), 182–191. https://doi.org/10.1107/S0021889887011567.

(315) Rice, J. R.; Thomson, R. Ductile versus Brittle Behaviour of Crystals. *Philos. Mag. J. Theor. Exp. Appl. Phys.* **1974**, *29* (1), 73–97. https://doi.org/10.1080/14786437408213555.

(316) Hochella, M. F.; Eggleston, C. M.; Elings, V. B.; Thompson, M. S. Atomic Structure and Morphology of the Albite {010} Surface; an Atomic-Force Microscope and Electron Diffraction Study. *Am. Mineral.* **1990**, *75* (7–8), 723–730.

(317) Heidelbach, F.; Post, A.; Tullis, J. Crystallographic Preferred Orientation in Albite Samples Deformed Experimentally by Dislocation and Solution Precipitation Creep. *J. Struct. Geol.* **2000**, *22* (11), 1649–1661. https://doi.org/10.1016/S0191-8141(00)00072-9.

(318) David, E. C.; Brantut, N.; Hansen, L. N.; Mitchell, T. M. Absence of Stress-Induced Anisotropy During Brittle Deformation in Antigorite Serpentinite. *J. Geophys. Res. Solid Earth* **2018**, *123* (12), 10,616-10,644. https://doi.org/10.1029/2018JB016255.

(319) Baer, D. R.; Blanchard, D. L. Studies of the Calcite Cleavage Surface for Comparison with Calculation. *Appl. Surf. Sci.* **1993**, *72* (4), 295–300. https://doi.org/10.1016/0169-4332(93)90365-I.

(320) Leeuw, N. H. de; C. Parker, S. Surface–Water Interactions in the Dolomite Problem. *Phys. Chem. Chem. Phys.* **2001**, *3* (15), 3217–3221. https://doi.org/10.1039/B102928M.

(321) Barber, D. J.; Heard, H. C.; Paterson, M. S.; Wenk, H. R. Stacking Faults in Dolomite. *Nature* **1977**, *269* (5631), 789–790. https://doi.org/10.1038/269789a0.

(322) Muntoz, A.; Rodriguez, A. D.; Castaing, J. Plastic Deformation of CaF_2 Single Crystals. *Radiat. Eff. Defects Solids* **1995**, *137* (1–4), 213–215. https://doi.org/10.1080/10420159508222722.

(323) Fenter, P.; Cheng, L.; Park, C.; Zhang, Z.; Sturchio, N. C. Structure of the Orthoclase (001)- and (010)-Water Interfaces by High-Resolution X-Ray Reflectivity. *Geochim. Cosmochim. Acta* **2003**, *67* (22), 4267–4275. https://doi.org/10.1016/S0016-7037(03)00374-0.

(324) Rignanese, G.-M.; De Vita, A.; Charlier, J.-C.; Gonze, X.; Car, R. First-Principles Molecular-Dynamics Study of the (0001) $\ensuremath{\alpha}\ensuremath{-}\mathrm{q}\mathrm{u}\mathrm{a}\mathrm{r}\mat

hrm{t}\mathrm{z}$ Surface. *Phys. Rev. B* **2000**, *61* (19), 13250–13255. https://doi.org/10.1103/PhysRevB.61.13250.

(325) Lide, D. R. *CRC Handbook of Chemistry and Physics, 85th Edition*; CRC Press, 2004.

(326) Survey (U.S.), G. *Geological Survey Professional Paper*; U.S. Government Printing Office, 1973.

(327) McCarthy, N. A.; Kelly, P. M.; Maher, P. G.; Fenelon, M. A. Dissolution of Milk Protein Concentrate (MPC) Powders by Ultrasonication. *J. Food Eng.* **2014**, *126*, 142–148. https://doi.org/10.1016/j.jfoodeng.2013.11.002.

(328) King, A. J.; Readman, J. W.; Zhou, J. L. Determination of Polycyclic Aromatic Hydrocarbons in Water by Solid-Phase Microextraction–Gas Chromatography–Mass Spectrometry. *Anal. Chim. Acta* **2004**, *523* (2), 259–267. https://doi.org/10.1016/j.aca.2004.07.050.

(329) Wagterveld, R. M.; Boels, L.; Mayer, M. J.; Witkamp, G. J. Visualization of Acoustic Cavitation Effects on Suspended Calcite Crystals. *Ultrason. Sonochem.* **2011**, *18* (1), 216–225. https://doi.org/10.1016/j.ultsonch.2010.05.006.

(330) Tang, X.; Liu, M.; Tang, Q.; Du, Z.; Bai, S.; Zhu, Y. Effect of Ultrasound on the Dissolution of Magnesium Hydroxide: PH-Stat and Nanoscale Observation. *Ultrason. Sonochem.* **2019**, *55*, 223–231. https://doi.org/10.1016/j.ultsonch.2019.01.023.

(331) Doktycz, S. J.; Suslick, K. S. Interparticle Collisions Driven by Ultrasound. *Science* **1990**, *247* (4946), 1067–1069. https://doi.org/10.1126/science.2309118.

(332) Suslick, K. S.; Nyborg, W. L. ULTRASOUND: Its Chemical, Physical and Biological Effects. **1990**, 3.

(333) Griffith, A. A. The Phenomena of Rupture and Flow in Solids. *Philos. Trans. R. Soc. Lond. Ser. Contain. Pap. Math. Phys. Character* **1921**, *221*, 163–198.

(334) Dove, P. M.; Han, N.; De Yoreo, J. J. Mechanisms of Classical Crystal Growth Theory Explain Quartz and Silicate Dissolution Behavior. *Proc. Natl. Acad. Sci. U. S. A.* **2005**, *102* (43), 15357–15362. https://doi.org/10.1073/pnas.0507777102.

(335) Blum, A. E.; Yund, R. A.; Lasaga, A. C. The Effect of Dislocation Density on the Dissolution Rate of Quartz. *Geochim. Cosmochim. Acta* **1990**, *54* (2), 283–297. https://doi.org/10.1016/0016-7037(90)90318-F.

(336) Plesset, M. S.; Chapman, R. B. Collapse of an Initially Spherical Vapour Cavity in the Neighbourhood of a Solid Boundary. *J. Fluid Mech.* **1971**, *47* (2), 283–290. https://doi.org/10.1017/S0022112071001058.

(337) Brotchie, A.; Grieser, F.; Ashokkumar, M. Effect of Power and Frequency on Bubble-Size Distributions in Acoustic Cavitation. *Phys. Rev. Lett.* **2009**, *102* (8).

(338) Merouani, S.; Hamdaoui, O.; Rezgui, Y.; Guemini, M. Effects of Ultrasound Frequency and Acoustic Amplitude on the Size of Sonochemically Active Bubbles – Theoretical Study. *Ultrason. Sonochem.* **2013**, *20* (3), 815–819. https://doi.org/10.1016/j.ultsonch.2012.10.015.

(339) Blum, A. E.; Yund, R. A.; Lasaga, A. C. The Effect of Dislocation Density on the Dissolution Rate of Quartz. *Geochim. Cosmochim. Acta* **1990**, *54* (2), 283–297. https://doi.org/10.1016/0016-7037(90)90318-F.

(340) Xu, J.; Fan, C.; Teng, H. H. Calcite Dissolution Kinetics in View of Gibbs Free Energy, Dislocation Density, and PCO2. *Chem. Geol.* **2012**, *322–323*, 11–18. https://doi.org/10.1016/j.chemgeo.2012.04.019.

(341) Schott, J.; Brantley, S.; Crerar, D.; Guy, C.; Borcsik, M.; Willaime, C. Dissolution Kinetics of Strained Calcite. *Geochim. Cosmochim. Acta* **1989**, *53* (2), 373–382. https://doi.org/10.1016/0016-7037(89)90389-X.

(342) Blake, J. R.; Leppinen, D. M.; Wang, Q. Cavitation and Bubble Dynamics: The Kelvin Impulse and Its Applications. *Interface Focus* **2015**, *5* (5), 20150017. https://doi.org/10.1098/rsfs.2015.0017.

(343) Blake, J. R. The Kelvin Impulse: Application to Cavitation Bubble Dynamics. *ANZIAM J.* **1988**, *30* (2), 127–146. https://doi.org/10.1017/S0334270000006111.

(344) Hosny, D. M.; Tibbetts, D.; Luenz, R. Cavitation Intensity Measurements for Internal Combustion Engines. *SAE Trans.* **1996**, *105*, 1390–1406.

(345) Conn, A. R.; Scheinberg, K.; Vicente, L. N. *Introduction to Derivative-Free Optimization*; MOS-SIAM Series on Optimization; Society for Industrial and Applied Mathematics, 2009. https://doi.org/10.1137/1.9780898718768.

(346) Barlow, R.; Beeston, C. Fitting Using Finite Monte Carlo Samples. *Comput. Phys. Commun.* **1993**, *77* (2), 219–228. https://doi.org/10.1016/0010-4655(93)90005-W.

(347) Dong, S.; Arnold, R.; La Plante, E. C.; Bustillos, S.; Kumar, A.; Simonetti, D.; Bauchy, M.; Sant, G. Additive-Free Dissolution Enhancement of Industrial Alkaline Wastes Using Acoustic Stimulation. *Manuscr. Prep.* **2020**.

(348) Wu, X.; Liu, L.; Li, W.; Wang, R.; Liu, Q. Effect of Temperature on Elastic Constants, Generalized Stacking Fault Energy and Dislocation Cores in MgO and CaO. *Comput. Condens. Matter* **2014**, *1*, 38–44. https://doi.org/10.1016/j.cocom.2014.10.005.

(349) Kisel, V. P. Mobility of Dislocations in NaCl Single Crystals at Low Temperatures. I. 77 to 298 K. *Phys. Status Solidi A* **1976**, *36* (1), 297–306. https://doi.org/10.1002/pssa.2210360132.

(350) Purnell, P.; Black, L. Embodied Carbon Dioxide in Concrete: Variation with Common Mix Design Parameters. *Cem. Concr. Res.* **2012**, *42* (6), 874–877. https://doi.org/10.1016/j.cemconres.2012.02.005.

(351) Humbert, P. S.; Castro-Gomes, J. CO2 Activated Steel Slag-Based Materials: A Review. *J. Clean. Prod.* **2019**, *208*, 448–457. https://doi.org/10.1016/j.jclepro.2018.10.058.

(352) Gholampour, A.; Ozbakkaloglu, T.; Etemadi, E.; Vincent, T. Sustainable Mortars Containing Fly Ash, Glass Powder and Blast-Furnace and Lead-Smelter Slag. *Mag. Concr. Res.* **2019**, *72* (9), 447–459. https://doi.org/10.1680/jmacr.19.00355.

(353) Teir, S.; Eloneva, S.; Fogelholm, C.-J.; Zevenhoven, R. Dissolution of Steelmaking Slags in Acetic Acid for Precipitated Calcium Carbonate Production. *Energy* **2007**, *32* (4), 528–539. https://doi.org/10.1016/j.energy.2006.06.023.

(354) Said, A.; Mattila, H.-P.; Järvinen, M.; Zevenhoven, R. Production of Precipitated Calcium Carbonate (PCC) from Steelmaking Slag for Fixation of CO2. *Appl. Energy* **2013**, *112*, 765–771. https://doi.org/10.1016/j.apenergy.2012.12.042.

(355) Ammonium Chloride Supplier Industry Grade - Buy Ammonium Chloride Product on Alibaba.com https://www.alibaba.com/product-detail/Ammonium-Chloride-Chloride-Ammonium-Chloride-Price_62266632290.html?spm=a2700.7735675.normalList.1.1422fe5fBZ54Pb&s=p (accessed Jul 28, 2020).

(356) Technical Grade Ammonium Acetate Ch3coonh4 - Buy Technical Grade Ammonium Acetate,Ammonium Acetate Ch3coonh4,Ammonium Acetate Product on Alibaba.com https://www.alibaba.com/product-detail/Ammonium-Acetate-Ch3coonh4-Ch3coonh4-Technical-Grade_60794375815.html?spm=a2700.7735675.normalList.2.456a6985b6AuaN&s=p (accessed Jul 28, 2020).

(357) Yadav, S.; Mehra, A. Dissolution of Steel Slags in Aqueous Media. *Environ. Sci. Pollut. Res.* **2017**, *24* (19), 16305–16315. https://doi.org/10.1007/s11356-017-9036-z.

(358) Yadav, S.; Mehra, A. Experimental Study of Dissolution of Minerals and CO2 Sequestration in Steel Slag. *Waste Manag.* **2017**, *64*, 348–357. https://doi.org/10.1016/j.wasman.2017.03.032.

(359) Altundogan, H. S.; Boyrazli, M.; Tumen, F. A Study on the Sulphuric Acid Leaching of Copper Converter Slag in the Presence of Dichromate. *Miner. Eng.* **2004**, *17* (3), 465–467. https://doi.org/10.1016/j.mineng.2003.11.002.

(360) Owais, M.; Järvinen, M.; Taskinen, P.; Said, A. Experimental Study on the Extraction of Calcium, Magnesium, Vanadium and Silicon from Steelmaking Slags for Improved Mineral Carbonation of CO2. *J. CO2 Util.* **2019**, *31*, 1–7. https://doi.org/10.1016/j.jcou.2019.02.014.

(361) Urosevic, D. M.; Dimitrijevic, M. D.; Jankovic, Z. D.; Antic, D. V. Recovery of Copper from Copper Slag and Copper Slag Flotation Tailings by Oxidative Leaching. *Physicochem. Probl. Miner. Process.* **2015**, *Vol. 51, iss. 1*. https://doi.org/10.5277/ppmp150107.

(362) Kaksonen, A. H.; Särkijärvi, S.; Puhakka, J. A.; Peuraniemi, E.; Junnikkala, S.; Tuovinen, O. H. Chemical and Bacterial Leaching of Metals from a Smelter Slag in Acid Solutions. *Hydrometallurgy* **2016**, *159*, 46–53. https://doi.org/10.1016/j.hydromet.2015.10.032.

(363) Bankole, L. K.; Rezan, S. A.; Sharif, N. M. Assessment of Hexavalent Chromium Release in Malaysian Electric Arc Furnace Steel Slag for Fertilizer Usage. *IOP Conf. Ser. Earth Environ. Sci.* **2014**, *19*, 012004. https://doi.org/10.1088/1755-1315/19/1/012004.

(364) Tang, X.; Liu, M.; Tang, Q.; Du, Z.; Bai, S.; Zhu, Y. Effect of Ultrasound on the Dissolution of Magnesium Hydroxide: PH-Stat and Nanoscale Observation. *Ultrason. Sonochem.* **2019**, *55*, 223–231. https://doi.org/10.1016/j.ultsonch.2019.01.023.

(365) Tang, L.; Dong, S.; Arnold, R.; La Plante, E. C.; Vega-Vila, J. C.; Prentice, D.; Ellison, K.; Kumar, A.; Neithalath, N.; Simonetti, D.; Sant, G.; Bauchy, M. Atomic Dislocations and Bond Rupture Govern Dissolution Enhancement under Acoustic Stimulation. *ACS Appl. Mater. Interfaces* **2020**. https://doi.org/10.1021/acsami.0c16424.

(366) Bond Work Index - an overview | ScienceDirect Topics https://www.sciencedirect.com/topics/engineering/bond-work-index (accessed Oct 16, 2019).

(367) Michaud, D. Table of Bond Work Index by Minerals. *Mineral Processing & Metallurgy*, 2015.

(368) Doll, A. Fine Grinding, A Refresher. 49th Annual Meeting of the Canadian Mineral Processors 2017.

(369) Josefin, Y.; Doll, A. G. Correction of Bond Ball Mill Work Index Test for Closing Mesh Sizes. 14th International Mineral Processing Conference 2018.

(370) Mueller, S.; Llewellin, E. W.; Mader, H. M. The Rheology of Suspensions of Solid Particles. *Proc. R. Soc. Math. Phys. Eng. Sci.* **2010**, *466* (2116), 1201–1228. https://doi.org/10.1098/rspa.2009.0445.

(371) Doran, P. M. Chapter 8 - Mixing. In *Bioprocess Engineering Principles (Second Edition)*; Doran, P. M., Ed.; Academic Press: London, 2013; pp 255–332. https://doi.org/10.1016/B978-0-12-220851-5.00008-3.

(372) Metzner, A. B.; Reed, J. C. Flow of Non-Newtonian Fluids—Correlation of the Laminar, Transition, and Turbulent-Flow Regions. *AIChE J.* **1955**, *1* (4), 434–440. https://doi.org/10.1002/aic.690010409.

(373) Convective Heat Transfer https://www.engineeringtoolbox.com/convective-heat-transfer-d_430.html#targetText=Typical%20convective%20heat%20transfer%20coefficients%20for%20some%20common%20fluid%20flow%20applications%3A&targetText=Free%20Convection%20%2D%20water%20and%20liquids,%2F(m2K)) (accessed Oct 16, 2019).

(374) Overall Heat Transfer Coefficient https://www.engineeringtoolbox.com/overall-heat-transfer-coefficient-d_434.html (accessed Oct 16, 2019).

(375) Rahman, M. S. *Handbook of Food Preservation*; CRC Press, 1999.

(376) Kikuchi, T.; Uchida, T. Calorimetric Method for Measuring High Ultrasonic Power Using Water as a Heating Material. *J. Phys. Conf. Ser.* **2011**, *279*, 012012. https://doi.org/10.1088/1742-6596/279/1/012012.

(377) Kimura, T.; Sakamoto, T.; Leveque, J.-M.; Sohmiya, H.; Fujita, M.; Ikeda, S.; Ando, T. Standardization of Ultrasonic Power for Sonochemical Reaction. *Ultrason. Sonochem.* **1996**, *3* (3), S157–S161. https://doi.org/10.1016/S1350-4177(96)00021-1.

(378) Zuda, L.; Rovnaník, P.; Bayer, P.; Černý, R. Thermal Properties of Alkali-Activated Slag Subjected to High Temperatures. *J. Build. Phys.* **2007**, *30* (4), 337–350. https://doi.org/10.1177/1744259106075234.

(379) Bentz, D.; Peltz, M.; Durán-Herrera, A.; Valdez, P.; Juárez, C. Thermal Properties of High-Volume Fly Ash Mortars and Concretes. *J. Build. Phys.* **2011**, *34* (3), 263–275. https://doi.org/10.1177/1744259110376613.

(380) Holdren, G. R.; Adams, J. E. Parabolic Dissolution Kinetics of Silicate Minerals: An Artifact of Nonequilibrium Precipitation Processes? *Geology* **1982**, *10* (4), 186–190. https://doi.org/10.1130/0091-7613(1982)10<186:PDKOSM>2.0.CO;2.

(381) Criscenti, L. J.; Kubicki, J. D.; Brantley, S. L. Silicate Glass and Mineral Dissolution: Calculated Reaction Paths and Activation Energies for Hydrolysis of a Q3 Si by H3O+ Using Ab Initio Methods. *J. Phys. Chem. A* **2006**, *110* (1), 198–206. https://doi.org/10.1021/jp044360a.

(382) Lagache, M. New Data on the Kinetics of the Dissolution of Alkali Feldspars at 200°C in CO2 Charged Water. *Geochim. Cosmochim. Acta* **1976**, *40* (2), 157–161. https://doi.org/10.1016/0016-7037(76)90173-3.

(383) Busenberg, E.; Clemency, C. V. The Dissolution Kinetics of Feldspars at 25°C and 1 Atm CO2 Partial Pressure. *Geochim. Cosmochim. Acta* **1976**, *40* (1), 41–49. https://doi.org/10.1016/0016-7037(76)90192-7.

(384) Petrovich, R. Kinetics of Dissolution of Mechanically Comminuted Rock-Forming Oxides and Silicates—I. Deformation and Dissolution of Quartz under Laboratory Conditions. *Geochim. Cosmochim. Acta* **1981**, *45* (10), 1665–1674. https://doi.org/10.1016/0016-7037(81)90002-8.

(385) Huber, F. C.; Reid, E. E. Influence of Rate of Stirring on Reaction Velocity. *Ind. Eng. Chem.* **1926**, *18* (5), 535–538. https://doi.org/10.1021/ie50197a027.

(386) Küçük, Ö.; Kocakerim, M. M.; Yartaşı, A.; Çopur, M. Dissolution of Kestelek's Colemanite Containing Clay Minerals in Water Saturated with Sulfur Dioxide. *Ind. Eng. Chem. Res.* **2002**, *41* (12), 2853–2857. https://doi.org/10.1021/ie010356z.

(387) Das, B.; Prakash, S.; Reddy, P. S. R.; Misra, V. N. An Overview of Utilization of Slag and Sludge from Steel Industries. *Resour. Conserv. Recycl.* **2007**, *50* (1), 40–57. https://doi.org/10.1016/j.resconrec.2006.05.008.

(388) Newlands, K. C.; Foss, M.; Matchei, T.; Skibsted, J.; Macphee, D. E. Early Stage Dissolution Characteristics of Aluminosilicate Glasses with Blast Furnace Slag- and Fly-Ash-like Compositions. *J. Am. Ceram. Soc.* **2017**, *100* (5), 1941–1955. https://doi.org/10.1111/jace.14716.

(389) Mysen, B. Silicate Solution, Cation Properties, and Mass Transfer by Aqueous Fluid in the Earth's Interior. *Prog. Earth Planet. Sci.* **2018**, *5* (1), 40. https://doi.org/10.1186/s40645-018-0198-1.

(390) Carletti, C.; De Blasio, C.; Miceli, M.; Pirone, R.; Westerlund, T. Ultrasonic Enhanced Limestone Dissolution: Experimental and Mathematical Modeling. *Chem. Eng. Process. Process Intensif.* **2017**, *118*, 26–36. https://doi.org/10.1016/j.cep.2017.04.012.

(391) Said, A.; Mattila, O.; Eloneva, S.; Järvinen, M. Enhancement of Calcium Dissolution from Steel Slag by Ultrasound. *Chem. Eng. Process. Process Intensif.* **2015**, *89*, 1–8. https://doi.org/10.1016/j.cep.2014.12.008.

(392) Löning, J.-M.; Horst, C.; Hoffmann, U. Investigations on the Energy Conversion in Sonochemical Processes. *Ultrason. Sonochem.* **2002**, *9* (3), 169–179. https://doi.org/10.1016/S1350-4177(01)00113-4.

(393) Luche, J.-L. *Synthetic Organic Sonochemistry*; Springer Science & Business Media, 2013.

(394) Henglein, A. T. J. Mason, J. P. Lorimer: Sonochemistry (Theory, Applications and Uses of Ultrasound in Chemistry), Ellis Horwood Limited. Chichester, and John Wiley and Sons, New York 1988. 252 Seiten, Preis: £ 38.50. *Berichte Bunsenges. Für Phys. Chem.* **1989**, *93* (10), 1150–1151. https://doi.org/10.1002/bbpc.19890931025.

(395) Niemczewski, B. Observations of Water Cavitation Intensity under Practical Ultrasonic Cleaning Conditions. *Ultrason. Sonochem.* **2007**, *14* (1), 13–18. https://doi.org/10.1016/j.ultsonch.2005.11.009.

(396) Raso, J.; Mañas, P.; Pagán, R.; Sala, F. J. Influence of Different Factors on the Output Power Transferred into Medium by Ultrasound. *Ultrason. Sonochem.* **1999**, *5* (4), 157–162. https://doi.org/10.1016/S1350-4177(98)00042-X.

(397) Horst, C.; Kunz, U.; Rosenplänter, A.; Hoffmann, U. Activated Solid–Fluid Reactions in Ultrasound Reactors. *Chem. Eng. Sci.* **1999**, *54* (13), 2849–2858. https://doi.org/10.1016/S0009-2509(98)00316-9.

(398) Tang, L.; Dong, S.; Arnold, R.; La Plante, E. C.; Vega-Vila, J. C.; Prentice, D.; Kumar, A.; Neithalath, N.; Simonetti, Dante; Sant, G.; Bauchy, M. Atomic Dislocations and Bond-Rupture Govern Dissolution Enhancement under Acoustic Stimulation. *Manuscr. Prep.*

(399) Vyazovkin, S.; Burnham, A. K.; Criado, J. M.; Pérez-Maqueda, L. A.; Popescu, C.; Sbirrazzuoli, N. ICTAC Kinetics Committee Recommendations for Performing Kinetic Computations on Thermal Analysis Data. *Thermochim. Acta* **2011**, *520* (1), 1–19. https://doi.org/10.1016/j.tca.2011.03.034.

(400) Manz, O. E. Coal Fly Ash: A Retrospective and Future Look. *Fuel* **1999**, *78* (2), 133–136. https://doi.org/10.1016/S0016-2361(98)00148-3.

(401) Wang, X.; Maroto-Valer, M. M. Dissolution of Serpentine Using Recyclable Ammonium Salts for CO2 Mineral Carbonation. *Fuel* **2011**, *90* (3), 1229–1237. https://doi.org/10.1016/j.fuel.2010.10.040.

(402) Szklarska-Smialowska, Z. Mechanism of Pit Nucleation by Electrical Breakdown of the Passive Film. *Corros. Sci.* **2002**, *44* (5), 1143–1149. https://doi.org/10.1016/S0010-938X(01)00113-5.

(403) Arafin, M. A.; Szpunar, J. A. A New Understanding of Intergranular Stress Corrosion Cracking Resistance of Pipeline Steel through Grain Boundary Character and Crystallographic Texture Studies. *Corros. Sci.* **2009**, *51* (1), 119–128. https://doi.org/10.1016/j.corsci.2008.10.006.

(404) Tedmon, C. S.; Vermilyea, D. A.; Broecker, D. E. Technical Note Effect of Cold Work on Intergranular Corrosion of Sensitized Stainless Steel. *CORROSION* **1971**, *27* (3), 104–106. https://doi.org/10.5006/0010-9312-27.3.104.